PERSONALIA

In memory of Boris Timofeevich Kolomiets (on the 90th anniversary of his birth)

[S1063-7826(98)00108-2]

The thirteenth of August, 1998 would have been the 90th birthday of the distinguished scientist in the physics and technology of semiconductors, Professor Boris Timofeevich Kolomiets. His name has entered into history in the field of physics and technology.

Boris Timofeevich was born in the Altai, where at the age of 13 he began his work activity in the train depot of Barnaul. In 1930 he entered as a laboratory assistant in the Ioffe Physicotechnical Institute of the Russian Academy of Sciences, with which all of his subsequent scientific activity was connected. It was his good fortune to have had as his teacher Professor A. F. Ioffe himself. With his first steps in the world of science he developed and, with the passage of time, solidified his characteristic style—a wide range of deep physical research in newly developing scientific fields with subsequent application of the results of these efforts to the semiconductor industry. The efforts of B. T. Kolomiets in the field of photoelectric phenomena in semiconductors led to the organization (first in Russia) of the production of selenium photoelements (1934) and to the creation, based on thallium sulfide, of the first solar batteries with a huge efficiency for that time (1938) of 1.1%. The research of Professor Kolomiets on the internal photoelectric effect in chalcogenides, in particular, in cadmium sulfide and selenide, culminated in the industrial development of the technology of photoresistors and the organization of their mass production (1948). He did much to introduce photoresistors into different branches of the national economy and is rightly considered as the founder of photoelectric automation. Later, under his leadership various types of varistors, photoresistors, thermoresistors, x-ray and gamma-ray detectors, bolometers and posistors—an entire branch of the electronics industry—were developed and brought into mass production.

During his work on the development of semiconductor materials for electronics he concluded that complex compositions based on three or more chemical elements provide a basis for creating new semiconductor materials with the properties necessary for electronic applications. Based on what he saw as the wide possibilities of multicomponent materials, starting in the early 1950s Professor Kolomiets initiated a systematic research program on complex semiconductor alloys of various composition. Together with other researchers, he was one of the first to synthesize and investigate solid solutions of III–V antimonide-based compounds.

A fundamental result in this branch of research was the discovery by Professor Kolomiets, together with N. A. Goryunova, of a new and broad class of semiconductor materials—glassy semiconductors. From this point on, re-

search in this new field became Professor Kolomiets's main life work. Under his guidance an extensive program of research was initiated. This research made it possible to elucidate the various aspects of electronic phenomena due to the breakdown of long-range order in the structure of glassy semiconductors. This activity stimulated research in the physics of disordered media throughout the world.

Professor Kolomiets, his students and coworkers discovered a number of new and interesting effects in glassy semiconductors. They created a scientific basis for the practical application of glassy semiconductors, which made it possible to improve a number of familiar devices and create fundamentally new ones. Glassy semiconductors have found application in instruments and devices used in television, holography, and opto- and micro-electronics, etc. He, together with his students and colleagues, made a substantial contribution to research into other types of semiconductor materials, such as narrow-gap and gapless semiconductors.

Professor Kolomiets devoted much of his time to admin-

istrative activities. He was an initiator and organizer of many international and local conferences, as well as schools in the physics of glassy and amorphous semiconductors. He created a large scientific school which included over 20 doctors of science and over a hundred candidates of science, most of whom now work in scientific and academic institutions in Russian and in other countries. For his scientific and public work Professor Kolomiets received numerous awards and honorary titles, including two State Prizes of the USSR.

Professor Kolomiets's life interests were not limited to science, technology, and advancing the cause of science. He loved life in all its manifestations—he sang beautifully, almost professionally, appeared in concerts, and enjoyed water skiing until the end of his life. He loved fishing and traveling. He had many friends in various parts of the world.

All who had the good fortune to work with him and know him will always remember his vibrant energy, his creative activity, his good will and readiness to support any interesting and promising endeavor.

Academician Zh. I. Alfërov, Academician B. P. Zakharchenya, V. I. Ivanov-Omskiĭ, A. O. Olesk, and V. M. Lyubin

Editorial Board of the Journal ''Fizika i Tekhnika Poluprovodnikov''

Translated by Paul F. Schippnick

AMORPHOUS, GLASSY AND POROUS SEMICONDUCTORS

Nanoscale mechanism of photoinduced metastability and reversible photodarkening in chalcogenide vitreous semiconductors

A. V. Kolobov

Joint Research Center of Atom Technology, National Institute for Advanced Interdisciplinary Research, 1-1-4 Higashi, Tsukuba, Ibaraki 305, Japan
A. F. Ioffe Physicotechnical Institute, Russian Academy of Sciences, 194201 St. Petersburg, Russia

K. Tanaka

Joint Research Center for Atom Technology—National Institute for Advanced Interdisciplinary Research, 1-1-4 Higashi, Tsukuba, Ibaraki 305, Japan

The present paper reviews the results oblained by the authors in the last three years. By applying *in-situ* (pamp and probe) EXAFS to reversible photostructural changes in chalcogenide vitreous semiconductors we have found an increase in the average coordination number of selenium species in the photoexcited state which comes from the formation of dynamic interchain bonds. Subsequent bond rupture, studied by optically induced ESR, results in the formation of over- and undercoordinated ESR-active defects, which are further transformed into charged valence-alternation pairs. Annealing close to the glass-transition temperature results in recovery of the initial structure. Relationship between the detected structural changes and photodarkening is also discussed. © *1998 American Institute of Physics.*
[S1063-7826(98)00208-7]

1. INTRODUCTION

Being intrinsically nonequilibrium materials, amorphous semiconductors undergo a number of metastable transformations under the action of photoexcitaion, typical examples are the Staebler–Wronski effect in hydrogenated amorphous silicon (a-Si : H) and reversible photostructural changes, also known as reversible photodarkening, in chalcogenide glasses. For recent reviews see Refs. 1–5.

Reversible photodarkening has been known since the early 1970 s. It has manifested itself in a reversible shift of the absorption edge to lower energies under irradiation with the bandgap light.[6,7] X-ray diffraction studies have demonstrated that the photodarkening is closely related to changes in the structure,[8] after which the terms ''photodarkening'' and ''photostructural changes'' have been used interchangeably.

Phenomenological explanation of the effect was given within the configuration-coordinated model which assumed double-well adiabatic potential for the ground state of the system with light transferring the system to the higher-energy, metastable, state.[9–12] Annealing returns the system to the ground state. This approach, which is quite successful in describing the phenomenon obviously could not yield information regarding the nanoscale mechanism of the process.

Raman scattering and EXAFS (extended X-ray absorption fine structure) studies have shown that the number of so-called ''wrong bonds'' (such as As–As bonds in stoichiometric As_2S_3 glass which ideally should contain only As–S

bonds) increased reversibly under irradiation.[13,14] This result, together with the finding that the photodarkening increased strongly in As-rich glasses,[15] suggested that arsenic plays a special role in the process. An attempt to find such structural changes in elemental amorphous arsenic has, however, failed.[16] At the same time, such an effect was clearly observed in elemental amorphous selenium (a-Se) Refs. 17–19, which made it clear that presence of chalcogen is crucial for the photostructural changes to take place.

Most of the studies were performed *ex-situ* when the sample before and after irradiation was studied. It is clear that under such conditions, at best, what happens as a result of the photoexcitation could be detected but not how it happens. We have undertook *in-situ* EXAFS, Raman, and ESR measurements on elemental a-Se and we have been able to detect several stages of the photostructural changes, whose description is the subject of this paper.

2. EXPERIMENTAL

The samples have been prepared by thermal evaporation of bulk material onto silica-glass or aluminum-foil substrates held at room temperature in a vacuum. The film thickness was ~ 1000 Å for the EXAFS and Raman studies and a few microns for the ESR measurements.

EXAFS experiments have been performed in the fluorescence mode at beamline 13B at the Photon Factory. Detailed description of the experimental procedure is given elswhere.[20] Raman scattering was measured in the back-
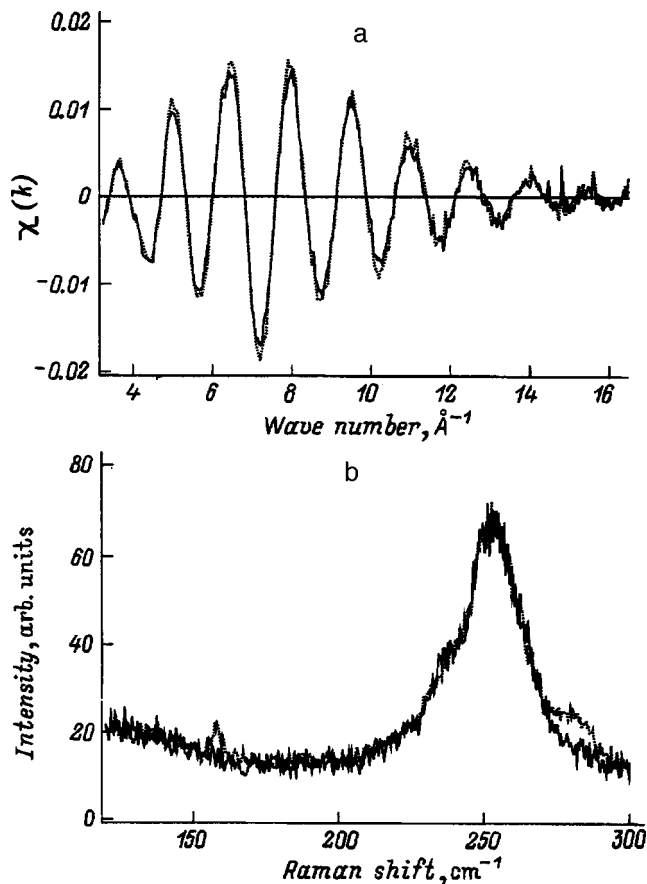
FIG. 1. Raw EXAFS oscillations measured at 30 K as a function of wave number (a) and Raman spectra at the same temperature (b) for the annealed (solid line) and photoexcited (dotted line) *a*-Se film. An increase in the amplitude of the EXAFS oscillation and appearence of new peaks in Raman spectra in the photoexcited state are clearly seen.

scattering geometry and is described in more detail in Ref. 21. Experimental details of the ESR measurement can be found in Ref. 22.

3. RESULTS AND DISCUSSION

3.1. Photoexcited state

Figure 1a, shows raw EXAFS oscillations measured at 30 K for an annealed film of *a*-Se and for the photoexcited *a*-Se as a function of wave number. One can clearly see that the amplitude of oscillations increases in the photoexcited state. Detailed data analysis based on the single scattering theory[23] and curve-fitting, as well as the so-called ratio-method,[24] have revealed that in the photo-excited state the average coordination number of selenium species increases (Fig. 2) dynamically, acquiring its original value after turning off the exciting light. This increase in coordination is believed to be caused by the following process.

Under the photoexcitation, one of the lone-pair (LP) electrons which form the top of the valence band is excited, while the other one is left unpaired in the former LP-orbital. If the time of the carrier localization is long enough, the unpaired LP electron interacts with the neighboring chain and forms an interchain bond, which increases the local coordination of selenium atoms. Once the third bond is formed,
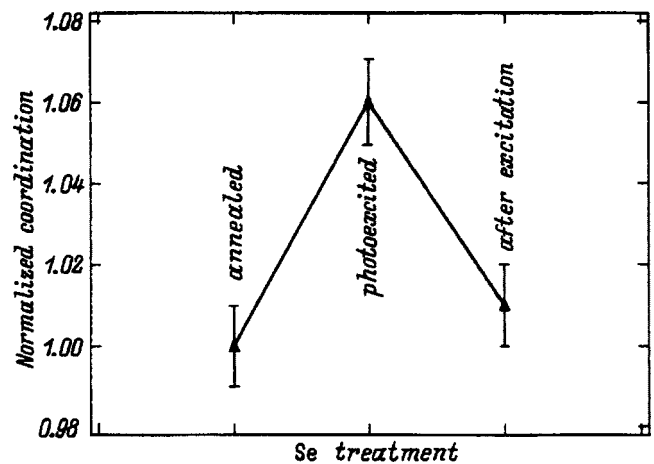

FIG. 2. Change in the average coordination number of *a*-Se at various stages of the film treatment. A reversible increase in the coordination appears in the photoexcited state.

with two electrons lowering their energy from the nonbonding state to the bonding state, the corresponding empty states move to the anti-binding state, leaving no empty state behind. For this reason, recombination of the photoexcited electrons is impossible in the threefold coordinated geometry, and bond rupture is a necessary condition for the recombination, which means that the newly formed bonds are essentially dynamic. It should be kept in mind that, once formed, the new bonds are identical to the ''old'' bonds subtended at the same over-coordinated atoms, which means the system possesses pairs of overcoordinated atoms dynamically incorporated into the rest of the matrix. Structure relaxation and bond rupture in these nanovolumes results in a metastable reversible change and explains recently observed photoinduced fluidity of chalcogenide glasses.[25] Our data demonstrate that the concentration of such pairs reaches 7%.

In order to confirm the conclusion made on the basis of the EXAFS experiment, an *in-situ* Raman scattering study of the photostructural change in *a*-Se has been performed.[21] Figure 1b shows polarized Raman spectra (*HV*-configuration) measured at 20 K for annealed and photoexcited films of *a*-Se. Two peaks, previously not reported, are clearly seen in the photoexcited state at 158 and 280 cm^{-1}. Although unambiguous assignment of these peaks is not straightforward, they clearly demonstrate that bonding in the photoexcited state is changed, and that it can be readily explained by the formation of the interchain bonds. Indeed, the formation of the third bond makes the structure more rigid and should result in an increase in the frequency (the peak located at 280 cm^{-1}). Neutron scattering study of liquid selenium, which is thought to possess about 15% of the threefold coordinated atoms,[26,27] has also shown a similar high-frequence shift.[28] The peak at 158 cm^{-1} possibly results from a shift of the 150 cm^{-1} peak due to E^0 mode to higer frequencies because of increased interchain interaction in the cross-linked geometry in the photoexcited state.

3.2. Bond reconstruction following the photoexcitation

Rupture of dynamic bonds following the photoexcitation should result in creation of unpaired electrons and hence an
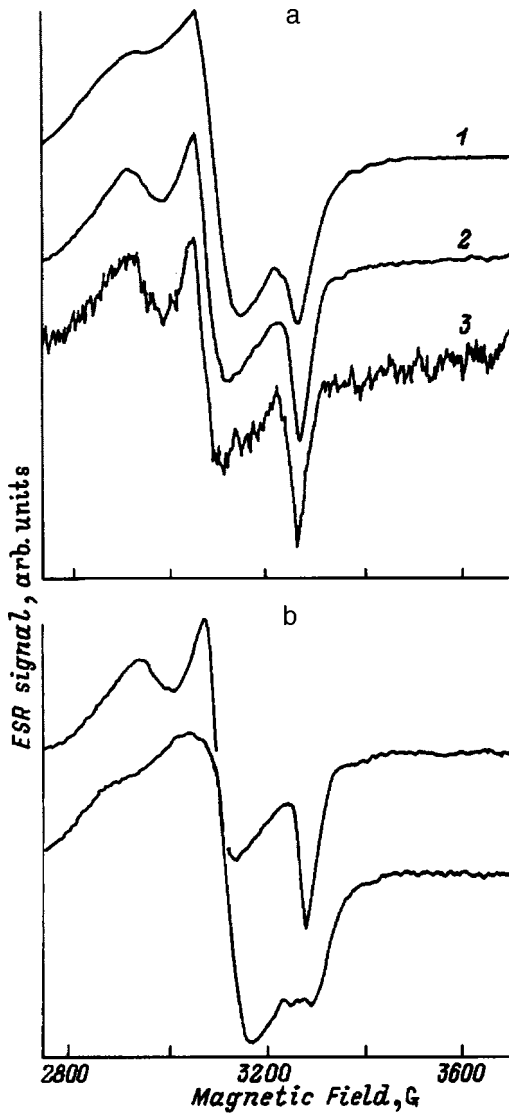
FIG. 3. a — Photoinduced ESR signal and its temperature evolution; an-nealing temperatrue is 20 (*1*), 90 (*2*), 150 (*3*)°C; all spectra were measured at 20 K. b — anisotropic (top) and isotropic (bottom) components of the ESR signal.

FIG. 4. Temperature dependences of partial concentration of the two kinds of ESR-active centers. Threefold coordinated centers (C°_3) are transformed into single coordinated centers (C°_1) in the temperature range from 20 to 90 K.

ESR signal which is not observed in annealed chalcogenide glasses.[29] Indeed, we were able to detect a strong photoin-duced ESR signal in our samples (Fig. 3). With annealing (measurements were always done at 20 K) the lineshape of the signal changed in the temperature range from 20 to 90 K suggesting the presence of more than one center (Fig. 3a), while annealing at higher temperatures resulted only in a decrease of the signal intensity. After annealing at 160 K ESR signal disappears. Deconvolution of the spectra into two components is shown in Fig. 3b. The more stable component is anisotropic and characterized by g-factors $g_1 = 2.22$, $g_2 = 2.099$, and $g_3 = 1.983$. The other one is isotropic and has g-factor value of 2.09.

The obtained g-factor values for the anisotropic center agree very well with the calculated values ($g_1 = 2.22$, $g_2 = 2.075$ and $g_3 = 2.0023$[30]) for the neutral chain end (sin-gly coordinated defect). We believe that the other one comes from a threefold coordinated defect. The observed density of
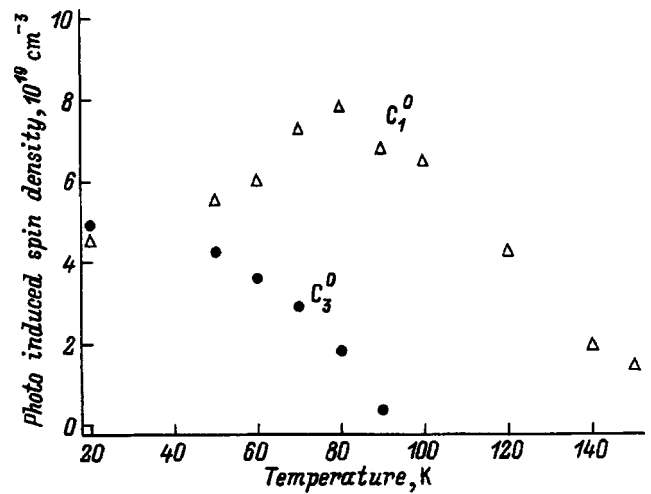
the photoinduced spins ($\sim 10^{20}$ cm^{-3}) agrees well with the concentration of the three-fold coordinated pairs detected in the EXAFS experiment.

Figure 4 shows the temperature dependence of partial concentrations of the two types of ESR-active centers. We see that the concentration of threefold coordinated defects gradually decreases with temperature increase and disappears at about 90 K. Interestingly, the concentration of the other species increases in the same temperature range, demonstrat-ing that there is a conversion of threefold coordinated defects into singly coordinated ones. This experiment is at variance with the simple considerations of the valence-alternation pair (VAP) model[31] but is in full agreement with the results of later calculations.[32] Our EXAFS measurements during the annealing of the irradiated sample in the range from 20 to 160 K (not shown, see Ref. 33) provide further evidence for the change in the defect coordination number upon anneal-ing.

At temperatures higher than 160 K the photoinduced ESR signal disappears but if the irradiation is performed again at low temperature, the builtup of the signal proceeds much faster than in the primary irradiation cycle. This result is similar to that reported for binary As_2S_3 glass[34] and im-plies that the photoinduced defects are not annealed out of 160 K, only their charge state is changed at that temperature. Subsequent irradiation at low temperature does not require creation of defects any more but just their excitation which proceeds at a much faster rate. We have argued[22,23] that at temeratures above 160 K charged valence-alternation pairs ($C_3^+ C_1^-$) are formed.

Annealing at temperatures close to room temperature (the glass-transition temperature for a-Se is about 30 °C) results in a complete recovery of the samples initial parameters.[17]

The complete structural change taking place in a-Se therefore consists in the following (Fig. 5). Under photoex-citation, lone-pair electrons are excited and dynamic inter-chain bonds are formed (step I). Lattice relaxation and bond
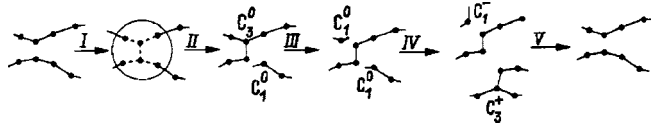
FIG. 5. Structural change taking place in *a*-Se under photoexcitation and during the relaxation process. See text for details.

FIG. 6. Temperature dependences of the photodarkening (a) (after[19]) and concentrations of neutral (c) and charged (b) VAPs.

rupture leads to the creation of neutral VAPs (step II) and appearance of the ESR signal. Threefold coordinated defects are unstable and decay (step III) into singly coordinated defects (dangling bonds). At higher temperatures, pairs of neutral dangling bonds form charged VAPs (step IV), which is accompanied by the disappearence of the ESR signal. Annealing at room temperature leads to recovery of the initial structure (step V).

Our main result, namely, the observed formation of additional (interchain) bonds in the photoexcited state is in sharp contrast to previous models,[1,18,35] which are summarized in Ref. 1 as follows: "One major aspect of light-induced changes in short-range order is breaking of the existing bonds and formation of new bonds" (Ref. 1, p. 124) and "new bonds are formed in place of those broken bonds" (Ref. 35, p. 80). Our results show that the realistic sequence of the processes is exactly the opposite: First dynamical interchain bonds are formed and the bond breaking follows. The crucial role in this process belongs to LP-electrons, whose presence allows the formation of such dynamic bonds. The obtained data make it clear why reversibly photostructural change take place only in amorphous chalcogenides and not in *a*-As or *a*-Si : H — the last two do not possess LP-electrons and cannot undergo the bond switching that easily.

Irradiation of amorphous chalcogenides with linearly polarized light results in the formation of dynamic bonds in the selected direction. This finally results in the redistribution of bonding and nonbonding electrons which manifests itself as photoinduced anisotropy.[36,37]

3.3. Photoinduced processes in binary chalcogenides

In order to check whether the mechanism active in *a*-Se is also valid for more complex glasses we undertook studies of reversible photostructural changes in a binary glass As$_2$Se$_3$. We have found that in the binary glass the coordination of selenium species also increases reversibly in the photo-excited state.[24] Just as in *a*-Se, irradiation of binary glasses results in the appearence of the ESR signal[34] which is annealed out at about room temperature. Secondary irradiation of the films at low temperature is characterized by faster kinetics.[34] Annealing at temperatures above room temperature leads to recovery of the initial parameters.[1–3]

We can thus see that all sets of phenomena are essentially the same for *a*-Se and complex glasses and we thus conclude that the underlying mechanism is also the same. It consists in bond switching via the formation of dynamic bonds due to photo-excitation of LP-electrons of chalcogen atoms. The process in binary chalcogenides is more complicated since, in addition to coordination defects, also stoichio-
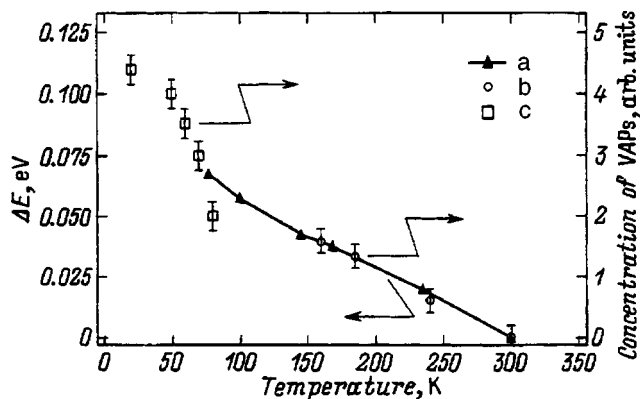
metric defects ("wrong bonds") can also be induced in the material through the formation of dynamic interchalcogen bonds.[13,14,21]

3.4. Relationship between the photostructural change and reversible photodarkening

After the valence-alternation model was first suggested,[31] it was argued that photoinduced VAPs were responsible for the reversible photodarkening[38]. Observed increase in the ESR buildup upon secondary irradiation of pre-irradiated and then annealed films[34] was considered as a further argument in favor of this hypothesis.

Later, however, it was argued[39] that temperature behaviors of the photoinduced ESR and photodarkening were quite different: ESR disappeared at temperatures considerably lower than the photodarkening. This result was the grounds for a conclusion that photoinduced ESR and photodarkening are not related. This concept became a consensus. We believe, however, that this conclusion is wrong, and that the earlier suggestion relating the photodarkening to the photoinduced creation of VAPs is correct.

One should realize that disappearence of ESR does not mean disappearence of defects. ESR is not related to the presence of defects as such but to unpaired spins which are localized at these defects. A much faster ESR buildup in the secondary irradiation cycle is a clear proof that defects have not disappeared after the disappearence of the ESR signal.

The faster component in the secondary irradiation process can be a measure of the concentration of the photoinduced charged defects. Figure 6 shows the temperature dependences of the concentration of charged VAPs calculated in this way (for more details see Ref. 33) and of the photodarkening. The data are normalized in such a way that the first point (at 160 K) for the data for the charged VAPs concentration coincides with the corresponding point for the photodarkening. Remarkable agreement between the two sets of data is clearly seen. Furthermore, we can estimate from Fig. 4 the concentration of neutral (ESR-active) VAPs and put on the same scale in the figure. One can see that the correspondence between the concentration of neutral VAPs and photodarkening is also quite good.

Detailed studies of the recovery of initial parameters in preirradiated[17] *a*-Si have revealed several steps of the process, where the characteristic temperatures for the stages are 100 and 180 K, which agrees with the characteristic temperatures of 90 and 160 K in the temperature behavior of the photoinduced ESR. We can thus claim that reversible photodarkening is directly related to the presence of VAPs (either neutral or charged) in the material. Below we discuss why creation of VAPs results in photodarkening.

The top of the valence band in *a*-Se (and also in binary chalcogenides) is formed by LP-electrons. In the annealed state, LP-orbitals subtended at neighboring atoms are oriented perpendicular to each other in order to minimize the energy. Any displacement from the equilibrium position will change the mutual positions of atoms and the orientation of LP-orbitals, which results in an increase in the energy of the system and causes broadening of the LP band, which manifests itself as photodarkening. It is worthwhile to notice that in all the studied chalcogenide glasses the reversible change in optical absorption is always photodarkening, although the irreversible component of such a change in nonequilibrated, as-prepared films can be either darkening or bleaching, depending on the sample composition and preparation conditions.[1,5]

We would like to stress here that photodarkening is not caused directly by the creation of photoinduced defects, although they obviously make a certain contribution. More important, the photoinduced defects act as knots around which a structural change involving a much larger number of atoms takes place. This change in the positions of the neighboring atoms is responsible for the reversible photodarkening. Similar approach was also used in Refs. 40 and 41. An electric field, introduced by charged defects present in high concentration, may also play a certain role, for example, through its effect on the excitonic absorption edge, as discussed in Ref. 42.

4. CONCLUSIONS

Application of *in-situ* EXAFS, ESR, and Raman scattering to studies of reversible photostructural changes on amorphous chalcogenides has allowed us to detect several stages of this process. The fundamental underlying process is the formation of dynamic interchain bonds in the photo-excited state due to excitaion of LP-electrons. Subsequent bond relaxation and bond rupture results in a metastable structural change.

Remarkable correlation between the photoinduced valence-alternation pairs and photodarkening has been shown and we claim that photocreation of VAPs is the origin of the reversible photodarkening.

One of us (AVK) has started his research work in 1977, joining as a research student the laboratory headed by Professor B. T. Kolomiets. Reversible photostructural changes in amorphous semiconductors have remained one of the main academic interests since that time. Abiding interest in this work shown by Professor B. T. Kolomiets and his guidence for many years are gratefully appreciated by the author (AVK).

[1] G. Pfeifer, M. A. Paesler, and S. C. Agarwal, J. Non-Cryst. Solids **114**, 130 (1989) and the bibliography cited there.

[2] Ke Tanaka, Rev. Solid State Sci. **4**, 641 (1990).

[3] A. Kolobov and S. R. Elliott, Adv. Phys. **40**, 625 (1991).

[4] *Amorphous Silicon Technology-1996*. MRS, Vol. 420, edited by M. Hack, E. Schiff, S. Wagner, R. Schropp, and A. Matsuda (Pittsburg, Pennsylvania, 1996).

[5] K. Shimakawa, A. V. Kolobov, and S. R. Elliott, Adv. Phys. **44**, 475 (1995).

[6] J. S. Berkes, S. W. Ing, and W. J. Hillegas, J. Appl. Phys. **42**, 4908 (1971).

[7] S. A. Keneman, Appl. Phys. Lett. **19**, 205 (1971).

[8] K. Tanaka, Appl. Phys. Lett. **26**, 243 (1975).

[9] K. Tanaka, H. Hamanaka, and S. Iijima, in *Proceedings of the 7th International Conference on Amorphous and Liquid Semiconductors*, edited by W. E. Spear (CICL, University of Edinburgh, 1977) p. 787.

[10] Ke. Tanaka, J. Non-Cryst. Solids **35−36**, 1073 (1980).

[11] A. V. Kolobov, B. T. Kolomiets, O. V. Konstantinov, and V. M. Lyubin, J. Non-Cryst. Solids **45**, 335 (1981).

[12] V. F. Krasnov and V. G. Remesnik, Avtometria **4**, 101 (1980).

[13] M. Frumar, A. P. Firth, and A. E. Owen, Philos. Mag. B **50**, 463 (1984).

[14] C. Y. Yang, M. A. Paesler, and D. E. Sayers, Philos. Mag. B **36**, 9160 (1987).

[15] S. B. Gurevich, N. N. Ilyashenko, B. T. Kolomiets, V. M. Lyubin, and V. P. Shilo, in *Proceedings of the 6th International Conference on Amorphous and Liquid Semiconductors*: *Structure and Properties of Non-Crystalline Semiconductors*, edited by B.T. Kolomiets (Leningrad, 1995), p. 451.

[16] E. Mytilineou, P. C. Taylor, and E. A. Davis, Solid State Commun. **35**, 497 (1980).

[17] R. Chang, Mater. Res. Bull. **2**, 145 (1967).

[18] V. L. Averyanov, A. V. Kolobov, B. T. Kolomiets, and V. M. Lyubin, Phys. Status Solidi A **57**, 81 (1980).

[19] Ke Tanaka and A. Odajima, Solid State Commun. **43**, 961 (1982).

[20] A. V. Kolobov, H. Oyanagi, K. Tanaka, and Ke Tanaka, Phys. Rev. B **55**, 726 (1997).

[21] A. V. Kolobov, A. Roy, and K. Tanaka, J. Non-Cryst. Sol. (to be published).

[22] A. V. Kolobov, M. Kondo, H. Oyanagi, R. Durny, A. Matsuda, and K. Tanaka, Phys. Rev. B **56**, R485 (1997).

[23] E. A. Stern, Phys. Rev. B **10**, 3027 (1974).

[24] A. V. Kolobov, H. Oyanagi, and K. Tanaka, Phys. Solid State **39**, 64 (1997).

[25] H. Hisakuni and Ke Tanaka, Science **270**, 974 (1995).

[26] D. Hohl and R. O. Janes, Phys. Rev. B **43**, 3856 (1991).

[27] C. Bichara, A. Pellegatti, and J.-P. Gaspard, Phys. Rev. B **49**, 6581 (1994).

[28] A. Axman, W. Gissler, A. Kollmar, and T. Springer, Discuss. Faraday Soc. **50**, 74 (1970).

[29] N. F. Mott and E. A. Davis, *Electronic Processes in Non-Crystalline Materials* (Oxford, Clarendon Press, 1979).

[30] M. Abkowitz, J. Chem. Phys. **46**, 4537 (1967).

[31] M. Kastner, D. Adler, and H. Fritzsche, Phys. Rev. Lett. **37**, 1504 (1976).

[32] D. Vanderbilt and J. D. Joannopoulos, Solid State Commun. **35**, 535 (1980).

[33] A. V. Kolobov, M. Kondo, H. Oyanagi, A. Matsuda, and K. Tanaka, Phys. Rev. B (to be published).

[34] D. K. Biegelsen and R. A. Street, Phys. Rev. Lett. **44**, 803 (1980).

[35] S. R. Elliott, J. Non-Cryst. Solids **81**, 71 (1986).

[36] A. V. Kolobov, V. Lyubin, T. Yasuda, and K. Tanaka, Phys. Rev. B **55**, 23 (1997).

[37] A. V. Kolobov, V. Lyubin, T. Yasuda, M. Klebanov, and K. Tanaka, Phys. Rev. B **55**, 8788 (1997).

[38] R. A. Street, Solid State Commun. **24**, 363 (1977).

[39] J. Hautala, W. D. Ohlsen, and P. C. Taylor, Phys. Rev. B **38**, 11 048 (1988).

[40] A. V. Kolobov and G. J. Adriaenssens, Philos. Mag. B **69**, 21 (1994).

[41] P. Nagels, E. Sleeckx, R. Callaerts, and L. Tichy, Solid State Commun. **94**, 49 (1995).

[42] J. D. Dow and D. Redfield, Phys. Rev. B **1**, 3358 (1970).

Transport properties of microcrystalline silicon at low temperatures

J.-H. Zhou

Joint Research Center for Atom Technology (JRCAT), 1-1-4 Higashi, Tsukuba, Ibaraki 305, Japan

S. D. Baranovskii, S. Yamasaki, and K. Ikuta

Angstrom Technology Partnership (ATP)

M. Kondo and A. Matsuda

Electrotechnical Laboratory, 1-1-4 Umezono, Tsukuba, Ibaraki 305, Japan

K. Tanaka

National Institute for Advanced Interdisciplinary Research (NAIR), Department of Physical Chemistry, Center for Material Sciences, Phillips University Marburg, D-35032 Marburg, Germany
(Submitted Janurary 28, 1998; accepted for publication February 23, 1998)
Fiz. Tekh. Poluprovodn. **32**, 905–909 (August 1998)

The dark conductivity and photoconductivity along with pulsed electron spin resonance have been measured over a wide temperature range with a high crystallinity hydrogenated microcrystalline silicon (μc-Si : H) sample. The transport mechanism in μc-Si : H is discussed on the basis of these measurements. Striking similarities in the temperature dependences of the dark conductivity and photoconductivity between μc-Si : H and some well-studied materials, such as hydrogenated amorphous silicon, suggest that at low temperatures hopping of carriers between localized states dominates the transport properties of μc-Si : H. © *1998 American Institute of Physics.* [S1063-7826(98)00308-1]

1. INTRODUCTION

As a potentially important material for realizing high-stability and high-efficiency low-cost electronic devices such as solar cells and thin-film transistors[1,2], hydrogenated microcrystalline silicon (μc-Si : H) is attracting increasing attention. For an electronic material, carrier transport is undoubtedly among the most important properties. μc-Si : H is a mixed-phase system. It consists of crystalline grains and amorphous tissue regions. Thus, the transport in μc-Si : H is of great interest also from the pure physical point of view.

In discussing transport mechanisms in μc-Si : H one should clearly distinguish between highly doped samples and undoped or lightly doped samples. Heavily doped samples demonstrate metallic-like dc conductivity. It has been recently shown[3] that for such samples the spread of the observed mean carrier densities, dc conductivities, and Hall mobilities can be well accounted for by the model of two-phase inhomogenity assuming that crystalline grains are highly conducting and amorphous regions are poorly conducting.

However, little is known about the carrier transport mechanism in undoped μc-Si : H. At temperatures close to room temperature, the dark conductivity and the thermoelectric power of undoped or lightly doped μc-Si : H greatly resemble the transport data for hydrogenated amorphous silicon (a-Si : H). It appears possible to adequately describe these high-temperature transport properties of μc-Si : H in terms of a homogeneous model similar to that developed for a-Si : H.[3] In particular, an adequate description of the

Meyer–Neldel rule in μc-Si : H has been performed in the homogeneous model by just taking into account the statistical shift of the Fermi energy.[3]

Much less is known about the transport properties of undoped or lightly doped μc-Si : H at temperatures considerably below room temperature. It was generally found that the dark conductivity of μc-Si : H does not exhibit a simple thermally activated temperature dependence at low temperatures,[4] and the reason is unclear. Below we present experimental data from the measurements of the dark conductivity and photoconductivity in μc-Si : H extended to low temperatures and the data of the pulsed electron-spin-resonance (ESR).[5] Possible transport mechanisms in μc-Si : H at low temperatures are discussed on the basis of these data.

It seems difficult, if not impossible, at the present stage of research to search for the transport mechanism by purely theoretical considerations. The reason is the lack of information on the basic properties of the material, among which is the band structure of μc-Si : H. Some studies claim the band discontimuties between crystalline grains and amorphous tissue regions to be most pronounced in the valence band,[6,7] whereas others attribute the discontinuity mainly to the conduction band.[8] It is also not clear whether the concepts of mobility edge and of band tail with localized stated, which were developed for homogeneous disordered semiconductors, can be applied to μc-Si : H without substantial modifications.

Therefore, we choose for our discussion the following approach. We compare the observed temperature depen-

dences of the dark conductivity and photoconductivity of μc-Si : H with those predicted by the transport mechanisms in various disordered semiconductors, and discuss whether the transport mechanisms, which predict the observed temperature dependences, can take place in μc-Si : H. It appears that the transport properties of undoped or lightly doped μc-Si : H at low temperatures can be well accounted for in an approach which treats the system as completely homogeneous, similar to the description suggested recently for transport in undoped μc-Si : H at high temperatures.[3]

2. EXPERIMENTAL RESULTS

The thin film μc-Si : H sample studied in this work was prepared from highly H_2-diluted SiH_4 using the conventional plasma-enhanced CVD method.[9] The substrate temperature was 250 °C. The main characteristics of the sample are as follows: thickness $d = 0.42$ μm, volume fraction of the crystallites $\rho = 90$ %, room temperature dark conductivity $\sigma_d(RT) = 1.5 \times 10^{-5}$ Ω^{-1} cm^{-1}, dark dangling bond density $N_{DB} = 1.4 \times 10^{16}$ cm^{-3}. The crystallinity was measured by Raman scattering spectroscopy and confirmed by transmission electron microscope (TEM) observation. The two-pulse electron-spin-echo envelope modulation (ESEEM) measurement[10,11] was carried out using an ESR spectrometer operated at 8 GHz. The classical Hahn echo pulse sequence was used, $P(90°)$-τ-$P(180°)$-τ-echo, where τ is scanned. The conductivity of the sample was measured using a coplanar electrode configuration and the electrodes were Al evaporated on top of the film. For the photoconductivity measurements, a red laser (Ti-sapphire, $\lambda = 710$ nm) was used to illuminate the sample. The photoconductivity is defined as the difference between the total conductivity measured under illumination and the dark conductivity.

The TEM measurement revealed that the film had a columnar structure, with the crystallites extending to almost the entire thickness of the film. No clear amorphous regions could be seen between the grains due to the high (90°) crystallinity. Two ESR signals were observed in the sample: one is the dangling bond (DB) center at $g = 2.005$ and the other is the conduction electron (CE) signal at $g = 1.998$. The ESEEM is capable of detecting the nuclear species surrounding the spin center,[10,11] making use of hyperfine interactions between the electron spin and its surrounding nuclear spins, and thus gives information on the spatial distribution of the electron spins.

Figure 1 shows the frequency domain ESEEM spectra for CEs and DBs in μ-Si : H obtained from the two-pulse ESEEM measurements. We find that for the CEs, only the double frequency of ^{29}Si nucleus appears, whereas for DBs both the double frequncy of ^{29}Si nucleaus and the fundamental frequency of ^{1}H nucleus appear. The fact that the CE echo decay is modulated by only Si nucleus and the DB echo decay is modulated by both Si and H nuclei indicates clearly that the CEs are located in low-H-concentration regions and the DBs in high-H-concentration regions. Given the structure of μc-Si : H, the above results are direct evidence that the CEs are located in the crystalline grains and the DBs in the grain boundary regions. The ESR results have important im-
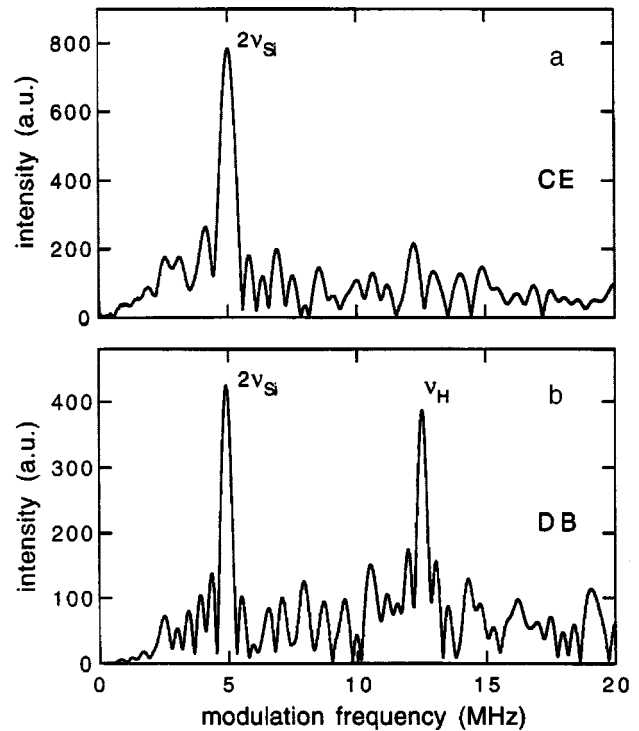

FIG. 1. Fourier transform ESEEM spectra for CE (a) and DB (b) in μc-Si : H.

plications for carrier transport in μc-Si : H. The fact that the CEs prefer to reside in the grains implies that inside a grain the electrons are at a local energy minimum. In other words, electrons have to overcome an energy barrier when they move from one grain to another. Naturally, the energy barriers separating the grains are most likely to be the grain boundaries.

To gain futher insight into the transport mechanism in μc-Si : H, we measured the dark conductivity (σ_d) and photoconductivity (σ_p) of the sample over a wide temperature range. Figure 2 shows the T dependence of the dark conductivity σ_d. Below room temperature the data are well fitted to

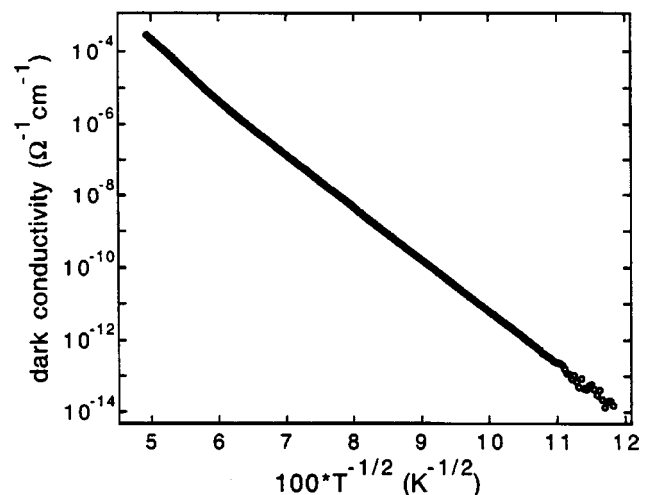$$\sigma_d / \exp[-(T_0/T)^{1/2}], \tag{1}$$

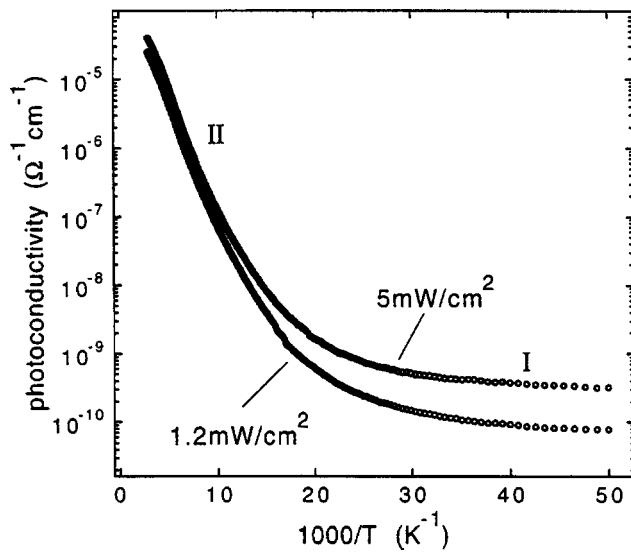FIG. 2. Temperature dependence of the dark conductivity.

FIG. 3. Temperature dependences of the photoconductivity at two light intensities.

where $T_0 \approx 2.6 \times 10^4$ K as determined between 80 and 120 K. The temperature dependences of σ_p are shown in Fig. 3 for two light intensities. Two regimes can be seen: the regime I below ~ 40 K, where σ_p is essentially independent of T and the regime II above ~ 40 K where σ_p increases rapidly with T. From the intensity dependence σ_p/F^γ, where F is the light intensity, we found that the recombination is strongly T dependent. The temperature dependence of the parameter γ is shown in Fig. 4.

3. DISCUSSION

As already mentioned, very little information is available regarding the band structure of μc-Si : H. Moreover, several rather contradictory reports have been published on the band edge discontinuities between crystalline silicon (c-Si) and a-Si : H.[6–8] From the measurements of the internal photoemission at c-Si/a-Si : H heterojunction, Mimura and Hatanaka[6] concluded that the major band edge discontinuity occurs in the valence band ($\Delta E_v = 0.71$ eV), while it is only 0.09 eV in the conduction band (ΔE_c). Cuniot and
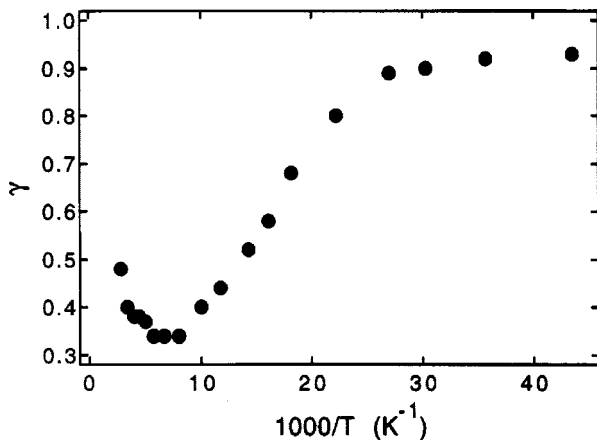

FIG. 4. Temperature dependence of the exponent γ in the relation σ_p/F^γ.

Marfaing,[7] on the other hand, used a structure of c-Si /⟨sputtered a-Si : H⟩ and found the discontinuity in the valence band negligible, with the main discontinuity existing in the conduction band. Xu *et al.*[8] found the discontinuity in the valence band $\Delta E_v \approx 0.26$ eV with a negligible discontinuity in the conduction band $\Delta E_c \approx -0.02$ eV between c-Si : H and a-Si : H. Under such circumstances it is not possible to discuss in detail the transport mechanism. Therefore, we just discuss below the possible mechanisms which in principle could account for our experimental data, and specify the physical conditions for their realization.

We start with the dark conductivity, described by Eq. (1). Such a temperature dependence is well known for two classes of materials — granular metals and those in which transport is by variable-range hopping (VRH), with the density of states (DOS) in the vicinity of the Fermi level possessing a Coulomb gap. Since no information is available on the DOS and on the localization of states in the vicinity of the Fermi level in μc-Si : H, we do not want to speculate on the Coulomb gap and on the VRH mechanism. Moreover, in systems such as doped crystalline semiconductors, where VRH leads to the T dependence of the conductivity described by Eq. (1), T dependence is observed in a very narrow range of low temperatures due to the small width of the Coulomb gap [usually less than 1 meV (Ref. 12)]. Therefore, it is unlikely that VRH is responsible for the observed T dependence of the dark conductivity.

The similarity to the dc current in granular metals is striking. In granular metals, the T dependence described by Eq. (1) is widely observed over a broad temperature range with $T_0 \approx 2 \times 10^4$ K.[13,14] There are some obvious structural similarities between μc-Si : H and granular metals. In both systems, grains are separated by a less conducting material and, as mentioned in the previous section regarding our ESR results, electrons have to overcome or to tunnel through an energy barrier when moving from one grain to another. Various mechanisms have been suggested to account for the T dependence by Eq. (1) for granular metals, among which the percolation model of Simanek[15] seems to be most plausible. However, all these mechanisms take into account just the temperature dependence of the carrier mobility $\mu(T)$, assuming the concentration of charge carriers $n(T)$ to be independent of temperature. Such a description can be applies to μc-Si : H provided that the Fermi energy is located above the mobility edge of the crystalline grains. In such a case the activated dc conductivity at high temperatures would correspond to thermal activation over the energy barriers that separate the crystalline grains, whereas the T dependence described by Eq. (1) at lower T would be due to transport mechanisms similar to those in granular metals.

If, however, the Fermi energy in μc-Si : H is located in the region of localized states in the mobility gap, typical of undoped or slightly doped disordered semiconductors, the conductivity arises from thermal excitation of carriers across the mobility gap into extended states or by hopping processes via localized gap states. In general, the temperature dependence of the dc conductivity is determined by both $n(T)$ and $\mu(T)$

$$\sigma_d = e\,\mu(T)n(T), \tag{2}$$

If one assumes that conduction via extended states dominates the transport, as suggested by Overhof and Otte[3] for high temperatures, $n(T)$ is the only temperature-dependent factor and

$$\sigma_d(T) = \sigma_0 \exp\{-[E_c(T) - E_f(T)]/kT\}, \tag{3}$$

where σ_0 is a conductivity characteristic of transport in extended states $[\approx 200\ \text{S/cm}$ for $a\text{-Si} : \text{H}$ (Ref. 16)], and $E_c(T) - E_f(T)$ is the difference in energies between the conduction level and the Fermi level. For transport in extended states, the T dependence described by Eq. (1) can appear only if $E_c(T) - E_f(T) \sim (kT)^{1/2}$. It is possible that such a relation is valid, and one can even try to search for a particular distribution of the DOS of localized states, which can provide such a relation, using, e. g., the model for the statistical shift of E_f suggested by Overhof and Beyer.[16]

Another possibility is that transport in $\mu c\text{-Si} : \text{H}$ at low temperatures is dominated by hopping processes via localized band tail states. In that case, some particular energy level $E_t(T)$ in the band tail is responsible for the dc current.[17] This temperature-dependent transport energy is determined by the interplay between the two temperature-dependent factors in Eq. (2). For localized states close in energy to the band edge, the mobility is higher but the concentration of electrons is lower than for deeper energy states. This transport level and hence the whole temperature dependence $\sigma_d(T)$ crucially depend on the form of DOS for localized states in the band tail.[18] For some particular form of DOS, hopping of electrons in the vicinity of the transport energy can, of course, give rise to the observed T dependence in Eq. (1). To find this particular DOS one should perform a series of computer simulations to those carried out in Ref. 17 with different forms of the DOS.

We now turn to discuss the temperature dependence of the photoconductivity (PC) shown in Fig. 3. The most remarkable feature of the PC is its similarity to the PC in $a\text{-Si} : \text{H}$.[19] At $T \lesssim 40\ \text{K}$ the magnitude of the PC essentially does not depend on temperature (regime I in Fig. 3) and at temperatures about 100 K the PC increases exponentially with temperature (regime II in Fig. 3). The PC of $a\text{-Si} : \text{H}$ in the regime I is attributed to the energy-loss hopping of photoexcited electrons and holes via localized band tail states.[20] In this regime, the charge carriers move by tunnel transitions to progressively deeper localized states in the band tail. The rates of such transitions are not influenced by temperature, and hence the magnitude of the PC is temperature independent.[20] In $a\text{-Si} : \text{H}$, this energy-loss hopping is usually observed at $T < 40\ \text{K}$.[19] It thus seems reasonable to assume that the same mechanism takes place in $\mu c\text{-Si} : \text{H}$ as well. One could argue that in our $\mu c\text{-Si} : \text{H}$ sample of 90 % crystallinity, the number of localized band tail states is probably not as large as in $a\text{-Si} : \text{H}$ for the same energy-loss hoping mechanism to work. However, the striking feature of the energy-loss hopping mechanism is that the conductivity is independent of the total density of the localized tail

states.[20] Therefore, it is not surprising at all that even the magnitude of the low-temperature photoconductivity of $\mu c\text{-Si} : \text{H}$ is so close to that of $a\text{-Si} : \text{H}$.

If one assumes the energy-loss hopping mechanism for the low-temperature PC of $\mu c\text{-Si} : \text{H}$ and $a\text{-Si} : \text{H}$, one should assume that the dark Fermi energy in $\mu c\text{-Si} : \text{H}$ is located in the region of localized states, as is the case in $a\text{-Si} : \text{H}$. If so, the temperature dependence of the dark conductivity $\sigma_d(T)$ cannot be determined solely by the temperature dependence of the carrier mobility $\mu(T)$. Hence, it seems unlikely that the transport mechanism responsible for the temperature dependence of the dc current in granular metals can take place in $\mu\text{-Si} : \text{H}$ as well. Therefore, an attempt should be made to explain the T dependence in Eq. (1) by using either the extended-state model of Overhof and Otte[3] or the transport-energy description of Gruenewald *et al.*[17]

It is worth noting that the same two models — that of the transport energy[21] and that of the extended-states transport[22] have been suggested to describe the PC in $a\text{-Si} : \text{H}$ at temperatures about 100 K. We do not think that it is possible to descriminate between these two approaches at the present stage of research, because even the band structure of $\mu c\text{-Si} : \text{H}$ is not yet clear. But we think that it is reasonable to search for the transport mechanism in undoped or slightly doped $\mu c\text{-Si} : \text{H}$ at low temperatures in the framework of homogeneous transport models similar to those suggested for $a\text{-Si} : \text{H}$.

4. CONCLUSIONS

Dark conductivity and photoconductivity along with pulsed electron spin resonance have been measured with a $\mu c\text{-Si} : \text{H}$ sample of 90 % crystallinity over a wide temperature range below room temperature. At least three mechanisms can provide the observed temperature dependence of the dark conductivity:

(i) hopping-mechanism for transport in granular metals with temperture-dependent mobility and temperature independent concentration of carriers;[13]

(ii) transport via extended states with temperature-dependent concentration of mobile carriers and temperature-independent mobility;[16]

(iii) hopping transport via localized band tail states, where the interaction between the temperature-dependent mobility $\mu(T)$ and the temperature-dependent concentration of carriers $n(T)$ determines the transport path, which corresponds to the maximum of the product $\mu(T)n(T)$, and hence determines the conductivity.[17]

However, the low-temperature photoconductivity of $\mu c\text{-Si} : \text{H}$ shows such a striking similarity to that of $a\text{-Si} : \text{H}$ that it seems reasonable to assume the same transport mechanism for $\mu c\text{-Si} : \text{H}$ and $a\text{-Si} : \text{H}$. This excludes possibility (i) above, because it is known that in $a\text{-Si} : \text{H}$ the concentration of carriers is temperature dependent at all temperatures, no matter whether the transport is via extended states or by hopping through the localized band tail states.[21,22] Therefore, our study suggests that it is reasonable to search for the transport mechanism in undoped or lightly doped $\mu c\text{-Si} : \text{H}$ at low

temperatures in the framework of homogeneous transport models similar to those suggested for a-Si : H. At very low temperatures (≤ 40 K), the energy-loss hopping seems to determine the photoconductivity in μc-Si : H. It is not possible, however, to discriminate between possibilities (ii) and (iii) for the photoconductivity at higher temperatures and for the dark conductivity, because neither the band structure of μc-Si : H or the DOS of localized states, or the value of the free carrier mobility is known for μc-Si : H.

[1] J. Meier, P. Torres, R. Platz, S. Dubail, U. Kroll, J. A. Anna Selvan, N. Pellaton Vaucher, Ch. Hof, D. Fischer, H. Keppner, A. Shan, K.-D. Ufert, P. Giannoules, and J. Koehler, Mater. Res. Soc. Symp. Proc. **420**, 3 (1996).

[2] S. Guha, J. Yang, P. Nath, and M. Hack, Appl. Phys. Lett. **49**, 218 (1986).

[3] H. Overhof and M. Otte, in *Proceeding of the International Symposium on Condensed Matter Physics* (ISCMP'96, Varna, 1996), p. 23.

[4] P. Hapke, U. Backhausen, R. Carius, F. Finger, and S. Ray, Mater. Res. Soc. Symp. Proc. **420**, 789 (1996).

[5] Some of these data were presented recently at the International Conference ''Hopping and Related Phenomena 7'' (Rackeve, August 1997) and can be found in the Proceedings of the Conference.

[6] H. Mimura and Y. Hatanaka, Appl. Phys. Lett. **50**, 326 (1987).

[7] M. Cuniot and Y. Marfaing, Philos. Mag. B **57**, 291 (1988).

[8] X. Xu, J. Yang, A. Banerjee, S. Guha, K. Vasanth, and S. Wagner, Appl. Phys. Lett. **67**, 2323 (1995).

[9] A. Matsuda, S. Yamasaki, K. Nakagawa, H. Okushi, K. Tanaka, S. Iizuma, M. Matsumura, and H. Yamamoto, Appl. Phys. **19**, L305 (1980).

[10] J. Isoya, S. Yamasaki, H. Okushi, A. Matsuda, and K. Tanaka, Phys. Rev. B **47**, 7013 (1993).

[11] L. Kevan, in *Time Domain Electron Spin Resonance*, edited by L. Kevan and R. N. Schwartz (John Willey & Sons, N.Y., 1979), p. 279.

[12] I. S. Shlimak, M. Kaveh, R. Ussyshkin, V. Ginodman, S. D. Baranovskii, P. Thomas, H. Vaupel, and R. W. van der Heijden, Phys. Rev. Lett. **75**, 4764 (1995).

[13] G.-F. Hohl, S. D. Baranovskii, J. A. Becker, F. Hensel, S. A. Quaiser, and M. T. Reetz, J. Appl. Phys. **78**, 7130 (1995).

[14] J. Heinrichs, A.A. Kumar, and N. Kumar, J. Phys. C: Sol. St. Phys. **9**, 3249 (1978).

[15] E. Simanek, Solid State Commun. **40**, 1021 (1981).

[16] H. Overhof and W. Beyer, Philos. Mag. B **47**, 377 (1983); H. Overhof and P. Thomas, in *Springer Tracts in Modern Physics* **114**, Chapter 4 (1989).

[17] M. Gruenewald and P. Thomas, Phys. Status Solidi B **94**, 125 (1979); M. Gruenewald, P. Thomas, and D. Wuertz, Phys. Status Solidi B **94**, K1 (1979).

[18] S. D. Baranovskii, T. Faber, F. Hensel and P. Thomas, J. Phys.: Condens. Matter **9**, 2699 (1997).

[19] M. Hoheisel, R. Carius, and W. Fuhs, J. Non-Cryst. Solids **97& 98**, 575 (1987); P. Stradins and H. Fritzsche, Philos. Mag. B **69**, 121 (1994).

[20] B. I. Shklovskii, H. Fritzsche, and S. D. Baranovskii, Phys. Rev. Lett. **62**, 2989 (1989).

[21] B. I. Shklovskii, H. Fritzsche, E. I. Levin, and S. D. Baranovskii, in *Advances in Disordered Semiconductors*, Vol. 3, edited by H. Fritzsche (World Scientific, Singapore, 1990), p. 161.

[22] J.-H. Zhou and S. R. Elliott, Phys. Rev. B **48**, 1505 (1993).

Synthesis and properties of Ge–Sb–S: NdCl$_3$ glasses

B. Frumarová

Joint Laboratory of Solid State Chemistry, Czech Academy of Sciences and University of Pardubice

P. Němec and M. Frumar

Department of General of Inorganic Chemistry, University of Pardubice, 53210 Pardubice, Czech Republic

J. Oswald

Institute of Physics, Czech Academy of Sciences, Prague, Czech Republic

High purity $(GeS_2)_{80-x}(Sb_2S_3)_{20}(NdCl_3)_x$ $x=0$, 0.01, 0.1, 0.5, glasses were prepared and their optical properties determined. The Ge–Sb–S system dissolves up to 0.5 mol.% of NdCl$_3$ and still forms stable glasses. The structure of these glasses is formed by interconnected GeS$_4$ tetrahedra and SbS$_3$ pyramids as it follows from the Raman spectra. The glasses are optically well transparent in the range from 15400 cm^{-1} to 1000 cm^{-1}. Doping with Nd creates new absorption bands which can be assigned to electron transfer from the $^4I_{9/2}$ level to $^2G_{5/2}$, $^2G_{7/2}$, $^2H_{11/2}$, $^4F_{9/2}$, $^4F_{7/2}$, $^4S_{3/2}$, $^2H_{9/2}$, $^4F_{5/2}$, $^4F_{3/2}$, $^4I_{13/2}$ and $^4I_{11/2}$ levels. The oscillator strengths and Judd-Ofelt parameters were evaluated. Their values are close to the values of those for Nd^{3+} in another chalcogenide hosts. The long-wavelength absorption edge was found near 1000 cm^{-1} and is due to multiphonon Ge–S and Sb–S vibrations. In doped glasses, several broad luminescence bands near 890, 1080, 1370, and 1540 nm were found. They can be attributed to the transitions from $^4F_{3/2}$ to $^4I_{9/2}$, to $^4I_{11/2}$, to $^4I_{13/2}$ and $^4I_{15/2}$ electron levels. The first luminescence band was excited also by 1064-nm line and represents probably the upconversion of light. © *1998 American Institute of Physics.* [S1063-7826(98)00408-6]

1. INTRODUCTION

The luminescence of rare-earth (RE)-doped glasses has been studied frequently for potential application in lasers, light amplifiers and light upconvertors (see, e.g., Refs. 1–7). For such applications, the quantum efficiency, which is different for the same RE ion placed in different hosts, is important.[3–5] The nonradiative transitions to the lower electron energy state, when several lattice vibrations are generated, compete with the radiative transitions. The emission from the $^4F_{3/2}$ level of Nd^{3+} ion to the underlying $^4I_{15/2}$ level can be quenched because of the above-mentioned multiphonon relaxation.[6,7] The total quantum efficiency can then be reduced.[3,4]

The nonradiative decay rate, σ_p, due to multiphonon relaxation, depends on the energy gap, ΔE, and phonon energy, $\hbar\sigma$, and is given by Miyakawa–Dexter equations[8]

$$\omega_p = \omega_0 \exp\left(\frac{-\alpha\Delta E}{\hbar\sigma}\right), \quad \alpha = \ln(p/g) - 1, \qquad (1)$$

where $p = \hbar\sigma$, g is the electron-phonon coupling strength, and σ_0 is a host-dependent constant.

For glasses with a small maximum phonon energy, the number of phonons required to bridge the energy gap, is large, which lead to a smaller multiphonon relaxation rate.[8] Because of the larger atomic weights of their constitutive elements, the chalcogenide glasses have smaller phonon energies than oxide glasses and the probability of multiphonon relaxation can be lower. The energy gap between $^4F_{3/2}$ and underlying $^4I_{15/2}$ level in Nd ions is relatively large [~ 6500 cm^{-1} (Ref. 9)]. Its value, in combination with low phonon energies, decreases the probability of multiphonon relaxation.

The RE compounds or elements are soluble in oxide and halide glasses, while their solubility in chalcogenides, e.g., in Ge–S system glasses, is generally lower. The achievable density of RE ions in these materials is often too small for many possible applications.[5] A search for homogeneous chalcogenide glasses, which can dissolve larger amounts of RE elements, is therefore useful. From this point of view, the glasses from the system Ge–Sb–S, similarly to the Ge–Ga–S glasses studied earlier,[6] are promising because they can dissolve larger amounts of RE elements or their compounds. The justification of this suggestion is given in Sec. 3 of this paper. The aim of steady work is:

a) the determination of the glass-forming ability in the system, Ge–Sb–S–NdCl$_3$; b) the preparation of homogeneous glasses; c) the determination of basic properties of these glasses, such as optical transmissivity and luminescence.

2. EXPERIMENTAL

Samples were prepared from high-purity elements (Ge, Sb, S, all of 5N-purity) and from neodymium chloride (NdCl$_3$ per analysis, p.a.) in evacuated silica cells

$(T \sim 960$ °C, 40 h) in a rocking furnace. After the synthesis, the cells were annealed at 800 °C for 8 h and then the cells with the melt were water quenched. The homogeneity of the samples was confirmed by optical and electron microscopy and by X-ray diffraction. The composition and its uniformity was also checked by an energy dispersive X-ray analyzer (EDAX).

The optical spectra of cut and polished plane parallel plates were measured using spectrophotometer (Perkin–Elmer Lambda 12, JASCO V-570 (VIS, NIR)) and FT spectrophotometer (BIO–RAD FTS 45 (R)).

The Raman spectra were measured at room temperature by FT Bruker IFS 55/FRA 106 spectrophotometer, the YAG : Nd line (1064 nm) was used for excitation of Raman spectra. The Ar$^+$ ion laser lines (476.5, 488 nm) and YAG : Nd laser line (1064 nm) were used for luminescence excitation.

3. RESULTS

The samples $(GeS_2)_{80-x}(Sb_2S_3)_{20}(NdCl_3)_x$ ($x = 0$, 0.01, 0.1, 0.5) were orange in color. The glasses were optically homogeneous to the eyes and to the methods given above. Their x-ray diffraction patterns did not contain any peaks attributable to crystals. Several broad bands typical of the amorphous state were observed. The densities of the samples increased slightly with increasing Nd^{3+} content ($\rho = 3.22 - 3.26$ g/cm^3).

The short-wavelength absorption edge lies between 500 and 600 nm in the visible region of the spectrum.

Doping of the samples with NdCl$_3$ (Fig. 1) creates new absorption bands near 16 892, 16 447, 14 493, 13 333, 12 315, 11 312 cm^{-1} (Fig. 1), which are similar to the bands of Nd^{3+} in fluoride glasses[10,11] and in GeS$_2$–Ga$_2$S$_3$ glasses.[6] The spectra of glasses with higher Nd content (~ 0.5 mol.%) reveal a weak absorption band near 1950 cm^{-1}, which can be assigned to electronic transitions between the level $^4I_{9/2}$ and $^4I_{11/2}$ of Nd^{3+} ion.

The infrared (IR) spectra revealed weak absorption bands near 1120 and 1310 cm^{-1}, weak bands in the region 1500–1700, 2510, 3240, and 3600–3800 cm^{-1}. The bands in the region 1500–1700 and 3600–3800 cm^{-1} can be assigned to the valence vibrations of OH groups of water sorbed on the surface of the glass. The weak band near 1600 cm^{-1} corresponds to the breathing vibration of OH groups of sorbed water (see, e.g. Refs. 5, 12, and 13). Weak absorption bands near 1120 and 1320 cm^{-1} can be assigned to the vibrations of Sb–O and Ge–O bonds, respectively. Vibrations of S–H bonds probably cause the absorption near 2510 and 3240 cm^{-1}.

The long-wavelength absorption edge of the samples was found near 1000 cm^{-1} and its position can be assigned to the multiphonon Ge–S and Sb–S vibrations. The absorption in the far-IR region behind this absorption edge is strong. The amplitudes and band positions in this region are identical to the undoped samples.

The reduced Raman spectrum of $(GeS_2)_{80}(Sb_2S_3)_{20}$ glass in given in Fig. 2. The broad band with maximum near 340 cm^{-1} can be apparently deconvoluted into four sub-
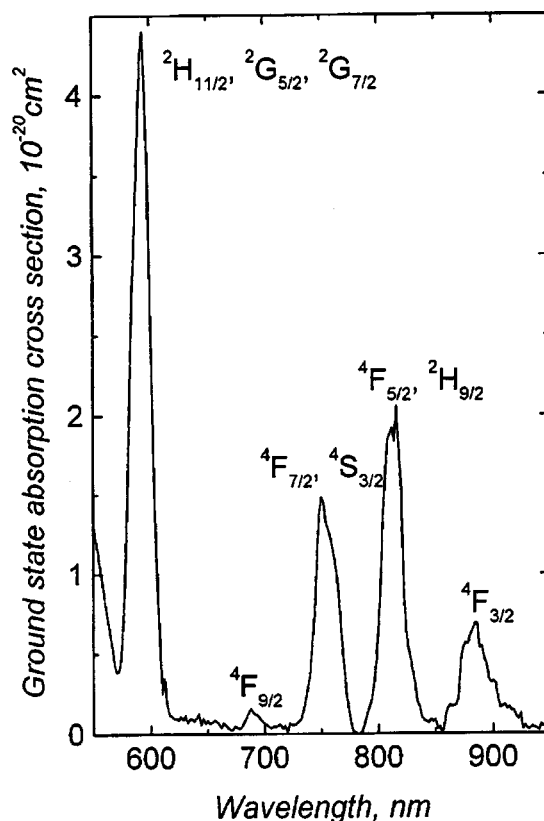

FIG. 1. Ground state absorption cross section of Nd^{3+} ions in $(GeS_2)_{79.5}$ $(Sb_2S_3)_{20}(NdCl_3)_{0.5}$ glass.

bands with maxima near 314 cm^{-1}, 340 cm^{-1}, 367 cm^{-1}, and at 416 cm^{-1}. They can be, in accordance with Ref. 14, assigned to the vibrations of SbS$_3$ pyramids (A_1), to the vibrations of GeS$_4$ tetrahedra (A_1, F_2) and to vibrations of S$_3$Ge–S–GeS$_3$ structural units, respectively. This means that the structure of host glass is formed mainly by the ''lattice'' of GeS$_4$ tetrahedra and SbS$_3$ pyramids, which are interconnected by bridging sulfur atoms. An identical result was obtained also from the analysis of IR reflectivity spectra. Since the Me–S–Me bond angle in germanium dichalcogenides is[15] $\sim 90 - 110°$, and since similar angle can be found in antimony sulfides, the GeS$_4$ tetrahedra and SbS$_3$ pyraminds are vibrating independently and can be considered as isolated oscillators.

The doping of Ge–Sb–S glass by Nd does not influence the IR and Raman spectra, as can be expected, because the density of NdCl$_3$ dissolved molecules in glassy matrix is low.

The luminescence spectra of Nd-activated glasses are given in Figs. 3a and 3b. Four broad luminescence bands are observed. These bands can be assigned to the transitions between the discrete electron levels of Nd^{3+} ions.

4. DISCUSSION

By analogy with Refs. 6, 7, 10, and 11, the absorption bands introduced by Nd doping in the visible (VIS) and near-infrared (NIR) regions of spectrum can be assigned to the electron transitions from the ground $^4I_{9/2}$ level to the $^2G_{5/2}$,
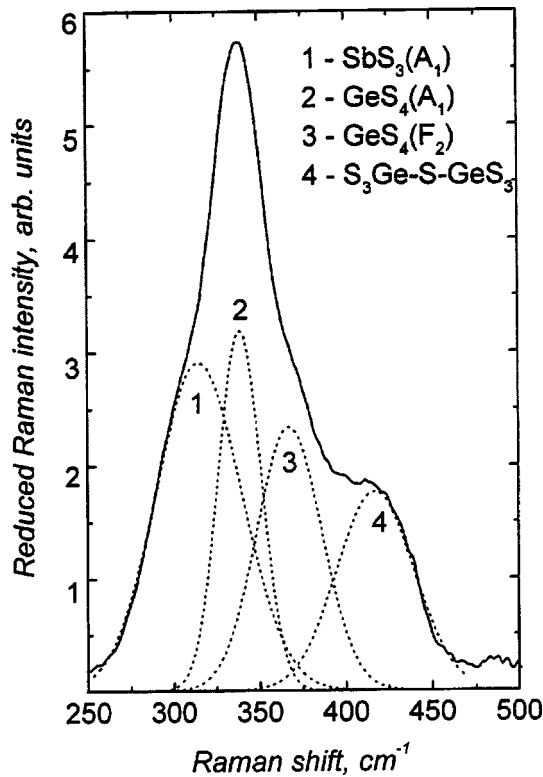
FIG. 2. Raman spectrum of $(GeS_2)_{80}(Sb_2S_3)_{20}$. Deconvoluted individual bands are given by dotted lines. *1* — the band corresponds to the vibrations of SbS_3 pyramids (A_1); *2,3* — the bands correspond to the vibrations of GeS_4 tetrahedra (A_1, F_2); *4* — the band corresponds to the vibrations of S_3Ge–S–GeS_3 structural units. The Raman spectra of doped(GeS_2)–(Sb_2S_3)–$(NdCl_3)$ glasses were identical with the spectra of undoped glasses.

$^2G_{7/2}$, $^2H_{11/2}$, $^4F_{9/2}$, $^4F_{7/2}$, $^4S_{3/2}$, $^2H_{9/2}$, $^4F_{5/2}$ and $^4F_{3/2}$ higher energy levels. The transitions from the $^4I_{9/2}$ level to $(^4G_{7/2}$, $^4G_{9/2}$, $^2K_{13/2})$ are hidden in short-wavelength absorption edge, the transition to $(^2H_{11/2}$, $^2G_{5/2}$, $^2F_{7/2})$, to $(^4F_{7/2}$, $^4S_{3/2})$, and to $(^2H_{9/2}$, $^4F_{5/2})$ levels are forming absorption with overlapping of individual bands (Fig. 1).

The oscillator strength f depends on the intensity of absorption bands and can be calculated from

$$f = \frac{mc}{\pi e^2 N} \int \sigma(\nu) \, d\nu, \qquad (2)$$

where m and e are the electron mass and charge, respectively, $\sigma(\nu)$ is absorption cross section and N is the density of Nd^{3+} ions. The absorption cross section is given by $\sigma(\nu) = \alpha(\nu)/N$, where α is the absorption coefficient, and N is the density of Nd^{3+} ions (cm^{-3}). The obtained values of the oscillator strengths are given in Table I.

A set of f_{exp} data served as the basis for calculation of the Judd-Ofelt parameters,[16,17] Ω_t, using Eq. (3)

$$f_{exp}(aJ, a'J') \cong f_{calc}(aJ, a'J') = \frac{8\pi^2 m\nu}{3h(2J+1)}$$

$$\times \left[\frac{(n^2+2)^2}{9n} \sum_{t=2,4,6} \Omega_t |\mathbf{h}aJ\mathbf{k}U^{(t)}\mathbf{k}a'J'\mathbf{i}|^2 \right],$$

$$(3)$$

where f_{exp} and f_{calc} are experimental and calculated oscillator strengths, respectively. The h is Planck's constant, m is electron mass, ν is mean wave number of the absorption band, J is the ground-state total angular momentum of Nd^{3+} ($J=9/2$), n is the refractive index of the material, Ω_t are the Judd-Ofelt phenomenological intensity parameters and the $\langle aJ\|U^{(t)}\|a'J'\rangle$ are the reduced matrix elements of the tensor operator, $U^{(t)}$ of rank t, which have been taken from Refs. 16 and 17. The obtained values of the Judd-Ofelt parameters are $\Omega_2 = (3.1\pm0.07)\times10^{-20}$ cm^2, $\Omega_4 = (3.2\pm0.1)$ $\times10^{-20}$ cm^2, and $\Omega_6 = (7\pm3)\times10^{-20}$ cm^2. The Ω_i parameters obtained are similar to those for Nd^{3+} in Ga–Ge–As–S glasses.[7]

The luminescence spectrum of Nd-activated glasses (Figs. 3a and 3b) consists of several broad luminescence bands which we assign to the transitions between discrete electron levels of Nd^{3+} ions: $^4F_{3/2}-^4I_{9/2}$ or $^4F_{7/2}-^4I_{11/2}$ (890 nm); $^4F_{3/2}-^4I_{11/2}$ (1080 nm); $^4F_{3/2}-^4I_{13/2}$ (1370 nm); and $^4F_{3/2}-^4I_{15/2}$ (1540 nm). The different shapes of the individual luminescence bands of $NdCl_3$ doped glasses may be caused by the difference in the coordination spheres of Nd^{3+} ions.

The luminescence band with a maximum near 890 nm has higher energy than the exitation light (1064 nm) and it is probably caused by an upconversion effect. The exciting light can transfer electrons of Nd^{3+} ions from the fundamental level $^4I_{9/2}$ to the excited level $^4F_{3/2}$ or to the $^4F_{7/2}(^4S_{3/2})$ level in two steps. The difference in energies between $^4F_{3/2}$ and $^4I_{9/2}$ levels is higher (Fig. 4) than the energy of excitation light (1064 nm$=9398$ cm^{-1} and the process of excitation can not proceed by absorption of one photon only. The suggestion of a two-step model for mechanisms of absorption is in accordance with the logarithmic dependence of the intensity of luminescence of the excitation intensity (Fig. 5). The slope of this line, $k=1.82$, strongly suggests two-photons upconversion process. The value of k is less than 2, which can be expected, because the downward electron transitions tend to equalize the populations of the pumped initial and final states. Such an effect is commonly observed in two-photon upconversion processes.[18] We assume that excited states produced by upconversion are $^4F_{3/2}$ or $^4F_{7/2}(^4S_{3/2})$ (Fig. 4). These states are accessible by excitation of 1064 nm (9398 cm^{-1}) photon from $^4I_{11/2}$ to $^4F_{3/2}$ electron level or from the $^4I_{13/2}$ to $^4F_{7/2}$ level. Transitions from the ground $^4I_{9/2}$ level to the $^4I_{11/2}$ level and to the $^4I_{13/2}$ level demand lower energy than the excitation light (~9400 cm^{-1}), and are therefore less efficient. This fact probably lowers the total luminescence intensity of the "up-

TABLE I. Experimental (f_{exp}) and calculated (f_{calc}) oscillator strengths for transitions from $^4I_{9/2}$ level of Nd^{3+} ion to the level given in the table.

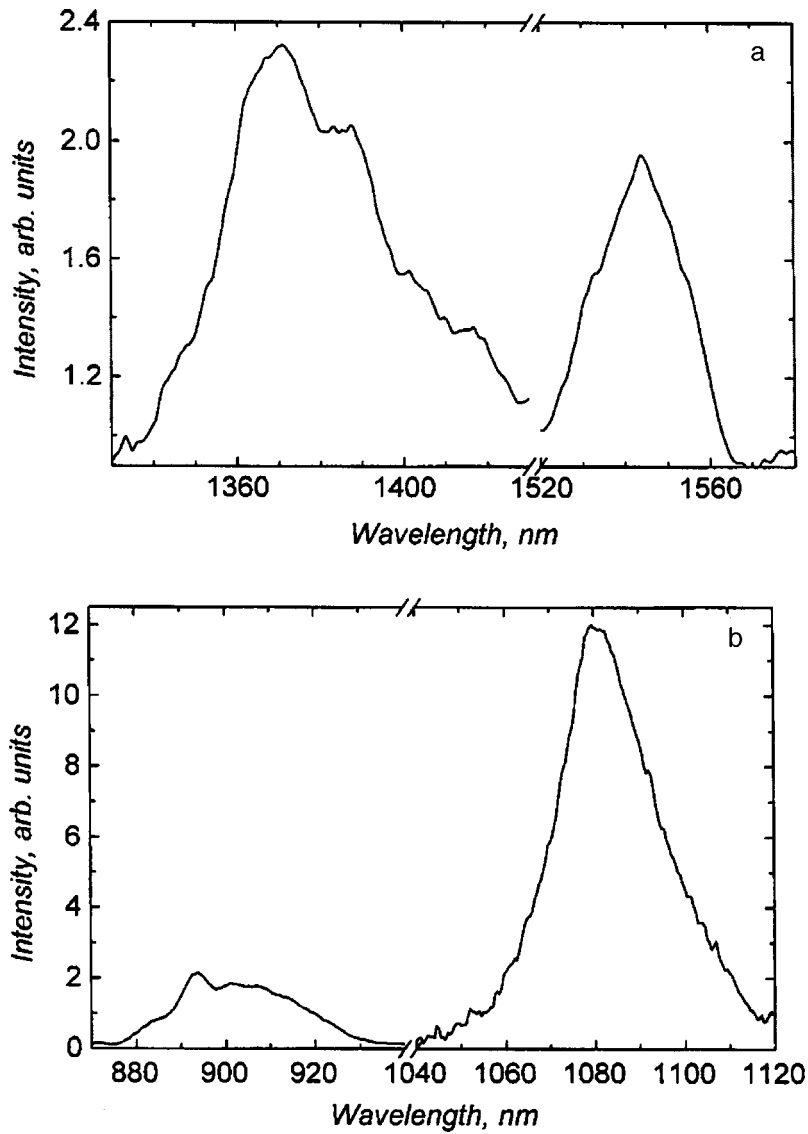| Level	Wavenumber, cm^{-1}	f_{exp}, 10^{-8}	f_{calc}, 10^{-8}
$^4F_{3/2}$	11 312	281	286
$^4F_{5/2}$, $^2H_{9/2}$	12 315	711	705
$^4F_{7/2}$, $^4S_{3/2}$	13 333	619	624
$^4F_{9/2}$	14 493	59	54
$^2H_{11/2}$, $^2G_{5/2}$, $^2G_{7/2}$	16 447, 16 892	2548	2550

FIG. 3. Luminescence spectrum of the glass $(GeS_2)_{79.9}(Sb_2S_3)_{20}(NdCl_3)_{0.1}$. a — the bands with maxima near 1370 and 1540 nm (excitation line 1064 nm); b — the bands with maxima near 890 and 1080 nm. The band with maximum near 890 nm was excited by 1064-nm laser line and corresponds apparently to the upconversion. The luminescence band near 1080 nm was excited by Ar^+ laser lines (476.5 or 488 nm). The intensity of excitation light for both bands was different.

converted'' light. Since the $^4F_{3/2}$ level of Nd^{3+} is generally relatively long lived,[18] the upconversion via this level is more probable.

It is also possible to explain the presence of a luminescence band with a maximum near 890 nm (when excited by 1064 nm light) as an anti-Stokes band which is excited with the contribution from several phonons. The energy difference between the excitation and luminescence light maxima is $\sim 1950\ cm^{-1}$, the highest energy of phonons in this type of glasses can be evaluated as $\sim 400\ cm^{-1}$.[5] This means that ~ 5 phonons should be absorbed for such luminescence excitation, which seems to be less probable.

The relatively small intensity of the luminescence transitions can be attributed to several factors: The wavelength used for excitation (476.5, 488 nm) was not optimal for Nd $^4F_{3/2}$ level excitation. This excitation is strongly absorbed due to fundamental absorption and the penetration depth of

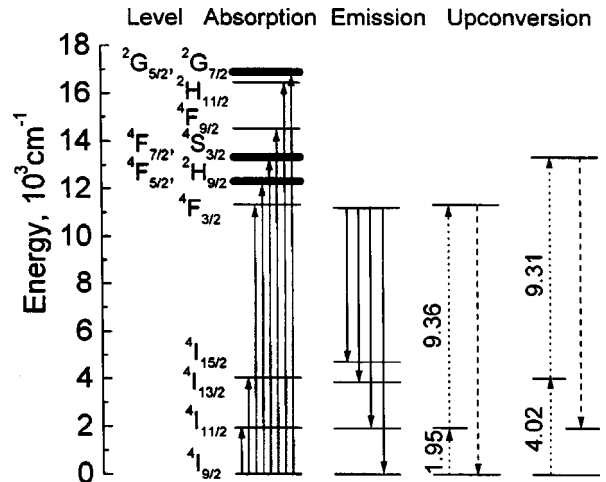FIG. 4. Energy level diagram of electron transitions in Nd^{3+} ion in $(GeS_2)_{79.9}(Sb_2S_3)_{20}(NdCl_3)_{0.5}$ glass. Possible upconversion transitions are given by the dotted lines; corresponding luminescence transitions are represented by the dashed lines.
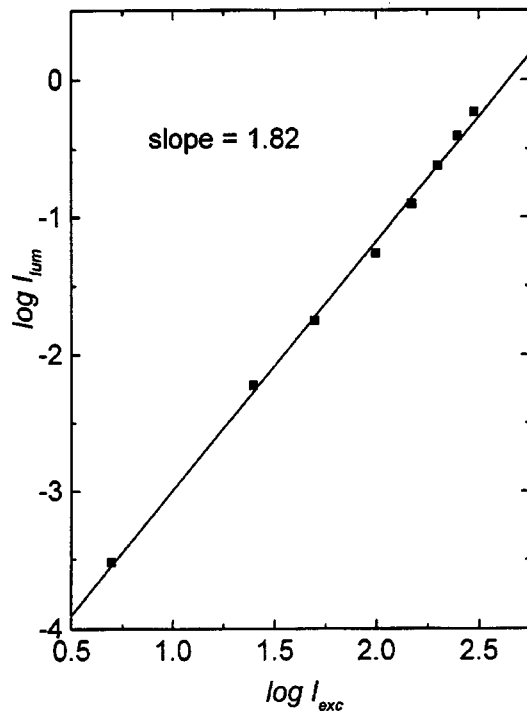
FIG. 5. Dependence of the luminescence intensity of the band near 890 nm on the intensity of excitation light (1064 nm).

excitation light is very low. In contrast, the 1064-nm excitation light is not absorbed in studied glasses. The efficiency of excitation is therefore very small, too. A relatively low intensity of luminescence could be also be attributed to the presence of small amounts of OH groups, which were identified by IR spectroscopy. It is known that OH groups can be effective quenchers of the radiation at 1070 nm (~ 930 cm^{-1}).[9] The intensity of luminescence can be also decreased by multiphonon relaxation. Since the energy gap between the $^4F_{3/2}$ level and the next lower level ($^4I_{15/2}$) of Nd is relatively high and since the phonon energy in chalcogenide glasses is low, the probability of such multiphonon relaxation is low, as we have mentioned above.

5. CONCLUSIONS

The $GeS_2 - Sb_2S_3$ glasses dissolve relatively large amounts of Nd^{3+} and form stable and homogeneous glasses.

Their properties are similar to Nd-doped Ge–Ga–S and Ge–Ga–As–S glasses.[6,7] Because the phonon frequencies in sulfide glasses are lower than in oxide or halide glasses, the Nd-doped chalcogenides may be good candidates for high-efficiency light amplifiers, up-converters, lasers, and other optoelectronic devices.

*)E-mail: Miloslav.Frumar@upce.cz

[1] A. C. Propper, J. N. Carter, R. D. T. Lauder, D. C. Hanna, S. T. Davey, and D. Szebesta, J. Opt. Soc. Am. B **11**, 886 (1994).

[2] W. S. Brocklesby and A. Pearson, J. Lumin. **59**, 333 (1994).

[3] D. W. Hewak, R. S. Deol, J. Wang, G. Wylangowski, J. A. Mederios Neto, B. N. Samson, R. I. Laming, W. S. Brocklesby, D. N. Payne, A. Jha, M. Poulain, S. Otero, S. Surinach, and M. D. Baro, Elec. Lett. **29**, 237 (1993).

[4] D. R. Simons, A. J. Faber, and H. De Waal, in *Proceedings of the 8th International Symposium on Halide Glasses,* Perros-Guirrec, France, 1992 (CNET, Lannion, France 1992), p. 448.

[5] B. Frumarová, J. Oswald, P. Krečmer, M. Frumar, V. Černý, and V. Smrčka, Opt. Mater. **6**, 217 (1996).

[6] B. Frumarová, M. Frumar, and J. Oswald, J. Non-Cryst. Solids **213–214**, 58 (1997).

[7] A. Belykh, L. Glebov, C. Lerminiaux, S. Sunter, M. Mikhailov, A. Pliukhin, M. Prassas, and A. Przhevuskii, J. Non-Cryst. Solids **213–214**, 238 (1997).

[8] R. S. Deol, D. W. Hewak, S. Jordery, A. Jha, M. Poulain, M. D. Baro, and D. N. Payne, J. Non-Cryst. Solids **161**, 257 (1993).

[9] H. Ebendorff-Heidepriem, W. Seeber, and D. Ehrt, J. Non-Cryst. Solids **183**, 191 (1995).

[10] P. Nachimuthu and R. Jaganathan, Phys. Chem. Glasses **36**, 194 (1995).

[11] S. X. Cardoso, Y. Messaddeq, L. A. O. Nunes, and M. A. Aegerter, J. Non-Cryst. Solids **161**, 277 (1993).

[12] M. Horák and D. Papuušek, in *Infrared Spectra and Structure of Molecules* (Academia, Praha 1976), p. 254 (in Czech).

[13] M. Frumar, B. Petrová, V. Černý, and I. Pavlik, in *Advanced Solid State Chemisty, Materials Science Monographs*, Vol. 60, edited by M. Frumar, V. Černý, and L. Tichý (Elsevier, Amsterdam 1989), p. 401.

[14] L. Koudelka, M. Frumar, and M. Pisárčik, J. Non-Cryst. Solids **41**, 171 (1980).

[15] Z. V. Popovic, Phys. Lett. **94A**, 2442 (1983).

[16] B. R. Judd, Phys. Rev. **127**, 750 (1962).

[17] G. S. Ofelt, J. Chem. Phys. **37**, 511 (1962).

[18] A. T. Stanley, E. A. Harris, T. M. Searle, and J. M. Parker, J. Non-Cryst. Solids **161**, 235 (1993).

Laser-induced anisotropic absorbtion, reflection, and scattering of light in chalcogenide glassy semiconductors

V. M. Lyubin and M. L. Klebanov

Department of Physics, Ben-Gurion University of the Negev, Beer-Sheva 84105, Israel
(Submitted February 2, 1998; accepted for publication February 23, 1998)
Fiz. Tekh. Poluprovodn. **32**, 915–922 (August 1998)

Anisotropy induced in thin–film and bulk samples of chalcogenide glassy semiconductors by the linearly polarized light of different spectral ranges is studied. Three different ranges of exciting photon energy can be distinguished. 1) Above-band-gap light excitation is studied in film samples, two distinct processes are identified in this range: creation of photoinduced defects and their photostimulated orientation and reorientation; a ″defect-based″ model of photoinduced anisotropy is further developed. 2) Subband-gap light excitation is studied in bulk samples; creation of anisotropically scattered centers is assumed to be the basis of all photoinduced vector phenomena in that spectral range. 3) Superband-gap light excitation is studied in film and bulk samples because the application of differential reflectance spectroscopy; it was shown that not only defects but also main covalent bonds of the glass can be oriented and reoriented by the linearly polarized light that generates the photoinduced dichroism in this spectral interval. © *1998 American Institute of Physics.* [S1063-7826(98)00508-0]

1. INTRODUCTION

It is an honor for us to write a paper for the special issue of *Physics and Technics of Semiconductors* in recognition of the outstanding role of our teacher, Professor Boris Timofeevich Kolomiets, in the field of disordered semiconductors. We wish to stress that Professor Kolomiets was not only the pioneer in the broad study of glassy semiconductors but also directly participated in the initial investigation of photoinduced anisotropy in these materials.

The phenomenon of photoinduced anisotropy (PA) was discovered when we studied the polarization state of light transmitted through the film of chalcogenide glassy semiconductor (ChGS) irradiated by a linearly polarized laser beam.[1,2] Both photoinduced dichroism and photoinduced birefringence of absorption, which were observed in the experiments, were explained by the interaction of light with optically anisotropic structural elements whose optical axes are oriented randomly.[2] Later, these phenomena were investigated by different authors, working with ChGS films of various compositions.[3–8] Different approaches to explain PA were developed. They are based on consideration of interaction of the inducing light with native quasiatomic defects,[7] with quasimolecular defects (three-center bonds)[9] or with bistable centers having a wide distribution of relaxation times.[10] Fritzsche discussed the photoinduced redistribution of anisotropic microvolumes as a base of PA,[11] and Tikhomirov and Elliott developed recently a new model,[8] in which the PA is connected with photostimulated orientation and reorientation of valence-alteration pairs (VAP's), which are characteristic defects in chalcogenide glasses.[12] All the above-mentioned effects were obtained in the investigation of thin ChGS films irradiated by above-band-gap light.

Phenomena of photoinduced dichroism were revealed also in bulk ChGS (As_2S_3 and $As_{34}S_{52}I_{14}$ bulk glasses)[13,14] and in As_2S_3 chalcogenide glassy fibers irradiated by the subband-gap light.[15] Later, investigation of PA in bulk ChGS samples was carried out by many research groups.[16,17]

In this paper we consider the results of a PA study conducted recently in the amorphous semiconductors laboratory of the Ben-Gurion University (Beer-Sheva, Israel) either independently or in close cooperation with colleagues from other research centers.

It is convenient to divide all data obtained into parts concerning the photoinduced anisotropic absorbtion, reflection, and scattering of light. We will consider additionally the cases of polarization-dependent, laser-induced crystallization of some amorphous chalcogenide films and of polarization-dependent photodoping of ChGS films with silver.

2. EXPERIMENTAL

Two groups of samples were investigated in this research. Thin-film samples were produced by thermal evaporation of starting glassy meterials onto silica glass substrates in vacuum under residual pressure $p \sim 10^{-6}$ Torr. The film thickness was $0.3 - 4.0$ μm. Bulk samples were prepared by polishing melt-quenched chalcogenide glasses and had typical thickness of several millimeters.

All measurements were done at room temperature using the experimental setups shown schematically in Fig. 1. The setup in Fig. 1a was used for investigation of thin film samples. Two beams of identical gas lasers (either He–Ne-lasers, working at $\lambda = 633$ nm or Ar^+-lasers, working at $\lambda = 515$ nm) illuminated simultaneously the same area of the film. The linear polarization state of one laser (inducing light) could be changed to the orthogonal one with a quarter-wave plate. The attenuated light beam from the other laser (probing light) passed through an electrooptical modulator,
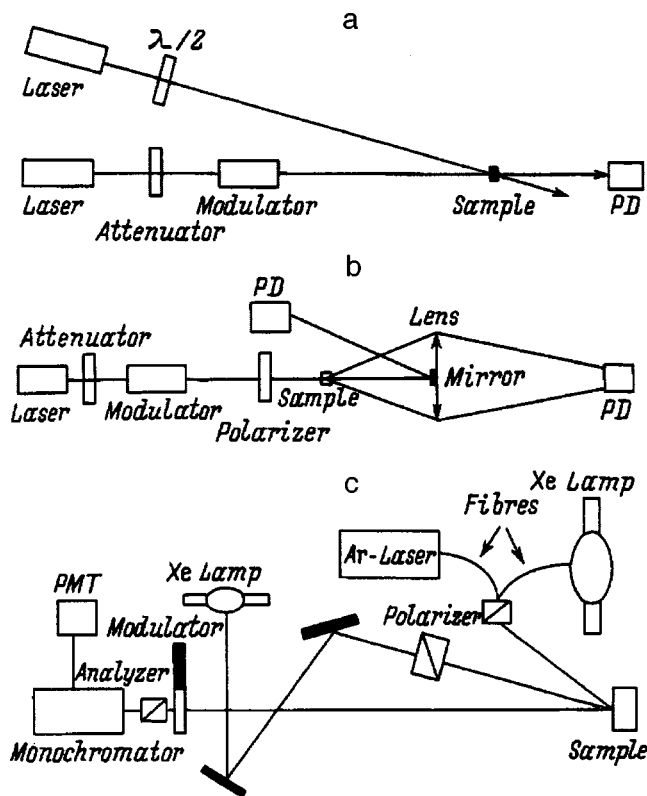
FIG. 1. Experimental setup for investigation of photoinduced anisotropy of absorbtion (a), scattering (b), and reflection (c) of laser light.

which modulated the polarization discontinuously between two orthogonal states at a frequency of 1 kHz. The laser beam was then passed through the sample and was incident on the Si photodiode (PD), permitting to measure the photoinduced transmission anisotropy $T_{II}-T_I=2(I_{II}-I_I)/(I_{II}+I_I)$, where I_{II} and I_I are the intensities of the beams with two orthogonal electric vectors. This setup permitted us to study initial periods of PA kinetics and relaxation. To measure the difference signal $I_{II}-I_I$ we used the method of synchronous detection.

In Figure 1b we show the setup that allowed us to measure simultaneously the laser radiation transmitted through the bulk ChGS sample and radiation scattered by the sample to various angles up to 230 mrad. The collecting lens, arranged behind the sample, focused the scattered ligth to a photodiode, and a small mirror, fixed in the central part of the lens, reflected the transmitted light beam to a second photodiode. He–Ne-laser radiation ($\lambda=633$ nm), which was the subband-gap radiation for the studied bulk glass samples (As_2S_3 glass), was used in this installation as an inducing or probing light.

The experimental setup for reflectance difference measurements is shown in Fig. 1c. It is again a two-beam setup. The anisotropy in this case was induced using the light of either a 1000 W xenon lamp equipped with an IR cutoff filter, which generated radiation in a wide energy range, including subband-gap and superband-gap light, or an Ar^+-laser ($\lambda=488$ nm) generating above-band-gap light for the test samples. The inducing light was passed through a Glan-prism polarizer; the light intensity on the surface of the

sample was about 100 mW/cm^2. The intensity of the linearly polarized measuring light, generated by small xenon lamp, was much smaller (about 5 mW/cm^2) and did not induce any noticeable change in the anisotropy during the measurements. Application of a monochromator allowed us to investigate the spectra of PA of light reflection. For a detailed acquaintance with the reflection-difference spectroscopy see Ref. 18.

3. RESULTS AND DISCUSSION

3.1. Anisotropic light absoption

In our recent research[19,20] we obtained the data which permit further development of Tikhomirov and Elliott's model.[8] We used the setup shown in Fig. 1a. Studying the AsSe films, we demonstrated that the whole process of dichroism generation in the case of above-band-gap light excitation can be divided into two subprocesses. The first process is the generation of some centers that can be oriented by the polarized light and the second one is the photostimulated orientation (and reorientation) of these centers.

The process of photoinduced dichroism appearance and reorientation in the AsSe film of 1.2 μm thickness at 2.75 W/cm^2 light intensity is illustrated in Fig. 2. It is seen from Fig. 2a, that the initial dichroism generation is rather prolonged (10–20 min), while the dichroism reorientation occurs much quicker ($<$1 min). Quick reorientation was observed not only after dichroism saturation, as shown in Fig. 2a, but also in the initial moments of dichroism growth. Moreover, in the case of long film irradiation with the nonpolarized light, the following irradiation with linearly polarized light results in the rapid appearance of dichroism, as shown in Fig. 2b.

When the dichroism generation and reorientation in the same AsSe film was excited by the action of linearly polarized light of different intensities, the dichroism reorientation always occured much quicker than the initial dichroism growth, although at smaller light intensity initial dichroism generation and its reorientation are more prolonged than at higher light intensity. An important point is that in all these cases the dichroism achieves approximately the same value. Similar peculiarities in the kinetics of dichroism generation and reorientation were observed also in amorphous $As_{45}Se_{55}$, As_2S_3 and Ge_2PbS_4 films. So, Fig. 2c demonstrates different kinetics of dichroism generation and reorientation in the As_2S_3 film. We wish to stress that a division into slow dichroism appearance and quick dichroism reorientation is especially dictinct in the films of certain thicknesses and at certain values of exciting light intensity.

Figure 3 shows the room-temperature kinetics of repeated photoinduced dichroism (D) generation after heating the film to a certain temperature, holding it at this temperature, and then cooling to room temperature. The kinetics of room-temperature dichroism reorientation in the nonannealed films is also shown. We see that the gradual increase of annealing temperature brings the form of the dichroism growing curve nearer to that in the virgin film, and we have a nearly perfect identity of the curves after annealing at 180 °C temperature, which is the softening tempera-

FIG. 3. Kinetics of room temperature dichroism (D) generation in virgin AsSe film of 1.2 μm thickness (*1*), repeated dichroism generation after annealing at 75 (*3*), 95 (*4*), 140 (*5*), 180°C (*6*) and kinetics of one cycle of room temperature dichroism reorientation in such film (*2*). Intensity of linearly polarized He–Ne-laser light is 2.75 W/cm^2.
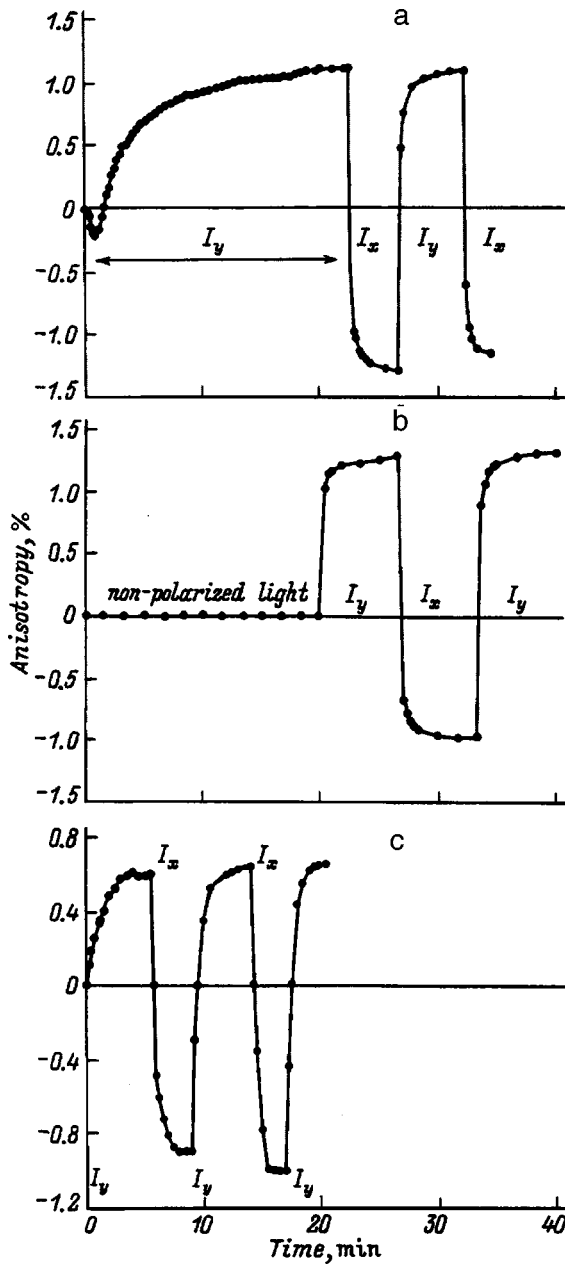
FIG. 2. Kinetics of dichroism generation and reorientation in AsSe (a, b) and As$_2$S$_3$ (c) films under the action of linearly polarized laser light with two orthogonal directions of electrical vector (y and x), when reorientation starts after dichroism saturation (a, c) or polarized light irradiation starts after long illumination with nonpolarized light (b).

suggest that the same centers (or perhaps some part of these centers that can be oriented) are responsible for the photodarkening and saturated value of PA. These centers can be created in the form of VAP's in the reactions:[12]

$$2\,C_2^0 + h\nu \rightarrow C_1^- + C_3^+ \quad \text{and} \quad C_2^0 + P_3^0 + h\nu \rightarrow C_1^- + P_4^+ , \tag{1}$$
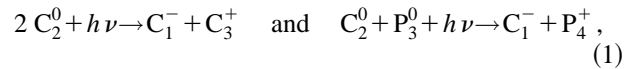
where C and P are the chalcogen and pnictide atoms.

Combining the ideas proposed in Refs. 18 and 11, we assume that the polarized light initiates the reactions

$$C_1^- + C_3^+ + h\nu \rightarrow C_1^+ + C_3^-$$

and

$$C_1^- + P_4^+ + h\nu \rightarrow C_1^+ + P_4^- , \tag{2}$$
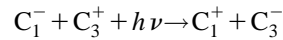
and these reactions occur much more often in the VAP's where the dipole moment is oriented parallel to the electric vector of the exciting light. Afterwards, the energetically advantageous reactions

$$C_1^+ + C_3^- \rightarrow C_1^- + C_3^+ \quad \text{and} \quad C_1^+ + P_4^- \rightarrow C_1^- + P_4^+ \tag{3}$$

take place, but now the $C_1^- + C_3^+$ and $C_1^- + P_4^+$ defects are oriented randomly. The whole process is accompanied by a decrease in the number of VAP's having the dipole moments co-directed with the electrical vector of the inducing light and by the growth of anisotropy that we have observed.

3.2. Anisotropic light scattering

The photoinduced light scattering in bulk ChGS, excited by the subband-gap light was revealed for the first time in Ref. 14. This effect was displayed as a change in the shape of the transmitted laser beam, as an appearance of speckled structure and as a photoinduced modification of the trace of the laser beam inside the irradiated ChGS bulk sample. Semiquantitative data confirming the light scattering were also obtained.[14]

ture of the AsSe film. We recall that the total bleaching of photodarkened AsSe film was also observed at a temperature close to the softening temperature, while a partial bleaching begins at lower temperatures.[21]

All the above–described results show that irradiation with polarized and nonpolarized above-band-gap light creates some centers in the nonirradiated film which can be oriented quickly by the subsequent irradiation with linearly polarized light (in the case of initial irradiation with polarized light, these centers are oriented during this irradiation). The constant dichroism saturation value at different light intensities testifies to the limited number of centers that can be oriented. The results of the heating experiments allow us to
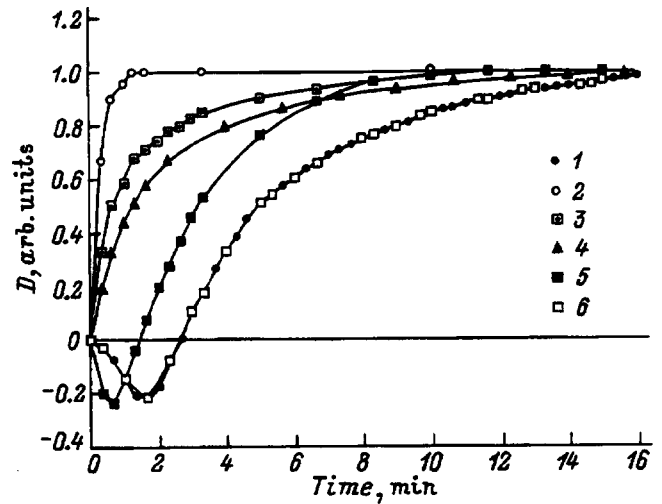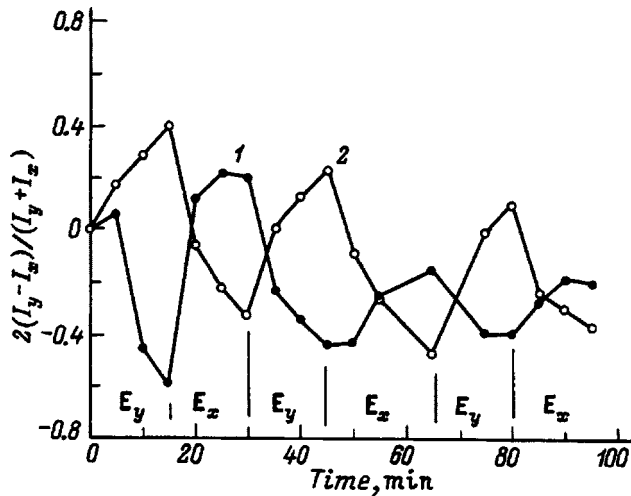
FIG. 4. Kinetics of transmittance anisotropy (*1*) and scattering anisotropy (*2*) changes in an As_2S_3 bulk glass sample induced by $\mathbf{E}_y$- and $\mathbf{E}_x$-laser radiation.

In this research we carefully investigated the photoinduced light scattering in bulk As_2S_3 glass and primarily, the anisotropy of light scattering. The results allowed us to propose some new ideas about the mechanism of the whole group of vectorial photoinduced phenomena in bulk ChGS.[22]

We used the setup shown in Fig. 1b. The He–Ne-laser light ($h\nu = 1.96$ eV, $W = 10$ mW), which was a subband-gap radiation for an As_2S_3 glass ($E_g = 2.3$ eV), was used in these experiments which were carried out at room temperature. Study of the angular distribution of the intesity of probing light transmitted through the sample (using a special movable diaphragm) before and after its irradiation with an exciting light beam permitted us to consider the light at angles up to 5 mrad as a directly transmitted light and the light at larger angles as a scattered light.

We studied the kinetics of the change in the scattered light intensity induced by strong, linearly polarized light with two orthogonal directions of the electrical vector ($\mathbf{E}_y$-radiation and $\mathbf{E}_x$-radiation). It was shown that the $\mathbf{E}_y$-radiation, for example, induces an increase of scattering of the corresponding light (I_y). Simultaneously, the intensity of I_x light usually decreases. In contrast, the $\mathbf{E}_x$-radiation induces a decrease of I_y-light and a growth of I_x-light.

Figure 4 shows typical kinetics of photoinduced changes in the scattered light anisotropy $2(I_{sy} - I_{sx})/(I_{sy} + I_{sx})$ and of the transmitted light anisotropy $2(I_{ty} - I_{tx})/(I_{ty} + I_{tx})$, which is related to the values of scattering dichroism β_s, absorption dichroism β, and sample thickness h by the simple relations

$$2(I_{sy} - I_{sx}) = (I_{sy} + I_{sx}) = \beta_s h,$$

$$2(I_{ty} - I_{tx}) = (I_{ty} + I_{tx}) = \beta h.$$

We see from the figure that the scattering anisotropy and transmittance anosotropy always change in opposite directions: an increase of one of them is accompanied by a decrease of the other one and vice versa. The anisotropy of scattering and transmittance was found to remain nearly

invariant during at least $3-5$ h. We conclude from the data of Fig. 4 that it is possible to reorientate the PA.

In some experiments the sample was first excited by nonpolarized light ($\mathbf{E}_y + \mathbf{E}_x$) and only then was irradiated by linearly polarized radiation. Nonpolarized radiation induced additional isotropic light scattering, while the subsequent linearly polarized radiation led to the appearance of scattering anisotropy, and this anisotropy could be reoriented.

The quantitative data on the photoinduced light scattering anisotropy obtained by us were used to draw some interesting conclusions. The oppositely directed changes in the photoinduced anisotropy of transmittance and scattering allow us to assume that the creation of anisotropically scattered centers is the basis of a whole group of photoinduced vector phenomena in ChGS. This hypothesis makes understandable the fact that anisotropy is excited by the subbandgap light. The energy of corresponding light quanta is not enough to break the interatomic covalent bond, but enough to produce some changes in the system of weaker bonds, for example, intermolecular van der Waals bonds or the so-called three-center bonds.[9] These changes can result in the appearance of scattering centers in the glass. We assume that only a finite number of scattering centers can be created by the inducing radiation. Such centers will scatter the light either isotropically or anisotropically, depending on the polarization state of the inducing radiation. The anisotropy of such centers can be reoriented when the polarization state of the inducing radiation is changed. The different states of scattering centers (*x*-oriented, *y*-oriented, isotropic) suggest the possibility for the existence of certain structural fragments in the glass in several quasi-stable states, as was considered in the case of photodarkening in ChGS.[21]

3.3. Anistropic light reflection

All previous studies of PA in ChGS used the transmittance measurements and for this reason only the effect of subband-gap and above-band-gap light was investigated. Interaction of ChGS with the photons whose energy substantially exceeds the optical gap of ChGS could not be studied because of strong absorbtion. Below we report the results of the reflectance-difference spectroscopy application, which allowed us to investigate the photoinduced anisotropy in ChGS in a broad spectral range.[23] We obtained in this research many new results. In particular, we showed that anisotropy can be excited by photons whose energy substantially exceeds the band-gap of the ChGS and found that PA can be detected at energies much higher than the photon energy in the exciting radiation.

We used the setup shown in Fig. 1c and investigated both thin films and bulk samples of As_2S_3, AsSe, and $Ge_{20}As_{20}S_{60}$ chalcogenide glasses. The measured value is defined as $\Delta r/r = 2(r_{II} - r_I)/(r_{II} + r_I)$, where r_{II} and r_I are the reflectance values for the polarization of the probing beam in the direction parallel or perpendicular to the polarization of the inducing beam.

In all thin films and bulk glassy samples studied we recorded PA in the whole investigated spectral range ($1.5-5.0$ eV), while the nonirradiated samples were either
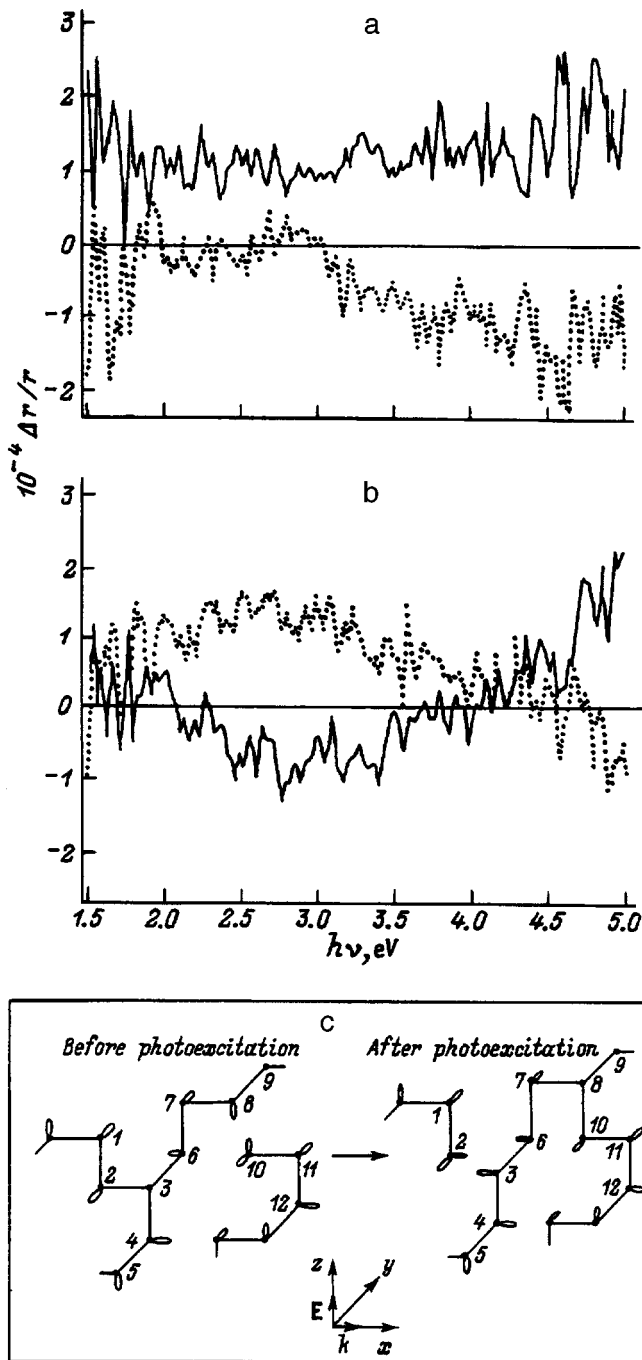
FIG. 5. Photoinduced reflectance anisotropy (solid line) and its reorientation (dotted line) in an As_2S_3 bulk glass sample irradiated by the light of 1000-W Xe-lamp (a) or Ar^+-laser (2) and schematic representation of photostructural changes induced by the above-band-gap light (c).

completely optically isotropic or showed very slight anisotropy due to preparation conditions. Upon changing the exciting light polarization to orthogonal, the reflectance curve indicated a change in the anisotropy sign.

Figure 5 shows the PA of light reflection in the bulk As_2S_3 induced by the linearly polarized light of Xe-lamp or Ar^+-laser. We see that the anisotropy appears in the whole $1.5 - 5.0$ eV range. Interestingly, for the glass excited by Xe-lamp light the trend in the reflectance change was the same (increase or decrease, depending on the polarization)

throughout the whole studied spectral range. At the same time, in the case of the Ar^+-laser excitation, sign variation of the effect is clearly seen. The increase in $\Delta r/r$ is observed for larger photon energies (above 4.0 eV) similar to the previous case of polychromatic light excitation, but for smaller photon energies an opposite change (decrease)is detected. We see also that a change in the light polarization to the orthogonal polarization results in a reversal of the PA with the same crossover energy of 4.0 eV.

We demonstrated also that the anisotropy of reflection is induced faster and to a larger magnitude if the test sample is preirradiated for $2 - 3$ h by the nonpolarized full light of the 1000 W Xe-lamp. All peculiarities of PA of reflection were shown to be characteristic not only for As_2S_3 glass but also for all ChGS studied.

The possibility of observing PA at energies much larger than the exciting photon energy indicates that by irradiating of ChGS with linearly polarized light the defects or the scattering centers can be oriented and reoriented by light and the main covalent network of the glass becomes anisotropic. This means that the main interatomic covalent bonds can be also oriented and reoriented.

The data on the anisotropy of reflection induced by the subband-gap and above-band-gap light can be understood in close analogy with the explanation given in Secs. 3.1 and 3.2. The most interesting results which must be explained are the data on the difference of reflection spectra for the cases of Xe-lamp and Ar^+-laser light excitation (Figs. 5a and 5b). A possible accounting for this difference is demonstrated in Fig. 5c for the simple case of elemental amorphous selenium. In the initial state, atom *3* is threefold coordinated and atom *10* is onefold coordinated. Following the photoexcitation by the light with polarization shown in the figure, lone-pair (LP) electrons oriented parallel to this orientation will predominantly be excited. As a result, atom *10* may form a covalent bond with a neighboring atom *8*, making the latter threefold coordinated. To keep the defect concentration and charge balance, initial threefold coordinated atom *3* decays into a singly coordinated defect and a twofold coordinated ''regular'' atom. We see here a redistribution of LP and bonding orbitals. Before photoexcitation the bond between atoms *2* and *3* was covalent (parallel to the *x* axis), while atoms *8* and *10* had LP orbitals parallel to the *z* axis. After the photoexcitation, atoms *8* and *10* became bonded by a covalent bond in the *z* direction, while the bond between atoms *2* and *3* is broken, and two LP orbitals parallel to the *x* axis are created. As a result, the total number of bonding electrons along the *z* axis decreases, while the number of nonbonding electrons along the *x* axis increases, which explains the opposite change in the anisotropy probed at lower and higher energies. In other words, conversion between bonding and nonbonding electrons proceeds. Both natural and photoinduced defects can participate in this process, as is clearly evidenced from the comparison of the kinetics of PA of reflection in the nonirradiated samples and in the samples preirradiated by the nonpolarized light.

In the case of broad-spectrum light (Xe-lamp), the above-considered process still exists but, additionally, the direct excitation of bonding electrons by the high-energy

light quanta becomes possible, resulting in the decrease in the number of bonding electrons in the direction of the light polarization. Since the density of states is larger for bonding electrons than for LP electrons, this latter process overcompensates the decrease in the number of covalent bonds caused by the excitation with the subband-gap light, which leads to the same change in the sign of anisotropy for the lower and higher energies.

3.4. Polarization-dependent, laser-induced anisotropic crystallization of some ChGS films

Laser-induced anisotropic absorbtion of light, considered in Sec. 3.1, was observed in various ChGS films irradiated by the above-band-gap linearly polarized light, but in some thermally treated Se–Ag–I films and in films of elemental amorphous selenium we observed very unusual kinetics of linear dichroism generation and reorientation.[24] As in the other cases, in those films the dichroism was generated slowly under the action of linearly polarized light, and a change in the polarization vector to the orthogonal one resulted in the reorientation of dichroism, but unlike the previously studied cases, the constant change of reorientation kinetics was observed and then the alteration of the dichroism sign was recorded (Fig. 6a). If at the beginning of the experiment, the vertical polarization vector stimulated increase of positive dichroism, while the horizontal polarization vector diminished positive dichroism and excited negative dichroism, in the following stages the reverse processes were observed.

The photoinduced dichroism excited by the He–Ne-laser light at a constant direction of polarization vector changed the sign very soon and grew slowly, achieving very large values of about $15-18\%$, as shown in Fig. 6b. The sign of the final dichroism always was determined by the direction of the exciting light polarization vector. The dichroism induced by irradiation of the same Se–Ag–I film with an Ar^{+}-laser light displayed similar dependence but the saturated dichroism value was essentially lower and was achieved quicker. Some relaxation of dichroism with time after cessation of irradiation was characteristic for the early periods and was not observed in the final stages of dichroism generation. Annealing of irradiated films at glass transition temperature ($55°C$) and at $80-90°C$ for several hours did not lead to a destruction of photoinduced dichroism, in contrast with the situation in the AsSe films.

Thus, all characteristics of PA in the treated Se–Ag–I and a-Se films were different from those in films studied previously. The results obtained (unusual kinetics, another sign and large value of photoinduced dichroism, absence of relaxation and thermal destruction) allowed us to assume that we are dealing with a photoinduced photocrystallization process.[25–27]

This assumption was confirmed by the direct structural investigation, including optical microscopy, electron microscopy, and x-ray diffraction study. Initially more or less homogeneous films with a uniform morphology indicate distinct crystallization after irradiation. X-ray analysis of irradiated Se–Ag–I films showed the presence of Se, Ag_2Se,
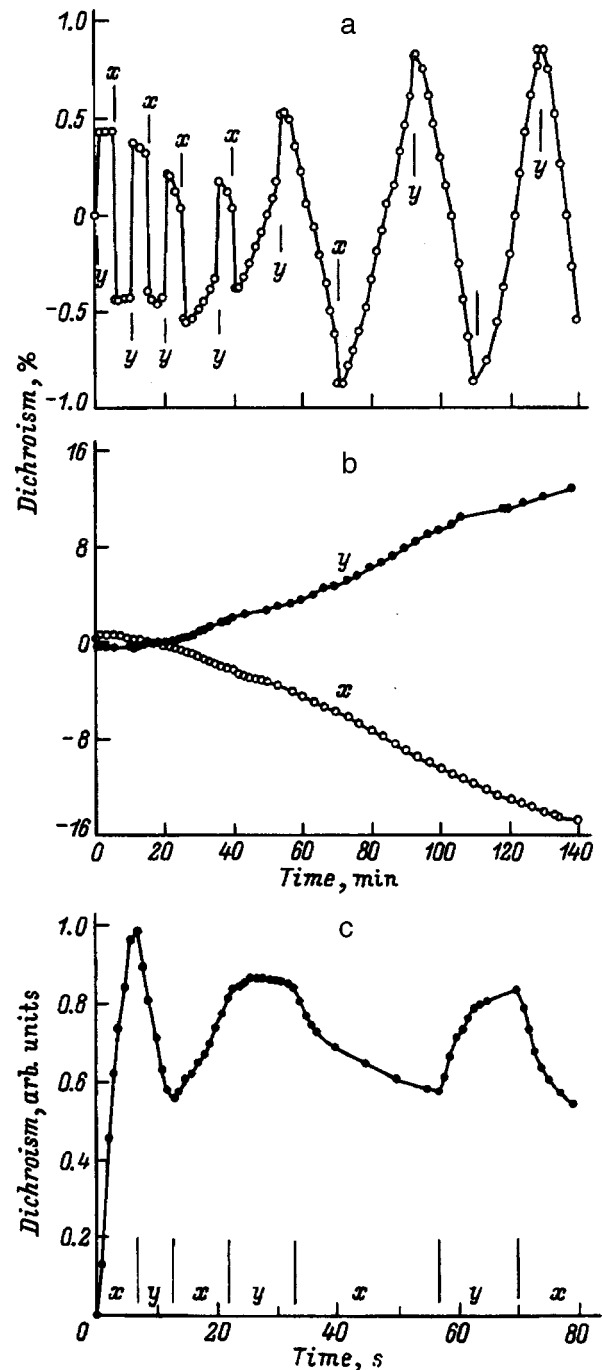

FIG. 6. Kinetics of dichroism generation and reorientation in a treated $Se_{70}Ag_{15}I_{15}$ film (a, b) and in AsSe film photodoped with silver (c) induced by a linearly polarized He–Ne-laser beam when generation and reorientation cycles are carried out by horizontal (x) and vertical (y) directions of the electrical vector.

and AgI microcrystals. Difference in the kinetics and the saturated values of photoinduced dichroism excited by He–Ne and Ar^{+} laser beams is explained by different values of light penetration depths connected with different absorbtion coefficients of red and green light. Thus, we observed for the first time the polarization-dependent, laser-induced anisotropic photocrystallization of Se–Ag–I and a-Se films. At the same time, investigating the structure of the samples by all the above-mentioned methods, we did not observe any

preferential orientation of the crystallites in the photocrystallized films.

3.5. Polarization-dependent photodoping of chalcogenide glassy films with silver

ChGs films are known to be photodoped with silver and other metals with the following drastic changes in the optical, electrical, and physico–chemical properties (see review articles[28,29]). It was shown also that the silver photodoping of As_2S_3 glassy films using linearly polarized light is accompanied by the generation of strong dichroism whose sign is opposite to that generated in Ag-free ChGS films.[29] This phenomenon is called "polarized photodoping" of ChGS films.

Recently, we investigated in detail the polarized photodoping in ChGS films of different compositions — As_2S_3, As_2Se_3, AsSe, and $GeS_{2.2}$ and observed in all these cases the same peculiarities of this phenomenon as were observed previously at the polarized photodoping of As_2S_3 films. Our attention was attracted to the kinetics of dichroism reorientation. We observed the constant change in the reorientation kinetics which was accompanied by a change in the dichroism sign. We realized that in the first cycles of dichroism reorientation, the horizontal polarization vector stimulated an increase of positive dichroism, while the vertical polarization vector decreased the dichroism value. In the following stages the reverse picture was recorded, as shown in Fig. 6c for a AsSe film photodoped with silver. This situation reminded us of the picture that we observed in the case of above-considered photoinduced polarized crystallization and we decided to investigate the structure of photodoped films. Using optical microscopy, we drew the conclusion that the prolonged laser-induced photodoping actually leads to a partial polarization-dependent photocrystallization of three-component As(Ge)–Se(S)–Ag materials obtained in the process of photodoping.

4. CONCLUSIONS

The detailed investigation of the interaction of linearly polarized light with ChGS allows us to conclude that a tendency to photoinduced macro-anisotropy is a common property of these materials. It manifests itself in the anisotropic light absorbtion, reflection, and scattering which can be observed in different spectral ranges using various exterimental techniques. The common base for this photoinduced macro-anisotropy is the existance in ChGS of a large number of micro-anisotropic fragments. In the nonirradiated ChGS such fragments are oriented randomly, making the samples optical macro-isotropic (we do not consider here the cases of natural optical anisotropy investigated in Refs. 30 and 31). Polarized light leads to the redistribution of these fragments. Such general idea was suggested in the first papers dealing with photoinduced anisotropy in ChGS.[1,2] One of the possible cases of such redistribution was considered in detail by Fritzsche.[11] Moreover, our experiments demonstrated that not only natural fragments, but also photoinduced fragments (defects) are micro-anisotropic, and that they can be oriented and reoriented by the linearly polarized light.

We are convinced now that such micro-anisotropic fragments in ChGS can produce different defects and even interatomic bonds that determine the anisotropy excited by the light of different spectral ranges: subband-gap, above-bandgap, and superband-gap light.

We wish to mention especially that irradiation with linearly polarized light can produce many unusual and interesting phenomena in ChGS. Examples of such phenomena, polarization-dependent photocrystallization and polarization–dependent Ag-photodoping were considered in this paper.

[1] V. G. Zhdanov and V. K. Malinovskii, Sov. Tech. Phys. Lett. **3**, 943 (1977).

[2] V. G. Zhdanov, B. T. Kolomiets, V. M. Lyubin, and V. K. Malinovskii, Phys. Status Solidi A **52**, 621 (1979).

[3] J. Hajto, I. Janossy, and C. Forgaes, J. Chem. Phys. **15**, 6293 (1982).

[4] R. Grigorovici, A. Vancu, and L. Ghita, J. Non-Cryst. Solids **59–60**, 903 (1983).

[5] K. Kimura, K. Murayama, and T. Ninomiya, J. Non-Cryst. Solids **77–78**, 1203 (1985).

[6] J. M. Lee and M. A. Paesler, J. Non-Cryst. Solids **97–98**, 1235 (1987).

[7] V. M. Lyubin and V. K. Tikhomirov, J. Non-Cryst. Solids **114**, 133 (1989).

[8] V. K. Tikhomirov and S. R. Elliott, Phys. Rev. B **51**, 5538 (1995).

[9] S. A. Dembovsky, Solid State Commun. **83**, 761 (1992).

[10] T. Kosa and I. Janossy, Philos. Mag. B **64**, 355 (1991).

[11] H. Fritzsche, J. Non-Cryst. Solids **164–166**, 1169 (1993).

[12] M. Kastner and H. Fritzsche, Philos. Mag. B **37**, 199 (1978).

[13] V. M. Lyubin and V. K. Tikhomirov, JETP Lett. **51**, 587 (1990).

[14] V. M. Lyubin and V. K. Tikhomirov, J. Non-Cryst. Solids **135**, 37 (1991).

[15] V. M. Lyubin and V. K. Tikhomirov, Sov. Tech. Phys. Lett. **15**, 804 (1989).

[16] V. K. Tikhomirov and S. R. Elliott, Phys. Rev. B **49**, 1746 (1994).

[17] K. Tanaka, M. Notani, and H. Hisakuni, Solid State Commun. **95**, 461 (1995).

[18] D. E. Aspnes, J. P. Harbison, A. A. Studna, and L. F. Florez, J. Vac. Sci. Technol. A **6**, 1327 (1988).

[19] V. Lyubin and M. Klebanov, Phys. Rev. B **53**, 11 924 (1996).

[20] V. Lyubin, M. Klebanov, V. Tikhomirov, and G. Adriaenssens, J. Non-Cryst. Solids **198–200**, 719 (1996).

[21] V. L. Averyanov, A. V. Kolobov, B. T. Kolomiets, and V. M. Lyubin, Phys. Status Solidi A **57**, 81 (1980).

[22] M. Kastner and H. Fritzsche, Philos. Mag. B **37**, 199 (1978).

[23] V. Lyubin, M. Klebanov, S. Rosenwaks, and V. Volterra, J. Non-Cryst. Solids **164–166**, 1165 (1993).

[24] A. V. Kolobov, V. Lyubin, T. Yasuda, M. Klebanov, and K. Tanaka, Phys. Rev. B **55**, 8788 (1997).

[25] V. Lyubin, M. Klebanov, M. Mitkova, and T. Petkova, Appl. Phys. Lett. **71**, 2118 (1997).

[26] J. Dresner and G. B. Stringfellow, J. Phys. Chem. Solids **29**, 303 (1968).

[27] R. Clement, J. C. Carballes, and B. J. de Cremoux, J. Non-Cryst. Solids **15**, 505 (1974).

[28] A. V. Kolobov and S. R. Elliott, Adv. Phys. **40**, 625 (1991).

[29] K. Tanaka, J. Non-Cryst. Solids **137–138**, 1021 (1991).

[30] A. V. Kolobov, V. M. Lyubin, and V. K. Tikhomirov, Philos. Mag. Lett. **65**, 67 (1992).

[31] T. F. Mazets, E. A. Smorgonskaya, V. K. Tikhomirov, and N. N. Faleev, Sov. Tech. Phys. Lett. **18**, 739 (1992).

Recombination in hydrogenated amorphous silicon

K. V. Koughia

St. Petersburg State Pediatric Medical Academy, 194100 St. Petersburg, Russia

E. I. Terukov

A. F. Ioffe Physicotechnical Institute, Russian Academy of Sciences, 194021 St. Petersburg, Russia

V. Fuhs

Hahn–Meitner Institute, D-12489 Berlin, Germany

Investigations of transient photoconductivity in a-Si : H lead to the conclusion that tunnel recombination of localized excess carriers may predominate in the temperature range from liquid-helium temperatures up to temperatures at which the material was synthesized. © *1998 American Institute of Physics.* [S1063-7826(98)00608-5]

INTRODUCTION

One of the characteristic properties of disordered semi-conductors is the presence in the band gap of localized states, which to a large extent determine the electronic properties of these materials and, in particular, the mechanisms for recombination of nonequilibrium carriers.

It is, in fact, possible to distinguish two main accessible recombination mechanisms. The first is classical recombination of the type ''band–center,'' in which the recombination rate is determined by the cross sections for the capture of delocalized nonequilibrium carriers by localized states in the band gap.[1,2] The second possible recombination mechanism is ''tunneling recombination'' of nonequilibrium carriers captured by localized states, in which the recombination rate determining process is tunneling under the potential barriers that separate the carriers.[3,4] In a number of cases a combination of these two processes is also possible, e.g., in the form of tunneling with variable hopping length.[5]

The concept of tunneling recombination was introduced to describe interimpurity radiative recombination in doped and compensated germanium. The experiments were carried out at liquid-helium temperatures and it was found that this phenomenon is manifested only in a very limited temperature range. However, further research on heavily doped and compensated four-coordinated semiconductors showed that tunneling recombination also plays a noticeable role in these materials, and its contribution becomes that much more significant, the higher is the degree of disorder of the structure.[6,7]

Recombination of nonequilibrium carriers in hydrogenated amorphous silicon (a-Si : H) has remained until now a topic of discussion, and in the literature it is possible to encounter both points of view (see, e.g., Refs. 8 and 9). Using the most general arguments, we can assert that since a-Si : H possesses an even more disordered structure, it is expected that tunneling processes in this material are even more pronounced. In this review article we discuss new data as well as those published previously which indicate, in our view, that tunneling recombination of nonequilibrium carriers in a-Si : H can play the key role in the temperature interval from liquid-helium temperatures to temperatures close to those at which the material was synthesized.

SAMPLES AND EXPERIMENTAL PROCEDURE

The investigated samples were prepared by high-frequency (HF) decomposition of silane-containing gas mixtures in a system with capacitance coupling. They were characterized by a photosensitivity $\geq 5 \times 10^4$ upon illumination by a source of type AM1 and possessed, according to electron-spin-resonance and constant-photocurrent data, an unpaired spin density $\sim 10^{15}$ cm^{-3}. To measure the photoconductivity, contacts were deposited on them in a coplanar configuration.

We gave primary attention to the kinetics of photoconductivity decay from the steady-state value after switching off the illumination. In our study of recombination such a method seems to us to be the most informative since decay of the photoconductivity from its steady-state value can proceed only via recombination of nonequilibrium carriers.

EXPERIMENTAL RESULTS AND DISCUSSION

Let us start with a description of results in the temperature range $\sim 77 - 120$ K, which we conventionally call the ''low-temperature'' region. At lower temperatures the predominance of recombination seems entirely natural and is excellently reflected in Refs. 10 and 11. The experimental results and a model of photoconductivity in a-Si : H at ''low'' temperatures are most thoroughly described in Refs. 12 and 13; we will restrict the discussion here to a brief enumeration of the main points of the model and note that in this temperature range the kinetics of the photoconductivity are independent of the temperature, which directly indicates that the recombination may be of a tunneling nature.

According to numerous experimental data, we assume that the electrons in undoped *a*-Si : H are significantly more mobile than the holes (which at low temperatures, to first order, may be assumed to be fixed and localized at "hole localization centers") and the photoconductivity is associated with electron transport due to thermally activated hops in the tail of the conduction band.[14] Numerical estimates show that after a typical photoresponse time the electron manages to diffuse a distance roughly 10 times greater than the distance between the localized holes; therefore, the electron can be assumed to be "smeared" over the arrangement of holes. The probability of tunneling recombination is proportional to $\exp(-2r/a)$, where $a = 12$ Å is the localization length of the electron,[15] and r is the distance between the electron and hole. Consequently, annihilation of the given hole takes place with overwhelming probability at the instant the electron, in the process of hopping along localized sticking levels, arrives at the level closest to the given hole. This ⟨hole localization center⟩–⟨nearest electron trap⟩ pair forms a "recombination channel" with characteristic lifetime of the hole that has fallen into it

$$\tau(r) = v_0^{-1} \exp(2r/a), \tag{1}$$

where $v_0 = 10^{12}$ Hz is the phonon frequency.[16]

If N_e is the concentration of electron traps and N_h is the concentration of hole localization centers, then if they are uncorrelated in space the distribution of recombination channels over distance r will have the form

$$g(r) = \frac{3r^2}{R^3} \exp\left(-\frac{r^3}{R^3}\right), \tag{2}$$

where $R^3 = 3/4\pi N_e$ (Ref. 17).

The steady-state channel filling function can be found by equating the level of generation and recombination per channel:

$$G[1 - f^{ss}(r,G)]/N_h = f^{ss}(r,G)/\tau(r);$$

$$f^{ss}(r,G) = \frac{1}{1 + N_h/G\tau(r)}, \tag{3}$$

where $f^{ss}(r,G)$ is the steady-state channel filling function, and G is the rate of generation of electron–hole pairs. As can be seen from Eq. (3), the fast channels with small r are for the most part empty, and the slow channels with large r are for the most part filled. Consequently, we can introduce a critical distance r_0 which separates the "mainly empty" channels from the "mainly filled" ones.

After switching on the light, a successive destruction of channels takes place in line with the lifetime of the carriers captured in them

$$p(t) = N_h \int_0^\infty g(r) f^{ss}(r,G) e^{-t/\tau(r)} dr, \tag{4}$$

where $p(t)$ is the nonequilibrium hole concentration. Taking the condition of electrical neutrality into account and assuming that the drift mobility of the electrons μ is independent of the time t, we obtain
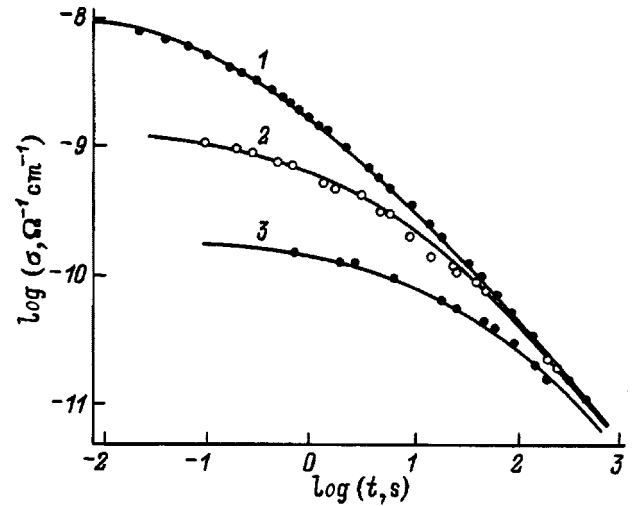

FIG. 1. Comparison of calculated curves of falloff of the photoconductivity (solid lines) with the experimental data (points) at $T = 110$ K for a variable level of generation of nonequilibrium carriers. The parameters chosen for calculations were *1*: $N_e = 3.5 \times 10^{17}$ cm^{-3}, $N_h = 2.5 \times 10^{18}$ cm^{-3}, $\mu = 8 \times 10^{-7}$ cm^2/V·s. G, cm^{-3}s^{-1}: *1* — 2.0×10^{18}, *2* — 4.8×10^{16}, *3* — 3.4×10^{15}. For curves *2* and *3* agreement was achieved automatically.

$$\sigma(t) e \mu n(t) = e \mu p(t)$$

$$= e \mu N_h \int_0^\infty g(r) f^{ss}(r,G) e^{-t/\tau(r)} dr. \tag{5}$$

Equation (5) can be used to calculate the shape of the falloff of the photoconductivity from steady state, using N_e, N_h, and μ as fitting parameters. Results of the calculations are plotted in Fig. 1; experimental data obtained at $T = 117$ K, are also plotted for comparison. Note the good agreement between the calculated and experimental curves in a wide time interval.

A critical test of the adequacy of the model would be to calculate the photoconductivity kinetics for different levels of photocarrier generation. In such a case, choice of the model parameters N_h and N_e would be made for only one curve, e.g., the one corresponding to maximum intensity. Then the illumination intensity would be varied the same number of times in the experiment and in the calculation, and coincidence of the calculated and experimental curves at the lower excitation intensities should be achieved without additional fitting.

The proposed model also enables one to calculate the shape of the photoinduced absorption relaxation curves. In such experiments a rectangular pulse of strongly absorbed light is used to create nonequilibrium carriers, and the level of absorption of additional infrared illumination allows one to estimate the concentration of these carriers. The results of such a calculation are plotted in Fig. 2; experimental data obtained in Ref. 18 are also plotted for comparison.

As the temperature is raised, the photoconductivity kinetics are accelerated. Figure 3 shows the experimental results which reflect the rate of decay of the photoconductivity from its steady-state level at different temperatures for a constant level of initial illumination. From the character of
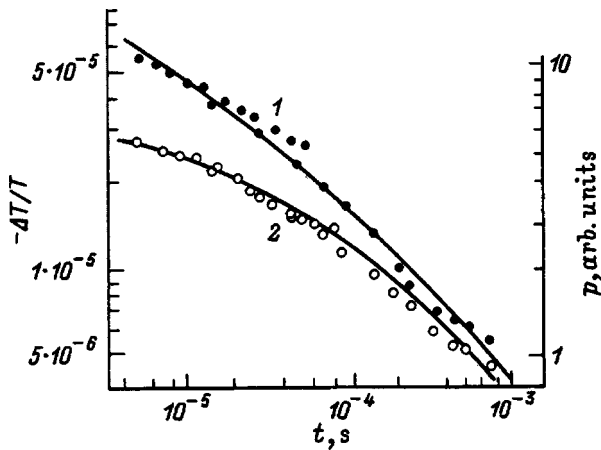
FIG. 2. Relaxation of photoinduced absorption $(-\Delta T/T)$ (Ref. 18) (points) and calculated falloff of the nonequilibrium hole concentration $p(t)$ (curves). Calculation parameters: $N_e = 6.0 \times 10^{17}$ cm^{-3} and G/N_h, s^{-1}: *1* — 1.0×10^6, *2* — 2.0×10^4.

the kinetics it is possible to distinguish three temperature ranges:

1) the previously discussed ''low-temperature'' range $T \leq 118$ K (curves *1* and *2*), in which the falloff rate of the photoconductivity does not depend on the temperature;

2) the range $118 \leq T \leq 293$ K (curves *3–6*), in which the photoconductivity kinetics are accelerated with growth of the temperature, but this acceleration can be compensated by lowering the generation level; i.e., the photoconductivity falloff curves measured at different temperatures can be identical for the corresponding choice of generation level; in
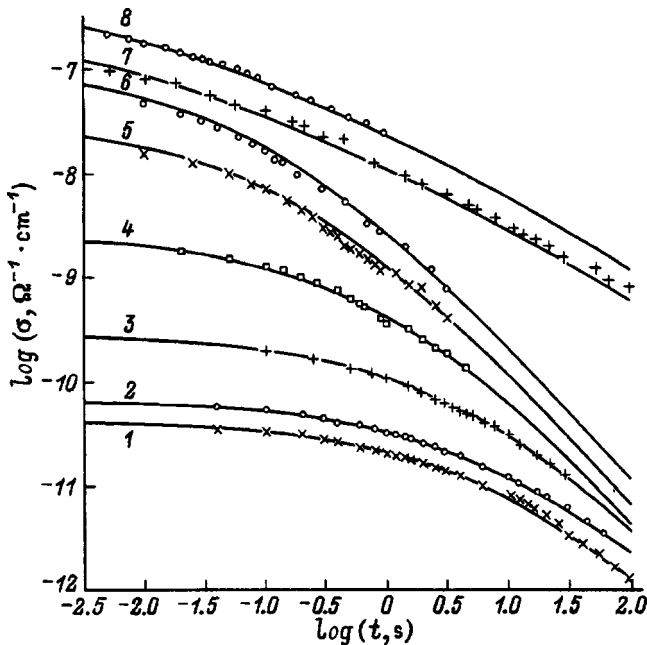

FIG. 3. Comparison of calculated photoconductivity falloff curves (solid lines) with the experimental data (points) for fixed rate of generation of nonequilibrium carriers $G = 4 \times 10^{17}$ cm$^{-3} \cdot$s^{-1} and variable temperature. Temperature of the experiment and calculation parameters are given in Table I. The stationary concentration p^{ss} was calculated according to formula (5) for $t = 0$.

TABLE I. Temperatures of experiment and calculation parameters of the curves in Fig. 3.

curve No.	T, K	N_e, 10^{17} cm^{-3}	N_h, cm^{-3}	log $(\mu, \text{cm}^2/V \cdot s)$	log (p^{ss}, cm^{-3})
1	108	3.5	2.5×10^{18}	-6.86	14.70
2	118	3.5	1.2×10^{18}	-6.93	14.70
3	158	4.0	1.9×10^{18}	-4.13	14.65
4	192	4.8	5.0×10^{17}	-2.52	14.23
5	230	5.0	5.0×10^{16}	-1.59	13.87
6	249	5.1	$2.3 \cdot 10^{16}$	-1.39	13.72
7	293	2.7	1.0×10^{15}	-1.40	13.66
8	323	2.7	8.2×10^{14}	-1.45	13.62

other words, inside this temperature range ''$T-G$ compensation'' is possible;[19]

3) the range $T \geq 293$ K (curves *7* and *8*), in which $T-G$ compensation becomes impossible since, despite the fact that the initial kinetics continue to accelerate as the temperature is raised, a long-time tail appears in the photoconductivity decay. As a result, changes in the kinetics, which cannot be compensated for by varying G, take place.

To explain these results, we modified the above model, and in Fig. 3 the solid lines plot the results of calculations carried out in the framework of the improved scheme. As can be seen from the figure, up to room temperature, the acceleration of the photoconductivity kinetics can be described by decreasing the parameter N_h which characterizes the concentration of hole recombination centers. The logic of such an operation can be treated as a ''conversion'' of some of the recombination centers into sticking levels. At the qualitative level, acceleration of the kinetics can be explained by the fact that the fixed-hole model no longer works and it is necessary to allow for the possibility of thermal transport of the holes from occupied (slow) recombination channels to empty (fast) ones. This entails an acceleration of the kinetics as a result of growth of the load at the remaining recombination centers and, in some sense, is analogous to the process taking place upon decrease of the photon energy, which also leads to a decrease of N_h and an acceleration of the photoconductivity kinetics.[13]

The model also explains the $T-G$ compensation effect. In fact, Eqs. (3)–(5) show that the photoconductivity falloff rate is governed by the ratio G/N_h and, consequently, a matched decrease of N_h (due to the temperature increase and thermal motion of the holes) and G (due to the corresponding choice of parameters) leaves the shape of the photoconductivity curve invariant.

As can be seen from the same figure, the parameter N_e characterizing the concentration of electron states remains unchanged all the way up to room temperature.

As was noted above, a good test of the adequacy of the model is a calculation of the photoconductivity kinetics at fixed temperature and different levels of photocarrier generation. Figure 2 shows satisfactory results of such a test at 211 K, i.e., in the $T-G$ compensation range.

It can be seen from Fig. 3 that at $T > 293$ K the model, as before, provides a good description of the photoconductivity falloff kinetics over a wide interval of times for one level of
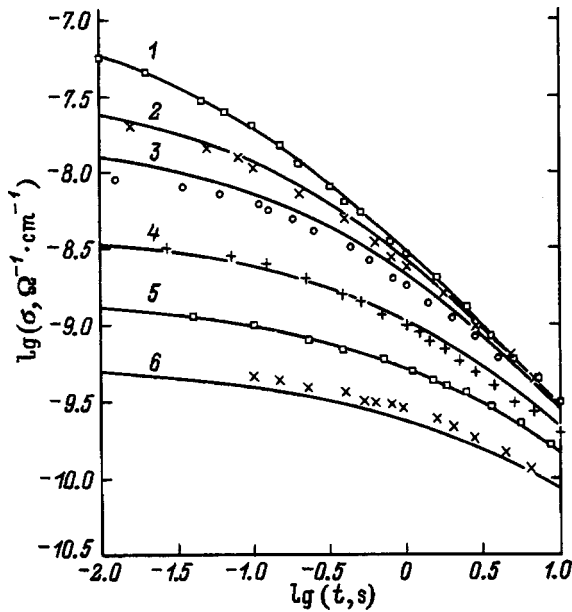
FIG. 4. Comparison of calculated photoconductivity falloff curves (solid lines) with the experimental data (points) at $T = 211$ K for a variable level of generation of nonequilibrium carriers. The parameters chosen for calculations were *1*: $N_e = 4.75 \times 10^{17}$ cm^{-3}, $N_h = 8.0 \times 10^{16}$ cm^{-3}, $\mu = 9 \times 10^{-3}$ cm^2/V·s. For curves *2–5* agreement was achieved automatically. G, cm$^{-3}\cdot$s^{-1}: *1* — 2×10^{18}, *2* — 3.4×10^{17}, *3* — 1.2×10^{17}, *4* — 2.0×10^{16}, *5* — 6.0×10^{15}, *6* — 2.0×10^{15}.
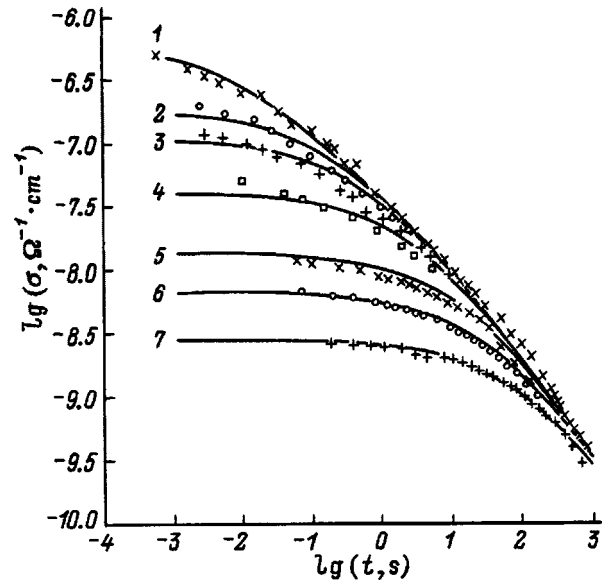

FIG. 5. Comparison of calculated photoconductivity falloff curves (solid lines) with the experimental data (points) at $T = 293$ K for variable level of generation of nonequilibrium carriers. The parameters chosen for calculations were as follows: $N_e = 2.7 \times 10^{17}$ cm^{-3}, $N_h = 1.0 \times 10^{15}$ cm^{-3}, $\mu = 4 \times 10^{-2}$ cm^2/V·s were chosen for curve *1*. For curves *2–6* agreement was achieved automatically upon introduction of the coefficient $\alpha = 1.8$ in Eq. (6). G, cm$^{-3}\cdot$s^{-1}: *1* — 4×10^{17}, *2* — 6.4×10^{16}, *3* — 3.2×10^{16}, *4* — 1.0×10^{16}, *5* — 3.2×10^{15}, *6* — 1.6×10^{15}, *7* — 6.8×10^{14}.

illumination; however, an effort to simultaneously describe the family of curves corresponding to different intensities (by analogy with Figs. 1 and 4) requires the introduction of a correction factor α in expression (3) for the steady-state filling function:

$$f^{ss}(r,G) = \frac{1}{1 + N_h / G^{\alpha}\tau(r)}. \tag{6}$$

Coincidence of the calculated and experimental curves for $\alpha = 1.8$ is shown in Fig. 5. The significance of introducing the coefficient α and also its magnitude can be explained in the following way. Let us calculate $f^{ss}(r,G)$ for a high temperature. By analogy with Eq. (3), under steady-state conditions we can write the following expression for an arbitrary localized state:

$$(G + \theta)[1 - f^{ss}(r,E)]/N_h$$
$$= f^{ss}(r,E)[1/\tau(r) + \nu_0 e^{(E_v - E)/kT}], \tag{7}$$

where E is the energy level of the localized state, $f^{ss}(r,E)$ is the steady-state filling function, E_v is the mobility edge of the valence band, and θ is the rate of total thermal ejection from all the localized states.

To simplify, dividing the localized states into sticking levels and recombination centers (of course, in reality this division is dictated not only by E, but also by r), we obtain for the filling function of the recombination centers

$$f^{ss}(r,G) = \frac{1}{1 + N_h/(G + \theta)\tau(r)}. \tag{8}$$

To estimate θ, we assume that the tail of the valence band is exponential with characteristic energy $\delta E_v = 45$ meV, i.e., $N(E) = N_v \exp[-(E - E_v)/\delta E_v]$ (Ref. 20). Then, introducing the Fermi quasilevel E_{fv}, we can estimate the steady-state hole concentration in some approximation as

$$p_{ss} \approx \int_{E_{fv}}^{\infty} N(E)dE = N_v \delta E_v \exp[-(E_{fv} - E_v)/\delta E_v], \tag{9}$$

and the total thermal ejection θ as

$$\theta \approx p_{ss}\nu_0 \exp[-(E_{fv} - E_v)/kT]. \tag{10}$$

Substituting expression (9) into formula (10), we obtain an estimate for the total thermal ejection

$$\theta \approx \frac{\nu_0 p_{ss}^2}{N_v \delta E_v} e^{-\delta E_v/kT}. \tag{11}$$

The exponent of the current–illuminance characteristic γ determines the dependence of the steady-state photoconductivity on the generation level $\sigma_{ph} \sim G^{\gamma}$. Since the steady-state nonequilibrium hole concentration is proportional to the photoconductivity, i.e., $p_{ss} \sim G$, we obtain

$$\theta \approx A G^{\alpha}, \tag{12}$$

where $\alpha = 2\gamma$, and A is a constant that does not depend on G. Numerical estimation of θ at 293 K gives the value $\theta \approx 10^{19}$ cm$^{-3}\cdot$s$^{-1} \gg G \geq 4 \times 10^{17}$ cm$^{-3}\cdot$s^{-1}. Therefore, substituting this value of θ in expression (8) and ignoring G in comparison with θ, and also taking into account that at 293 K the exponent of the current–illuminance characteristic
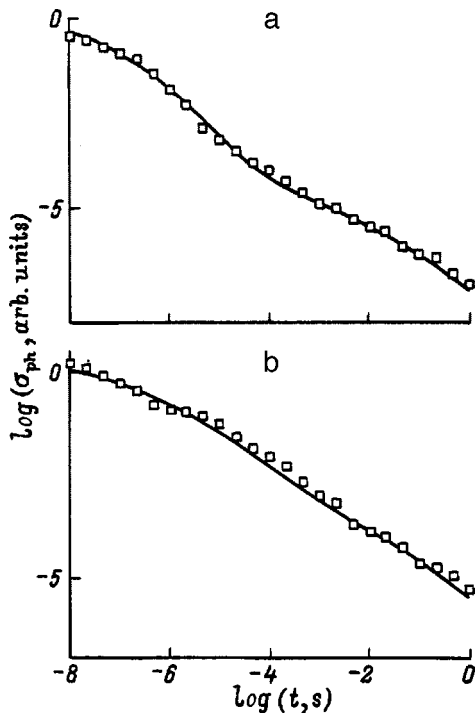
FIG. 6. Time dependence of falloff of the photoconductivity after pulsed illumination in samples of *a*-Si : H prepared for substrate temperature $T_s = 200$ (a) and 300 °C (b). Points—experimental data, solid curves—calculated result.

$\gamma = 0.9$ and, consequently, $\alpha = 1.8$, we finally obtain formula (6) for $f^{ss}(r, G)$, which is found to be in complete agreement with the experimental data.

The proposed recombination scheme can be used to explain the experimental data obtained in Refs. 21 and 22 on the relaxation of the photoconductivity after a short light pulse. In the present work we are not able to judge the specifics introduced by the short duration of the pulse in either the distribution function (2) or the filling function (3), and we present only the calculated results in Fig. 6 together with the experimental data for comparison.

With further increase of the temperature, the nonequilibrium carriers become essentially delocalized. The dark (i.e.,

equilibrium) conductivity starts to exceed the photoconductivity in magnitude, as shown in Fig. 7, which plots the temperature dependence of the dark conductivity, the photoconductivity, and the photoresponse time given by

$$\tau_0 = \lim_{t \to 0} \frac{\sigma(t)}{d\sigma(t)/dt}, \tag{13}$$

and the characteristic decay rate of the photoconductivity at the initial instant of time. As could be expected, in this temperature range the exponent of the current–illuminance characteristic is close to unity and the photoconductivity kinetics do not depend on the generation rate of the nonequilibrium carriers. Therefore, the fact that under such conditions the kinetics are, as before, substantially nonexponential is completely unexpected. That this is indeed so can be seen from Fig. 8, which plots the time dependence of the instantaneous lifetime $\tau(t)$, defined as

$$\tau(t) = \frac{\sigma(t)}{d\sigma(t)/dt}, \tag{14}$$

for different temperatures of the experiment.

The preservation at high temperatures of the dependence of $\tau(t)$ typical at lower temperatures gives us reason to believe that the previous recombination mechanism, i.e., tunneling recombination of nonequilibrium carriers, predominates. Here it should be recalled that such a combination, namely, the presence of carriers in delocalized states together with tunneling recombination, was encountered earlier in studies of such classical objects as compensated gallium phosphide[23,24] and plastically deformed, monocrystalline silicon.[25] Granted, in such objects at temperatures above room temperature tunneling recombination does not play a central role, but there is reason to believe that in amorphous semiconductors the role of tunneling recombination should be weightier. This has to do with the fact that the wave function of even a delocalized carrier in an amorphous semiconductor is strongly modulated and that it differs substantially from the wave function in a crystal, where the envelope is a plane wave. Strong modulation means that the probability of finding a carrier (for definiteness, say, an electron) is
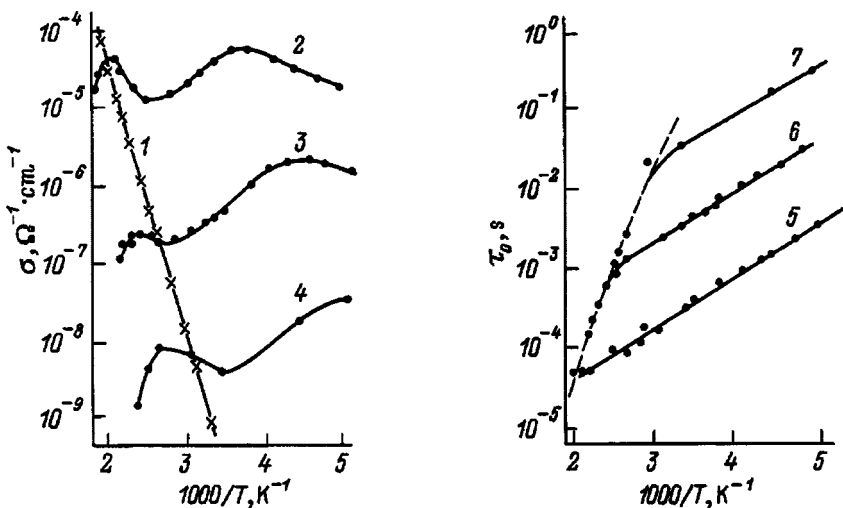

FIG. 7. Temperature dependence of the dark conductivity (*1*), photoconductivity (*2–4*), and photoresponse time (*5–7*) in the ''high'' temperature range. Dashed line — calculated according to formulas (15) and (16). Photon flux intensity I_0, $cm^2 \cdot s^{-1}$: *2, 5* — 10^{16}; *3, 6* — 10^{14}; *4, 7* — 10^{12}.
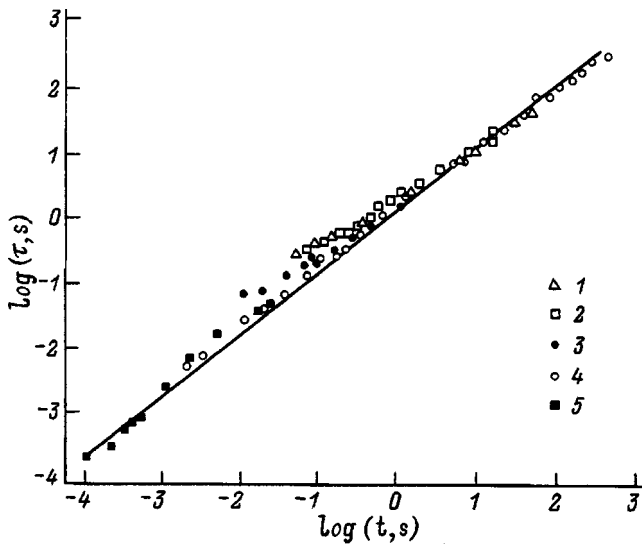
FIG. 8. Dependence of the instantaneous lifetime τ on time t for various temperatures of experiment, T, K: *1* — 115, *2* — 160, *3* — 211, *4* — 293, *5* — 467.

substantially different in different regions of space and, consequently, there are regions which are classically inaccessible for electrons with energy at the percolation level. Electrons can penetrate into these regions only by tunneling. It is precisely in such regions, which represent potential wells for the holes, that most of the holes are concentrated. Therefore, despite delocalization of the electrons, the electrons and holes are spatially separated and their recombination can, as before, have a tunneling character.

This assumption allows us to explain the contradiction between the nonexponential nature of the photoconductivity kinetics, on the one hand, and its independence of the generation level as well as the linearity of the current–illuminance characteristic, on the other. Indeed, the nonexponential character of the falloff, as at lower temperatures, is explained by a tunneling mechanism of recombination, whose lifetime τ_i continues to depend exponentially (and strongly so) on the distance between the recombining carriers r_i situated on the electron and hole localization centers. The independence of the kinetics on the generation level and, consequently, the linearity of the current–illuminance characteristic are explained by the fact that recombination proceeds under conditions in which the dark conductivity predominates. Consequently, the set of distances r_i is determined by the equilibrium carrier concentrations, which are fixed for a given temperature.

In such a model, acceleration of the kinetics with growth of the temperature is connected with a decrease in the scale of the characteristic distances as a result of growth of the equilibrium hole (p_{dark}) and electron (n_{dark}) concentrations. Moreover, proceeding from the idea that the setting-up mechanisms of the thermal equilibrium concentration and steady-state concentration are the same (i.e., under steady-state conditions the tunneling recombination rate of the carriers via localized states and their generation rate, be it optical or thermal, equalize. In other words, thermal generation is analogous to strong illumination) it is possible to calculate the dependence of the photoresponse times on the temperature.

In order to find this dependence, we recall that the photoconductivity decay is attributable to the successive emptying of the recombination channels from slow to fast. Since the photoresponse time is measured from the initial falloff of the photoconductivity, it is determined by the emptying of the fastest of the filled recombination channels, and the problem of calculating τ_0 reduces to a calculation of the critical distance r_0, introduced above, which separates the predominantly filled and predominantly empty states. In this case

$$\tau_0 \approx v_0^{-1} \exp(2r_0/a). \tag{15}$$

The problem of finding r_0 can be solved by substituting the following system of equations for the concentrations of the equilibrium electrons and holes:

$$n_{\text{dark}} = \sigma_{\text{dark}}/e\mu_D = (\sigma_0/e\mu_0)\exp[-(E_\sigma - E_\mu)/kT],$$

$$p_{\text{dark}} = N_h \int_{r_0}^{\infty} (3r^2/R^3)\exp(-r^3/R^3)dr \approx N_h\exp(-r_0^3/R^3),$$
$$\tag{1a}$$

$$n_{\text{dark}} = p_{\text{dark}}, \tag{1b}$$

where $\sigma_{\text{dark}} = \sigma_0\exp(-E_\sigma/kT)$ is the dark conductivity, and $\mu_D = \mu_0\exp(-E_\mu/kT)$ is the drift mobility of the nonequilibrium electrons. Solving the system of equations (16a)–(16c), we can calculate the temperature dependence of the critical distance r_0 and, consequently, the photoresponse time τ_0. Results of such a calculation are plotted in Fig. 8 by the solid line, together with the experimental data, for comparison. The calculation parameters were chosen both from the data in the literature, $\mu_D[\text{cm}^2/\text{V}\cdot\text{s}] = 10\exp(-0.2/kT[\text{eV}])$, and from the condition of best fit of calculation to experiment, $N_e = 3.5 \times 10^{17}$ cm^{-3}, $N_h = 3.0 \times 10^{16}$ cm^{-3}. Note that the obtained values are close to those that appear in the low-temperature region.

The good agreement between the calculated curve and the experimental points for a reasonable choice of calculation parameters serves as additional validation of the proposed model.

CONCLUSIONS

With growth of the degree of disorder in a semiconductor, it is possible to expect a broadening of the temperature range in which recombination is controlled by subbarrier tunneling transitions. In the case of hydrogenated amorphous silicon we have shown that recombination in a disordered material can have a tunneling character even up to temperatures near the temperature at which the material was synthesized.

To explain the experimental results we can use the model of donor–acceptor recombination in doped and compensated crystalline semiconductors. This model was modified to take into account the presence in a-Si : H of a developed spectrum of localization states and the possibility of thermally activated diffusion of nonequilibrium carriers over these states.

The conclusions drawn here are to a significant degree confirmed by the results of studies of the spectral dependence of the photoconductivity kinetics, which, for lack of space, have not been included here and will be published subsequently.

One of us (K. V. K.) would like to thank I. S. Shlimak (Bar-Ilan University, Israel) for a collaboration extending over many years that paved the way to the present work.

[1] R. H. Bube, *Photoconductivity of Solids* (Wiley, New York, 1960).

[2] S. M. Ryvkin, *Photoelectric Effects in Semiconductors* (Consultants Bureau, New York, 1964).

[3] F. E. Williams, J. Phys. Chem. Solids **12**, 265 (1960).

[4] V. P. Dobrego and S. M. Ryvkin, Fiz. Tverd. Tela (Leningrad) **4**, 553 (1962) [Sov. Phys. Solid State **4**, 402 (1962)].

[5] N. F. Mott and E. A. Davis, *Electron Processes in Non-Crystalline Materials* (Clarendon Press, Oxford, 1979).

[6] R. Rentzch and I. S. Shlimak, Phys. Status Solidi A **43**, 231 (1977).

[7] V. I. Safarov, I. S. Shlimak, and A. N. Titkov, Phys. Solid State **41**, 439 (1970).

[8] R. H. Bube, in *Hydrogenated Amorphous Silicon*, edited by Hans Neber-Aeschbacher (Scitec Publications, Ltd., Switzerland, 1995), Part 1, p. 463.

[9] T. Pisarkewitz and T. Stapinski, J. Non-Cryst. Solids (to be published).

[10] .M. Hoheisel, R. Carius, and W. Fuhs, J. Non-Cryst. Solids **63**, 313 (1984).

[11] B. I. Shklovskii, E. I. Levin, H. Fritzsche, and S. D. Baranovskii, in *Advances in Disordered Semiconductors, Vol. 3: Transport, Correlation and Structural Defects*, edited by H. Fritzsche (World Scientific, Singapore, 1990), p. 161.

[12] A. A. Andreev, A. V. Zherzdev, A. I. Kosarev, K. V. Koughia, and I. S. Shlimak, Solid State Commun. **52**, 589 (1984).

[13] K. V. Koughia and I. S. Shlimak, in *Advances in Disordered Semiconductors, Vol. 3: Transport, Correlation and Structural Defects*, edited by H. Fritzsche (World Scientific, Singapore, 1990), p. 213.

[14] T. Tiedje, in *The Physics of Hydrogeneted Amorphous Silicon II: Electronic and Vibrational Properties*, edited by J. D. Jonnopoulos and G. Lucovsky (Springer-Verlag, Berlin, 1984), p. 329.

[15] C. Tsang and R. A. Street, Phys. Rev. B **19**, 3027 (1979).

[16] V. Chech, F. Schauer, and J. Stuchlik, J. Non-Cryst. Solids (to be published).

[17] H. Reiss, C. S. Fuller, and F. J. Morin, Bell Syst. Tech. J. **35**, 535 (1956).

[18] Z. Vardeny, P. O'Connor, S. Ray, and J. Tauc, Phys. Rev. Lett. **44**, 1267 (1980).

[19] K. V. Koughia and E. I. Terukov, J. Non-Cryst. Solids **137−138**, 603 (1991).

[20] R. H. Bube, L. E. Benator, and K. P. Bube, J. Appl. Phys. **79**, 1926 (1996).

[21] H. Oheda, *Researches of the Electrotechnical Laboratory*, 886 (1978).

[22] H. Naito, in *Hydrogenated Amorphous Silicon*, edited by Hans Neber-Aeschbacher (Scitec Publications, Ltd., Switzerland, 1995), Part 1, p. 647.

[23] M. Gershenson, F. Trumbore, R. Mikulyak, and K. Kovalshik, J. Appl. Phys. **36**, 1528 (1965).

[24] M. H. Pilkum and M. R. Lorentz, Bull. Am. Phys. Soc. **11**, 188 (1966).

[25] V. S. L'vov, L. S. Mima, and O. V. Tret'yak, Preprint No. 182 [in Russian] (Institute of Automation and Electronics, Siberian Branch of the Academy of Sciences of the USSR, Novosibirsk, 1982).

Modification of the electron spectrum and vibrational properties of amorphous carbon by copper doping

V. I. Ivanov-Omskiĭ and É. A. Smorgonskaya

A. F. Ioffe Physicotechnical Institute, Russian Academy of Sciences, 194021 St. Petersburg, Russia

The near-gap electron spectrum and the effective charge distribution in graphite-like carbon nanoclusters of simple geometry in a-C : H containing a single Cu atom are calculated in the tight-binding approximation. Only the coupling between π electrons of the constituent C atoms and one valence s electron of the Cu atom is taken into account. The binding energy of the Cu atom in the clusters and the static dipole moment of the clusters are calculated. The results are invoked to interpret the experimentally observed activation of the Raman G band in the IR spectrum of a-C : H : Cu as a consequence of a lowering of the symmetry of the graphite-like clusters due to copper intercalation. Experimental data on the time dependence of the G band intensity during isothermal annealing of a-C : H : Cu are presented. The data suggest the possibility of reversible transfer of Cu atoms between the impurity states in the copper-carbon clusters and the impurity states in the purely copper clusters. The average activation energies of direct and reverse transfer are estimated from the experiment. © *1998 American Institute of Physics.* [S1063-7826(98)00708-X]

INTRODUCTION

Amorphous carbon a-C : H or, as it is frequently called, diamond-like carbon is a promising material for fabrication of hard, chemically stable and optically transparent film coatings. At the same time, a-C : H has aroused great interest as a nanosecond material manifesting quantum-well effects. Luminescence, optical absorption, infrared (IR) spectral data, and Raman scattering data indicate that graphite-like clusters, $5-20$ Å in diameter with sp^2 valence bonds, built into a diamond-like matrix with sp^3 bonds, are nanosize objects in a-C : H (Ref. 1). The quantum-well effects lead to the appearance of a gap in the electron spectrum of the graphite-like nanoclusters, which defines the optical absorption edge of a-C : H, thereby converting graphite from a semimetal to a semiconductor.[2]

Over the course of many years, B. T. Kolomiets and co-workers investigated the modification of amorphous semiconductors by metals (see, e.g., Ref. 3). They showed that a small fraction of some impurity atoms can, as a rule, create electrically active centers by raising the crystallizability of the system and cause impurity conduction of the solid solution,[3] as in crystalline semiconductors. However, when such a two-phase disordered medium as a-C : H is modified by a non-carbide-forming impurity such as Cu, it is more likely that the Cu atoms will be incorporated as sp^2-nanoclusters via an intercalation mechanism characteristic of crystalline graphite with agglomeration of the copper into clusters, which forms a more complex heterogeneous nanosystem. Fabrication of semiconductor nanostructures based on copper-modified, diamond-like carbon (a-C : H : Cu) with a corresponding study of their physical properties has become an important direction of research

based on the efforts initiated by B. T. Kolomiets in the study of noncrystalline semiconductors.

In earlier studies[4–6] it was shown that a copper impurity, introduced into a-C : H by combined magnetron sputtering of graphite and copper targets, leads to a nonmonotonic dependence of the conductivity of a-C : H : Cu on the Cu concentration: at first, the conductivity increases to eight orders of magnitude as the Cu content is increased to $14-16$ at. %, and then abruptly (by roughly six orders of magnitude) falls with continued growth of the Cu concentration, reaches a minimum at $20-25$ at. % Cu, and then increases again. In the optical transmission spectra of a-C : H : Cu, measured in the interval $0.6-5.0$ eV, growth of the extinction coefficient was observed in the region of the absorption edge with growth of the Cu content, accompanied by the appearance of a peak at Cu concentrations of about 14 at. % (Ref. 7). The intensity of the peak increased with increasing concentration, and the spectral position (~ 1.78 eV for all of the investigated concentrations) and shape did not depend on the temperature in the interval $77-300$ K. Features were also observed in the spectral dependences of the real and imaginary parts of the dielectric constant constructed from ellipsometry data on a-C : H : Cu samples with different Cu concentrations.[7] Copper-induced changes in the electrical and optical properties of diamond-like carbon have been interpreted as the result of formation in the material of two systems of copper-containing clusters, specifically, copper–carbon clusters with Cu content below roughly 15% and purely copper clusters with higher Cu content.[8]

This model was corroborated by direct studies of a-C : H : Cu nanostructures (see the review article in Ref. 9). For example, from the position of the maximum and from

the power-law nature of the asymptotic behavior of the intensity of small-angle x-ray scattering $I(\theta)$, as the scattering angle θ was increased, the characteristic correlation length of copper-containing clusters (R) and the variation of the fractal dimension D of the surface or of the scattering nanoclusters were estimated as functions of the copper concentration.[10] A study of the structure of immediate environment of the Cu atoms utilizing EXAFS and XANES spectroscopy[11] showed that at low Cu concentrations (<14 at. %) correlations are essentially absent in the positions of the Cu atoms and they interact mainly with the carbon matrix. At the same time, at higher concentrations the mean coordination number Z for a Cu atom surrounded by Cu atoms is 6 ± 3. This value is substantially lower than for bulk metallic copper, where $Z=12$, which gives an idea of the nanometer dimensions of the Cu clusters and, possibly of their nonspherical shape. The copper-containing nanoclusters built into the a-C : H matrix were directly visible in images of a-C : H : Cu samples obtained with a transmission electron microscope.[12]

In this article we consider the influence of a copper impurity on the electron spectrum and the vibrational properties of diamond-like carbon. The energy levels and the effective charge distribution in graphite-like carbon nanoclusters of simple configurations containing one Cu impurity atom are calculated in the tight-binding approximation. The binding energy of a Cu atom in a cluster and the static dipole moment of the cluster are calculated. The manifestation of dipole-active vibrations of carbon rings in the IR spectra of a-C : H : Cu as a function of temperature is discussed. Experimental results which indicate the possibility of a thermally activated, reversible transition between impurity states in a copper–carbon and in a purely copper cluster are presented.

1. MODEL OF STRONGLY BOUND ELECTRONS FOR GRAPHITE-LIKE CLUSTER WITH IMPURITY

In our treatment of the interaction of a Cu impurity with the a-C : H host matrix we assume that the Cu concentration is small, Cu–Cu interimpurity correlations is absent, and only one Cu atom is located in the region of the graphite-like cluster. In addition to the above-mentioned EXAFS and XANES spectroscopy data, this was also indicated by IR spectroscopic data. It was found that copper activates the so-called G band (1580 cm^{-1}) in the IR absorption of a-C : H : Cu films, which was observed in the Raman spectrum but hardly evident in the absorption (reflection) of impurity-free a-C : H (Refs. 13 and 14). As is well known, vibrations of the C–C bonds between carbon atoms in the plane of the six-member carbon rings in the graphite-like nanoclusters are responsible for the 1580 cm^{-1} Raman band (see, e.g., Ref. 15 and the bibliography cited there). It follows, therefore, that at least at moderately high concentrations the Cu atoms are built into the a-C : H structure in the region of the graphite-like nanoclusters. In addition, since copper does not form valence bonds with carbon, it may be assumed that the Cu atoms interact mainly with the π electrons of the C atoms in the graphite-like nanoclusters and the

perturbation of the strong C–C σ bonds in the presence of the Cu atoms can be ignored. The formation of ''copper–graphite'' nanoclusters in a-C : H : Cu leads to an increase in the extinction coefficient of a-C : H in the region of the optical absorption edge when copper is added and to the appearance of an absorption peak at sufficiently high Cu concentrations, as was mentioned earlier. This region of the spectrum is attributed to transitions between gap-separated binding π and antibinding π^* states of the carbon atoms in the graphite-like nanoclusters. Consequently, these states are subjected to the most noticeable modification in the presence of the Cu atoms. This allows us, for simplicity, to limit the calculation to the π electrons of the carbon atoms of the cluster and take into account their interaction with the s valence electrons of the Cu atom.

In the well-known tight-binding approximation (see, e.g., Ref. 16) the wave function of the jth state in the cluster $|\psi_j\rangle$ is sought in the form of a linear combination of atomic orbitals (LCAO) $|\chi_i\rangle$

$$|\psi_j\rangle = \sum_i u_{ji}|\chi_i\rangle, \tag{1}$$

where u_{ji} are the unknown coefficients, and the index $i=1,2,\ldots n$ numbers the atomic basis functions of all the atoms comprising the cluster. If only one electron function from each atom participates in the LCAO, then n is equal to the number of atoms in the cluster. The energy eigenvalues $E_j = \langle \psi_j | H | \psi_j \rangle$ and eigenfunctions $|\psi_j\rangle$ of the Hamiltonian H in the LCAO representation can be found by a variational procedure, which under the assumption of orthogonality of the functions $|\chi_i\rangle$ gives a system of equations in the coefficients u_i

$$\sum_i \langle \chi_j | H | \chi_i \rangle u_{ji} - E_j u_{ji} = 0. \tag{2}$$

The energies of the electron states E_j are found by diagonalizing the matrix $H_{ji} \equiv \langle \chi_j | H | \chi_i \rangle$. For each energy eigenvalue E_j the system of equations (2) yields a set of coefficients u_{ji}. The electron density distribution in the jth state over the atoms of the cluster can be found from the squared moduli of the coefficients, $|u_{ji}|^2$, calculated for all atoms of the cluster (the index i numbers these atoms).

The eigenenergies and eigenfunctions were calculated in the nearest-neighbor approximation; i.e., the matrix elements H_{ji} are assumed to be nonzero only if the indices i and j correspond to nearest-neighbor atoms in a cluster. To calculate these matrix elements we used the well-known universal Harrison formula, which has been successfully applied in approximate band calculations for semiconductors, and in the notation used in Ref. 16 we have

$$V_{ll'm} = \eta_{ll'm} \hbar^2 / \mu d^2. \tag{3}$$

Here $V_{ll'm}$ denotes the matrix element of the Hamiltonian H, taken over the atomic wave functions with orbital quantum numbers l and l' and magnetic quantum number m for two neighboring atoms located a distance d apart, μ is the mass of the electron, and $\eta_{ll'm}$ are universal dimensionless factors, whose values are tabulated in Ref. 16. If the valence
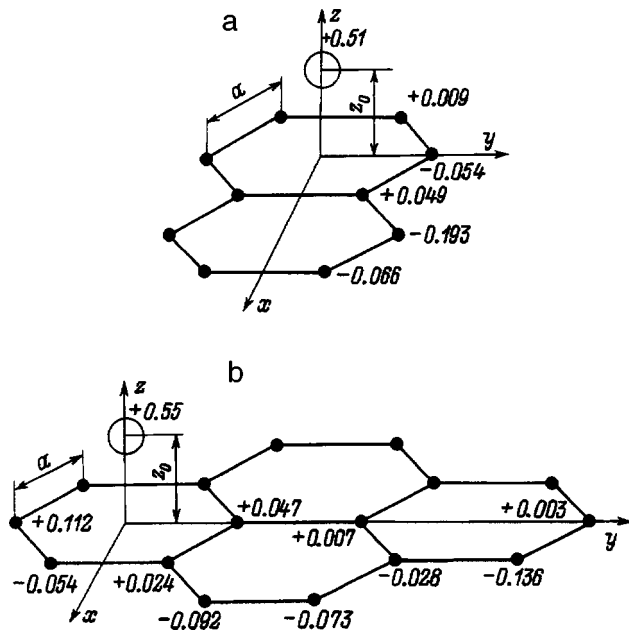
FIG. 1. Schematic representation of two graphite-like nanoclusters of simple configuration, containing 10 (a) and 16 (b) carbon atoms and one copper atom. The C atoms are represented by filled circles, and the Cu atoms—by the empty circle. The numbers indicate the effective charge of the given ion e_i^*/e.
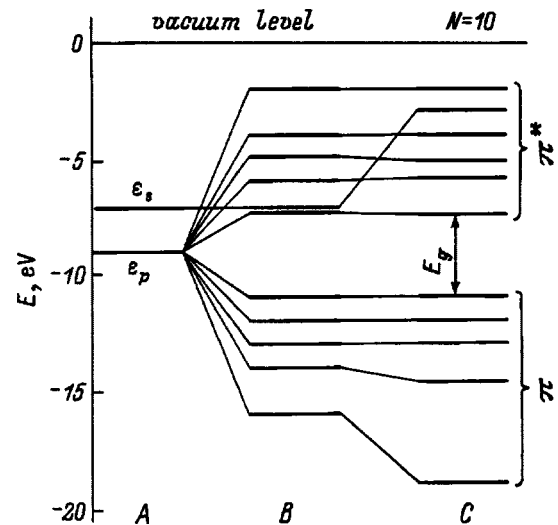

FIG. 2. Calculated distribution and shift of the $2p_z$ and $4s$ levels of the C and Cu atoms: A — for the isolated atoms; B — allowing only for the π-interaction of two carbon atoms (C–C) in the flat carbon layer; C — combined account of the π-interaction of two carbon atoms (C–C) in the flat carbon layer and of a copper atom and a carbon atom (Cu–C) in the body of a nanocluster containing 10 carbon atoms. The braces group together the antibinding π^* states and binding π states, respectively.

electrons in the atoms are s- and p-type states, then the coefficients $\eta_{ll'm}$ can take only four values corresponding to interatomic interactions of four types: $ss\sigma$, $sp\sigma$, $pp\sigma$, and $pp\pi$.

Numerical calculations were performed for several configurations of the graphite-like clusters, each of which consisted of several regular six-member rings of C atoms in the xy plane and one Cu impurity atom, located near the plane on the hexagonal axis $z\perp xy$ of one of the rings. Two examples of such clusters with several carbon atoms $N=10$ and $N=16$ are shown schematically in Fig. 1. By analogy with a crystal of graphite, it was assumed that the distance between individual carbon layers in the nanocluster greatly exceeds the C–C and Cu–C interatomic distances for nearest neighbors in one layer, so that it is possible to ignore the interlayer interaction and take into account the interaction of a Cu atom with the nearest C atoms only in one graphite layer. As was demonstrated above, only π-state forming $2p_z$ orbitals of all the C atoms of the nanocluster and the $4s$ orbital of the Cu atom were included in the LCAO (1).

The calculations reduce to a diagonalization of a matrix of order $N+1$, which contains four parameters: ε_p and ε_s, $V_{pp\pi}$ and $V_{sp\sigma}$. The diagonal matrix elements of the Hamiltonian

$$\varepsilon_p = \langle p_z|H|p_z\rangle = -8.97 \text{ eV}$$

and

$$\varepsilon_s = \langle s|H|s\rangle = -6.92 \text{ eV}$$

are the energy of the $2p$ state of the C atom and of the $4s$ state of the Cu atom relative to the vacuum, respectively. The nonzero nondiagonal matrix elements $V_{pp\pi} = \langle p_{zj}|H|p_{zi}\rangle$ for pairs of nearest-neighbor C atoms of a ring

were calculated according to formula (3) for $\eta_{pp\pi} = -0.81$ on the assumption that the distance between them $d = 1.42$ Å corresponds to the length a of a C–C covalent bond. The nondiagonal elements $\langle s|H|p_z\rangle$ describing the interaction of a Cu atom with the nearest C atoms of the carbon ring depend on the position z of the Cu atom relative to the plane of the ring:

$$\langle s|H|p_z\rangle = V_{sp\sigma}\frac{z}{(z^2+a^2)^{1/2}}. \tag{4}$$

The quantity $V_{sp\sigma}$ was calculated from Eq. (3) for $\eta_{sp\sigma} = 1.84$ and $d = (z^2+a^2)^{1/2}$.

2. ELECTRON SPECTRUM OF A CLUSTER CONTAINING A CU IMPURITY ATOM

First of all, it is possible to see from Eqs. (3) and (4) that for a Cu impurity atom in the considered geometry of nanoclusters there exists an optimal position z_0, which provides maximum overlap of the wave functions of the $2p_z$ and $4s$ states of the C and Cu atoms when the energy of interaction of the Cu atom with the carbon atoms is maximum. It is easy to show that $z_0 = a/\sqrt{2} \cong 1$ Å. The results presented below were obtained for the equilibrium position of the Cu atom in the cluster, z_0.

Figures 2 and 3 show the structure of the energy levels which we calculated for clusters with $N=10$ and 16 [see Fig. 1(a) and 1(b)], which arises as a result of splitting of the $2p_z$ states of the C atoms that do not interact (the B spectra in Figs. 2 and 3) and interact (the C spectra in Figs. 2 and 3) with the $4s$ electron of the Cu atom. These figures show the $2p_z$ and $4s$ levels ε_p and ε_s of the isolated C and Cu atoms (the A spectra in Figs. 2 and 3). The spectrum of the small clusters is discrete with number of states $N+1$; nevertheless,
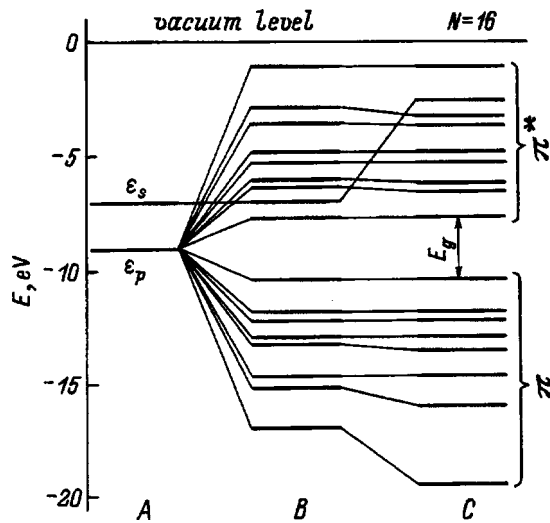
FIG. 3. The same as in Fig. 2, but for a nanocluster containing 16 carbon atoms.

a gap E_g, which separates the binding π and antibinding π^* states of the carbon atoms, is clearly revealed in it. As could be expected, the value of E_g decreases with increasing size of the cluster, in complete agreement with the calculations reported in Ref. 2 for purely carbon clusters. In our case, for a large cluster with $N=16$ the value $E_g=2.6$ eV is found to be in satisfactory agreement with the experimental data for the optical gap.[9]

In the absence of the Cu atom at zero temperature $T=0$, all the binding π states are filled with electrons, and the antibinding π^* states are free. As can be seen from Figs. 2 and 3, the $4s$ state of the Cu impurity atom falls in the energy interval which corresponds to the antibinding π^* states of the carbon atoms. Therefore, when the Cu atom interacts with the C atoms, the unpaired ''extra'' electron of the Cu atom shows up in the lowest antibinding state and its localization length is bounded by the size of the cluster. For a strong enough intercluster interaction these electrons make a substantial contribution to the conductivity of a-C : H : Cu. In fact, when the concentration of copper–carbon nanoclusters is high enough, because of homogeneous broadening of levels as a result of the intercluster interaction and because of inhomogeneous broadening due to differences in the geometry of the clusters, the discrete spectrum of the isolated clusters is transformed into a band spectrum with quasicontinuous bands of binding π and antibinding π^* states, i.e., into a spectrum with a π valence band and a π^* conduction band. In this limiting case the electrons of the Cu atoms, which are situated in the conduction band even at $T=0$, account for the metallic character of the electrical conductivity of a-C : H : Cu. At low concentrations of the copper–carbon nanoclusters, bulk conductivity is possible as a result of tunneling or thermally activated electron hopping between antibinding states of different clusters. As was already mentioned, an abrupt growth in the conductivity of a-C : H : Cu with Cu impurity concentration up to 14–16 at. % at $T=300$ K was observed.[4–6] However, the question concern-

ing the conductivity mechanism at different Cu concentrations requires special study.

3. BINDING ENERGY OF A CU ATOM IN A CLUSTER

The interaction of a Cu atom with a carbon ring [described by the matrix element (4)] in the two nanoclusters considered by us leads to a noticeable deepening of the lower bound states and, consequently, for essentially unchanged position of the upper levels, to a lowering of the mean energy of the occupied binding states. In this case, the occupied antibinding states in the given cluster configurations shift only slightly. The energy that binds the Cu atom with carbon atoms of the cluster ($E_b^{\text{Cu–C}}$) is easily estimated as the gain in the total energy of all the electrons of the cluster due to the Cu–C interaction compared with the case of an isolated impurity-free carbon cluster and an isolated Cu impurity atom:

$$E_b^{\text{Cu–C}}=(N+1)^{-1}\sum \; [2(E_b^{ud}-E_b^{d})+E_{nb}^{ud}-E_{ab}^{d}]. \qquad (5)$$

Here the sum is taken over the occupied states; the subscripts b, ab, and nb pertain respectively to the occupied binding, antibinding, and nonbinding states, and the superscripts ud and d correspond to an undoped and a copper-doped cluster. The $4s$ state of an isolated Cu atom is nonbinding: $E_{nb}^{ud}\equiv\varepsilon_s$. According to our estimates, for the two clusters considered [Figs. 1(a) and 1(b)] $E_b^{\text{Cu–C}}\cong0.67$ eV ($N=10$) and 0.43 eV ($N=16$). Thus, in a large cluster a Cu impurity atom is more weakly bound with the graphite plane than in a smaller cluster. Clearly, this is explained by the greater degree of delocalization of the electrons in a large cluster and the smaller relative contribution of the Cu–C interaction to the total energy of the cluster.

4. EFFECTIVE CHARGE OF THE ATOMS AND DIPOLE MOMENT OF THE CLUSTER

We calculated the effective charge distribution over the atoms of a cluster in the jth state from the squared moduli of the coefficients $|u_{ji}|^2$. Summing over all occupied states j gives the effective charge e_i^*/e on each atom i, expressed in fractions of the absolute value of the charge of an electron e:

$$e_i^*/e=(N+1)^{-1}\sum_j \; (2|u_{bi}|^2+|u_{abi}|^2). \qquad (6)$$

The subscripts b and ab, as before, pertain, respectively, to the occupied binding and antibinding states (the index j has been dropped). Calculated values of the effective charge on the atoms, e_i^*/e, for both clusters are indicated in Figs. 1(a) and 1(b), written alongside the corresponding atoms.

As follows from the calculations, the Cu impurity atom in a graphite-like nanocluster enters as a donor with negative ionization energy and is thus ionized even at $T=0$. In both clusters the positive charge of the Cu ion is a little larger than $+0.5e$. The flat carbon layer, taken as a whole, has the opposite charge $-0.5e$. Thus, a static dipole moment in the z direction arises in the cluste because of the Cu atom. In addition, because of the asymmetric position of the Cu atom relative to the carbon layer, a static dipole moment arises in

TABLE I.

N	P_x	P_y	P_z
10	−0.95	0	0.36
16	0	−1.53	0.38

the plane of the layer. The calculated components P_x, P_y, and and P_z of the resulting dipole moment **P** for both nanoclusters are given in Table I.

The quantities P_x, P_y, P_z are expressed in units of ea, where $a = 1.42$ Å is the length of the covalent C–C bond. The zero values of P_x and P_y, respectively, are connected with the symmetry of the specific nanocluster configurations relative to the x or y axis.

5. INFLUENCE OF THE CU IMPURITY ON THE VIBRATIONAL PROPERTIES OF *a*-C : H : Cu (CONSEQUENCES OF THE ADOPTED MODEL)

The presence of a Cu impurity atom in the graphite-like nanoclusters under consideration lowers their symmetry and converts them from two-dimensional (in reality, quasi-two-dimensional) objects into three-dimensional objects possess internal polarization. Structural changes of such type should be manifested in the vibrational properties of *a*-C : H : Cu. In particular, it is expected that new low-frequency bands, which are associated with dipole-active local vibrations of the Cu ion relative to the plane of the graphite-like layer, will appear in the infrared spectra of *a*-C : H upon the addition of copper. The corresponding frequency range is yet to be investigated experimentally.

As can be seen from our calculations, in the presence of the Cu atom neighboring pairs of carbon atoms in the plane of the rings become substantially nonequivalent in their charge state (Fig. 1), whereas in the absence of Cu, only the C atoms located in the interior and on the periphery of a bounded cluster are nonequivalent (the Raman D band at 1350 cm^{-1} in *a*-C : H is usually linked with limits on the size of the clusters). Therefore, in graphite-like clusters polarized by Cu atoms, vibrations of the C–C bonds in the plane of the rings and out of it can alter the corresponding components of the dipole moment and should thus be active in infrared absorption.

It is well known that for an isolated crystalline graphite layer, the E_{2g} vibrational mode due to symmetric vibrations of the C–C bonds in the plane of the rings is active in the Raman spectrum and is forbidden in the absorption. In a pair of neighboring layers, because of the well-known shift of one layer relative to another, the symmetry of the structure is lowered in comparison with an isolated layer, and the E_{2g} mode splits into an E_{2g} mode, which is active in the Raman spectrum, and an E_{1u} mode, which is weakly active in infrared absorption.[17] In amorphous carbon (*a*-C : H,), because of the absence of a correlation in the arrangement of the layers, the E_{1u} mode is usually not observed in the IR spectra. The role of the Cu impurity that interacts with a solitary layer of C atoms is essentially similar to the role of a neighboring carbon layer in graphite. However, the effect of lowering the

symmetry of a layer, which is associated with copper, is much more highly pronounced, and in the experiment a noticeable increase in the intensity of the G band with increasing Cu concentration is observed in *a*-C : H : Cu.[13,14] Since the spectral position of the G band hardly changes, it may be assumed that copper doping has a negligible effect on the geometry of the carbon layers, i.e., on the C–C σ bonds, as was assumed. In other words, copper intercalates the graphite-like structures.

Calculations for single-layer graphite-like nanoclusters of other configurations show that the closer the Cu impurity atom is located to the peripheral carbon rings of the cluster, the stronger will the inhomogeneity in the effective charge distribution over the C atoms be manifested and the larger will be the static dipole moment in the plane of the carbon layer. Qualitatively, this conclusion is supported by copper-impurity activation of the Raman D band in the infrared absorption of *a*-C : H, also observed experimentally. Note that when *a*-C : H is doped with nitrogen, a significant increase in the intensity of the G and D bands is also observed in the IR spectra. This has been interpreted as a result of substitution by nitrogen atoms of C atoms in the peripheral carbon rings of the nanoclusters.[15]

6. REVERSIBLE TRANSITION BETWEEN TWO STATES OF A CU ATOM IN *a*-C : H : CU

The above-found binding energy of a copper atom to a cluster $E_b^{\mathrm{Cu-C}}$ can be assumed approximately equal to the activation energy of removal of a Cu atom from its equilibrium position in this cluster to infinite separation (ΔE_d). Thus, as the temperature is raised, the probability of detachment of a Cu atom from a cluster per unit time τ_d^{-1} will increase according to the usual Boltzmann dependence

$$\tau_d^{-1} = \tau_{d0}^{-1} \exp[-(\Delta E_d / kT)]. \tag{7}$$

Here τ_{d0} is the characteristic time of nonactivation detachment. These considerations point to a means for obtaining a rough estimate of $E_b^{\mathrm{Cu-C}}$ from the experimental data if we compare the concentration of bound atoms Cu(N) with any observable quantity. On the basis of the discussion above, we assume that the G band absorption intensity in the IR spectra of *a*-C : H : Cu is such a quantity; i.e., we assume that the concentration N is proportional to the fraction of radiation absorbed in the sample, A: $N \propto A \equiv (I_0 - I)/I_0$, where I_0 and I are the intensity of the incident and transmitted IR radiation.

Figure 4 shows a typical dependence of the fraction of IR radiation A absorbed at the maximum of the G band on time of thermal annealing t, which we recorded on a sample of *a*-C : H : Cu of 0.4 μm thickness with Cu content 9 at. %. The IR spectrum in the corresponding frequency region was reported in Refs. 13 and 14. The samples were prepared by the technique of magnetron co-sputtering graphite and copper targets, described in detail in Ref. 9. In the measurements of as-grown samples it was found that annealing at 220 °C for one hour causes a noticeable decrease in the absorption, and that subsequent annealing for an additional hour at 310 °C lowers the intensity of the G band by more than an order of magnitude [region I of the curve $A(t)$]. From the
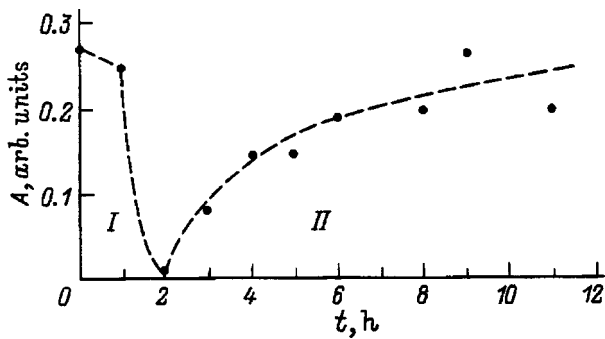
FIG. 4. Variation of the absorption (A) at the maximum of the vibrational G band in the IR spectrum of a-C : H : Cu with time t during isothermal annealing of a sample of thickness 0.4 μm with Cu content equal to 9%. Annealing temperature $T = 220$ °C with the exception of the first two hours of annealing, when $T = 310$ °C. The dashed line is the dependence $A(t)$ calculated with parameters giving the best fit to the experimental data.

experimental data it is difficult to establish the exact form of $A(t)$ in region I (see Fig. 4), but if we assume that

$$A(t) = A_0 \exp(-t/\tau_d), \qquad (8)$$

where A_0 is the fraction of the IR radiation absorbed by the as-grown sample at the maximum of the G band, then we can roughly estimate the characteristic time τ_d for two annealing temperatures and, employing expression (7), estimate the mean activation energy of detachment of the Cu impurity from the graphite-like clusters. According to estimates, $\Delta E_d \cong 0.9$ eV.

Note that graphite-like clusters of different sizes and configurations are, in fact, present in the disordered system in question, so that expression (8) can serve as an approximation of the true decrease of $A(t)$ only over a narrow time interval. Because of the spread in the values of the activation energy ΔE_d, the parameter τ_d depends on time, and in a wide interval of time t the function $A(t)$ most likely has a power-law character. If, on top of that, we have in mind theoretical estimates of only a very approximate sort for $E_b^{\text{Cu}-\text{C}}$, then their correspondence to the experimentally obtained value of ΔE_d may be assumed completely reasonable.

As can be seen in Fig. 4, the almost complete disappearance of the G band with further isothermal annealing is accompanied by its recovery; the absorption grows with time, so that after roughly 9 h of annealing at 220 °C the absorption intensity at the maximum of the G band almost reaches its original value (region II in Fig. 4). Relaxation of absorption in the G band in similar samples was detected earlier at room temperature;[14] in this case the time of complete recovery was roughly 15 days. It can thus be concluded that return of the Cu atoms to the graphite-like nanoclusters after thermal destruction of the intercalation state also has an activation character. By analogy with the foregoing discussion, we assume that the absorption in region II varies in accordance with

$$A(t) = A_0 [1 - \exp(-t/\tau_r)], \qquad (9)$$

where τ_r is a characteristic relaxation time, which depends activationally on the temperature, with activation energy

ΔE_r. Comparison of our data on the recovery kinetics of $A(t)$ at 220 °C (Fig. 4) with the data of Ref. 14 gives a rough estimate of the activation energy of relaxation: $\Delta E_r \cong 0.2$ eV.

Thus, at a moderately high a temperature, intercalation of the graphite-like nanophase of a-C : H with copper is a thermally activated, reversible process. At temperatures above $330-350$ °C the process of destruction of intercalation is irreversible.[9] In this case it can be asserted that in the reversible process of destruction–recovery of the intercalation state two possible structural positions of the copper atoms in a-C : H : Cu are manifested: in the graphite-like cluster and outside of it. At any given temperature thermodynamic equilibrium is established between these two positions. At equilibrium the relative values of the concentrations of the Cu atoms at a given position are determined by the difference in the mean activation energies ΔE_d and ΔE_r, which were discussed above. According to our estimates, $\Delta E_d > \Delta E_r$, so that at temperatures below $330-350$ °C under equilibrium conditions the intercalation state in a graphite-like cluster is preferable for a copper impurity in a-C : H : Cu.

CONCLUSIONS

Application of the simple model of tightly bound electrons to single-layer graphite-like nanoclusters in a-C : H with regular six-member carbon rings has demonstrated that copper doping in this material leads to partial filling of the antibinding states and, consequently, to ''metallization'' of semiconductor clusters. Individual copper-modified nanoclusters become similar to a degenerate n-type semiconductor, for which the Fermi level is found in the conduction band with the difference that due to its small size, the antibinding states of the cluster are localized and the electron spectrum is discrete. In this case, copper-doped amorphous carbon can be represented as a system of ''quasimetallic'' nanoclusters built into an insulating diamond-like matrix. The constant-current conductivity in such a system is determined by the probability of electron hops between clusters, which depends on the concentration and configuration of the copper-modified clusters and the temperature. The rapid increase in the conductivity of a-C : H : Cu, with Cu concentration observed experimentally in Refs. 4–6, is consistent with this model.

Interaction of the Cu impurity atom with the graphite-like sp^2-nanoclusters leads to a redistribution of the electron density in the cluster and to the appearance of a static dipole moment with nonzero components in the plane of the carbon layer fragments and normal to them. For this reason, the natural vibrations of the carbon rings in the plane of the layers become dipole-active, and the corresponding G and D bands, allowed in undoped a-C : H only in the Raman spectrum, become observable in the IR spectra of a-C : H : Cu and intensify as the Cu content is increased.

Studies of the temperature dependence of the intensity of the G band in the IR absorption spectrum during isothermal annealing have shown that in a-C : H : Cu at least two types

of states of the Cu atom coexist: an intercalation state in the graphite-like nanoclusters and a state outside of these clusters. At temperatures below $330-350\,^{\circ}\mathrm{C}$ a thermally activated, reversible transition is possible between these two states. This transition controls the equilibrium copper concentration in each of these states at the given temperature. From rough estimates of the corresponding mean activation energies ΔE_d and ΔE_r it follows that at moderately Cu concentrations in the equilibrium states a large fraction of the Cu atoms should be found in the intercalation state. In this case, as follows from the aforementioned EXAFS spectroscopy data,[11] the Cu atoms are distributed in an uncorrelated way, virtually without any interaction with each other. Approximate estimates of the energy that binds a Cu atom to a cluster in the tight-binding model are found to be in satisfactory agreement with the value of ΔE_d found experimentally.

The data reported here do not allow us to draw an unambiguous conclusion about the second structural state of Cu impurity in a-C : H : Cu. Judging from the electron microscopy data[9] and the EXAFS spectra,[11] this second state can be a state of purely copper, metallic nanoclusters embedded in the a-C : H matrix. At high enough Cu concentrations (greater than 14 at. %) the interaction between the Cu atoms exceeds their binding energy in the copper–carbon graphite-like clusters, and the state of purely copper clusters turns out to be the only one possible. At a certain concentration, agglomeration of Cu atoms into clusters with growth of the Cu content in a-C : H : Cu can cause a fall in the constant-current conductivity, as was observed experimentally.[4–6] Annealing at temperatures above $330-350\,^{\circ}\mathrm{C}$ also irreversibly destroys the copper–carbon clusters. Note that structural rearrangements in the system $\mathrm{Cu}-a$-C : H should manifest itself in the behavior of the electrical conductivity of a-C : H : Cu as a function of temperature.

We wish to thank G. S. Frolova for carrying out the optical measurements.

[1] J. Robertson, Adv. Phys. **35**, 317 (1986).

[2] J. Robertson and E. P. O'Reilly, Phys. Rev. B **35**, 2946 (1987).

[3] *Electronic Phenomena in Glassy Chalcogenide Semiconductors* [in Russian], edited by K. D. Tséndin, (Nauka, St. Petersburg, 1996).

[4] V. L. Aver'yanov, N. E. Bazieva, V. F. Masterov, A. V. Prikhod'ko, and S. G. Yastrebov, Pis'ma Zh. Tekh. Fiz. **19**, No. 12, 77 (1993) [Tech. Phys. Lett. **19**, 388 (1993)].

[5] V. I. Ivanov-Omskiĭ, M. I. Abaev, and S. G. Yastrebov, Pis'ma Zh. Tekh. Fiz. **20**, No. 22, 61 (1994) [Tech. Phys. Lett. **20**, 55 (1994)].

[6] N. E. Bazieva, S. G. Yastrebov, V. F. Masterov, and A. V. Prikhod'ko, Mol. Mater. **4**, 143 (1994).

[7] V. I. Ivanov–Omskii, A. V. Tolmatchev, and S. G. Yastrebov, Philos. Mag. **73**, 715 (1996).

[8] V. I. Ivanov-Omskii, A. B. Lodygin, and S. G. Yastrebov, Fiz. Tverd. Tela (St. Petersburg) **37**, 1693 (1995) [Phys. Solid State **37**, 1694 (1995)].

[9] V. I. Ivanov-Omskii, in *Diamond-Based Composites and Related Materials*, edited by M. Prelas *et al.*, NATO ASI Ser. **3**. *High Technology* (1997), Vol. 38, p. 171.

[10] V. I. Ivanov-Omskii, V. I. Siklitsky, and M. V. Baydakova, in *Diamond-Based Composites and Related Materials*, edited by M. Prelas *et al.*, NATO ASI Ser. **3**. *High Technology* (1997), Vol. 38, p. 191.

[11] A. V. Kolobov, K. Takanaka, H. Oyanagi, S. G. Yastrebov, V. I. Ivanov-Omskii, and V. I. Siklitsky, in *Diamond-Based Composites and Related Materials*, edited by M. Prelas *et al.*, NATO ASI Ser. **3**. *High Technology* (1997), Vol. 38, p. 197.

[12] V. I. Ivanov-Omskii, V. I. Siklitsky, A. A. Sitnikova, A. A. Suvorova, A. V. Tolmatchev, T. K. Zvonariova, and S. G. Yastrebov, Philos. Mag. B **76**, 973 (1997).

[13] V. I. Ivanov-Omskiĭ and G. S. Frolova, Zh. Tekh. Fiz. **65**, No. 9, 186 (1995) [Tech. Phys. **40**, 94 (1995)].

[14] V. I. Ivanov-Omskii and G. S. Frolova, in *Application of Diamond Films and Related Materials: Third International Conference* (NIST Special Publication 865, Gaithersburg, Maryland), p. 779.

[15] J. H. Kaufman, S. Metin, and D. D. Saperstein, Phys. Rev. B **39**, 13 053 (1989).

[16] W. A. Harrison, *Electronic Structure and the Properties of Solids* (W. H. Freeman, San Francisco, 1980).

[17] R. J. Nemanich, G. Lucovsky, and S. A. Solin, Solid State Commun. **23**, 117 (1977).

Translated by Paul F. Schippnick

Phase transitions occurring in glassy chalcogenide semiconductors induced by electric field or laser pulses

É. A. Lebedev and K. D. Tséndin

A. F. Ioffe Physicotechnical Institute, Russian Academy of Sciences, 194021 St. Petersburg, Russia

Order-disorder phase transitions in thin films of glassy chalcogenide semiconductors of the system Ge-As-Te, which take place during times on the order of microseconds in micron-sized volumes, have been studied and analyzed. The relationship between the reversible structural transitions induced by laser light pulses and the reversible semiconductor–metal transition taking place in a strong electric field is discussed. It is shown that the film can be taken repeatedly through a reversible phase transition in the conductivity at $\sim 500-600$ K, as previously established. It has been shown that repeated transition from the crystalline to the glassy state is possible without destruction of the material for a wide range of power levels for durations of the laser light pulse less than a few microseconds, and that this fact plays a decisive role in the reversible structural transformations. It is shown that the existence of such a range of power levels is attributable to overheating. © *1998 American Institute of Physics.*
[S1063-7826(98)00808-4]

INTRODUCTION

During the mid-1950s B. T. Kolomiets and N. A. Goryunova discovered a new class of materials—glassy chalcogenide semiconductors. This discovery served as a powerful stimulus for the creation of an entirely new branch of physics—the physics of disordered semiconductors. At present, along with glassy chalcogenide semiconductors, such broad families of disordered semiconductors as amorphous, porous, and microcrystalline silicon, semiconducting polymers, and amorphous carbon are the subjects of intense study.

In glassy chalcogenide semiconductors a wide range of unique phenomena has been detected. These phenomena have been described in detail by B. T. Kolomiets,[1–4] and in the recently published monographs in his memory.[5] Among these phenomena, a special place is occupied by the phenomenon of the electric instability, discovered in the course of a study of thin films of glassy chalcogenide semiconductors in strong electric fields.[6–8] The discovery of this effect has, in its time, attracted the attention of a large number of physicists and has played an important role in the quickening and expansion of studies of glassy chalcogenide semiconductors (GCS).

The phenomenon consists in an abrupt and rapid (in films of thickness $L \sim 1~\mu$m during a time $t \sim 1~\mu$s) transition of a small volume of the GCS (on the order of several cubic microns) from the semiconducting high-resistance state (HS) to the metal-like low-resistance state (LS). The transition takes place locally in fields with field strength $F \sim 10^5$ V/cm, at sites of enhanced current density (current filaments), and the decrease in the resistance at such sites reaches many orders of magnitude. Depending on the composition of the material, the geometry of the samples, and the characteristics of the electric field pulses, as a result of de-

velopment of the electric instability different final states can result. If the reverse transition to the high-resistance state takes place after removal of the applied voltage, then the ''semiconductor–metal'' reversible phase transition in the conductivity takes place since in the low-resistance state, in contrast to the high-resistance state, the conductivity is large and does not depend on the temperature of the surrounding medium. This phenomenon is frequently called the switching effect, and it is generally considered not to be connected with the structural transformations. In the case where the low-resistance state is remembered and exists without the applied voltage, we call it a memory effect. The appearance of the latter usually requires that the film be stored for a significant time under voltage in the low-resistance state. It is assumed, therefore, that the initial phase in the development of both effects is fundamentally the same, and differences arise only at later stages. These differences are due mainly to differences in composition. In studies of the memory effect, glassy chalcogenide semiconductors with an enhanced tendency to crystallize are generally used. As was shown in Ref. 9, the memory effect is associated with the appearance at the site of a current thread of a crystallized channel. In this case, one speaks of a reversible structural phase transition since, having chosen definite voltage pulse parameters, it is possible to return the crystalline channel to its original glassy state. The appearance of a crystalline channel is frequently accompanied by a noticeable change in the resistance of the low-resistance state. Thus, although the low-resistance state, which arises as a result of the reversible transition in the conductivity, and the low-resistance state due to a reversible structural transformation, are closely related, they are different. The low-resistance state associated with structural transformations may be assumed to be due to the appearance in the channel of either a degenerate doped crystalline semicon-

ductor or a metallic filament since it is well known that the crystalline channel is enriched with heavy elements such as tellurium.

Repeated cycling of reversible transitions—both structural transitions and transitions in the conductivity—is observed in relatively narrow-band glassy chalcogenide semiconductors with a narrow band gap $E_g \sim 1$ eV. In the case of wide-band glassy chalcogenide semiconductors with $E_g \sim 2$ eV at the site where a current filament has appeared, only reversible structural changes arise in the film.[10] Thus, in narrow-band glassy chalcogenide semiconductors irreversible and reversible transformations are possible, while in wide-band glassy chalcogenide semiconductors only irreversible transformations are possible.

Despite the large number of studies addressing the nature of the low-resistance, metal-like state arising as a result of a reversible transition in the conductivity (see Refs. 11–13), its nature is still unclear. There is no unity of opinion on the temperature that develops in a current filament[13] or on the electronic processes underlying the low-resistance state in a strong electric field. To shed some light on these questions, a knowledge of the conditions which distinguish reversible structural phase transitions from reversible transitions in the conductivity plays a large role.

Glass ↔ crystal phase transformations are usually investigated in large bulk samples of glassy chalcogenide semiconductors with relatively low rates of temperature change. Peculiarities of the structural phase transformations taking place during short time intervals and in small volumes, as is the case in optical and electric writing and rewriting of information in micron and submicron GCS films, have not been studied adequately. In the present paper we are reporting the results of an experimental study of reversible phase transitions in small volumes which are initiated by short, powerful laser pulses.

EXPERIMENT AND DISCUSSION OF RESULTS

We chose for study glassy chalcogenide semiconductors with the composition $Te_{0.81}Ge_{0.15}As_{0.04}$ and $E_g = 0.9$ eV with an enhanced tendency to crystallize. We used short laser pulses, whose characteristics, especially the temporal characteristics, were similar to the electric field pulses used in electric writing of information. Data obtained using laser pulses and a comparison with data obtained using electric pulses are of independent interest since the technology of creating information carriers in glassy chalcogenide semiconductors with writing and rewriting by laser radiation or an electric field has already reached a high level of development.[11,14,15]

Pulses of different duration τ are typically used to trigger the reversible phase transition from the glassy state to the crystalline state and its reverse. Thus, for $Te_{0.81}Ge_{0.15}As_{0.04}$ films in the case of electric field pulses the state with a crystallized channel (electric writing to memory) is obtained using $\tau = 2 \times 10^{-2}$ s, and for the reverse transition to the glassy high-resistance state (erasing) pulses of duration $\tau = 5 \times 10^{-7}$ s are used.[7] A similar ratio of durations of writing and erasing pulses also holds when using laser pulses (optical recording and erasure).
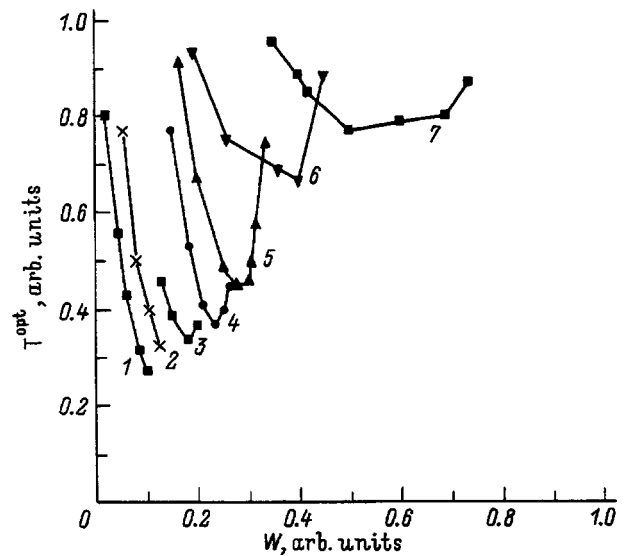

FIG. 1. Variation of the transmittance (T^{opt}) of $Te_{0.81}Ge_{0.15}As_{0.04}$ glassy films as a function of the power (W) for various durations of the light pulse, τ, μm: 1 — 50, 2 — 20, 3 — 10, 4 — 5, 5 — 3, 6 — 2, 7 — 1.

Experiments were performed on films of thickness about 0.1 μm, prepared by vacuum evaporation of the starting material onto glass substrates. The initial films were glassy. Together with these films, we also studied films that had been subjected to heat treatment at about 540 K. As a result of this treatment, these films were crystallized over their entire area, and in them it was possible to study the transition from the crystalline to the glassy state under the action of optical or electric pulses. The crystallization of the films was determined from a decrease in the transmittance of weak probe light by $5-10$-fold[17] or by a decrease in their resistance by several orders of magnitude. The softening point T_g of the composition under study was 410 K, the crystallization temperature (a $5-10$-fold decrease in the transmittance) was ~ 540 K, and the melting point $T_m = 650$ K (Ref. 17).

For optical recording, laser radiation with wavelength $\lambda = 0.51$ μm was used. The laser beam, focused on the film, created a spot several microns in diameter. The maximum power of the laser radiation incident on the film was about 140 mW. Single light pulses with duration 2×10^{-1} μs were obtained with the help of an acousto-optical modulator. The result of the action of the film of the recording light pulses was monitored by measuring the transmittance of the probe light beam (laser radiation with $\lambda = 0.63$ μm), focused on the spot on which the recording beam was incident, and also by subsequent inspection with a transmission microscope.

The following quantities were measured: the minimum power W_1 needed to burn a hole in the film; the power intervals corresponding to reversible crystallization of the glassy films and reversible amorphization of pre-crystallized films.

Figure 1 plots curves of the optical transmittance (T^{opt}) of glassy films as a function of the power (W) for different durations of the laser pulse. A few general trends of the variation of the transparency of the films as a function of pulse duration follow from the data plotted in Fig. 1. For
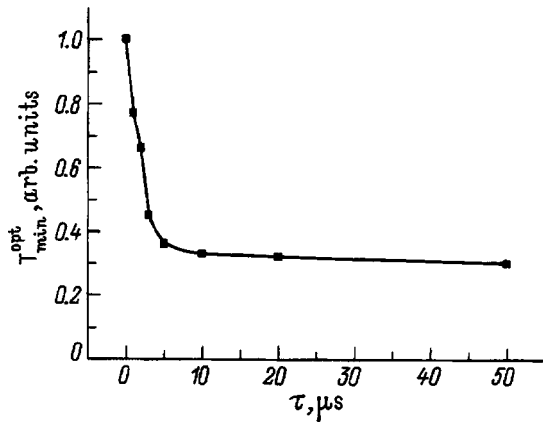
FIG. 2. Smallest value of the transmittance (T^{opt}) of $Te_{0.81}Ge_{0.15}As_{0.04}$ glassy films as a function of the duration of the light pulse.

FIG. 4. The limiting power W_1 (*1*) and the power leading to a twofold increase in the transmittance, W_2 (*2*), plotted as functions of the duration of the light pulse in annealed films. The horizontal bars labelled a and b correspond to a decrease in the transmittance by 30% and by a factor of 2 from its value in the original glassy film.

pulse durations above $10\,\mu$s, as the light intensity is increased, a gradual decrease in the transparency is observed. Such a pattern of variation of the transparency is maintained for durations of the light pulses up to 100 ms. For pulse durations below $10\,\mu$s, a minimum is observed in the transmittance–power curves. The magnitude of the greatest change in the transmittance of the glassy films as a function of pulse duration is shown in Fig. 2. This decrease in the transparency over the investigated interval of pulse durations is connected mainly with structural phase transformations similar to those that occur during thermal annealing of the films.[17] The appearance of a minimum in the transmittance curves for short light pulses is explained by a competition between crystallization and vitrification processes. Times on the order of $1\,\mu$s may be considered as limiting for phase transformations resulting in a decrease in the optical absorption of the films.

The transition from the crystalline to the glassy state was investigated on thermally pre-treated films. The nature of the variation of their transparency as a function of power for different durations of the light pulses is shown in Fig. 3. For pulse durations less than $1\,\mu$s it is possible to distinguish two segments in the curve of the transmittance as a function of the power (Fig. 3, curve *1*). In the first segment, as the
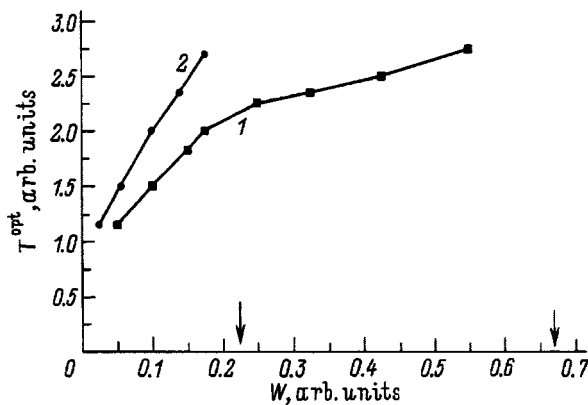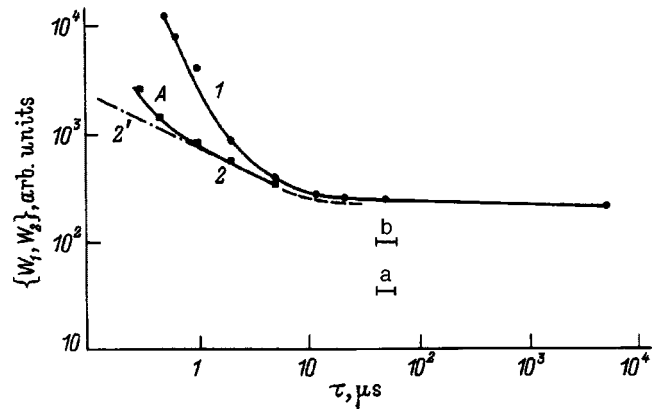

FIG. 3. Variation of the transmittance (T^{opt}) of annealed films as a function of the power for various durations of the light pulse. Arrows indicate the values of the limiting power W_1. τ, μs: *1* — 0.7, *2* — 1.5.

power is increased, a relatively rapid increase in the transmittance is observed. It stems mainly from an increase in the area of the segment of the film which undergoes a transition to the glassy state due to the nonuniform distribution of the power along the radius of the laser beam. At some power level a turning point in the curve is reached. This point is associated with a transition of the entire area monitored by the probe beam to the glassy state, beyond which is the saturation segment. In the saturation segment growth of the transparency is slowed down. A further increase in the power leads to an abrupt increase in the transparency as the limiting power W_1 is reached and local destruction of the film is achieved. The extent of the saturation segment decreases with increasing duration of the light pulses, and for pulse durations greater than $1.5\,\mu$s it virtually disappears (Fig. 3, curve *2*).

For thermally crystallized films we determined the minimum pulse power W_1 needed to burn a hole in the film as a function of pulse duration τ (Fig. 4, curve *1*). This figure also plots the dependence on τ of the power W_2 needed to increase the transparency (lighten the film) by a factor of 2 as a result of partial amorphization (Fig. 4, curve *2*). In films with $L \leqslant 1\,\mu$m the transition in an electric field takes place in 10^{-6} s or less. Therefore, in what follows we will give our main attention specifically to this time interval.

We will show that the strong dependence of W_1 on τ for short pulse durations is evidence that the nonsteady-state temperature of heating T_i significantly exceeds the melting temperature T_m (the phenomenon of overheating) and that T_i increases with decreasing pulse duration for points lying deep into region A in Fig. 4. Each point of this region corresponds to power levels which lighten the crystallized films by more than a factor of 2, $W(\tau) > W_2(\tau)$, but do not burn holes in them, $W(\tau) < W_1(\tau)$. For many points of region A the cycle ''darkening–lightening'' was repeatedly observed.

Let us first consider how the power should depend on the time if heating takes place all the time up to the same constant temperature, which does not depend on τ. The natural thermal relaxation time τ_r of a film of thickness

$L \approx 0.1 \ \mu\text{m}$ is equal in order of magnitude to 0.03 μs (Ref. 18), which significantly exceeds times of the order of $3 - 10 \ \mu$s, at which the quantity W in Fig. 4 ceases to depend on time. Consequently, for $\tau > \tau_r$ the heating volume also includes part of the substrate so that the characteristic linear dimension of this volume, l, is equal to $(D\tau)^{1/2}$, where $D = \varkappa / \rho c$, $\varkappa$ is the thermal conductivity, ρ is the density, and c is the specific heat. Assuming the thermal constants of the substrate and film to be similar, denoting the area of the spot as S, and substituting the quantity l into the equation of heat balance

$$W\tau = \rho c l S (T - T_0), \tag{1}$$

we obtain the dependence $W \sim 1/\tau^{1/2}$. The temperature of the surrounding medium is denoted as T_0. Such a dependence corresponds approximately to curve 2 in Fig. 4 for times up to $\sim 3 \ \mu$s. With further growth of τ, equilibrium is established and W ceases to depend on time. Just such independence of W on τ is observed for $\tau > 10^{-5}$ s. In this case, neither W_1 nor W_2 depends on τ, and the difference between W_1 and W_2 amounts to only $10 - 20\%$, so that it is difficult to distinguish them. Therefore, the curve $W_2(\tau)$ in Fig. 4 is shown schematically for these times by the dot–dashed line. We estimate the steady-state heating temperature T_s in this region as follows. As was mentioned above, crystallization of an initial glassy film can be achieved not only by heat treatment, but also by the action of laser radiation. The marker a in Fig. 4 indicates the power W_a and duration of a laser pulse bringing about the onset of structural transformations (decrease of transparency by $\sim 30\%$). As can be seen from Fig. 4, the power W_a which brings about the onset of structural transformations is about seven times less than W_1. Hence we obtain $W_1 / W_a = \Delta T_{s1} / \Delta T_{sa} = 7$, where $\Delta T_{s1,sa} = T_{s1,sa} - T_0$. According to Ref. 17, the onset of structural transformations during thermal annealing occurred for heating equal to only $\Delta T = 50$ K. Identifying this level of heating with ΔT_{sa}, we obtain $\Delta T_{s1} = 350$ K, i.e., $T_{s1} = 650$ K. We can obtain an upper estimate by comparing W_1 and the power W_b (the marker b) necessary to darken a fresh film by a factor of ~ 2. According to Ref. 17, such a level of darkening was achieved by thermal annealing for heating by ~ 210 K. Since $W_1 / W_b \approx 2$, it follows that $\Delta T_{s1} = 420$ K, i.e., $T_{s1} = 720$ K. Thus, for $\tau > 10 \ \mu$s T_{s1} lies in the interval $650 - 720$ K, whose lower boundary coincides with the melting point of the investigated glassy chalcogenide semiconductor. This estimate is also supported by the fact that in this time interval the power W_2 bringing on lightening associated with melting and subsequent amorphization is only $10 - 20\%$ less than W_1.

Completely different behavior is observed for $\tau < 10 \ \mu$s, where a strong increase of W_1 and a large disparity between W_1 and W_2 are seen. Let us first consider the dependence of W_2. In the time interval $\sim 0.3 - 3 \ \mu$s this dependence follows closely the law $\sim 1/\tau^{1/2}$, which, for guidance, is plotted by the line segment 2'. Consequently, for $\tau < 3 \ \mu$s the dependence of W_2 is determined by heating to a constant temperature. The large difference by which W_1 exceeds W_2 in this time interval implies a strong growth of the temperature corresponding to the power W_1 with decrease in

time. We estimate this temperature for $\tau \approx 0.4 \ \mu$s, assuming that the heating corresponding to W_2 is the same as for long times, equal to just $\Delta T_{i2} \sim 350$ K. Then equating the ratio W_1 / W_2, which for the given time value is equal to ~ 7, to the ratio $\Delta T_{i1} / \Delta T_{i2}$, we find that ΔT_{i1} is equal to ~ 2250 K. Thus we have found that while for longer times the temperatures T_1 and T_2 are similar and roughly coincide with the melting temperature, for shorter times the temperature T_1 significantly exceeds T_2, reaching at the end of the interval a value not less than 2250 K. Consequently, over the entire range $W_1 > W > W_2$ corresponding to region A in Fig. 4, the films withstand repeated heating without damage up to temperatures significantly above the melting point.

CONCLUSIONS

In Refs. 18 and 19 it was assumed that the phase transition in the conductivity occurs at a temperature, which, based on a large body of experimental data for a glassy chalcogenide semiconductor similar to the one investigated here, was assumed to be equal to $500 - 600$ K, which significantly exceeds the temperature of the surrounding medium $T_0 = 300$ K and is close to the softening point T_g of films of corresponding compositions. At the same time, the temperature $500 - 600$ K is much lower than the temperature of the transition from semiconductor conductivity to metallic conductivity T_{ft}, obtained directly from measurements on bulk samples in a weak field and equal to ~ 1000 K (Ref. 20). In Refs. 13 and 18 it was therefore concluded that to realize the phase transition in the conductivity in a strong field, heating (Joule current heating) and modification of the electronic properties of the glassy chalcogenide semiconductor in a strong field (thereby lowering T_{ft} from 1000 K to a value in the range $500 - 600$ K) are equally important.

According to another point of view, the phase transition in the conductivity in a field takes place without any heating, i.e., $T_{ft} = T_0$ and it is due only to a change in the microscopic electronic properties of the medium in a strong electric field. Numerous studies addressing this hypothesis are discussed in Refs. 11 and 12.

An important argument of the proponents of the hypothesis $T_{ft} = T_0$ is the high reversibility of the phase transition in the conductivity since it is assumed that repeated cycling from the semiconductor state to the metallic state and back without substantially altering the properties of the material can take place only in the absence of any noticeable heating. At the same time, the results of the present study show that for short-duration actions some regions of the glassy chalcogenide semiconductor can heat up to very high temperatures and cool down repeatedly without destroying the material.

Thus, the results obtained here indicate that the reversible phase transition ''semiconductor–metal'' can take place repeatedly at the temperatures $500 - 600$ K, determined in Refs. 18 and 19 since the GCS films withstand much greater heating without damage.

The data obtained in the present study are significant from an applied point of view since they show that the familiar advantages of optical and electric writing and rewriting of information by short pulses are attributable to the

existence at early times of a wide dynamic range of power levels (region *A*), while at later times this range is significantly narrowed.

[1] B. T. Kolomiets, Phys. Status Solidi **7**, 359 (1964); Phys. Status Solidi **7**, 713 (1964).

[2] B. T. Kolomiets, Vestn. Akad. Nauk SSSR **6**, 54 (1969).

[3] B. T. Kolomiets, in *Proceedings of the Sixth International Conference on Amorphous and Liquid Semiconductors: Electronic Properties in Non-Crystalline Semiconductors* [in Russian] (Nauka, Leningrad, 1975), p. 23.

[4] B. T. Kolomiets, Preprint of the Ioffe Physicotechnical Institute, Academy of Sciences of the USSR (Leningrad, 1981), p. 1.

[5] *Electronic Phenomena in Glassy Chalcogenide Semiconductors*, edited by K. D. Tséndin [in Russian] (Nauka, St. Petersburg, 1996).

[6] A. D. Pearson, W. R. Nothover, I. F. Dewald, and W. I. Peck, in *Advances in Glass Technology* (Plenum Press, New York, 1962), p. 357.

[7] B. T. Kolomiets and É. A. Lebedev, Radiotekh. Elektron. **8**, 2037 (1963).

[8] S. R. Ovshinsky, Phys. Rev. Lett. **21**, 1450 (1968).

[9] C. H. Sie, M. P. Dugan, and S. C. Moss, J. Non-Cryst. Solids **8-10**, 877 (1972).

[10] B. T. Kolomiets, É. A. Lebedev, I. A. Taksami, and V. Kh. Shpunt, Fiz. Tekh. Poluprovodn. **7**, 2045 (1973) [Sov. Phys. Semicond. **7**, 1368 (1973)].

[11] A. Madan and M. P. Shaw, *The Physics and Applications of Amorphous Semiconductors* (Academic Press, San Diego, 1988).

[12] S. A. Kostylev and V. A. Shkut, *Electronic Switching in Amorphous Semiconductors* [in Russian] (Naukova Dumka, Kiev, 1978).

[13] É. A. Lebedev and K. D. Tséndin, in *Electronic Phenomena in Glassy Chalcogenide Semiconductors*, edited by K. D. Tséndin [in Russian] (Nauka, St. Petersburg, 1996), p. 224.

[14] G. Bouwhuis, J. Braat, A. Huijser, J. Pasman, G. van Rosmalem, and K. Schouhamer Immink, *Principles of Optical Disk Systems* (Adam Hilger Ltd., Bristol, England, 1985).

[15] K. K. Shvarts, *Physics of Optical Recording in Insulators and Semiconductors* (Zinatne, Riga, 1986).

[16] V. Kh. Shpunt, in *Electronic Phenomena in Glassy Chalcogenide Semiconductors*, edited by K. D. Tséndin [in Russian] (Nauka, St. Petersburg, 1996), p. 300 [*sic*].

[17] N. K. Kiseleva, V. I. Kochenov, and É. A. Lebedev, Fiz. Tverd. Tela (Leningrad) **30**, 1965 (1988) [Sov. Phys. Solid State **30**, 1135 (1988)].

[18] B. T. Kolomiets, É. A. Lebedev, and K. D. Tséndin, Fiz. Tekh. Poluprovodn. **15**, 304 (1981) [Sov. Phys. Semicond. **15**, 175 (1981)].

[19] P. J. Walsh, R. Vogel, and E. J. Evans, Phys. Rev. **178**, 1274 (1969).

[20] D. L. Thomas and J. C. Male, J. Non-Cryst. Solids **8−10**, 522 (1972).

Translated by Paul F. Schippnick

Modeling of hypervalent configurations, valence alternation pairs, deformed structure, and properties of *a*-S and *a*-As$_2$S$_3$

S. A. Dembovskiĭ,[a)] A. S. Zyubin, and F. V. Grigor'ev

N. S. Kurnakov Institute of General and Inorganic Chemistry, Russian Academy of Sciences,
117907 Moscow, Russia
(Submitted February 13, 1998; accepted for publication February 23, 1998)
Fiz. Tekh. Poluprovodn. **32**, 944–951 (August 1998)

Quantum-chemical modeling of the structure, stability parameters, and electronic structure of defects (deformational, topological, bond) in *a*-S and *a*-As$_2$S$_3$ was performed. The position of localized states in the band gap, which correspond to defects, including states excited by light with energy $\hbar\omega \lesssim E_g$, was established. It was shown that the generally accepted concept of valence aternation pairs (VAPs) must be reexamined, at least in our case, since the formation of pairs of separated charged point defects of the type C_3^+ and C_1^- requires too much energy. On the other hand, it is shown by analogy with *a*-Se that centers connected by a strong bond can coexist in the form of rigid VAP dipoles. It was found that nonrigid, metastable, hypervalent configurations (HVCs) exist in the form of HVC dipoles, which are neutral and diamagnetic in the ground state and lie below C_1^0 on the energy scale. Defects of the hypervalent configurations type can be used to explain the increase in the coordination number in the noncrystalline state, as compared with their crystalline analogs, and to discuss several properties which are determined by such defects. The effect of HVC and VAP dipoles on the properties of glassy semiconductors, including their role in photoinduced defects, is discussed. © *1998 American Institute of Physics.* [S1063-7826(98)00908-9]

As a rule, defects determine the properties of not only crystalline but also noncrystalline semiconductors — chalcogenide glassy semiconductors (CGSs), discovered by B. T. Kolomiĭts and N. A. Goryunova. Before the notion of chemical-bond defects was introduced, fluctuations of the parameters of noncrystalline structure, which Gubanov associated with localized states in the band gap,[1] were studied. Ovshinsky assigned to *LP* electrons a special role.[2] The introduction of Anderson's hypothesis of an effective negative correlation energy at U^- centers,[3] which was used to explain the absence of an ESR signal and to pin the Fermi level in CGSs, made it possible to introduce the notion of defects D^+, D^-, and D^0 (Ref. 4) and even specific chemical-bond defects of the valence alternation pair (VAP) type with overcoordinated and undercoordinated atoms, for example, the states C_3^+ and C_1^- in Se, which, according to Ref. 5, are more stable than C_3^0 (C_1^0), where C is the chalcogen atom (the superscript denotes the charge and the subscript denotes the coordination number). It was implicitly assumed that the large amounts of energy, comparable to the ionization potential, required to produce C_n^+ are compensated by the interaction with the environment. In particular, C_1^+ stabilizes, forming a bond with the nearest chains (C_3^+). This assumption leads to a very large overestimation of the stability of positively charged defects, as first pointed out in Ref. 6. The notion of soft atomic configurations, which explained the existence of U centers, was introduced.[6,7]

There exist other models of defects, based on hypervalent and, in particular, three-center bonds (TCBs).[10] These models are essentially ignored by the scientific community.

They were intensively developed during the last 20 years by one of the present authors,[11–16] including in the form of hypervalent configurations (HVCs) which are neutral and diamagnetic in the ground state.[17,18]

A direct proof for the existence of HVCs is that, according to x-ray diffraction, the coordination Z_1 in many CGSs is greater than the valence, for example, in plastic *a*-S and in *a*-Se $Z_1 > 2$ (2.1–2.2),[19] which formally corresponds to ~20% of the atoms with $Z_1 = 3$. Therefore, VAPs ($Z_1 = 2$) cannot explain the increase in $Z_1 > 2$. This was the starting point of Ref. 11, where a connection was first made between $Z_1 > 2$ in *a*-Se and TCBs. The materials *a*-S and *a*-Se are not the only CGSs whose value of Z_1 is greater than the valence. Such evidence also exists for As$_2$X$_3$ (X=S, Se, Te) and *l*-Te,[19,20] which indicates the prevalence of HVCs in macroscopic ($>1\%$) concentrations, which greatly exceed the VAP concentration ($<10^{17}$ cm^{-3}). HVC defects in the form of TCBs were used to explain the continuous mechanism of bond switching accompanying atomic transport,[10,11] photostructural transformations,[12] paramagnetism, including photoparamagnetism,[12] and the first sharp diffraction peak,[21] to explain the photoinduced anisotropy and gyrotropy[14,15] since they have the symmetry of the point group C_1 and are therefore polar and chiral,[14] and to explain the excess entropy[22] $\Delta S_0 > 0$ ($0 < T < T_g$) and the configurational entropy[23] $\Delta S_c > 0$ ($T_s < T < T_m$). HVC-type defects have been confirmed in *a*-Se by calculations based on the local-density functional[24] and in *a*-Se[17] and GeS$_2$[18] by quantum-chemical modeling. Quantum-chemical modeling has also

shown HVCs in g-SiO_2,[25] GeO_2,[26] and B_2O_3,[27] and TCBs in g-SiO_2[28] and a-SiH.[29]

We shall give an expanded definition of a defect as anything that distinguishes a noncrystalline material from the corresponding crystal in short-range order (interatomic distances, valence angles) and medium-range order (MRO), including in the so-called near-MRO (torsional angles), following the classification given in Ref. 30. Then, two basic groups can be distinguished on the basis of this definition. The first group contains:

1. Deformational defects (interatomic distances, valence and torsional angles);

2. topological defects — chains and rings with a different number of atoms or structural polyhedra — C_N;

3. irregular (or homopolar) As–As and S–S bonds in As_2S_3.

A common feature of the defects 1–3 is that the chemical bond type — the coordination Z_1 and the valence — is preserved.

The second group contains chemical-bond defects. Most of these defects in CGSs have not been studied previously at the quantum-chemical level or, as in the case of VAP, they have been modeled for a long time and only for Se[31,32] and did not confirm the existence of U^- centers.[32] A search for HVC-type defect structures has not been made. In the scientific literature arbitrariness reigns in the description of VAP-type defects and their transformations in processes and virtually any properties are attributed to them, especially in complex substances of the type As_2S_3. The scientific community is even less familiar with HVC-type defects. In the present paper defects of the first and second types in a-S and a-As_2S_3 will be modeled and they will be compared with the properties of CGSs. The modeling was performed using the semiempirical MNDO method for a-S and the PM3 method for a-As_2S_3 in the cluster approximation, checked in Refs. 17 and 18. This approach gives a satisfactory description of the structural and energy characteristics of a-S and can be used for qualitative and semiquantitative modeling of defects in it.

1. MODELING OF DEFECTS

1.1 Deformational defects

1.1.1. Bond stretching. In this section, defects arising as a result of fluctuations of bond lengths and valence and torsion angles are modeled. Accordingly, the initial clusters, consisting of the ring S_8 and the chain HS_7H in the case of a-S and a C_6 type ring in the case of a-As_2S_3, were subjected to deformation by increasing the distance between the terminal atoms of the corresponding clusters. The dependence of the energy required for deformation on the relative elongation is shown in Fig. 1.

1.1.2. Modeling of soft and multiwell potentials. The change in the properties of the local atomic potential with a substantial stretching of the bonds was investigated for a-S. The results of such an investigation, undertaken in Ref. 28 for g-SiO_2, demonstrate the possibility for the formation of local soft and multiwell potentials with participation of TCBs in the presence of sufficiently strong bond stretching.
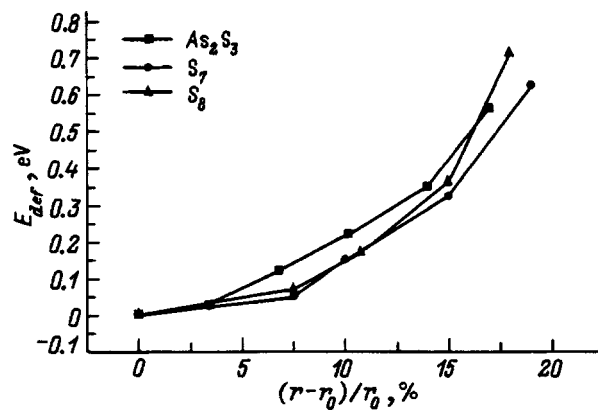

FIG. 1. Deformation energy E_{def} in a ring S_8 and chain S_7 in sulfur and in the ring C_6 in arsenic sulfide as a function of the relative deformation $(r-r_0)/r_0$ (r and r_0 — cluster size in the stretched and unstretch states).

The distance r_{1-3} was fixed and the distance r_{2-3} was varied (Fig. 2). If $r_{1-3} \simeq r_{1-3}^{(0)} = 3.13$ Å (curve *1*), the dependence of the potential energy on the distance r_{2-3} is found to be almost the same as for an ordinary covalent bond. As the distance r_{1-3} is increased, the minimum of the energy in the equilibrium position increases, while the local elasticity constant decreases. In this kind of modeling of soft potentials it is necessary to take into consideration the possibility of a transition from a singlet state to a triplet state, since for a strongly stretched bond the latter could become more favorable. In this case the dependence of the potential energy on the distance r_{2-3} has several local minima (see Fig. 2 and the caption there).

1.1.3. Low-energy defects. Low-energy excitations in the a-As_2S_3 structure, such as inversion of an As atom located at the apex of the structural pyramid AsS_3 and rotation of the ''bridge'' sulfur atom around an axis formed by the As atoms, were investigated. Inversion, for which the energy barrier equals 0.4 eV, could be responsible for the presence of a peak in the curve of the tangent of the dielectric loss
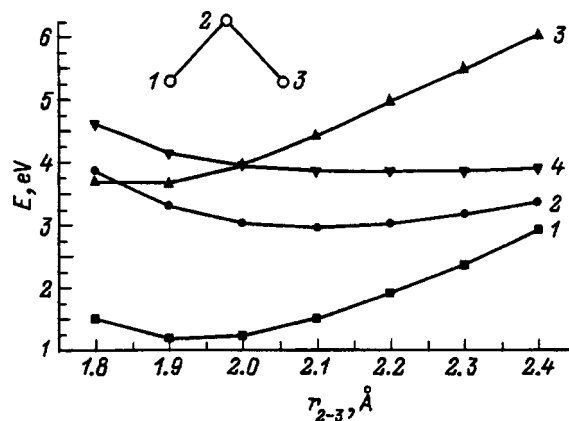

FIG. 2. Cluster formation energy E as a function of the distance r_{2-3} between the closest sulfur atoms for different values of r_{1-3} (in Å): *1* — 3.13; *2*, *3* — 4; *4* — 4.2. The decrease in the local coefficient of elasticity with increasing r_{1-3} is demonstrated. Curves *1*, *2*, and *4* correspond to singlet states, curve *3* corresponds to a triplet state. The crossing of curves *3* and *4* illustrates the possibility of a transition from a singlet into a triplet state as a result of a change in r_{2-3}.
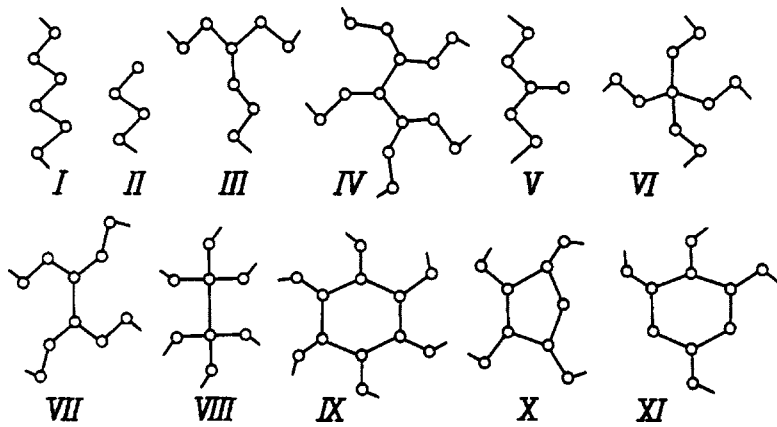
FIG. 3. Schematic representation of different defects in noncrystalline sulfur. For the configurations V (VAP-*d*) the charges $Z(C_n)$ in units of the elementary charge, the bond order Q, and the bond length r in Å for C_3^+, C_1^-, and C_2^0 centers are, respectively: $Z(C_3^+) = 0.36$, $Z(C_1^-) = -0.25$, $Z(C_2^0) = -0.1$; $Q(C_3^+ - C_1^-) = 1.22$, $Q(C_3^+ - C_2^0) = 0.77$; $r(C_3^+ - C_1^-) = 1.86$, $r(C_3^+ - C_1^-) = 2.02$.

angle ($\tan\chi$) at frequencies $\cong 400{-}1000$ kHz. The transition frequency of an As atom from one position into another falls in the frequency interval where a peak of $\tan\chi$ is observed.[33] Rotation of the bridge sulfur atom occurs with a very low barrier on the order of several hundredths of an eV.

1.2 Homopolar bonds in *a*-As$_2$S$_3$

The concentration of ''irregular'' As–As and S–S bonds in *a*-As$_2$S$_3$, which is determined from IR-spectroscopy data, reaches 5–6%.[34] The modeling of such bonds was performed in a cluster consisting of a C_6 ring. The inner sulfur atom and the arsenic atom changed places, so that the two As–S bonds changed into S–S and As–As bonds. According to the results obtained, the formation of S–S and As–As bonds requires $\simeq 0.7$ eV, which is close to the value 0.5 eV presented in Ref. 35.

1.3 Topological defects

The structural differences of *a*-S, *a*-As$_2$S$_3$, and the corresponding crystals are due to the existence of different structural elements in CGSs. These are rings C_N with a different number of atoms, predominantly with $N = 6{-}8$ for *a*-S, as well as chains S$_N$ of different length. According to our modeling results, rings with $N = 6{-}8$ are energetically favored in both *a*-S and *a*-As$_2$S$_3$. However, this does not rule out the existence of rings with $N < 6$ in *a*-S and *a*-As$_2$S$_3$.

1.4 Chemical bond defects

1.4.1. VAP model. As already mentioned above, the VAP model postulates that in *a*-Se the decomposition of a chain consisting of atoms in the state C_2^0 (Fig. 3, configura-

tion I) into paramagnetic fragments C_1^0 (Fig. 3, configuration II) is energetically less favorable than the formation of charged defects. However, the ratio of the stability of $2C_1^0$ and the pair C_3^+, C_1^- was estimated mainly on a qualitative level, using very rough approximations.[35] The modeling of the properties of such defects in Se in the local-density functional approximation[32] showed that the pair C_3^+, C_1^- is still less stable than $2C_1^0$. These results cast doubt on the admissibility of the VAP model, and in the present work we investigated it with the aid of the quantum-chemical calculations of defects in *a*-S.

According to the results obtained by us, much more energy is required to form the charged defects C_1^+ and C_1^- than for homolytic breaking of a bond (Table I). The interaction with one and two neighboring chains (Fig. 3, configurations II, III) greatly decreases this difference, but it still remains too large. More than two chains do not attach to a charged defect, so that further stabilization of charged defects as a result of an interaction with the environment will no longer be important. In the configurations III and IV, substantial changes in the geometric and electronic structure occur in the first coordination sphere around a charged center — the bond lengths increase to 2.0–2.1 Å, while the bond orders Q decrease by approximately a factor of 2; the excess charge becomes delocalized — for negatively charged clusters mainly on atoms of the first coordination sphere (CS), while for positively charged clusters the atoms of the second CS are also affected. The changes in the third and more distant CSs are negligible. Thus, the interaction of charged defects with the environment results in a substantial polarization of the closest fragments of the main network of the glass and a substantial lowering of the energy of the system. Nonetheless, this stabilization cannot completely compensate for the

TABLE I. Relative energy stability DE of different defects in noncrystalline sulfur. The plus (+) sign indicates that there is no chemical bond between the charged centers and the minus (−) sign indicates that such a bond does exist. KEY: 1) Configuration 2) Model

Configuration	Model	DE, eV	Configuration	Model	DE, eV	Configuration	Model	DE, eV
I	C_2^0	0.0	IV	$C_3^+ \cdot C_3^-$	5.2	VIII	$C_3^+ \cdot C_3^-$	3.6
II	$2C_1^0$	2.0	V	$C_1^- \cdot C_1^-$	1.9	IX	$C_3^+ \cdot C_3^-$	1.2
II	$C_1^+ + C_1^-$	9.2	VI	$C_3^+ \cdot C_1^-$	1.7	X	V·I	1.5
III	$C_3^+ + C_3^-$	5.9	VII	$C_3^+ \cdot C_1^-$	0.6	XI	V·I	2.1

energy expended on ionization, so that the correlation energy $U > 0$, in agreement with the results obtained in Refs. 31 and 32 for *a*-Se. When two type-II defects interact, besides reduction of the chain I, there can arise a metastable configuration V in which the negatively and positively charged atoms are bound together, which leads to the formation of a dipole (in what follows — VAP-*d*) (Table I, configuration V; the parameters are given in the caption to Fig. 3). Such a structure is a local minimum of the potential surface and possesses a singlet ground state for $U < 0$. A similar configuration with excess energy 1.2 eV was found in Ref. 31 in modeling *a*-Se.

1.4.2. Hypervalent configurations (HVCs). It can be expected that if oppositely charged defects are located next to one another and are incorporated into a single structure, then their total energy decreases substantially as a result of the Coulomb interaction and transfer of electronic density between charged fragments. On this basis we estimated the structure and stability of HVCs arising when oppositely charged configurations II, III, and IV ... join together. The joining of defects II and III also leads to the formation of a metastable singlet (in the ground state) configuration VI if centers C_1 and C_3 interact. When they are displaced by one link, a VII-type complex, which is stable against decay into two chains, is formed; in the case of a larger displacement, unstable complexes consisting of two chains and a fragment S_N between them are formed. If the distance between C_3 centers in a type-VII configuration is fixed at the same value as in the configuration III (2.0 Å), then its structure and energy characteristics can be estimated. It turns out that it possesses a singlet state and is much more stable than two C_1^0 defects (Table I). All bond orders in a hypervalent fragment of this configuration are substantial — $Q \simeq 0.3$ between C_3 centers and $Q \simeq 0.9$ between C_3 and C_2. All this signifies that the fragments of a chain broken by the drift of the environment should interact with the nearest chain upon lowering the energy and upon a transition to a singlet state, i.e., instead of rupture, the bond switches with the help of type-VII HVCs. When two centers C_3 in a type-III fragment interact, a type-VIII configuration, which is stable in the singlet state against spontaneous decay but lies on the energy scale far above $2C_1^0$, forms. The most stable product of the interaction of type-III fragments is a type-IX configuration — a nonplanar six-member ring consisting of C_3 atoms. It can also be obtained in the interaction of type-II and -IV fragments. This configuration transforms into three isolated chains. If the configuration is prevented from decomposing, having set a limit on the distance in a ring, on the energy scale it will lie below the pair of defects C_1^0, i.e. a dangling bond, which is sandwiched between two chains, should transform into a singlet HVC which effects bond switching.

The interaction of type-V configurations with chains could provide additional possibilities for the formation of HVCs. The five-member ring X formed in this manner is unstable with respect to decay into two chains and lies 1.5 eV higher on the energy scale, if the distances r_{1-2} and r_{3-4} are fixed and equal 2.0 Å. Connection of fragments I and V into a six-member ring (Fig. 3, XI) gives the most interesting result. Its ground-state electronic structure is a singlet, and it
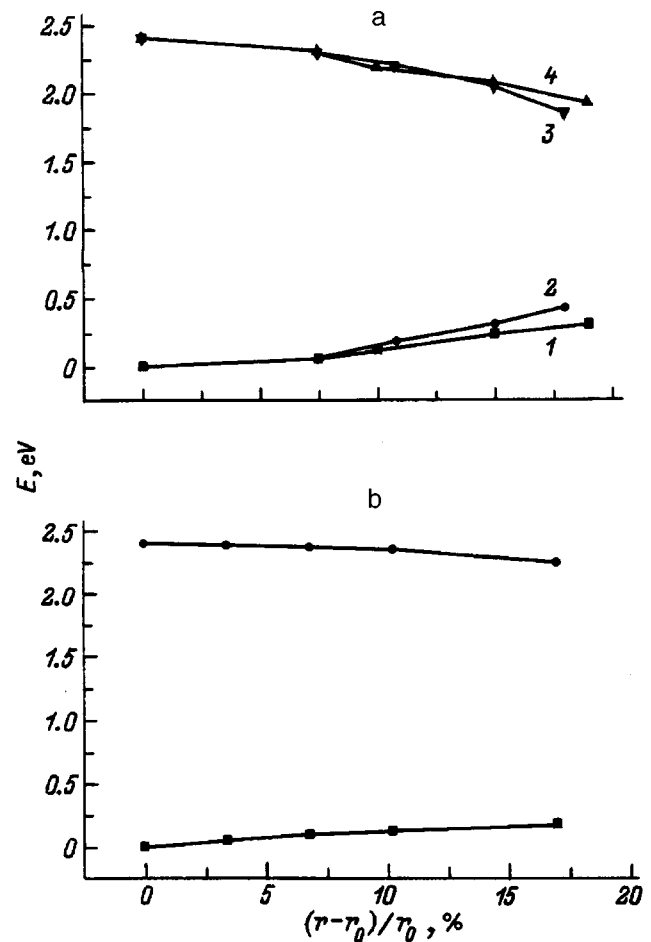

FIG. 4. Shift of the valence band edge E_v (bottom curves) and conduction band edge E_c (top curves) as a function of the relative deformation $(r - r_0)/r_0$ on stretching: a — S_8 rings (*1*, *4*) and S_7 chains (*2*, *3*); b — C_6 rings in *a*-As$_2$S$_3$. The energy is measured from the position of E_v in the undeformed structure.

lies above X on the energy scale, but its zero-barrier decay into chains is impossible. This configuration is slightly unstable with respect to separation into fragments I and V, but the energy difference is small (0.2 eV), and a rigid environment can keep this complex from decomposing. Type-XI HVCs are apparently similar to a soft atomic configuration, since in order to form it much less energy is required for a chain and a VAP-*d* defect to draw together to a distance corresponding to the S–S bond length than for atoms to draw together in ordinary chains. We did not consider the formation of larger rings, since they should be less stable. It should be emphasized that the charges of the atoms in the configurations VII–XI are small, i.e., their electronic structure does no correspond to a pair of charged centers.

2. DEFECT-ASSOCIATED PROPERTIES OF CGSS

2.1 Localized states in the band gap

The appearance of any defect in a structure is accompanied by the appearance of a level in the band gap. The displacement of E_v and E_c as a function of the relative elongation accompanying stretching of the rings and chains (deformational defects) is shown in Fig. 4; fluctuations of E_v
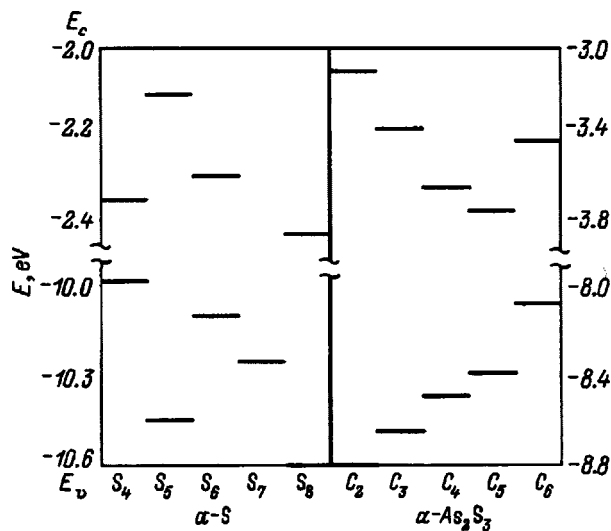
FIG. 5. Energy levels in the top occupied and bottom vacant molecular orbitals, which model the positions of the valence-band edge E_n and conduction-band edge E_c in different structural elements in a-S (S_N rings with $N = 4 - 8$) and in a-As$_2$S$_3$ (C_N rings with $N = 2 - 6$, bound together by covalent bonds). To estimate E_g correctly, the energy difference between the vacant and occupied levels must be decreased by an amount equal to the integral of the Coulomb repulsion between them ($\sim$6 eV).
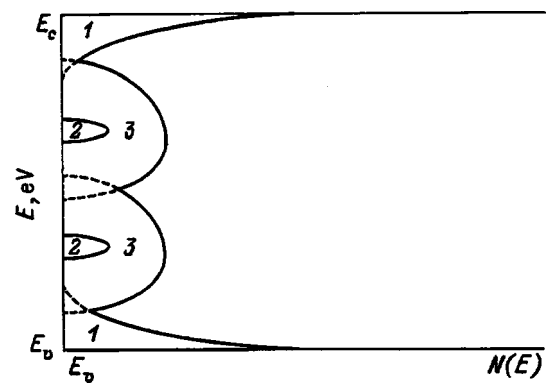

FIG. 6. Diagram illustrating the position of localized electronic levels in the band gap which are associated with different structural defects in a-S and in a-As$_2$S$_3$. The tails of the density of states (region *1*) are formed by deformational and topological defects, as well as by homopolar bonds in the case of a-As$_2$S$_3$. The scale of the decrease in the density of states in this region is formed mainly by the topological defects. The deep-lying levels in the band gap (region *2*) are associated with VAP-*d* defects, while in region *3* they are associated with HVCs. The curves bounding the regions *1*–*3* are arbitrary.

and E_c due to the existence of C_N rings in a-As and a-S are shown in Fig. 5.

The appearance of irregular bonds is also accompanied by splitting off of levels from the valence- and conduction-band edges into the band gap. Here $\Delta E_v = 0.13$ eV and $\Delta E_c = -0.34$ eV. The values of E_v and E_c for VAP-*d* and HVCs are given in Table II. A general diagram demonstrating the position of levels in the band gap, which are associated with the defects listed above, is shown in Fig. 6.

2.2 Interaction of a defect-free network and defects in it with $\hbar\omega \lesssim E_g$ light

2.2.1. Defect-free fragments and topological defects. The optical characteristics (the energy E_{ss}^1 of the first singlet-singlet transition and the corresponding change $\Delta\mu$ in the dipole moment) of fragments of a defect-free glass network were estimated for the sulfur clusters considered above. We

TABLE II. Displacements of levels relative to the valence band ΔE_v and conduction band ΔE_c, energy E_{ss}^1 of the first singlet–singlet transition, change $\Delta\mu$ in the dipole moment for this transition in hypervalent configurations arising in noncrystalline sulfur (in units of D).

Configuration	ΔE_v, eV	ΔE_c, eV	E_{ss}^1, eV	$\Delta\mu$, D
C_6	-	-	2.5	0.0
C_7	-	-	2.8	6.0
C_8	-	-	2.4	0.0
I, HS$_7$H	-	-	3.7	1.7
V	0.9	-1.0	1.2	3.9
VI	1.3	-0.5	1.7	3.3
VII	0.6	-1.2	2.3	0.9
IX	1.1	-1.1	2.2	2.0
X	1.1	-1.2	2.0	6.3
XI	1.3	-1.5	2.0	13.9

note that it is in principle incorrect to use for this purpose the difference between the energy levels of the highest occupied and lowest vacant molecular orbital (MO) and that doing so introduces an error equal in order of magnitude to the integral of the Coulomb repulsion between these MOs, which for sulfur clusters equals approximately 4–5 eV.

Despite the similarity of the stability parameter, the electronic structure, and the geometric parameters of long chains and ring structures S_N in a-S,[17] the values of E_{ss}^1 for them are substantially different (Table II). The difference increases with increasing chain length. The reasons for such behavior is unclear at present, and additional calculations using nonempirical approaches with more complete bases are required. The character of the transition in rings and chains is the same — from a nonbonding MO into a weakly antibonding orbital. They are both formed mainly by lone pairs of sulfur. In the excited state the electron density alternates in the range of 0.1 eV and the bond orders (BOs) decrease by 10–15% around atoms with a negative charge. The changes affect the entire cluster; i.e., the first excited state of the fragments of the main network of the glass is delocalized.

2.2.2. Deformational defects. The effect of excitation on deformed bonds in a-As$_2$S$_3$ was investigated. The transition into an excited state is accompanied by an approximately 30% decrease in the order Q_{As-S} of the bond between the atoms. Therefore it can be concluded that if the bond in the ground state is sufficiently strongly stretched (by 20–30%), then excitation followed by relaxation leads to rupture of the bond.

2.2.3. Interaction of light with homopolar bonds. It is believed[34] that As–As bonds play an important role in photostructural transformations. For this reason, we examined the excitation of the electronic subsystem in a-As$_2$S$_3$ that contain these bonds. In this case the changes in the electronic structure are localized in a region close to the As and S atoms that participate in the formation of As–As and S–S bonds. The As–As bond weakens by 15%, while Q_{S-S}

remains nearly the same. We note that an unstressed As–As bond does not rupture as a result of excitation.

2.2.4. Interaction of light with VAP-d and HVCs. In the defects shown in Fig. 3, levels are split off from the valence band and the conduction band into the band gap. The shifts in E_v and E_c are equal to approximately 1 ± 0.5 eV. As a result, the energy E_{ss}^1 decreases to 1.5–2.0 eV; i.e., such defects can be expected to absorb optical-range radiation. For type-VII and -IX defects the changes in the dipole moment as a result of excitation are small — of the same order of magnitude as for an ordinary chain; for type-V, -VI, and -X defects the changes are appreciably larger, while for a type-XI defect the changes are very large; i.e., light absorption on it should be substantial. The restructuring of the electronic density affects mainly the region of a defect and the first coordination sphere around it; i.e., the excited states of defects are localized. As a rule, in the process the electron density distribution changes in such a way that the electronic structure of a defect approaches a configuration with a dangling bond. For example, in the case of the VAP-d structure the charges at centers C_1 and C_3 equalize, the BOs between C_3 and C_2 decrease by 30%, and a similar decrease occurs for type-VII defects, but in this case the BO between C_3 centers increases; i.e., in the first case decay into $2C_1^0$ is facilitated, while in the second case decay into $2C_1^0$ and C_2^0 is facilitated. The changes for the type-XI configuration are more complicated: The electronic density transfers to an isolated C_3 center and the nearest fragment of the chain coupled with it, the BOs around this center decrease by 10–15%, and they remain nearly the same in the rest of the cluster, i.e., in this case excitation does not give rise to decay of a defect.

2.3 Photoinduced effects in CGSs

For the present, type-XI HVC defects (Fig. 3) are the best candidates for explaining the value $Z_1>2$ in a-S and possibly in a-Se. However, our calculations have shown that they can exist only in the presence of an external force that prevents them from decaying. In a solid noncrystalline state, the rigid environment could become such a force. It is quite possible that type-XI HVCs, together with VAP-d, participate in all photoinduced phenomena. This assumption is based on a simple model which is based on the fact that in type-XI HVCs as a result of photoexcitation with energy $\hbar\omega\lesssim E_g$ optical transitions that lead to a large increase in the dipole moment — up to $14D$ (Table II) — can occur. The large dipole which arises can strongly polarize the environment — type-I chains, in which bonds become weaker, longer, and softer under the action of the light; in the process a small dipole moment ($\sim1.7D$, Table II) appears in a chain as a result of photoexcitation. Therefore, an additional dipole-dipole interaction can arise. An estimate of its magnitude (provided that the HVC dipole is located at a distance of the order of 5 Å from the excited chain) gives ~0.2 eV. This is sufficient for activation of inversions or rotations, which can result in a restructuring of the environment, especially on the "near-MRO" scale, in which the C_2^0 atoms will occupy new metastable positions. These will be the photostructural transformations (PSTs). In this connection, we mention the

model of a PST associated with near-MRO.[36] Our simple model explains the photoinduced anisotropy, since a HVC dipole can be oriented by the vector **E** of linearly polarized light, while the environment surrounding the dipole will be oriented following it — at least on the near-MRO scales. The appearance of gyrotropy as a result of irradiation is better associated with HVCs than VAP, since a HVC has the symmetry of the point group C_1 and is therefore polar and chiral, while a VAP possesses C_{2v} symmetry and is therefore polar but not chiral.

It is obvious that an optical transition accompanying the excitation of HVCs can lead not only to photodarkening but also to decomposition of the complex into VAP $+ nC_2^0$ followed by the decay VAP$\rightarrow 2C_1^0$, i.e., to paramagnetism, which is more characteristic of a-S and l-S than for a-Se and CGSs. This result agrees with the weak thermal paramagnetism of plastic a-S and strong paramagnetism for l-S at $T>160\,°$C. Photoluminescence can also be related to the excitation of HVC dipoles and their decay into C_1^0 followed by relaxation to the initial state with thermal insulation and deexcitation. It is very likely that VAP-d and HVC dipoles can be oriented in very strong electric fields and can in turn orient their environment. The participation of dipoles is presupposed in the electron-thermal model of the low-resistance state.[8] The drift mobility in a-S and a-Se is effected by neutral localized states near E_c and E_v,[9] which are apparently related to the deformational, topological, and HVC defects. Finally, the medium-range order itself, especially near-MRO (and sometimes intermediate MRO also), could be due to noncrystalline ordering, which is induced by HVC and VAP dipoles in the melt and by freezing of the melt as a result of vitrification.

In closing, we indicate the metastable equilibria

$$nC_2^0 = 2C_1^0 = \text{VAP} + nC_2^0 = \text{HVC},$$

which depend on the external conditions — $T, P, \hbar\omega, E$ etc. — and which determine the properties of the CGSs under study. It is also important to point out the multiplicity of the states responsible for the HVC states, and their special position, since the density of HVC defects is much higher than that of VAP in the CGSs mentioned above, which determines the value $Z_1>2$. States of the HVC type are not a substitute or alternative but rather a very important complement to VAP.

a)Fax: (095) 9522382

[1] A. I. Gubanov, *Quantum-Electronic Theory of Amorphous Semiconductors* [in Russian], Soviet Academy of Sciences Press, Moscow, 1966.
[2] S. R. Ovshinsky, Phys. Rev. Lett. **36**, 1469 (1976).
[3] P. V. Anderson, Phys. Rev. Lett. **34**, 953 (1975).
[4] R. A. Street and N. F. Mott, Phys. Rev. Lett. **35**, 1293 (1975).
[5] M. Kastner, D. Adler, and H. Fritzsche, Phys. Rev. Lett. **37**, 1504 (1976).
[6] M. I. Klinger, Phys. Rep. **165**, 275 (1988).
[7] K. D. Tséndin and K. D. Tséndin [Ed.], in *Electronic Phenomena in Chalcogenide Glassy Semiconductors* [in Russian], Nauka, St. Petersburg, 1996, p. 68.

[8] É. A. Lebedev and K. D. Tséndin, *ibid.*, p. 263.
[9] É. A. Lebedev and L. P. Kazakova, *ibid.*, p. 141.
[10] N. A. Popov, Fiz. Tekh. Poluprovodn. **16**, 344 (1982) [Sov. Phys. Semicond. **16**, 216 (1982)].
[11] S. A. Dembovsky, Mater. Res. Bull. **16**, 1331 (1981).
[12] S. A. Dembovsky and E. A. Chechetkina, Philos. Mag. B **53**, 367 (1986).
[13] S. A. Dembovskiĭ and E. A. Chechetkina, *Glass Formation* [in Russian], Nauka, Moscow, 1990.
[14] S. A. Dembovsky, Solid State Commun. **87**, 179 (1993).
[15] S. A. Dembovsky, Phys. Lett. A **189**, 233 (1994).
[16] S. A. Dembovsky, in *Physics and Applications of Non-Crystalline Semiconductors in Optoelectronics*, edited by A. Andriesh and M. Bertolotti, Kluwer Academic Publishers, 1997, p. 275.
[17] A. S. Zyubin and S. A. Dembovsky, Solid State Commun. **89**, 335 (1994).
[18] A. S. Zyubin, S. A. Kozyukhin, and S. A. Dembovskiĭ, Zh. Neorg. Khim. **43**, 650 (1998).
[19] Yu. G. Poltavtsev, *Structure of Semiconductor Melts* [in Russian], Metallurgiya, Moscow, 1984.
[20] V. P. Zakharov and V. S. Gerasimenko, *Structural Features of Semiconductors in the Amorphous State* [in Russian], Naukova Dumka, Kiev, 1976.
[21] E. A. Chechetkina, J. Phys.: Condens. Matter **7**, 3099 (1995).
[22] S. A. Dembovsky, J. Non-Cryst. Solids **82**, 761 (1992).
[23] S. A. Dembovskiĭ, Fiz. Khim. Stekla **20**, 785 (1994).
[24] D. Holh and R. O. Jones, Phys. Rev. B **43**, 3856 (1991).
[25] A. S. Zyubin and S. A. Dembovski, in *Glass Formation and Structure, Proceedings of 17th International Congress on Glass, Vol. 2,* Beijing, 1995, p. 408.
[26] A. S. Zyubin, O. A. Kondakova, and S. A. Dembovskiĭ, Fiz. Khim. Stekla **23**, 86 (1997).
[27] A. S. Zyubin, S. A. Dembovsky, and O. A. Condakova, J. Non-Cryst. Solids **224** (3), 291 (1998).
[28] E. M. Dianov, V. O. Sokolov, and V. B. Sulimov, J. Non-Cryst. Solids **211**, 197 (1997).
[29] A. S. Zyubin and S. A. Dembovsky, Solid State Commun. **87**, 175 (1993).
[30] S. R. Elliot, Nature (London) **354**, 445 (1991).
[31] J. D. Joannopoulous and D. Vanderbilt, Phys. Rev. B **22**, 2927 (1980).
[32] J. D. Joannopoulos and D. Vanderbilt, Phys. Rev. B **27**, 6311 (1983).
[33] R. A. Street and A. D. Ioffe, J. Non-Cryst. Solids **8**, 745 (1972).
[34] M. Frumar, A. P. Firth, and A. E. Owen, Philos. Mag. B **50**, 463 (1984).
[35] A. Feltz, *Amorphe und Glasartige Anorganishe Festkörper* [Mir, Moscow, 1986].
[36] M. A. Paersler and G. Pfeifer, J. Non-Cryst. Solids **137–138**, 967 (1991).

Translated by M. E. Alferieff

Toward understanding the photoinduced changes in chalcogenide glasses

H. Fritzsche

Energy Conversion Devices, Inc., 1675 West Maple Road, Troy, MI 48084

The various irreversible and reversible photoinduced phenomena in chalcogenide glasses, among them isotropic and anisotropic effects, were considered until now to have different origins. Upon reexamination, we find that the elemental photostructural steps are the same for all these phenomena. These are nonradiative recombinations via transient excitons yielding changes in local bonding configurations. The anisotropic changes arise from geminate recombinations of electron-hole pairs, which fail to diffuse out of the microvolume in which they were excited. A unified explanation of the large variety of photoinduced changes is presented. © *1998 American Institute of Physics.* [S1063-7826(98)01008-4]

1. INTRODUCTION

Academician B.T. Kolomiets and his distinguished school of scientists laid the groundwork for the study of the large and fascinating family of materials known as chalcogenide glasses. Perhaps the most interesting phenomena exhibited by these glasses are the light-induced changes of their properties. Nearly 30 years ago, reversible and irreversible photostructural changes in a variety of physico-chemical properties were discovered[1] and soon thereafter, by Kolomiets and his collaborators,[2] the photoinduced optical anisotropies. These discoveries were followed by the observation of irreversible giant photocontraction[3] of freshly deposited films of these materials, of photoinduced crystallization[4] and amorphization,[5] of photodoping by metals,[6] and more recently by the astonishing findings of photoinduced fluidity[7] and an anisotropic optomechanical effect.[8] These phenomena result from illumination with bandgap light or subgap light of the Urbach absorption region at both ambient and low temperatures.[9]

Indeed, this is a surprising variety of photoinduced phenomena and the time for discovery of new ones might not yet be over. It would be most unsatisfactory if one had to search for a different origin and microscopic mechanism for each one of these effects. This has been the tendency recently. For example, it was stated[10,11] that there is a fundamental difference between centers in the chalcogenide glasses that yield photoinduced anisotropies, on the one hand, and photodarkening, on the other, which is one of the reversible photostructural changes. Moreover, most of the literature makes a clear distinction of the origins of reversible and irreversible photostructural changes.[12] Any model which is based on specific centers[6,11,13–16] such as valence alternation defects[17] obviously cannot explain large morphological changes such as photoinduced fluidity,[7] photopolymerization,[18,19] the giant photoexpansion[20] and contraction[3] or the new reversible anisotropic optomechanical effect,[8] because the number of these defects never exceeds a small fraction of one percent of the constituent atoms.[15,21]

In this article we explore the possibility that there is a type of microscopic mechanism that leads to different photoinduced effects.

Since the first step shared by all these phenomena is the photoexcitation of an electron-hole pair and its recombination, we discuss this event in the following section. We then examine various photoinduced effects and see how they might originate from the recombination events.

2. RECOMBINATION

Chalcogenide glasses have a low photoluminescence efficiency. This suggests, as Street pointed out,[22] that these materials provide a nonradiative recombination channel which allows the dissipation of a rather large recombination energy. This recombination occurs via a transient exciton which can be visualized as a transient intimate valence alternation defect pair.[17,23] The local deformation associated with its formation and subsequent annihilation is the anharmonic energy dissipation process.

Of primary interest for our discussion of photoinduced changes is the fact that the local bonding configuration after recombination and before photoexcitation need not be the same.[9,24] An elementary step of photostructural change can occur. Examples of such elementary steps are illustrated in the Figure 1, where (a) shows the local structure before photoexcitation, (b) shows the transient exciton or transient intimate valence alternation pair (IVAP) state, and (c) shows the structure after recombination. We note that atoms can move over atomic distances during such an elementary step.

The change in covalent coordination associated with a change in the local charge or valence state, which is the basis for the valence-alternation model, subsumes that the charges are quite localized. Indeed, such localization seems to be a general feature of amorphous and vitreous semiconductors. Even photocarriers excited into extended band states localize quickly into band tail states before recombining. Chalcogenide glasses, moreover, favor structural changes because of the steric freedom of their low coordination atoms.[25]

Which optical excitation can result in an elementary photostructural step? Certainly bandgap and Urbach tail ex-
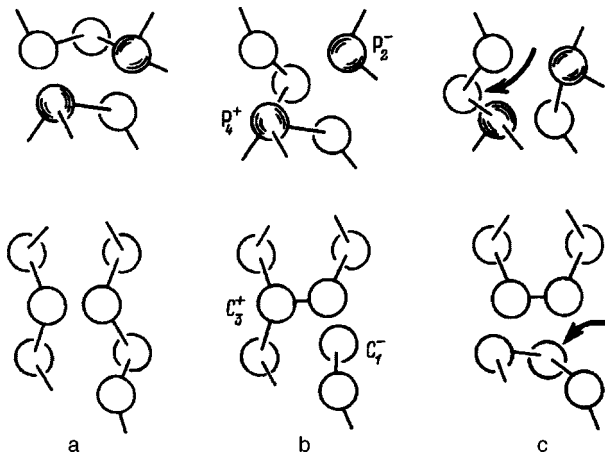
FIG. 1. Examples of elementary steps of photostructural changes. White balls are chalcogens (C) and shaded balls are pnictide atoms (P). a — Initial bonding configuration; b — transient self-trapped exciton after photon excitation; c — one of several new bonding configurations after recombination, where the motion of the atom is indicated by the arrow.

citations, but also excitations between band states and charged valence alternation defect states, as well as an electronic excitation, i. e., an electron transfer, within an IVAP. In the latter case, the transient exciton consists of two neutral valence alternation defects which can relax to an IVAP of different configuration than the original one.[11,15]

3. PHOTOINDUCED FLUIDITY

The illuminated chalcogenide glass flows under uniaxial stress[7] since local band changes and atomic motions, which tend to decrease the local strain energy, are favored.[26] The macroscopic nature of photoinduced fluidity proves that essentially all atoms are involved in these recombination-induced local bonding changes and not only specific and relatively rare defects or structures. In view of the recently discovered anisotropic optomechanical effect,[8] one would predict that the photoinduced fluidity is larger for light polarized along the uniaxial stress than for perpendicular polarization.

It is useful to visualize the illuminated state of the glass as a dynamic state with constantly occurring changes in local bonding and atomic motions.[24] They foster phase separation[27] and phase changes.[4,5] This internal activity stops when the light is turned off, and the frozen-in structure may relax over time, depending on the temperature.

4. GIANT DENSIFICATION AND PHOTOPOLYMERIZATION

Films which are strongly voided or have columnar structure are obtained with oblique vapor depositions onto cool substrates.[3] Such films can have up to 20% lower density. This density deficit can largely be removed by prolonged illumination.[3] Moreover, vapor deposition of binary and ternary chalcogenide films contain bond-saturated molecular units that exist in the depositing vapor, such as As_4 and As_4S_3. The degree of molecularity greatly diminishes with exposure to light and the films polymerize and resemble more the structure of a bulk glass.[18,19]

Both these major topological and structural changes induced by light require motion of atoms and bonding rearrangements. They can result from the cumulative effect of a large number of elementary steps of photostructural changes caused by recombination events.[24] In other words, the dynamic illuminated state will bring about structural changes until a quasi-equilibrium is reached. This so-called light-saturated state is still a dynamic state during illumination, because local changes still occur without changing the macroscopic properties. Since thermal annealing will also densify and polymerize freshly deposited films, it is easy to understand that this occurs during illumination in the dynamic state.[24] These photostructural changes are, of course, irreversible.

5. REVERSIBLE ISOTROPIC CHANGES

One of many examples, but a typical one, is the reversible shift of the optical absorption edge.[1,9,12,29–32] Illumination produces a redshift of the edge, which increases the absorpsion. This photodarkening can be reversed by thermal annealing near the glass transition temperature. Annealing actually starts after turning off the light and progresses with a wide spectrum of anneal energies.

During illumination, we have the dynamic state with all the recombination-induced local bonding changes and atomic motion. The macroscopic physico-chemical properties will change until a balance is reached between thermal annealing, light-induced annealing, and light-induced creation of higher-energy local bonding arrangements. This balance is called the light-saturated state which depends on light intensity and ambient temperature.[24] It is a state of higher energy relative to the annealed state, because otherwise it would not return to the annealed state. Its structure differs from that of the annealed state. Diffraction experiments[1,28,29] and computer modeling have taught us that the light-saturated state has less medium-range order,[32] i. e., it is more disordered than the annealed state. Photodarkening is believed to arise from enhanced ⟨lone pair⟩–⟨lone pair⟩ interactions which broaden the valence band and thus cause a redshift of the absorption edge.[1,9,28,33]

We see that the microscopic processes driving the reversible and irreversible photostructural changes are the same.[24] The difference arises from the initial states. Only the annealed state can be recovered by annealing, but not the voided and molecular structures of freshly deposited films. Both the reversible and the irreversible changes move toward the light-saturated state. They might not reach it when hindered by topological obstacles which cannot be overcome by the elementary photostructural steps.

The light-saturated state differs in a number of ways from the annealed state. Besides the decrease in medium-range order, there is a larger concentration of IVAP defects and of wrong bonds. However, they play at most a minor role in the numerous physico-chemical changes associated with the reversible photostructural changes. This is supported by observations of Tanaka *et al.*[34] that the efficiency of photodarkening is essentially the same for bandgap and

subgap Urbach tail light, but is essentially zero for light absorbed in the defect band.

6. PHOTOINDUCED ANISOTROPIES

Optically isotropic materials such as chalcogenide glasses can become optically anisotropic because they consist of and contain entities which are optically anisotropic.[35,36] The original macroscopic isotropy originates from the random orientations of the microscopic anisotropic entities. Because of their transverse nature, electromagnetic waves are anisotropic. Therefore, light-induced structural changes will inevitably produce macroscopic anisotropies not only of the optical or dielectric tensor,[35-37] but also of other physico-chemical properties. For practical purposes, experiments are carried out with linearly or circularly polarized light. The resultant anisotropies are reversible if the photostructural changes are reversible.

A recombination event, which leads to a structural change of a microscopic anisotropic entity will change the orientation or nature of this anisotropy. This constantly happens everywhere in the material during illumination, without necessarily producing a macroscopic anisotropy. For this event to occur, it is necessary that the recombining electron-hole pair be excited in the same microscopic anisotropic entity which undergoes the structural change. This means essentially that macroscopic anisotropies result from geminate recombinations of electron-hole pairs, which do not diffuse out of the microscopic entity in which they were created by absorbed photons.[35,36] The lack of electron-hole pair diffusion and the geminate nature distinguishes the recombination events which lead to anisotropies from all the other events which yield isotropic (or scalar) photoinduced changes. This important difference accounts for the fact that the dependences on temperature, light intensity, and photon energy among other parameters are different for the anisotropic (vectoral) and isotropic (scalar) photoinduced effects.

What are these microscopic, optically anisotropic entities in chalcogenide glasses? Intimate valence alternation pair defects (IVAPs) have a dipole moment and form one kind of entities of this sort. After a photostructural bonding change, its dipole moment will change. However, IVAPs are not the only anisotropic entities. Optical excitations from the valence band to the conduction band are transitions from lone-pair electron states to antibonding states.[33] These transitions are polarization dependent because of the low covalent coordination of chalcogens. Hence, any tiny microvolume of the material is optically anisotropic and is altered with a photostructural change. Hence, all optical transitions, i. e., interband, Urbach tail, and defect transitions, are polarization dependent. Each elemental step of photosructural charge alters the local anisotropy. However, a macroscopic anisotropy can result only from nonradiative recombinations of electron-hole pairs that have not diffused away. Which of the various optical excitations satisfies this requirement can be determined by measuring the quantum efficiency for a given anisotropic effect as a function of photon energy.

These arguments can clearly be extended to anisotropies involving circularly polarized light, because the small coordination number of chalcogenide glasses provides a local structure with sizable helicity.[35,36]

7. ANISOTROPIC OPTOMECHANICAL EFFECT

Krecmer et al.[8] discovered a reversible anisotropic volume change induced by polarized light in a thin film of $As_{50}Se_{50}$. Contraction occurs along the direction of the electric field vector and dilatation occurs perpendicular to that direction. Light from a He–Ne-laser, whose energy $h\nu \sim 2$ eV falls into the Urbach absorption region, was used. This experiment shows that these anisotropies extend to other material properties besides the optical tensor. The magnitude of the effect suggests that the anisotropic microvolumes of the whole material are involved and not only IVAP defects. This is also the interpretation of Krecmer et al.[8]. These new results imply that the elastic properties, sound propagation, and probably many other material parameters of chalcogenide glasses become anisotropic, as a result of exposure to light.

8. PHOTOINDUCED DICHROISM AND BIREFRINGENCE

These phemomena were discovered by B.T. Kolomiets and his group[2] in 1979. The sign of the anisotropies of the absorption coefficient and refractive index agrees with the prediction of the model which attributes the change to a photostructural change in the anisotropic entities or microvolumes, which results in a decrease of the oscillator strength of the chosen light polarization and an increase for the other polarization directions.[35,36]

There is no agreement on whether the anisotropic entities are microvolumes of the inherently anisotropic local bonding structures of the chalcogenide material[9,35,36] or whether they are IVAP defects.[11,13-15,38,39] Both of course contribute with their relative contributions, depending on the exciting photon energy, as explained in Sec. 6. If the light in the defect absorption band is below the Urbach absorption region, only IVAPs can be excited. Larger photon energies can produce changes in the whole material. In the optomechanical experiment discussed in the previous section, the authors detected photoinduced dichroism which originates in the anisotropic local bonding structures that are present throughout the material.

In earlier experiments on dichroism, Lyubin et al.[10] emphasized that the effect observed was the same at the beginning and at the end of photostructural changes that lead to photodarkening. This suggests that IVAP centers, whose concentration increases with light exposure,[21] contribute negligibly in those experiments. More recently, it was found that the kinetics of the photoinduced anisotropies change with light exposure.[15,36] The observed change in kinetics is no proof that IVAPs are involved. In contrast, one would expect a much larger change in the magnitude of the anisotropies than those observed when the IVAP concentration increases by several orders of magnitude. As discussed in Sec. 5, essentially all local bonding structures change as the material goes from the annealed to the light-saturated state. This is accompanied by a change in the density, elastic constants, hardness, and other properties. Therefore, a

change in kinetics of the photoinduced anisotropies is not surprising. Moreover, more light is absorbed as the material photodarkens with time, which affects the kinetics.

The anisotropic matrix elements governing optical excitations within a microvolume or an IVAP defect region depends on the photon energy. Therefore, if the photon energy of the probe light differs greatly from that of the exciting light, it is possible that the photoinduced anisotropy will disappear at a certain energy of the probe light or that it will reverse its sign. While dichroism depends on the anisotropic absorption coefficient at the photon energy of the probe, the refractive index which governs birefringence is a Kramers–Kronig weighted average of excitations over all energies larger than the probe energy. The reflectivity near the bandgap energy is governed solely by the refractive energy. The reflectivity near the bandgap energy is governed solely by the refractive index, while the extinction coefficient should be considered only at relatively high photon energies. A more complete picture of the physical processes would require measuring the induced anisotropy of the complex dielectric tensor as a function of photon energy.

Even in the light-saturated state, the optical axis of the induced anisotropy can be reoriented at will by changing the polarization direction of the exciting light. This illustrates the dynamic nature of the light-saturated state discussed in Sec. 5. This state is a dynamic equilibrium between constantly occurring local bonding changes during illumination and local thermal relaxation processes.[36]

9. PHOTOINDUCED ANISOTROPIES IN LIGHT SCATTERING

Many experiments studying photoinduced anisotropies are conducted by sending a laser beam of inducing polarized light through the sample and measuring with a polarized probe beam of greatly reduced intensity the transmitted light intensity and its polarization. Inhomogeneities and density fluctuations will cause scattering, which, in addition to absorption, decrease the transmitted light intensity.[40] Scattering can be measured separately in directions away from the beam axis.[41]

Inhomogeneities are self-enhancing as localities, which photodarken, absorb more photons from the inducing beam, and darken further. The increase in refractive index associated with photodarkening produces light-scattering inhomogeneities. With polarized inducing light, all these phenomena carry isotropic and anisotropic components. The scattered light, in turn, produces photoinduced changes and inhomogeneities while passing through the material. Concurrently, the inducing light beam experiences self-focusing due to the increased refractive index caused by photodarkening in the laser beam channel. It is clear, therefore, that the rates of recombination events change with time and location even when the intensity of the inducing light remains constant.

These complex and interrelated processes may explain why one observes such a variety of interesting and often puzzling phenomena in these experiments.

10. DISCUSSION

While trying to find a unifying explanation of the photoinduced changes in chalcogenide glasses, we should address particular observations which stand in the way of such a unifying picture. The overemphasis on defects, in particular, IVAPs, as the origin of reversible photoinduced isotropic and anisotropic effects isolated major structural changes such as photoinduced fluidity, the optomechanical anisotropy, and the irreversible photostructural changes into a separate category. Defects which number much less than one percent of the atomic sites obviously cannot account for the major changes. We now understand that any atomic site of low coordination can participate in photoinduced changes, which makes the distinction between major and minor effects unnecessary.

In terms of defects, it was pointed out that the centers responsible for the optical anisotropies must be essentially different in origin from those responsible for isotropic effects, in particular, for photodarkening.[11] The reasons for this conclusion are (i) the different kinetics, (ii) different spectral excitation dependence, (iii) different annealing temperature, and (iv) the observation that photoinduced anisotropies are seen even in glass compositions that show no or hardly any photodarkening.

As was discussed earlier, the main difference between scalar and vectoral effects is that the latter result only from geminate recombinations of electron-hole pairs, which fail to diffuse out of the absorption microvolume. It is conceivable that certain defects favor this subset of recombination events. This, however, is not generally the case since the vectoral optical effect is coupled with the optomechanical effect of Sec. 7, which essentially involves the majority of atomic sites and not specific defects. The different spectral excitation dependence is explained by the special conditions imposed on the subset of recombinations which can remember the polarization of the absorbed photon, as discussed in Sec. 6.

The kinetics of the two groups of effects is naturally different. When photodarkening has saturated (zero kinetics) in the light-saturated state, the optical axis of the photoinduced anisotropy can still be reoriented, because photostructural changes continually occur in the dynamic balance of the light-saturated state. The local bonding orientations and thus the oscillator strengths are changed preferentially in accordance with the inducing light polarization. This process in turn saturates when it becomes energetically unfavorable to continue.

The elemental photostructural step is the same for both the isotropic and anisotropic effects. The manifestations are different, however. Photodarkening results from the cumulative effect of many photostructural steps, which decrease the medium-range order and increase the lone-pair interactions and therefore the width of the valence band. It seems that such major photostructural change requires a higher anneal temperature than the local bonding configuration changes required for optical anisotropies.

Some chalcogenide glass compositions might not exhibit photodarkening, because they might not develop a pro-

nounced medium-range order in their relaxed annealed state and, hence, might not experience an appreciable increase in the lone-pair interactions in the light-saturated state. These same glasses will nevertheless show photoinduced optical anisotropies due to changes in the local bonding structure.

11. SUMMARY AND CONCLUSIONS

Great strides have been made in the understanding of the photoinduced changes in chalcogenide glasses. Most, if not all, of them are caused by elemental steps of photostructural change resulting from nonradiative recombination events via transient excitons. These elemental steps occur essentially everywhere in the material where there is freedom from steric hindrance.

Different manifestations of photoinduced changes occur when the initial structural states or conditions of the material are different. Reversible changes occur from the annealed state, while irreversibility necessarily results when the initial structural state of the material is of higher energy than the annealed state, as is the case for voided and molecular films which are vapor deposited. Both the reversible and irreversible changes move toward the structure of a light-saturated state, which has less medium-range order and is of higher energy than the annealed state.

During illumination, the material is in a dynamic state, which leads at high intensities to photoinduced fluidity, diffusion, and phase changes.

Among the many recombination events, there are some that remember the polarization of the absorbed light. These are geminate recombinations that occur in the microvolume of the absorption process. This subset of nonradiative recombination processes yields photoinduced anisotropies of physico-chemical properties. They occur even for unpolarized light because of the transverse nature of electromagnetic waves, but are more easily observed with polarized light. Since the probability for the recombinations falling into this special subset depends on the light intensity, temperature, photon energy, and material properties, one finds that the behavioral differences between isotropic and anisotropic photoinduced changes depend on these parameters.

Among the photoinduced anisotropies are those of the optical properties such as dichroism, birefringence, light scattering, and others. They are sometimes difficult to determine quantitatively, because the changing optical properties change locally the intensity and direction of the inducing light. This complex set of problems, in which the light-producing changes at one location depend on changes in the optical properties which occurred previously at other locations, is peculiar to studies of the change in the optical properties caused by light. At present, there is no reason to believe that the observed phenomena result from anything different than the changes in the transition matrix elements which result from the local bonding changes that occur in all the elemental steps of photostructural changes.

[1] S. R. Ovshinsky, in *Proceedings of the 5th Annual National Conference: Industrial Research* (Chicago, IL, Industrial Research, Inc., 1969), p. 86; S. R. Ovshinsky and H. Fritzsche, Metallurgical Trans. **2**, 641 (1971); J. P. deNeufville, S. C. Moss, and S. R. Ovshinsky, J. Non-Cryst. Solids **13**, 191 (1974).

[2] V. G. Zhadanov, B. T. Kolomiets, V. M. Lyubin, and V. K. Malinovskii, Phys. Status Solidi A **52**, 621 (1979).

[3] S. Rajagopalan, K. S. Harshavardhan, L. K. Malhotra, and K. L. Chopra, J. Non-Cryst. Solids **50**, 29 (1982).

[4] J. Feinleib, J. P. deNeufville, S. C. Moss, and S. R. Ovshinsky, Appl. Phys. Lett. **18**, 254 (1971); J. E. Griffiths, G. P. Espinosa, J. P. Remeika, and J. C. Phillips, Phys. Rev. B **25**, 1272 (1982).

[5] S. R. Elliott and A. V. Kolobov, J. Non-Cryst. Solids **128**, 216 (1991).

[6] A. V. Kolobov and S. R. Elliott, Adv. Phys. **40**, 625 (1991), and the bibliography cited there.

[7] H. Hisakuri and Ke. Tanaka, Science **270**, 974 (1995).

[8] P. Krecmer, A. M. Moulin, R. J. Stephenson, T. Rayment, M. E. Welland, and S. R. Elliott, Science **277**, 1799 (1997).

[9] Ke. Tanaka, J. Non-Cryst. Solids **50 & 60**, 925 (1983); Jpn. J. Appl. Phys. **25**, 779 (1986); Rev. Solid State Sci. **2−3**, 641 (1990).

[10] V. Lyubin and V. K. Tikhomirov, J. Non-Cryst. Solids **114**, 133 (1989).

[11] S. R. Elliott and V. K. Tikhomirov, J. Non-Cryst. Solids **198−200**, 669 (1996).

[12] G. Pfeiffer, M. A. Paesler, and S. C. Agarwal, J. Non-Cryst. Solids **130**, 111 (1991).

[13] V. K. Tikhomirov and S. R. Elliott, Phys. Rev. B **51**, 5538 (1995).

[14] V. K. Tikhomirov, G. J. Adriaenssens, and S. R. Elliott, Phys. Rev. B **55**, R660 (1997).

[15] V. Lyubin and M. Klebanov, Phys. Rev. B **53**, R11924 (1996).

[16] K. Shimakawa, A. V. Kolobov, and S. R. Elliott, Adv. Phys. **44**, 475 (1995).

[17] M. Kastner, D. Adler, and H. Fritzsche, Phys. Rev. Lett. **37**, 1504 (1976).

[18] S. A. Solin and G. N. Papatheodorou, Phys. Rev. B **15**, 2084 (1977).

[19] D. J. Treacy, U. Strom, P. B. Klein, P. C. Taylor, and T. P. Martin, J. Non-Cryst. Solids **35−36**, 1035 (1980).

[20] H. Hisakuni and Ke. Tanaka, Appl. Phys. Lett. **65**, 2925 (1994).

[21] D. G. Biegelsen and R. A. Street, Phys. Rev. Lett. **44**, 803 (1980).

[22] R. A. Street, Solid State Commun. **24**, 363 (1977).

[23] M. Kastner and H. Fritzsche, Philos. Mag. **37**, 199 (1978).

[24] H. Fritzsche, Philos. Mag. B **68**, 561 (1993).

[25] S. R. Ovshinsky and K. Sapru, in *Amorphous and Liquid Semiconductors*, edited by J. Stuke and W. Brenig (Taylor & Francis, London, 1974), p. 447.

[26] H. Fritzsche, Solid State Commun. **99**, 153 (1996).

[27] J. S. Berkes, S. W. Ing, and W. J. Hillegas, J. Appl. Phys. **42**, 4908 (1971).

[28] J. P. deNeufville, in *Optical Properties of Solids. New Developments*, edited by B. O. Seraphin (North-Holland, Amsterdam, 1976), Chap. 9.

[29] K. Tanaka, *Structure and Excitations of Amorphous Solids*, edited by G. Lycovsky and G. L. Galeener [A.I.P. Conf. Proc. **31**, 148 (1976)].

[30] V. L. Averianov, A. V. Kolobov, B. T. Kolomiets, and V. M. Lyubin, Phys. Status Solidi A **57**, 81 (1980); J. Non-Cryst. Solids **45**, 343 (1981).

[31] A. E. Owen, A. P. Firth, and P. J. S. Ewen, Philos. Mag. B **52**, 347 (1985).

[32] S. R. Elliott, Phys. Rev. Lett. **67**, 711 (1991); M. Paesler and G. Pfeiffer, J. Non-Cryst. Solids **137−138**, 967 (1991).

[33] M. Kastner, Phys. Rev. Lett. **28**, 355 (1972).

[34] Ke. Tanaka and H. Hisakuni, J. Non-Cryst. Solids **198−200**, 714 (1996).

[35] H. Fritzsche, J. Non-Cryst. Solids **164−166**, 1169 (1993).

[36] H. Fritzsche, Phys. Rev. B **52**, 15854 (1995).

[37] V. K. Tikhomirov and S. R. Elliott, Phys. Rev. B **49**, 17476 (1994).

[38] V. Lyubin, M. Klebanov, V. Tikhomirov, and G. Adriaenssens, J. Non-Cryst. Solids **198−200**, 719 (1996).

[39] A. V. Kolobov, V. Lyubin, T. Yasuda, M. Klebanov, and K. Tanaka, Phys. Rev. B **55**, 8788 (1997).

[40] V. Lyubin, M. Klebanov, S. Rosenwaks, and V. Volterra, J. Non-Cryst. Solids **164−166**, 1165 (1993).

[41] V. K. Tikhomirov and S. R. Elliott, J. Phys.: Condens. Matter **7**, 1737 (1995).

Plasma-enhanced chemical vapor deposition and structural characterization of amorphous chalcogenide films

P. Nagels

RUCA-University of Antwerp, B-2020 Antwerpen, Belgium
(Submitted February 16, 1998; accepted for publication February 23, 1998)
Fiz. Tekh. Poluprovodn. **32**, 958–963 (August 1998)

We describe the preparation of layers of amorphous Se, As_xS_{1-x}, As_xSe_{1-x}, Ge_xS_{1-x}, and Ge_xSe_{1-x} by plasma-enhanced chemical vapor deposition using the hydrides of the elements as precursor gases. We discuss the influence of the gas ratios and the deposition conditions (pressure, rf power input) on the chemical composition and the homogeneity of the binary systems. Information concerning the structure of the films was obtained from infrared and Raman spectroscopy. © *1998 American Institute of Physics.* [S1063-7826(98)01108-9]

1. INTRODUCTION

Intensive research on amorphous chalcogenides started about 30 years ago, mainly under the impulse of B.T. Kolomiets in the Joffe Institute, Russia. A first milestone in the study of these materials was the discovery in 1968 by Ovshinsky of nondestructive switching in thin films of amorphous multicomponent chalcogenides. Reliable switching and memory devices were produced, but their penetration in the market was not succesful. A second milestone was the observation that illumination with bandgap light of thin chalcogenide films resulted in a blue shift (photobleaching) of red shift (photodarkening) of the absorption edge. This change in optical properties is accompanied by a change of some other properties, e.g., density, elastic constants, electronic properties, photo-dissolution of metals, etc. In the studies related to the above-mentioned fields the films were usually prepared by thermal evaporation or by sputtering; i.e., the solid state is realized by rapid condensation of the vapors. The as-deposited films have a more or less disordered network.

In our study we have prepared films of amorphous chalcogenides, including elemental Se and the binary As and Ge chalcogenides As_xS_{1-x}, As_xSe_{1-x}, Ge_xS_{1-x}, and Ge_xSe_{1-x}, by plasma-enhanced chemical vapor deposition (PECVD), a technique widely used for the preparation of amorphous silicon. In amorphous silicon the incorporation of hydrogen during the plasma-deposition process plays a very important role in saturating the dangling bonds responsible for high densities of electrically active gap states. The effect of hydrogen incorporation in amorphous chalcogenides on the basic physical properties is probably not that drastic. Indeed, the defect chemistry of chalcogenide glasses differs greatly from that of the tetrahedrally coordinated amorphous semiconductors. It is generally accepted that neutral dangling bonds are transformed into positively and negatively charged dangling bonds which pin the Fermi level close to the middle of the gap.

The purpose of our study is to make a comparison between the structure and the photoinduced effects of amorphous chalcogenide films prepared either by plasma decomposition or by vacuum evaporation. In this way we hope to gain futher insight into the origin of the structure-related phenomena. Furthermore, we believe that PECVD is a promising technique for growing layers of amorphous chalcogenides, in particular, with respect to their possible technological application.

2. MATERIAL PREPARATION BY PECVD

We have deposited thin films of amorphous Se, As_xS_{1-x}, As_xSe_{1-x}, Ge_xS_{1-x}, and Ge_xSe_{1-x} (1–2 μm thick) in a plasma discharge stainless-steel reactor. The precursor gases were high purity hydrides, H_2Se, H_2S, AsH_3, and GeH_4, pure or diluted in hydrogen (15 vol% of the hydrides). A low-pressure plasma, varying between 0.1 to 1 mbar, was created by an rf discharge (13.56 MHz) between two parallel-plate electrodes, 8 cm in diameter. The reactant gases were mixed before entering the reactor and were admitted through an inlet in the reactor wall at the height of the electrodes. The gases were pumped away through an outlet at the opposite side, so that the gas flow was parallel to the electrodes. The rf power coupled into the reactor varied from 10 to 80 W. Crystalline silicon and glass substrates were fixed on both electrodes. Depositions were made without additional heating of the substrates by a furnace, but due to plasma heating the temperature was approximately 50 °C.

For determination of the chemical composition of the layers, a silicon wafer was positioned from the middle to the gas inlet side of the grounded and the powered electrode. The atomic ratios of the elements were measured in the middle of the wafer at regular distances by means of electron microprobe analysis. Infrared transmission spectra were recorded in the wave–number range from 4000–150 cm^{-1} on films deposited onto polished crystalline Si wafers using a Beckman 4240 and a Bruker IFV 113 spectrometers. Raman measurements were made with the help of a Bruker 66-V spectrometer in a reflection mode using a 1.06-μm YAG:Nd^{+3} laser source.

3. COMPOSITION ANALYSIS AND STRUCTURAL PROPERTIES

A. Amorphous selenium (*a*-Se)

Films of *a*-Se were deposited using pure H_2Se. The deposition conditions were: flow rate 6 sccm; pressure 0.1 mbar; rf power 30 W; deposition time 10 min; film thickness ~ 1 μm. Films growth only occurred on the grounded electrode. X-ray diffraction showed that the film was completely amorphous.

From the knowledge that the short-range order in crystalline and amorphous materials is generally the same, it is reasonable to assume that the two existing crystalline allotropes of Se can be present in amorphous Se. The stable form of crystalline Se is trigonal. Its lattice consists of spiral-like chains parallel to the **c**-axis. The helices contain three atoms per turn and are in an hexagonal array (close packing for rods). The interchain bonding is covalent, while the intrachain bonding is due to weaker van der Waals attractions. Two similar metastable monoclinic forms of crystalline Se exist, α-monoclinic Se and β-monoclinic Se. The structural unit in both structures is a finite molecule in the form of a Se_8 ring. The difference between the α- and β-monoclinic allotropes is a different stacking pattern within the respective unit cells. Thus monoclinic Se is molecular, whereas trigonal Se is polymeric. In all three crystalline forms, selenium is twofold coordinated and the covalent bond lengh is essentially the same (2.32 Å). In the past, the structure of amorphous Se has been studied by several authors using different techniques. By ordinary analysis of the x-ray radial distrubution functions it is difficult to differentiate rings from chains and these results have been interpreted in very different manners. A clearer picture of the structure of amorphous Se emerges from Raman spectroscopy. These experiments gave evidence that the amorphous state can consist of the two allotropic forms which are mixed together: one is the Se_8 ring and the other form is the helical chain. The Raman spectrum of an as-deposited Se film is shown in Fig. 1a. It shows a strong peak at 250 cm^{-1} and two small bands at 80 and 112-cm^{-1}. Moreover, a small shoulder appears at 235 cm^{-1} on the 250 cm^{-1} band. We also recorded the Raman spectra of an amorphous Se film prepared by vacuum evaporation and of a bulk glass quenched from 250 °C. Both spectra were similar to that of the plasma CVD film. The Raman peaks of amorphous Se have been identified by Lucovsky *et al.*[1] They observed a much closer resemblance of the Raman spectrum of melt-quenched selenium to that of Se_8 in monoclinic Se than to that of trigonal Se. In that paper they assigned the dominant peak at 250 cm^{-1} and the smaller bands at 80 and 112 cm^{-1} to vibrations in the Se_8 ring. In trigonal Se the predominant Raman band lies at 235 cm^{-1}. In a later paper Lucovsky[2] formulated some objections against a structural model, which presumes a significant ring fraction in amorphous Se. He presented an alternative interpretation of the vibrational spectra that does not require discrete molecules. He proposed a structural model based on chains which include both helical chain-like and ring-like segments of the Se atoms (a "meandering" chain). Lucovsky assumed that a band at about 250 cm^{-1} can origi-
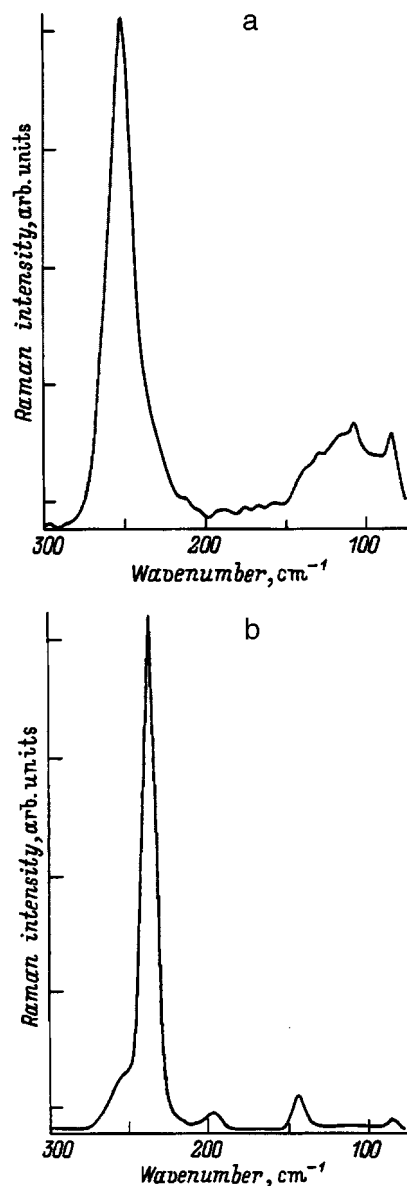

FIG. 1. Raman spectra o as-deposited amorphous Se film (a) and a film annealed at 150 °C for 1 h (b).

nate from bond stretching vibrations in Se_8 fragments, as well as in chain fragments. If we adopt these ideas, then the Raman spectrum of our plasma CVD film indicates that the structure contains predominantly Se_8 rings and Se_8 molecular ring fragments containing 5 and 6 Se atoms. The band at 250 cm^{-1} can be assigned to bond stretching vibrations and the band at 112 cm^{-1} to bond bending vibrations in the meandering chain. The shoulder that appears at 235 cm^{-1} can be associated with a small fraction of ''pure'' helical chains. There is another piece of experimental evidence that speaks against a structural model which assumes a dominant fraction of Se_8 rings in amorphous Se. In the evaporated Se film we observed an identical Raman spectrum. In the past the composition of selenium vapour has been studied by a variety of experimental techniques. It is generally accepted that the vapor contains types of species with predominance of Se_5, Se_2, Se_4, and Se_7 fragments. The Se_8 ring is not a favored species in the vapor phase and it seems unlikely that
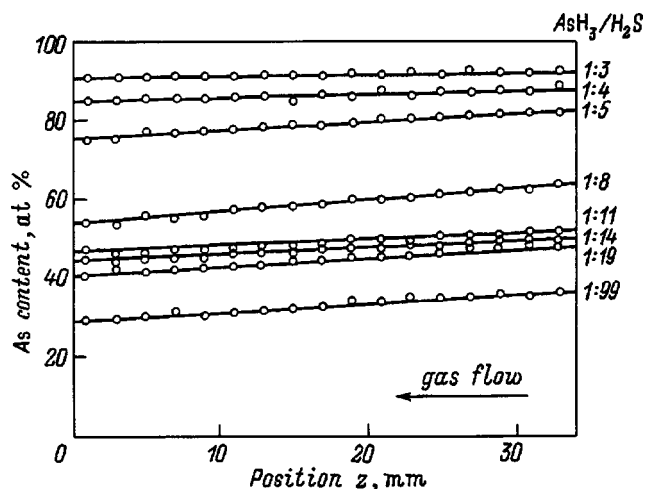
FIG. 2. As content of As_xS_{1-x} layers vs. sample position z on the powered electrode for various AsH_3/H_2S ratios ($z=0$: middle of the electrode).
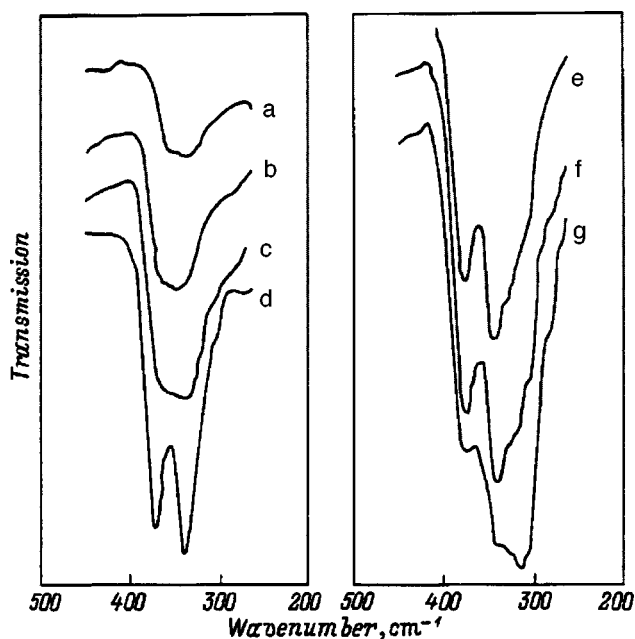

FIG. 3. IR spectra of As_xS_{1-x} layers deposited on the powered electrode with $x=0.90$ (a); 0.86 (b); 0.78 (c); 0.60 (d); 0.48 (e); 0.46 (f); 0.43 (g).

a rearrangement of the shorter molecular species to form eight-membered rings will occur on the substrate as the amorphous state is deposited.

Upon heating at 150 °C for 1 h the film was crystallized. The Raman spectrum (see Fig. 1b) showed a sharp peak at 235 cm^{-1} and a small shoulder at 250 cm^{-1}. Upon crystallization the meander-like chains and the Se_8 rings undergo transformation to the orderly array of chains of trigonal Se.

B. Amorphous As_xS_{1-x}

Details of this work have already been reported in previous publications.[3] In order to obtain layers in a broad chemical composition range the AsH_3/H_2S ratio was varied from 1/3 to 1/99. The decomposition of AsH_3 is exothermic ($\Delta H° = +715$ kJ·mol^{-1}), whereas the decomposition of H_2S is endothermic ($\Delta H° = -259$ kJ·mol^{-1}); thus we expect more rapid and complete dissociation of AsH_3. In Fig. 2 the As content of the layers expressed in at. % is given for the various AsH_3/H_2S ratios. The composition of each layer was measured from the middle of the powered electrode ($z=0$) to its outer circumference at regular distances. The deposition conditions were: pressure 0.25 mbar; rf power 15 W.

In agreement with previous work by Fritzsche *et al.*,[4] we observed that the composition of the film deposited at a given AsH_3/H_2S ratio changed with the position z on the substrate along the gas flow direction. The chemical homogeneity was better in the samples with the highest As content. In Fig. 3 are shown IR spectra recorded in the range 500–200 cm^{-1} on layers of different chemical composition. The IR spectrum of the nearly stoichiometric layer ($x=0.42$) clearly manifests a strong absorption mode at 311 cm^{-1}, which corresponds to an asymmetric stretching vibration in a AsS_3 pyramid, the structural unit in crystalline As_2S_3. In layers richer in As ($x>0.42$) two strong absorption bands at 341 and 374 cm^{-1} become dominant. The IR spectra of the crystalline modifications of As_4S_4 and As_4S_3 show absorption bands close to those observed in our spectra: 346 and 374 cm^{-1} in an As_4S_4 crystal; 341 and

370 cm^{-1} in an As_4S_3 crystal. Because of the small differences in wave number for the crystals, the 341 and 374 cm^{-1} bands in our spectra may be due to vibrations of As_4S_4 units or As_4S_3 units, or a mixture of both. From the IR study we may conclude that increasing overstoichiometry of As causes the breaking of As–S bonds with the formation of structural units of the As_4S_4 and As_4S_3 type, containing As–As bonds. Raman spectra gave futher evidence for the presence of As_4S_4 and As_4S_3 molecular units in layers with an As overstoichiometry. Figure 4 represents Raman spectra of two films with composition $As_{0.46}S_{0.54}$ (a) and $As_{0.78}S_{0.22}$ (b). Spectrum (a) shows a strong peak at 340 cm^{-1}, which is attributed to vibrational modes of pyramidal AsS_3 units. Two meaker bands, clearly visible in spectrum (a), located at 235 cm^{-1} and 188 cm^{-1}, indicate the presence of As_4S_4 units. In an As-rich sample with $x=0.78$ a narrow peak appears at 273 cm^{-1} (see Fig. 4b), which is the most intense band in the Raman spectrum of crystalline As_4S_3. The strong band at 219 cm^{-1} in spectrum (b) can be assigned to pure As clusters. In a layer with very high As content ($As_{0.90}S_{0.10}$) the peak at 340 cm^{-1} associated with AsS_3 units is drastically reduced and the band at about 210 cm^{-1} typical of amorphous As, becomes the dominant feature in the Raman spectrum.

C. Amorphous As_xSe_{1-x}

The chemical composition of the As_xSe_{1-x} films obtained for the various gas ratios is listed in Table I. All compositions were in the Se-rich side compared to the stoichiometric composition $As_{0.40}Se_{0.60}$. An increase of the AsH_3/H_2Se ratio from 1/2 to 2/1 did not yield the expected increase in As content. A decrease of the rf power from 60 to 30 W had a minor effect on the chemical composition.

Information concerning the structure of the films was obtained from Raman spectroscopy. Based on the work of
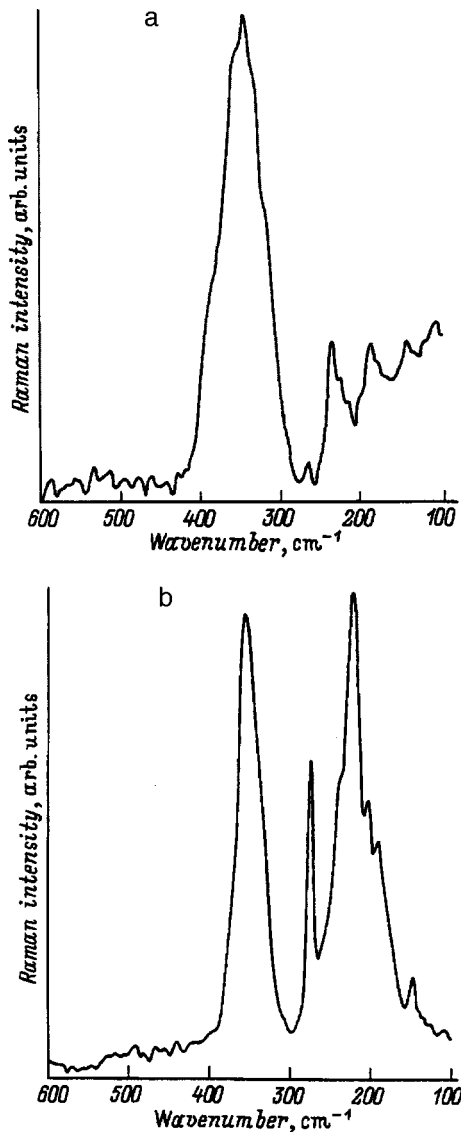
FIG. 4. Raman spectra of As_xS_{1-x} layers with $x=0.46$ (a) and 0.78 (b).

FIG. 5. Raman spectra of amorphous As_xSe_{1-x} films: a — pure Se; b — $As_{0.20}Se_{0.80}$; c — $As_{0.31}Se_{0.69}$, d — $As_{0.36}Se_{0.64}$.

Lucovsky,[2] it is generally accepted that the structure of amorphous Se consists of chains which include both helical chain-like and ring-like segments of Se atoms. A stoichiometric $As_{0.40}Se_{0.60}$ glass is considered to be built up by pyramidal $AsSe_3$ units with the threefold coordinated As atom at the apex. The pyramids are interconnected by the twofold coordinated Se atoms. When extra Se atoms are added to the stoichiometric composition, the atoms can be incorporated in the chains linking the pyramidal molecules. This yields a replacement of the As–Se–As links with As–Se–Se–As

TABLE I. Chemical composition and optical bandgap E_g at room temperature of amorphous As_xSe_{1-x} films deposited by PECVD.

AsH_3/H_2Se volume ratio	Chemical composition	E_g, eV
0/100	Se	1.95
1/25	$As_{0.08}Se_{0.92}$	1.95
1/7	$As_{0.20}Se_{0.80}$	1.93
1/2	$As_{0.31}Se_{0.69}$	1.89
2/1	$As_{0.36}Se_{0.64}$	1.83

chains. Thus, for concentrations in the chalcogen-rich regime ($x<0.40$) Se–As and Se–Se bonds occur but As–As bonds are excluded. With increasing Se content, the number of Se–Se units grows, leading to large atomic clusters of Se. The analysis of the Raman spectra of the arsenic selenides is complicated by the fact that the observed frequencies for the chain of pure selenium and those for the pyramid and As–Se–Se–As chains are close to one another.

Figure 5 shows the Raman spectra of amorphous As_xSe_{1-x} films. The main features can be summarized as follows. In pure Se an intense band occurs at 250 cm^{-1} with a small shoulder at 235 cm^{-1}. The band at 250 cm^{-1} has been attributed by Lucovsky[2] to stretching vibrations in a meandering Se chain. The shoulder that appears at 235 cm^{-1} (typical of crystalline trigonal Se) can be associated with a small fraction of helical chains. At 8 at. % As the peak at 250 cm^{-1} is still the dominant spectral feature with a small shoulder at 227 cm^{-1}. A broad band at 227 cm^{-1} was attributed to an antisymmetric As–Se–As stretching vibration in stoichiometric $As_{0.40}Se_{0.60}$. As the As content is increased (20 at. %), the band at 227 cm^{-1} grows steadily. The Raman spectrum of 31 at. % As shows a broad band extending from ~ 200 to 290 cm^{-1}, which consists of a band at 227 cm^{-1} with increased intensity and a side band at 250 cm^{-1}. At 36 at. % the broad band at 227 cm^{-1}, the signature of the $AsSe_3$ network, dominates the spectrum.

D. Amorphous Ge_xS_{1-x}

The preparation of amorphous Ge_xS_{1-x} and Ge_xSe_{1-x} films by PECVD was discussed in previous publications.[5] For the preparation of the Ge–S system, the GeH_4/H_2S was varied from 1/6 to 1/96. The total gas pressure was held constant at 0.1 mbar and the rf power input at 20 W. Figure

FIG. 7. IR spectra of Ge–S layers: a — $Ge_{0.30}S_{0.70}$ as-deposited; b — $Ge_{0.30}S_{0.70}$ after air exposure; c — $Ge_{0.50}S_{0.50}$ as-deposited; d — crystalline GeO_2; e — $Ge_{0.50}S_{050}$ after air-exposure.
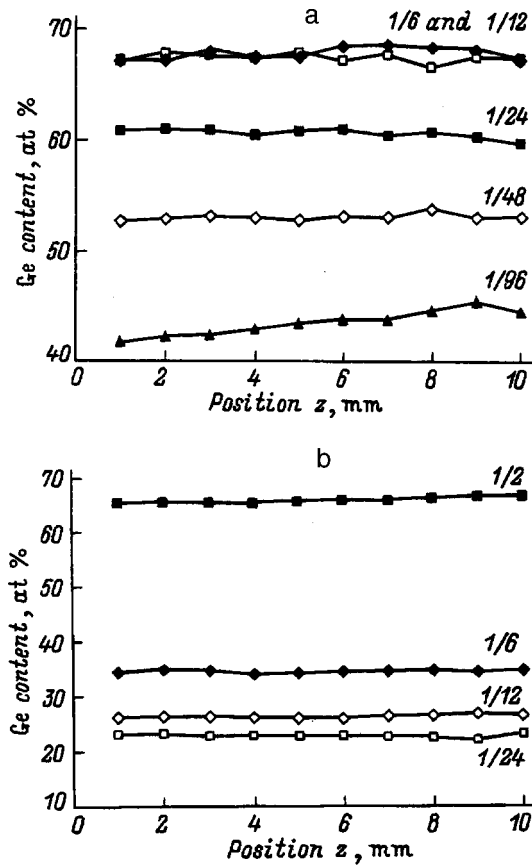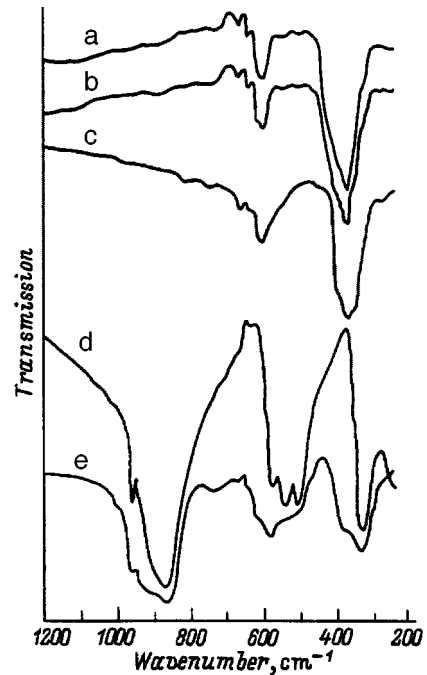
FIG. 6. Ge content of amorphous Ge_xS_{1-x} layers (a) and of Ge_xSe_{1-x} layers (b) ($z = 10$ mm: middle of the electrode) for various $GeH_4/H_2Se(H_2Se)$ gas ratios.

6a shows the Ge content in at.% of layers deposited on the grounded electrode as a function of the position of the microprobe beam. Although the germanium chalcogenides have been studied extensively during the last fifteen years, the knowledge of their structure is still ambiguous. Both amorphous GeS_2 and $GeSe_2$ have a tetrahedral XY_4-type local structure. The ordering of these tetrahedral molecules was explained by different models. Figure 7 shows IR spectra of a $Ge_{0.30}S_{0.70}$ layer (a) and a $Ge_{0.50}S_{0.50}$ layer (c). The strong absorption at about 370 cm^{-1} is the most characteristic feature of the Ge–S system. It is usually assigned to the stretching vibration of the GeS_4 tetrahedral unit (v_3 mode). The IR spectra of both samples recorded after exposure to air for several weeks are also shown in Fig. 7b and 7e. The Ge-rich film ($Ge_{0.50}S_{0.50}$) (spectrum e) showed strong absorption in a broad range originating from Ge–O vibrations. In the same figure the IR absorption spectrum of crystalline GeO_2 is represented (spectrum d). The GeO_2 units show three typical vibrations at about 860, 550 and 330 cm^{-1}. By comparing the spectra of the oxidized Ge–S films and the one of GeO_2, it is clear that the absorption bands observed in the Ge-rich film after air exposure are a consequence of the formation of GeO_2 units.

E. Amorphous Ge_xSe_{1-x}

Figure 6b shows the Ge content of Ge_xSe_{1-x} layers prepared with a GeH_4/H_2Se ratio which varies from 1/2 to 1/24

at a pressure of 0.1 mbar and an rf power of 80 W. A broad composition range can be achieved, which is of interest for a study of photostructural changes in this system.

The IR spectra measured in a $Ge_{0.34}Se_{0.66}$ and a $Ge_{0.64}Se_{0.36}$ layer (see Fig. 8) show a strong absorption band at 260 cm^{-1}, which is due to the v_3 mode of the $GeSe_4$ tetrahedra. The Ge-rich films were also unstable in air and showed in their IR spectra strong absorption bands of Ge–O vibrations, increasing in intensity when keeping them in air for a long time.
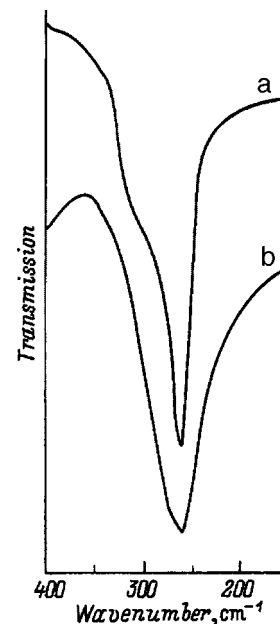

FIG. 8. IR spectra of $Ge_{0.34}Se_{0.66}$ (a) and $Ge_{0.64}Se_{0.36}$ (b).
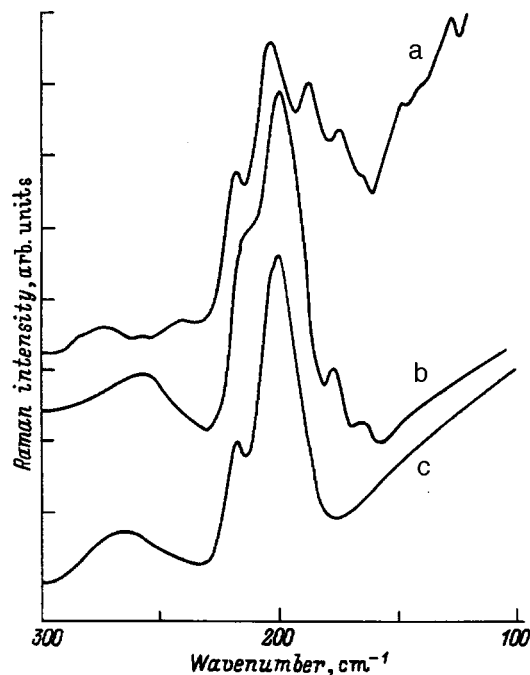
FIG. 9. Raman spectra of $Ge_{0.34}Se_{0.66}$ as-deposited (a); after annealing at 300 °C (b); $Ge_{0.26}Se_{0.74}$ as-deposited (c).

In Fig. 9 the Raman spectrum of an as-deposited $Ge_{0.34}Se_{0.66}$ film is shown (curve a). We observed five significant bands: a strong band at 200 cm^{-1} (A_1 peak), a side band at about 210–220 cm^{-1} (called the companion line, A_1^c), a peak at 188 cm^{-1}, a broad band at 280 cm^{-1} and a peak at 175 cm^{-1}. The A_1 peak at 200 cm^{-1} can be assigned to the symmetric-stretch breathing mode of the $GeSe_{4/2}$ corner sharing tetrahedra.[6] The companion line A_1^c at 220 cm^{-1} has been assigned to vibrations of the Se atoms in four-membered rings comprised of two edge-shared tetrahedra.[7] The bands at 280 and 175 cm^{-1} were assigned to the vibrational modes of a structural unit which contain Ge–Ge bonds

such as Se_3–Ge–Ge–Se_3.[8] The peak at 188 cm^{-1} can be associated with the vibration of selenium atoms in a tetrahedral molecule in which a Se atom is replaces by a Ge atom.[9] All these features indicate that homopolar Ge–Ge (and probably Se–Se) bonds are present in the sample with slight overstoichiometry of Ge.

The $Ge_{0.34}Se_{0.68}$ film was annealed at 300 °C for 1 h in nitrogen atmosphere. The Raman spectrum recorded after heating (curve b in Fig. 9) suggests that structural changes have occurred: the intensity of all the bands associated with Ge–Ge bonds has decreased. The new spectrum resembles that of $Ge_{0.26}Se_{0.74}$ (curve c), which is less Ge rich.

4. CONCLUSION

We have been able to prepare layers of amorphous Se, and of the As and Ge chalcogenides (S and Se) by using plasma-enhanced chemical vapor deposition. The composition range of the binary systems which can be achieved by this technique is very broad.

[1] G. Lucovsky, A. Mooradian, W. Taylor, G. B. Wright, and R. C. Keeze, Solid State Commun. **5**, 113 (1967).
[2] G. Lucovsky, in *The Physics of Selenium and Tellurium*, edited by E. Gerlach and P. Grosse (Springer-Verlag, Berlin, 1979), p. 210.
[3] P. Nagels, R. Callaerts, M. Van Roy, and M. Vlček, J. Non-Cryst. Solids **136&137**, 1001 (1991); in *Proceedings of the International Conference: Cond. Matter. Phys. and Appl.*, edited by W.E. Alnazer (Bahrain, 1992), p. 67.
[4] H. Fritzsche, V. Smid, H. Ugur, and P. J. Graczi, J. Phys. C **4**, 699 (1981).
[5] E. Sleeckx, P. Nagels, R. Callaerts, and M. Van Roy, J. Phys. IV **C3**, 419 (1993); J. Non-Cryst. Solids **164−166**, 1195 (1993).
[6] S. E. Griffiths, G. P. Espinosa, J. P. Remeika, and J. C. Phillips, Phys. Rev. B **25**, 1272 (1982).
[7] G. Lucovsky, C. K. Wong, and W. B. Pollard, J. Non-Cryst. Solids **59−60**, 839 (1983).
[8] Nemanich, G. A. Connell, G. A. Hayes, and R. A. Street, Phys. Rev. B **18**, 6900 (1978).
[9] H. Kawamura, M. Matsumura, and S. Ushioda, J. Non-Cryst. Solids **35-36**, 1215 (1980).

Photoinduced structural changes in amorphous semiconductors

K. Tanaka

Department of Applied Physics, Faculty of Engineering, Hokkaido University, Sapporo 060, Japan

A variety of photostructural changes observed in tetrahedral and chalcogenide amorphous semiconductors are reviewed from physical and chemical points of view. In particular, observations of the photodarkening and related phenomena in chalcogenide glasses are summarized, and structural models which have been proposed so far are criticized. © *1998 American Institute of Physics.* [S1063-7826(98)01208-3]

1. INTRODUCTION

It is known that many substances exhibit structural changes when exposed to visible light. A well-known example in physical science may be the photographic reaction, in which migration of Ag^+ ions is induced in Ag-halide crystals by photoelectronic excitation.[1]

Recently, it was found that amorphous semiconductors exhibit a variety of photoinduced phenomena.[2–8] The following three features peculiar to amorphous semiconductors appear to be responsible for the observations: 1) valence electrons in semiconductors tend to be optically excited; 2) electron-lattice interaction appears to be strong in flexible networks; and 3) amorphous materials can possess a number of metastable structures.

The phenomena observed in amorphous semiconductors can be classified into two groups. One is bulk effects or photoinduced phenomena in single amorphous phases.[3–8] The other is a kind of photochemical reaction such as the photodoping, the photoinduced oxidation, etc., for which the reader may refer to some publications.[2,4,6,9]

In the present paper we describe the bulk photoinduced phenomena. First, unified views common to tetrahedral and chalcogenide systems are pointed out and then characteristic differences are discussed. Second, the reversible photodarkening and related phenomena induced in chalcogenide glasses with illumination and annealing are considered.

2. PROMISING OUTLOOK FOR BULK PHOTOINDUCED PHENOMENA

2.1. Observations

As shown in Table I, the bulk photoinduced phenomena observed in tetrahedral and chalcogenide systems can be classified into some groups, depending on the densities of atomic sites involved.[10]

Photoinduced crystallization is the most dramatic phenomenon observed in both tetrahedral[11] and chalcogenide amorphous semiconductors.[12,13] The phenomena appear to be induced electronically[13,14] and thermally,[11,12] and the thermal process has been utilized as phase-change erasable memories.[12] Clearly, the photocrystallization is irreversible, in the sense that the initial amorphous state cannot be recov-
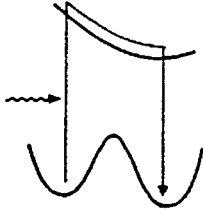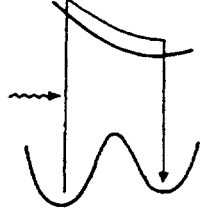
ered with annealing,[1] since the illuminated state is thermodynamically more stable (see, the inset in Table I).

The number of covalent bonds interchanged in the photo-crystallization processes seem to depend on the material of interest. For instance, in amorphous Se, which consists of distorted chain molecules,[16,17] interchange of a few atomic bonds ($\sim 1\%$) seems to be sufficient to align the distorted chains into hexagonal crystals.[2] In contrast, in a ternary compound such as Ge–Sb–Te (Ref. 12), bond breakage and reconstruction of a greater number ($\sim 10\%$) may be needed to produce polycrystals, since compositional disorder is inherent in compound materials. In Table I, therefore, the atomic density contributing to the photocrystallization is represented roughly as 10^{22} cm^{-3}. This phenomenon is understood to accompany structural changes in the long-range order, since crystals are produced.

Also observed in tetrahedral and chalcogenide systems are reversible phenomena involving sturctural changes at atomic sites of 10^{17}–10^{18} cm^{-3}, approximately ppm order.[5] The density is comparable to that of point defects in crystals, e.g., color centers in alkali halides,[1] and it is far below a detection limit of experimental techniques such as x-ray diffraction, which can provide direct structural information. Accordingly, mechanisms of these photoinduced phenomena are largely speculative, specifically, when related sites are ESR-inactive. The Staebler–Wronski effect, which refers to a degradation of photoconductive properties in amorphous hydrogenated Si, is a reversible phenomenon which has been studied extensively.[5] In chalcogenide glasses held at low temperatures ($\leqslant T_g/2$), illumination generates unpaired electron spins (photoinduced ESR), which accompany an increase in optical absorption (photoinduced mid-gap absorption) and decrease in the photoluminescence intensity (photoinduced photoluminescence fatigue).[5] Common to all these phenomena is that dangling bonds are assumed to be photocreated.[5]

Between the high- and low-density photoinduced phenomena described above, there exist several phenomena involving atomic sites of $\sim 1\%$.[5] Interestingly, these kind of phenomena the demonstrated only in chalcogenide glasses. In tetrahedral materials, such photostructural changes seem to be still speculative.[19,20] In these photoinduced phenomena in chalcogenide glasses, some are irrevers-

TABLE I. A classification of bulk photoinduced phenomena observed in tetrahedral (a-Si:H) and chalcogenide amorphous semiconductors. The atomic densities are representative. SRO, MRO, and LRO stand for short-, medium-, and long-range orders.

Atomic density, cm^{-3}	Structural change	Material		Reversibility
		a-Si:H	Chalcogenide	
$\sim 10^{22}$	LRO	Photo-crystallization	Photo-crystallization Giant photo-contraction Photo-polymerization Photo-decomposition	Irreversible
$\sim 10^{20}$	MRO		Photo-darkening Photo-induced anisotropy Photo-induced ESR	Reversible
$\sim 10^{18}$	Defective SRO	Staebler–Wronski		

ible and others are reversible, and, in general, irreversible phenomena exhibit greater structural changes. A well-known irreversible change is the photopolymerization phenomenon observed in as-evaporated As_2S_3 films.[7,8] On the other hand, at least, two reversible changes, i.e. the photodarkening and the photoinduced anisotropy, are known to exist.[3,5,6,8] The details will be discussed in Sec. 3.

2.2. Discussion

It is interesting to note in Table I that all the photoinduced phenomena involving atomic sites less or more than $\sim 10^{20}$ cm^{-3}, $\sim 1\%$ of the total atom density, are reversible and irreversible. It can be understood that the irreversible phenomena can involve greater atom numbers, since the changes occur toward more stable atomic structures (see Table I). Why, then, should the atomic sites be less than 1% in the reversible changes?

This fact can be accounted as follows: The density of 1% reads one photoinduced atomic site per cube with a side length of $5-6$ atoms, which is $1-3$ nm, depending on the atomic bonds involved, i.e., covalent and/or van der Waals bonds. This length implies that, in a reversible change, a photoinduced atomic configuration can be metastable, provided that produced strain is confined in this cube. It can then be relaxed into a stable structure with thermal relaxation induced by annealing. Alternatively, if more defective sites were generated in the cube, interaction between the defective sites would be stronger, and hence cooperative relaxation (annihilation) might occur toward stable atomic configurations. We can thus assume that the defective atomic density of 1% is the limit arising from the structures which can localize photoinduced strains.[3] It is interesting to note that the critical length of $1-3$ nm is comparable to the medium-

range structural length in chalcogenide glasses.[16,17] We can envisage one photoinduced defect in a crystalline structure with a scale of $1-3$ nm.

Why, then, should the site density of the photoinduced dangling bonds be less than 10^{18} cm^{-3}? The density may be related to the nature of nonequilibrium disordered structures.[10]

It may also be worthwhile to consider the photoinduced phenomena from a chemical point of view. We note in Table I that chalcogenide glasses exhibit a variety of photoinduced phenomena, while the tetrahedral material possesses a fewer. How can we understand these contrasting features?

The origin can be sought in the chemical bonding structures. As illustrated in Fig. 1, chalcogenide glasses are assumed to consist of covalent clusters held together with weak intermolecular forces of the van der Waals type.[16] In other words, the glass possesses a dualistic bonding nature and $2 \leq Z \leq 3$, where Z is the covalent coordination number averaged over the constituent atoms.[16] This flexible structure with the low coordination number seems to cause many kinds of photoinduced phenomena. For instance, the photopolymerization mentioned in 2.1 can occur because there exist intra- and inter-molecular bonds.[7,8] We will also see in the next section that the photodarkening can be attributed to the existence of strong and weak bonds. In contrast, the atomic bond involved in the tetrahedral material is of one kind, i.e., only covalent, and, accordingly, photoinduced changes are restricted in variety. Actually, Shimizu argues that the Staebler–Wronski effect could not occur if all Si atoms were tetrahedrally bonded with each other ($Z=4$) (Ref. 5).

Here, it is tempting to consider whether photoinduced phenomena appear in amorphous rare-gas solids. The material contains only van der Waals bonds ($Z=0$), and it may be very soft.[16,21] Unfortunately, as we know, photoinduced
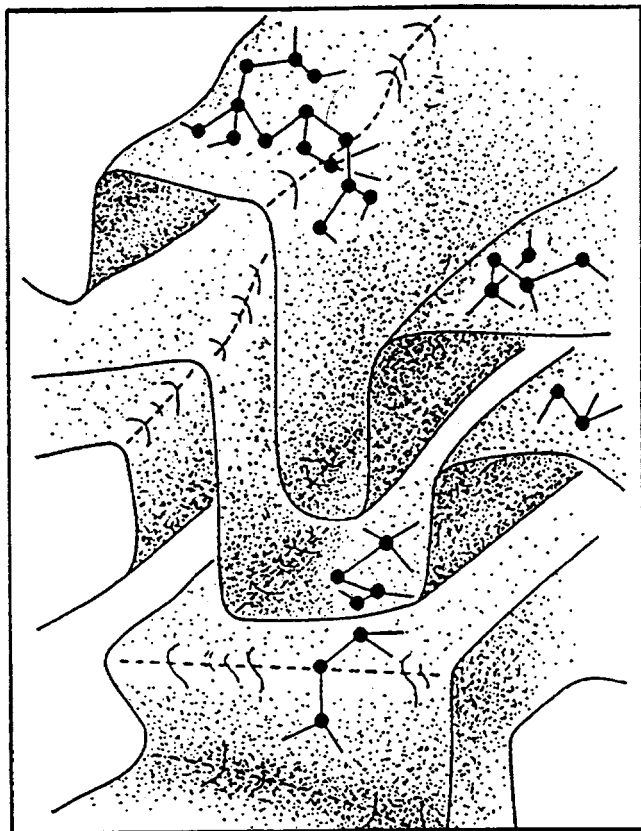
FIG. 1. A schematic illustration of a chalcogenide glass consisting of fourfold (Ge), threefold (As, Sb), and twofold (S, Se, Te) coordianted atoms.

FIG. 2. Photodarkening in deposited and bulk As_2S_3 at room temperature. Solid and dashed lines show annealed and iluminated states. The film characteristics are measured using the photothermal spectroscopy [K. Tanaka, Y. Ichimura, and K. Sindoh, J. Appl. Phys. **63**, 1815 (1988)].

phenomena in such materials, have not been studied so far. However, it is plausible that only photoinduced crystallization can occur, since the van der Waals bond is nondirectional and flexible. Phenomena similar to the Staebler–Wronski effect cannot appear, since there exist no covalent bonds and local bistable configurations cannot be sustained.

Summarizing these considerations, we conclude that the existence of two kinds of bonds in chalcogenide glasses is responsible for a variety of photoinduced phenomena. In other words, the low Z is essential.[4)]

3. PHOTODARKENING AND RELATED STRUCTURAL CHANGES

The photodarkening phenomenon observed in chalcogenide glasses has so far attracted considerable interest, and the structural changes have been studied extensively. Below we give a brief review of the photodarkening and related phenomena, and then consider some structural models proposed so far.

3.1. Observations

When a chalcogenide glass such as As_2S_3, which has been annealed at T_g in advance, is illuminated at room temperature, or at temperatures substantially lower than T_g, the sample exhibits reversible changes in volume, optical, electrical, photoelectrical, mechanical, chemical, and thermal properties.[4–6,8] Here, the optical change includes the photodarkening, which refers to the feature that illuminated mate-
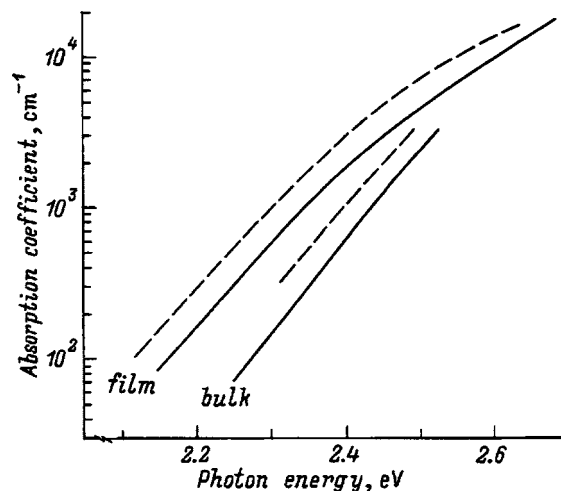
rials appear to be darkened. As shown in Fig. 2, this darkening is caused by a reduction of the optical bandgap energy. An increase in the refractive index ($\Delta n/n \simeq 0.03/2.6$ in As_2S_3) accompanies this absorption change. The electrical change appears as an increase in the ac conductivity,[5] while dc conductivity change cannot be examined, since the material is nearly insulating.[17] As for the photoelectrical change, photoconductive degradation was found to occur as a result of the spectral change.[5,22] It is not conclusive whether the hole mobility undergoes some modifications as a result of illumination.[6,7] The mechanical, chemical, and thermal changes imply that the material becomes softer and unstable upon illumination.[5] Also consistent with these rigidity changes is the volume expansion ($\Delta V/V \simeq 0.5\%$ in As_2S_3) upon illumination. More surprisingly, Tanaka *et al.* have demonstrated giant volume expansion with sub-bandgap illumination, which can be utilized to produce microlenses.[6] However, the expansion does not occur if a sample is illuminated under hydrostatic compression, despite the appearance of photodarkening.[5] We assume therefore, that photoexpansion and photodarkening are not directly related.[23]

To obtain insight into microscopic structural changes accompanying the photodarkening, diffraction, extended x-ray absorption fine structure (EXAFS) and vibrational spectroscopic studies have been performed.[3–8] However, it seems difficult to extract a unified model for the structural change from these studies, since the structure itself is controversial.[16,17] In addition, as implied above, it is plausible that different kinds of structural changes are induced by illumination.

Diffraction studies using x-rays and neutrons have been reported by some groups.[3,5] Figure 3 shows an x-ray result reported by the present author using bulk As_2S_3 glass.[23] Illumination and diffraction measurements have been performed at room temperature *in situ*, in order to exclude thermal expansion effects and to detect minute changes. We see that the x-ray intensity difference (annealed–illuminated) is positive at about the first sharp diffraction peak (FSDP),
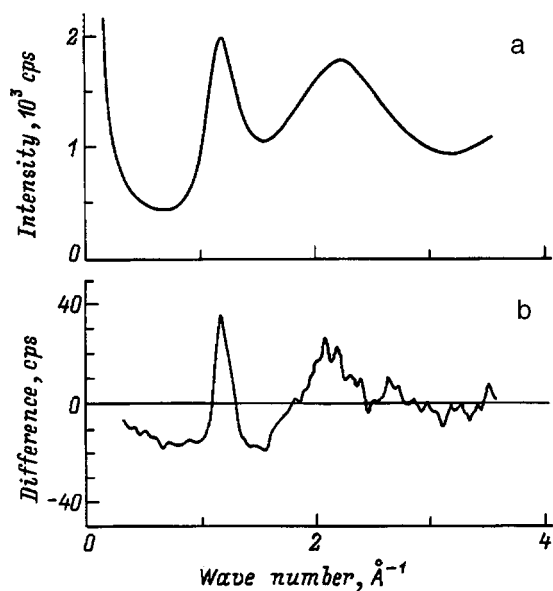
FIG. 3. X-ray diffraction patterns of an As_2S_3 bulk glass before and after illumination. a — shows the annealed state, and b — shows the difference obtained by subtracting the x-ray intensity of the illuminated pattern from that of the annealed pattern.
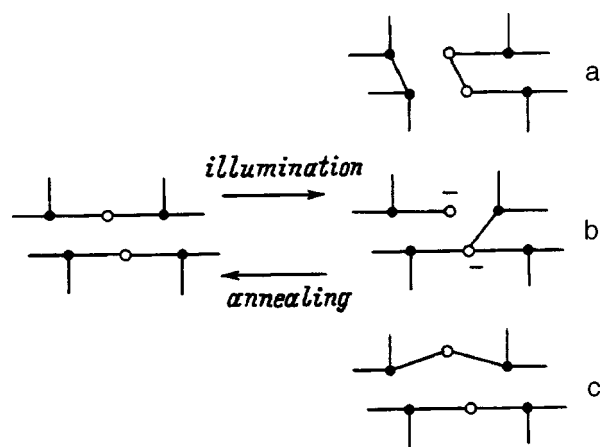
FIG. 4. Schematic illustration of structural models proposed for the photodarkening and related phenomena. a and b show defect models, and c represents distortion models.

which indicates photoinduced disordering in the medium-range order. This experimental result has been confirmed by some researchers,[3,5] while the interpretation of the FSDP remains controversial.[16,17] The author prefers the so-called distorted-layer model,[16] while others use three-dimensional models, etc.[17]

Some EXAFS studies have been reported.[3,5,24] However, the results reported for binary glasses are not necessarily consistent.[3,5] Creation of homopolar bonds and fluctuation enhancement of As–S–As bond angles have been pointed out. Kolobov *et al.* report *in situ* investigation for amorphous Se.[24]

Vibrational spectra have been obtained through Raman and infrared (IR) studies.[4–8] In Raman scattering spectra of illuminated As_2S_3 films, a trace of As–As bonds has been detected at 231 cm^{-1}, and the intensity of the low-frequency Raman peak located at $\sim 25 \text{ cm}^{-1}$, the so-called boson peak, is substantially reduced.[5,7,8] No marked changes in the As–S vibrational band centered at 340 cm^{-1} are reported. In contrast, in the IR spectroscopy, which may be more amenable to quantitative evaluation, slight broadening of the As–S vibrational band has been detected.[4]

3.2. Discussion

How can we understand these macroscopic and microscopic changes? Taking the reversible features into account, we can assume a configuration-coordinate diagram such as shown in Table I (Ref. 5), in which an illuminated state is shown as quasi-stable. Then, the problem turns to the structural element involved.

Here, as illustrated in Fig. 4, the structural models proposed so far can be classified into two groups. In all models, relatively ordered structures are assumed to be the annealed state. For the illuminated state, the defect models (a) and (b)

presume creation of some kind of defects and, in contrast, the distortion models (c) postulate that randomness increases in normal bonding configurations.

3.2.1. Defective structure models.

Owen and others have emphasized through their Raman scattering measurements that As–As bonds are formed in illuminated states (Fig. 4a).[5,7,8] It is theoretically predicted that As–As bonds provide electronic states in the bandgap,[3,17] and hence the photodarkening may appear if the homopolar bonds are created. Nonetheless, the model cannot be a universal explanation of the photoinduced change, since the photodarkening appears in elemental materials, S and Se.[5] In addition, no evidence of photoinduced Ge–Ge bonds is obtained throught Raman studies.[23]

Street and others have developed defective models using the charged-defect concept which was originally proposed by Mott.[5] The charged defects are assumed to produce electronic states in the band-tail regions,[17] and hence the bandgap is reduced upon illumination. These defects with the density of $\sim 1\%$ would manifest specific vibrational peaks, which were investigated by Kolobov *et al.*[25]

3.2.2. Distorted structure models.

In the last model illustrated in Fig. 4, some kind of photoinduced distortions in normal bonding configurations are assumed. Since modifications of covalent bond lengths requires substantial energy, and since the strained structures may not be quasi-stable, such distortions cannot be envisaged in the reversible photodarkening.

Plausible structural changes can then be sought in the distortions in bond angles, dihedral angles, and van der Waals distances. For instance, Utsugi and Mizushima emphasize the angular distortion in the short-range order, on the basis of their IR studies.[4] Angular fluctuation will increase the width of the conduction band, since the conduction band in chalcogenide glasses consists of the antibonding state of

covalent bonds.[16,17] As a result, the photodarkening can appear.

On the other hand, distortions in the dihedral angle and the van der Waals distance enhance the randomness in the medium-range structural order. Pfeiffer *et al.*, assume distortion of dihedral angles on the basis of their EXAFS studies.[3] In contrast, the present author has proposed the intermolecular distortion through bond-twisting motion of chalcogen atom.[5] These two kinds of structural changes appear to be consistent with the FSDP weakening and broadening, shown in Fig. 3. The structural changes will modify the width of the valence band, since the width of the valence band is strongly influenced by the interaction between lone-pair p-orbital electrons of chalcogen atoms.[16,17]

At present, it difficult to determine which structural change is the most responsible. We expect that further insight can be provided if it is disclosed that photodarkening is caused by the changes in the bottom of the conduction band and/or in the top of the valence band. However, the accuracy of the photoelectron spectroscopy, which is capable to determine the position of the band edges, is not sufficient to resolve a shift of ~ 50 meV. Alternatively, we can assume that the three structural changes are interrelated, since the structural relaxation is characteristic of chalcogenide glasses that possess low Z. In other words, if an intermolecular bond is distorted upon illumination, structural relaxation will necessarily occur, which would lead to appreciable angular distortions.

3.2.3. Miscellaneous.

When dealing with the photodarkening in As_2S_3 and similar materials, we should note characteristic differences and similarities between the bulk and the annealed films. In general, structures of the bulk and the annealed films are assumed to be similar, while it has been demonstrated that the annealed film still contains an appreciable number ($\sim 1\%$) of As–As bonds.[7,8] In fact, Fig. 2 shows that the absorption edges of an annealed film and the corresponding bulk are clearly different. Wrong bonds (homopolar bonds in stoichiometric compounds) seem to cause the difference. Surprisingly, however, the photoinduced red-shifts are nearly the same, ~ 50 meV, in both materials.

We should also note that when As_2S_3 is exposed to linearly polarized light, the photodarkening and the photoinduced anisotropy appear simultaneously. The mechanisms of these phenomena were found to be different.[5,26,27] Accordingly, it is clear that at least two kinds of structural changes are induced upon illumination. Further studies are needed in order to obtain one-to-one correspondences between macroscopic changes and microscopic structural changes, in which the latter is largely speculative.

4. SUMMARY

Overall features of the photoinduced phenomena observed in amorphous semiconductors are considered from two aspects. From the atomic density, it appears that the

reversible phenomena cannot accompany structural changes at atomic sites more than $\sim 1\%$ of the total atom density. From a chemical point of view, the reason why chalcogenide glasses exhibit a variety of phenomena can be sought in the dualistic bonding nature which involves covalent and van der Waals bonds.

The photodarkening and related phenomena are critically reviewed. Many macroscopic features have been revealed, while the mechanism remains speculative. This is because the structural changes appear to extend to medium-range scales, for which no convincing experimental tools are yet available. In contrast, the phenomena appear to be promising for fabrication of functional devices.[5,6]

This article is dedicated to Professor Kolomiets, who is undoubtedly the founder of amorphous semiconductor physics. He also brought up many able scientists such as Professor Lyubin and Dr. Kolobov. I cannot forget his strength and warmth at the Ioffe Institute in 1987.

[1)] The phase-change process can be reversible with thermal annealing and quenching, which are induced with pulsed illumination at different light intensities and different pulse widths. In the reversible photoamorphization of crystalline $As_{50}Se_{50}$ films, substrates are responsible for the peculiar phenomenon.

[2)] Breaking of covalent bonds and reptile motion of chain fragments are probably needed, like the crystallization process in chain polymers (see Ref. 18).

[3)] In order to confirm this speculation, however, lattice dynamical calculation in large amorphous networks is needed.

[4)] In this sense, photoinduced phenomema can appear also in oxide glasses, as they do.[5] Nonetheless, the atomic bond is more ionic, and the dualistic bonding nature is not prominent. Accordingly, they exhibit fewer kinds of photoinduced phenomena, like a-Si : H.

---

[1] N. F. Mott and R. W. Gurney, *Electronic Processes in Ionic Crystals* (Dover, N.Y., 1964).

[2] A. V. Kolobov and S. R. Elliott, Adv. Phys. **40**, 625 (1991).

[3] G. P. Pfeiffer, M. A. Paesler, and S. C. Agarwal, J. Non-Cryst. Solids **130**, 111 (1991).

[4] Y. Utsugi and Y. Mizushima, Jpn. J. Appl. Phys. **31**, 3922 (1992).

[5] K. Shimakawa, A. Kolobov, and S. R. Elliott, Adv. Phys. **44**, 475 (1995).

[6] K. Tanaka, *Current Opinion in Sol. St. and Mater. Sci.* **1**, 567 (1996).

[7] V. I. Mikla, J. Phys.: Condens. Matter **8**, 429 (1996).

[8] M. Frumar, M. Vlcek, Z. Cernosek, Z. Polak, and T. Wagner, J. Non-Cryst. Solids **213&214**, 215 (1997).

[9] G. Dale, A. E. Owen, and P. J. S. Ewen, in *Physics and Applications of Non-Crystalline Semiconductors in Optoelectronics*, edited by A. Andriesh and M. Bertolotti (Kluwer, Dortrecht, 1997) p. 45.

[10] K. Tanaka, J. Non-Cryst. Solids **139**, 179 (1992).

[11] M.-C. Lee, C.-J. Tseng, C.-R. Huang, and T.-H. Huang, Jpn. J. Appl. Phys. **26**, 193 (1987).

[12] T. Ohta, N. Akahira, S. Ohara, and I. Satoh, Opto-Electron. **10**, 361 (1995).

[13] M. Nakamura, Y. Wang, O. Matsuda, K. Inoue, and K. Murase, J. Non-Cryst. Solids **198−200**, 740 (1996).

[14] J. Solis, C. N. Afonso, S. C. W. Hyde, N. P. Barry, and P. M. W. French, Phys. Rev. Lett. **76**, 2519 (1996).

[15] A. V. Kolobov and S. R. Elliott, J. Non-Cryst. Solids **189**, 297 (1995) [*sic*].

[16] R. Zallen, *The Physics of Amorphous Solids* (John Wiley & Sons, N.Y., 1983).

[17] S. R. Elliott, *Materials Science and Technology*, edited by Zarzycki (VCH, Weinheim, 1991). Vol. 9, p. 375.

[18] T. P. Russell *et al.*, Nature (London) **365**, 235 (1993).

[19] H. Fritzsche, Solid State Commun. **94**, 953 (1995).

[20] K. Shimizu, T. Shiba, T. Tabuchi, and H. Okamoto, Jpn. J. Appl. Phys. **36**, 29 (1997).

[21] A. Kouchi and T. Kuroda, Jpn. J. Appl. Phys. **29**, L807 (1990).

[22] N. Toyosawa and K. Tanaka, Phys. Rev. B **56**, 7416 (1997).

[23] K. Tanaka, Phys. Rev. B (in press).

[24] A. V. Kolobov, H. Oyanagi, Ke. Tanaka, and K. Tanaka, Phys. Rev. B **55**, 726 (1997).

[25] A. V. Kolobov *et al.*, (in press).

[26] K. Tanaka, K. Ishida, and N. Yoshida, Phys. Rev. B **54**, 9190 (1996).

[27] K. Ishida and K. Tanaka, Phys. Rev. B **56**, 206 (1997).

Chalcogenide glasses in optoelectronics

A. M. Andriesh

Center of Optoelectronics of the Institute of Applied Physics Academy of Sciences of Moldova,
MD-2028 Chisinau, Moldova

1. INTRODUCTION

Professor B. T. Kolomiets was one of the discoverers of electronical semiconductor properties of chalcogenide glasses. He developed a complex investigation of the structure and physical properties of a large group of chalcogenide glasses. He often stressed the importance of this class of materials for the understanding of noncrystalline solid physics. This can be found, for example, in one of the last of his summary papers entitled ''Chalcogenide glasses,'' written by him in 1981 on the occasion of the jubilee of St. Petersburg Physical-Technical Institute. In that paper the main attention was given to describing the unique features of the glassy semiconductors, the the new phenomena, first theoretical notions and potentialities for practical applications were mentioned. Professor Kolomiets was reminiscent and noted in that article the contribution of Professor A.F. Ioffe and Professor N.A. Goriunova in the discovery of the new group of semiconductors — glassy semiconductors.

I am happy that my scientific activity began in the famous laboratory of Prof. B.T. Kolomiets in 1959 where the first research of the chalcogenide glasses was developed, especially research concerning optical, electrical, photoelectrical phenomena. I remain grateful to Prof. B.T. Kolomiets for giving me the opportunity to work in his laboratory and to deal with the new class of noncrystalline semiconductors which became then materials of great interest in many laboratories of the world.

This is why it is a particular pleasure for me to contribute this article in honor of Professor B.T. Kolomiets's ninetieth birthday. First of all, it is worth to noting the reason for mentioning that class of materials. The main reason for the interest in the scientific community in this class of materials is the fact that this class of glassy semiconductors successfully complements the properties of well known groups of crystalline semiconductors.

If an insignificant change in the composition or the content of the crystals is sufficient for achieving a marked change of physical parameters, then chalcogenide glasses have a smooth change of the properties even in the case of a considerable change in the composition or the strong alloy.

If many electronic processes in the crystals are controlled by the redistribution of charge carriers on the separate, discrete local levels, then in the chalcogenide semiconductors a quasicontinous distribution of localized states will be seen.This which generates a great peculiarity of electronic

processes, in particular, in the transport phenomenon and in the optical and photoelectric processes.

For example, in the chalcogenide glass semiconductors the mobility of the charge carriers may differ from the mobility of crystals by a million or more orders of magnitude.

If the crystals with hard crystal structures do not permit removing the atoms from their fixed position in the network, the chalcogenide glasses, and other disordered materials with a more labile structure make it possible to change the position of the neighbor atoms already on the insignificant energetic influence by means of optical and x-ray radiation or electron beam.

Comparing the properties of crystals and glasses, the enumeration of these peculiarities of the chalcogenide glasses may be continued, but probably, even those mentioned above are quite sufficient for stressing the originality of the properties of chalcogenide glasses, allowing us to propose the above-mentioned class of materials for wide application.

We will restrict the discussion confine ourselves to presenting only a short information concerning the peculiarities of the energetic spectrum and its contribution to the photo-induced phenomena. Some results of application of this group of materials in optoelectronics will be also presented.

2. PECULIARITIES OF THE DISTRIBUTION OF LOCALIZED ELECTRON STATES

A few models for the distribution of localized states in noncrystalline solids were formulated in Refs, 1–7. The key point of these models is the quasicontinuous distribution of localized states in the band gap, which arise as a result of the structural disorder in noncrystalline solids.

According to Gubanov,[2] the absence of further order in the distribution of atoms leads to the blurring of allowed band edges and to the appearance of fluctuation levels. Cohen, Frizsche, and Ovshinsky[3] have proposed a model of tail density of electron states which are spread in the band-gap. In the dependence of the degree of order of the semiconductor the tail density of states are distributed near the edges of allowed bands or are spread deeply in the bandgap up to their mutual overlap. In the models by Mott and Davis[1] besides tails of allowed bands near the middle of bandgap the existence of rather narrow band (~ 0.1 eV) of the localized state is assumed. According to Ref. 4, in vitreous semiconductors against the background monotone levels distribu-

tion zones with heightened state density can be observed. Marshall and Owen[5] localize the zones with heightened density of localized state both in the upper and lower half of the bandgap. It was demonstrated by Bonch-Bruevich[6] that in the bandgap of an unregulated semiconductor there can be peaks of density of localized states, conditioned by the presence on impurities of other defects, which with assumptions can be called discrete localized levels. The nature of localized states in vitreous semiconductors have not yet been studied sufficiently. In some studies it is connected with the presence of defects. The first study of this kind is the article by Street and Mott[7] where the localized states, by broken bonds, are analyzed. These states, depending on the level of engaged condition of electron bonds, correspond to the neutral, positive, or negative charged centers.

We have applied many experimental methods to obtain the adequate distribution of localized states in the gap: thermostimulated currents, thermostimulated electrical depolarization, spectral distribution and kinetics of photoconductivity, transport phenomena, photoinduced absorption, etc.[8]

On the basis of these experiments, we have not only confirmed the quasicontinous distribution of localized states in the gap with some portions of states with greater density but we even were able to calculate in some energy range the precise parameters of the energy distribution.

For example, the parameters of energy distribution of localized states $N(E)$ in As_2S_3 and As_2Se_3 thin films were studied by the method of electrophotography spectroscopy of deep levels. For a long period of time, there was a discrepancy between data of the energy distribution of localized states obtained from different experiments. The transit time method[9] and the photoinduced absorption method[10] therefore, indicate the exponential type of distribution of localized states. The other methods such as temperature dependence of photocurrent,[11] photoluminescence,[12] thermostimulated depolarization[13] indicate the presence of groups of relative discrete levels. The indicated discrepancy can be eliminated in the case of electrophotography spectroscopy deep levels proposed dy Abkowitz.[14] This method allows us to determine the concentration of deep filled traps and their energy distribution. As was found in Ref. 15, the energy distribution of traps in As_2Se_3 and As_2S_3 has the region of discrete levels in the range $0.55-0.6$ eV for As_2Se_3 and $0.75-0.80$ eV for As_2S_3. This confirms the data obtained in Refs 11 and 13. The total concentration of traps was in the range $(1-5) \times 10^{16}$ cm$^{-3} \cdot$ eV^{-1}.

Using the charging and discharging characteristics of metal$-$ChG$-$semiconductor$-$dielectric$-$semiconductor structure Me$-As_2S_3(As_2Se_3)-SiO_2-$Si the authors[16] determined that the energy distribution of the filled traps is quasicontinous with the asymmetrical maximum in the energy range $0.70-0.90$ eV for As_2Se_3 and $0.85-0.15$ eV for As_2S_3 (Fig. 1).

Studying the change with time of the transient capacitance of the space charge region at a Shottky barrier due to thermal relaxation of localized centers preliminary filled by a pulse of zero bias, the authors[17] determined the density$-$of$-$states distribution in the upper half of the gap of As_2Se_3 in the interval of 0.35 eV above the Fermi level.
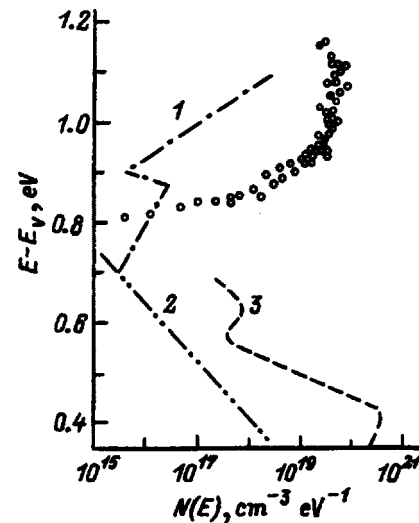

FIG. 1. Sketch of the localized density-of-states distribution in the gap of a-As_2Se_3, according to the data of Ref. 9 (1), [D. Momroe and M.A. Kastner, Phys. Rev. B **33**, 8881 (1986)] (2), [R.P. Barclay, J.M. Marshall, and C. Main, J. Non-Cryst. Sol. **77** & **78**, 1269 (1985)] (3) and 10 (circles).

The data concerning the spectral distribution of localized states obtained by different authors are shown in Fig. 1. As was shown the density of states has a broad maximum about 6×10^{19} cm$^{-3} \cdot$ eV^{-1} at 1.15 eV, after which it rapidly decays toward the middle of the gap to 10^{16} cm$^{-3} \cdot$ eV^{-1} (Ref. 17). The concentration mentioned last was confirmed in many previous papers.

3. OPTICAL PROPERTIES

3.1. Photoinduced absorption on the basis of electron processes

As was mentioned above, disorder in noncrystalline solids causes a quasicontinuous distribution of localized states in the band gap. While the ChG samples are excited by light with energy of $h\nu > E_g$, nonequilibrium carriers appearing in the free bands are very quickly captured by the localized states and participate in the photoinduced absorption at the energies $E < E_g$ (Fig. 2).

As was approved by many experiments, the characteristic time of the photoinduced processes can be in a wide range of values from $\sim 10^{-12}$ to 10^3 s.

The long-lived photoinduced processes are connected with the change of the physicochemical properties of the ChG and are called as photostructural transformations in scientific literature. As a rule, the photostructural transformations are observed in these glass films and they are accompanied by a shift of the absorption edge to the lower energy, by a decrease in the steepness of the edge and, by a change of the observed dynamic reversible change of the optical parameters.[8]

The use of fiber samples rather than thin film or bulk samples enabled us to better observe the small changes in the mid-gap optical absorption at low intensity of exciting light because of the longer optical path of probing light in the fiber.
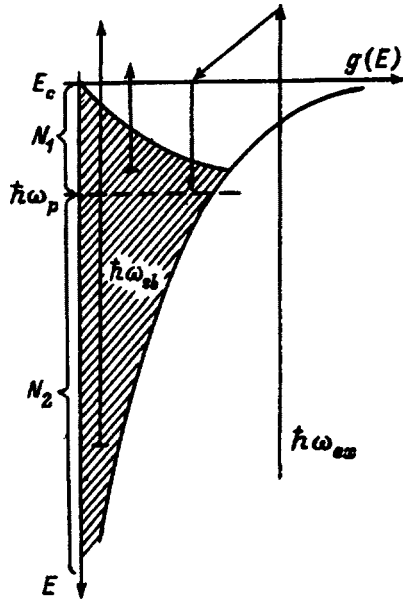
FIG. 2. The steady-state excess carrier distribution in the exponential tail of the localized states.

The probing light with photon energy $h\nu < E_g$ from the mid-gap energy range was launched into the input face of the fiber. At the output of the fiber we measured the intensity of probing light transmitted through the fiber. When illuminating the fiber lateral surface with continous bandgap light, the intensity of probing light at the output of the fiber decreases from its initial value (in the dark) I_0 to a new one I. The photoinduced absorption coefficient $\Delta\alpha$ is determined as follows: $\Delta\alpha = L^{-1} \ln(I_0/I)$, where L is the length of the illuminated segment of the fiber. In should be noted that the intensity of the probing light in the PA measurements was chosen to be so weak that it did not cause any significant change in the PA coefficient.

The main feature of the PA in our experiments is a full restoration of the minimal optical transmittance after the cessation of illumination. The restoration rate depends on the illumination conditions and the glass composition. The spectral distribution of the PA coefficient measured in the energy range of probing light $0.6-1.9$ eV is presented in Fig. 3.
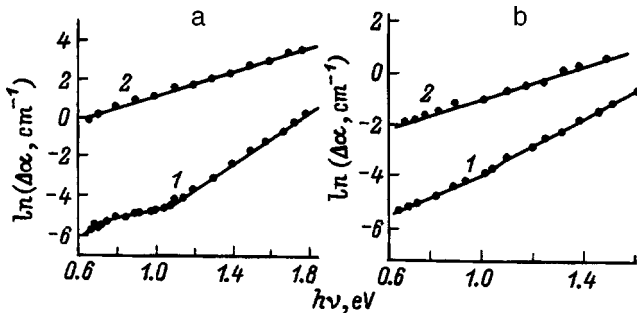

FIG. 3. Spectral distribution of PA steady-state coefficient $\Delta\alpha$ in As_2S_3 (a) and As–S–Se (b) fibers after irradiation with Ar-laser light ($\lambda_{exc} = 0.46 - 052\ \mu m$). The intensity of exciting light $P_{exc} = 10$ mW/cm^2, 1 — 300 K, 2 — 77 K.
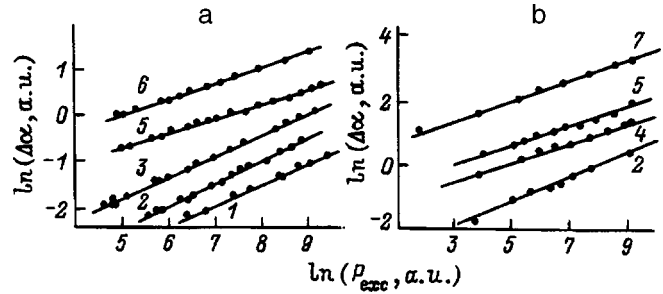

FIG. 4. Intensity dependence of the PA steady-state coefficient in As_2S_3 (a) and As–S–Se (b) fibers at room temperature for various probing light photon energies eV: 1 — 0.7, 2 — 0.8, 3 — 0.95, 4 — 0.98, 5 — 1.08, 6 — 1.2, 7 — 1.3. The wavelength of exciting light $\lambda_{exc} = 0.35 - 0.75\ \mu m$.

We note that the character of the $\Delta\alpha(h\nu)$ dependence is exponential for a rather large energy range. Illumination of the fiber at a lower temperature (77 K) leads to a significant increase of PA with respect to room-temperature illumination.[18]

The intensity dependence of the PA coefficient exhibits a power-law behavior, $\Delta\alpha \sim P_{exc}^n$, when the intensity of the exciting light (P_{exc}) is varied by about four orders of magnitude ($10^{-6} - 10^{-2}$ W/cm^2) (Fig. 4). The value of n changes with probing light photon energy in the range $0.3 - 0.5$.

Experimental results can be interpreted in terms of the model with carrier multiple trapping in localized states (Fig. 2), distributed continuously in the gap.[18] Illumination of the fiber with bandgap light leads to excitation of non-bonding electron states and injection of excess carriers into the conduction band. Shortly after excitation the electrons are captured by the tail states proportionally to their density, since the capture coefficient is assumed to be the same for different values of the trap energy E. The appearance of excess carriers in the localized states in the gap leads to an additional absorption of probing light in a wide energy range, $h\nu < E_g$.

The fact that the dependence of photoinduced absorption has a power law character following the square-root function confirms that carriers excited in the process of photoabsorption, as well as carriers participating in photoconductivity, recombine according to the bimolecular mechanism. As was shown in Ref. 19, this can be used for determining the magnitude of the bimolecular coefficient from photoinduced absorption data and to calculate on this basis the magnitude of the drift mobility. This is very important in the case of highly resistive semiconductors such as As_2S_3 and As_2Se_3 glasses.

3.2. Photoinduced absorption on the basis of phase change

Some challogenides have two or more distinct atomic structural states characterized by different amounts of disorder.[20] An energy barrier, as suggested in Ref. 20 separates the structural states, thereby providing the temporal stability required by a memory device. The change in the atomic configuration can be realized by exposure to a laser beam, electron beam or electrical field. Incidentally, a laser

beam can be used not only for recording but also for erasing and rewriting processes, each of which occurring at different levels of intensity of the beam. Selecting the compositions of the ChG, it is possible to produce transformation between amorphous and crystalline structural states. An example of such materials are materials from the pseudobinary system[20] GeTe and Sb_2Te_3. The phase-change materials were successfully used for optical memory disks with 650-Mbyte capacity and the next product to be introduced will be 2.6-Gbyte DVD–RAM disk.[20]

Studying the process of Ag-migration in Ag–As(Ge)–S(Se) glasses, Yoshida and Tanaka[21] proposed the mechanism of photo- and electron-induced chemical modifications. As was shown, light illumination and electron beams accelerated at low voltages can induce Ag-gathering effects. The mechanism is assumed to be caused by interval electric fields built up by photoexcited carriers and by electrons.[22]

Studying the physico-mechanical and structural modifications induced by UV — light in $Ge_xAs_{40-x}S_{60}$ amorphous films, Popescu et al.[23] observed that irradiation is accompanied by a significant release of sulfur, which leads to a giant film contraction.

FIG. 5. The kinetics of diffraction efficiency of the microholograms recorded in the $Al–In_2S_3/As_2Se_3–Al$ heterostructure when a series of negative and positive (''−'' and ''+'' in the figure) voltage pulses is applied.

ementary holograms recorded on the $Me–In_2S_3/As_2Se_3–Al$ when negative and positive voltage impulses are applied is shown in Fig. 5.

3.3. Electrically controlled photoinduced absorption

The change in the surface relief by means of mechanical residual deformations under the simultaneous action of illumination and applied electric field was established Refs. 24–26 by using the thin-film structure Me–ChG–Me. The nature of the electrostimulated and photoinduced surface microdeformations can be explained by a rapid increase in the density of the photocurrent in the illuminated portions of the sample and by a strong heating of the GhG up to a T_g temperature. As a result, the viscous forces in the illuminated portions are relaxed under the action of the electrostatic forces of the conductor, causing the optical properties of the structure to change. We therefore obtain the effect of optical image recording, which is manifested through changing of transmittance and reflectance. It is important to note that when an interference picture is projected on the surface of a sample, the deformation grains lie strongly along the illuminated bands, making it possible to record holographic information. When the illumination of the structure rapidly develops deformations, it is necessary to apply an electric field with less intensity. In this case, the value of the recording light intensity is a photographic characteristic of the recording structure. It was shown that the recording process strongly correlates with the photoconductivity, its kinetics, and the dependence of spectrum or light intensity. This allowed the authors[26] to utilize the heterostructures $Me–In_2S_3(In_2Se_3)/As_2Se_3–Al$ as a recording medium which had better photoconductivity parameters and consequently better photographic characteristics. On the basis of the phenomenon and heterostructures mentioned above, the new photographic process and new meterials were proposed for its realization. The diffraction efficiency growth of the el-
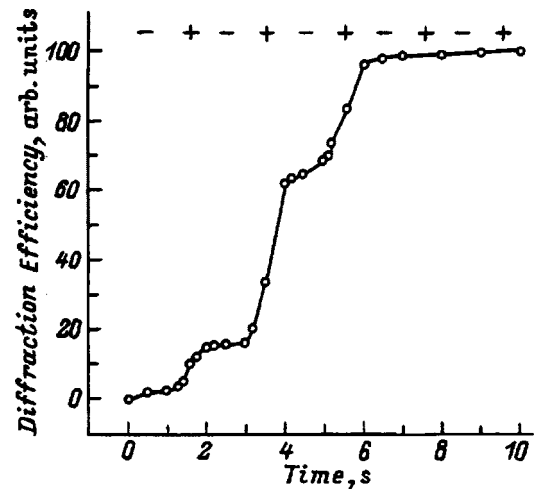
3.4. Optical hysteresis and nonlinear absorption laser pulses in ChG

The interest in the study of nonlinear propagation peculiarities of the laser radiation in noncrystalline semiconductors is determined not only by the new fundamental physical mechanisms in these materials, which can appear in the strong laser pumping fields, but also by a wide spectrum of possible applications in the optoelectronic devices and photonic switching. The promising effects are the optical bistability and optical hysteresis, on the basis of which it is possible to build fast-acting, all-optical switching and logical elements (see, for example, Ref. 8 and the bibliography cited there).

Thin-film samples of chalcogenide glass semiconductors As–S, As–Se, Ge–Se, As–S–Ge, and others (0.2 to 5.0 μm thickness) have been obtained by the vacuum thermal sputtering method. It was shown that when the input light pulse (with $h\nu \geq E_g$) intensity is relatively low, the transmission of the thin ChG films decreases according to the usual exponential law with the corresponding linear light absorption coefficient for the given wavelength. However, on increasing the incident light intensity in the ragne of some threshold values (I_0) leads to a nonlinear character of the light transmission by the ChG films.[11] The characteristic value of the threshold light intensity depends on the ChG film composition, excitation wavelength, temperature, and laser pulse duration.

As a result of nonlinear light absorption, a change in the time profile of the laser pulses is observed. This leads to a hysteresis-line dependence of the output light intensity of the corresponding value of the input intensity.

Nonlinear absorption in chalcogenide glasses was observed even in the femtosecond range, which is due to either intraband or interband transitions.[27]
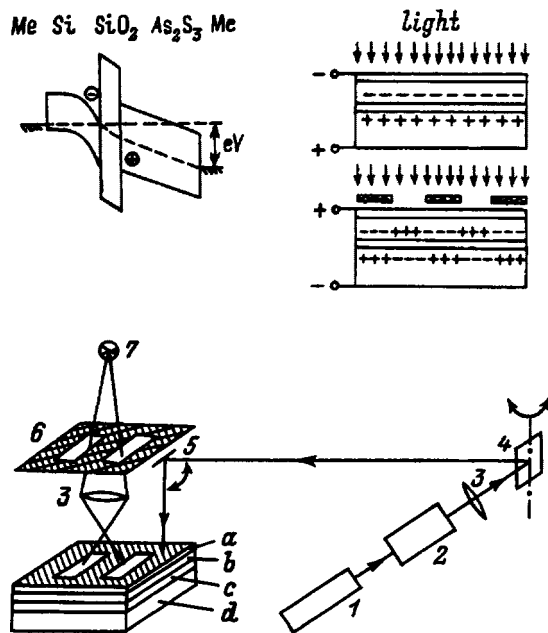
FIG. 6. The schematic energy-band diagram of Me–ChDS structure during the positive charge writing process and the scheme of writing and readout of image. *1* — He–Ne-laser (0.6328 μm); *2* — modulator, *3* — condensers; *4, 5* — galvanometer mirrors; *6* — mask (object); *7* — illumination source; *8* — Me–ChDS structure: *a* — semitransparent Al electrode, *b* —As$_2$S$_3$ layer, *c* — SiO$_2$ layer, *d* — Si.

4. DEVICES BASED ON ChG

The function of many devices is based on ChG, which can change their electrical and optical parameters by applying an electrical field, by exposing them to light, to an electron beam, x-irradiation, etc. At the same they manifest resistance to nuclear radiation. In addition, that, ChG could be obtained using very simple technologies and in many cases (but not in all cases) they do not need very high purity. It makes it possible to produce industrial electrical switches, xerographic and thermoplastic media, photoresistant and holographic media, optical filters, optical fibers, optical sensors, thin-film waveguides, nonlinear elements, and other devices.

In the 1960s, considerable attention was given to threshold switching elements, which were able under voltage pulsed to pass from a state with a very high resistivity in a state with low resistivity.[20]

The industrial technology was developed by R.S. Ovshinschy, who called the optimized element ovonic threshold switching.[20]

The switching process is very short, less than 10 nanoseconds.

The ChG thin films were very successfully utilized as the target for vidicon image tube (for TV cameras).

Another successful application was the use of ChG thin films in photocopying electrophotography machines. Thin films of Se, As$_2$Se$_3$, and other materials store the charge distribution produced by the image projected onto it. The image presented by the charge distribution is transferred to the paper using electrostatic method.[8]

Observed photoinduced phenomena in ChG allowed us to use these materials as recording media for registration of

the optical information using ChG thin-film heterostructures, phototermoplastic structures, thin waveguides, and fibers.

The Me-chalcogenide glassy semiconductor–dielectric–semiconductor ChDS (Me–As$_2$S$_3$–SiO$_2$–Si) structure allows writing and readout processes of the optical images with high resolution.[8] The structure makes the positive and negative images possible. The device works in regimes of small-signal accumulation and real time. The space functional separation of the recording and readout allows carrying out undestroyed repetition readout of the image and other operations (Fig. 6).

Photoinduced phenomena in chalcogenide glass fibers were utilized in order to propose a novel type of variable fiber-optic attenuator.[8] It can be used in visible and near-infrared range of the spectrum for continuous change of light intensity in fiber-optic circuits. If the lateral surface of chalcogenide glass fiber is illuminated by light with photoenergy near the glass bandgap, a strong decrease of the fiber-attenuating light at the output and of the fiber occurs. This process changes the optical signal from its initial value I_0 (in the dark) to a new one:

$$I = I_0 \exp(\Delta \alpha L),$$

where L is the length of the illuminated segment of the fiber, and $\Delta \alpha$ is the photoabsorption. The proposed fiber-optic attenuator provides the attenuation in the range $0-20$ dB in the 0.8 to 1.8-μm wavelength range.

Chalcogenide glass thin films are promising materials for the integrated optic devices such as lenses, gratings, optical filters, multiplexor and demultiplexor optical scanners, printer heads, multiple-output logical elements, and other devices.[8]

[1] N. Mott and E. A. Devis, *Electronic Processes in Noncrystalline Materials* (Mir, Moscow, 1974).
[2] A. I. Gubanov, *Quantumelectron Theory of Amorphous Semiconductors* (Nauka, Moscow–Leningrad, 1963).
[3] M. H. Cohen, H. Fritzsche, and S. R. Ovshinsky, Phys. Rev. Lett. **22**, 1965 (1969).
[4] B. T. Kolomiets, in *Proceedings of the IX International Conference on Physics of Semiconductors* (Nauka, Moscow–Leningrad, 1969), p. 1335.
[5] J. M. Marshall and A. E. Owen, Philos. Mag. **24**, 1281 (1971).
[6] V. L. Bonch-Bruevich, JETP **61**, 1168 (1971).
[7] R. A. Street and N. F. Mott, Phys. Rev. Lett. **35**, 1293 (1975).
[8] M. Popescu, A. Andriesh, V. Chimas, M. Iovu, S. Sutov, and D. Tiuleanu, *Physics of Chalcogenide Glasses* (Stiinta, Chisinau, 1996).
[9] J. Orenstein and M. Kastner, Phys. Rev. Lett. **46**, 1421 (1981).
[10] D. Monroe and M. Kastner, Phys. Rev. B **33**, 8881 (1986).
[11] G. J. Adriaenssens, Philos. Mag. B **62**, 79 (1990).
[12] S. P. Depinna, B. C. Covenett, and W. E. Lamb, Philos. Mag. B **47**, 99 (1983).
[13] A. M. Andriesh, M. S. Iovu, D. I. Tsiuleanu, and S. D. Shutov, *Vitreous Arsenicum Sulphide and its Alloys* (Chisinau, Stiinta, 1981).
[14] M. Abkowitz and J. M. Marcovies, Philos. Mag. B **49**, L31 (1984).
[15] A. M. Andriesh, S. A. Malkov, and V. I. Verlan, Semiconductors **29**, 1319 (1995).
[16] A. M. Andriesh, S. A. Malkov, V. I. Verlan, and N. A. Gumeniuk, Phys. Status Solidi A K39 (1991).
[17] S. D. Shutov and A. A. Simashkevich, J. Non-Cryst. Solids **176**, 253 (1994).
[18] A. M. Andriesh, I. P. Culeac, and V. M. Loghin, Pure Appl. Opt. **1**, 91 (1992).

[19] A. M. Andriesh, I. P. Culeac, P. J. S. Ewen, and A. E. Owen, in *Proceedings of the International Conference of Semiconductors* (Sinaia, 1997) p. 45.

[20] S. R. Ovshinsky in *Proceedings of the International Conference of Semiconductors* (Sinaia, 1997), p. 33.

[21] N. Yoshida and K. Tanaka, J. Non-Cryst. Solids **210**, 119 (1997).

[22] N. Yoshida, M. Itoh, and K. Tanaka, J. Non-Cryst. Solids **198**, 749 (1996).

[23] M. Popescu, F. Sava, A. Lorinezi, E. Scordeva, P. Y. Koch, and H. Bra-daczek, in *Proceedings of the International Conference of Semiconductors* (Sinaia, 1997), p. 467.

[24] A. M. Andriesh, S. D. Sutov, D. I. Tsiuleanu, *Sposob zapisi informatii na*

besserebr. nositelei (Kiev, 1976), Vol. 7, p. 55.

[25] A. M. Ahdriesh *et al.*, *Stecloobraznie poluprovodniki v photoelectriceschix sistemah zapisi opticescoi informatsii* (Shtiinta, Chsinau, 1984), p. 53.

[26] A. M. Andriesh, M. S. Iovu, V. V. Bivol, and E. G. Khanchevskaya, J. Opt. Memory and Neuaral Networks **4**, 69 (1995).

[27] E. Fazio, D. Hulin, V. Chumash, F. Michelotti, A. M. Andriesh, and M. Bertolotti, J. Non-Cryst. Solids **168**, 213 (1994).

Copper-induced changes in the properties of arsenic chalcogenides

N. Bollé, P. Hertogen, and G. J. Adriaenssens

K.U. Leuven, Laboratorium voor Halfgeleiderfysica, Celestijnenlaan 200D, B3001 Heverlee, Belgium

C. Sénémaud and A. Gheorghiu-de La Rocque

Université Pierre et Marie Curie, Laboratoire de Chimie-Physique, UMR CNRS 7614, 75231 Paris, cedex 05, France

The influence of the presence of Cu in the amount between 1% and 6% in arsenic chalcogenide glasses is examined through a study of the electronic energy levels by means of x-ray photoelectron and x-ray emission spectroscopy, through an investigation of the low-energy tunneling systems by means of phonon echoes at 0.37 K, and through an examination of the photodarkening and the photoinduced dichroism caused by polarized Ar^+ laser irradiation. Possible links between the various effects are examined. The Cu atoms become an integral part of the amorphous lattice structure and strongly influence the photodarkening, but they do not have a significant effect on the tunneling systems or the dichroism. It is concluded that the tunneling levels and the dichroism involve only local configurations, while the photodarkening involves larger-scale areas of the lattice. © *1998 American Institute of Physics.*
[S1063-7826(98)01408-2]

1. INTRODUCTION

Almost from the beginning of experimental studies of vitreous chalcogenide semiconductors in the laboratory of Professor Kolomiets, the effects of adding nonmetallic and metallic elements to the glasses were investigated. This early interest was undoubtedly generated by the desire to find appropriate dopants for the amorphous semiconductors, and it explains why most attention was given to the changes in electrical properties of the samples. A review of these results can be found in Ref. 1. Subsequently, the interest in the chalcogenides shifted to their optical properties, especially their ability to sustain reversible photoinduced changes to these properties.[2] Much attention was given to the photoinduced shifts of the optical absorption edge of the glasses,[3] the so-called photodarkening and photobleaching, and later to the optical anisotropies that are induced by polarized light beams.[4] These two types of effects became known as the scalar and vector phenomena. These photoinduced changes in the optical parameters were found to be the result of structural changes in the amorphous lattice[5] which can even result in macroscopic deformations of the chalcogenide materials.[6] A wide range of models has already been proposed to account for the effects, but most deal with part of the observations only. Although some models attempt to link scalar and vectoral effects, not a single one of those models has so far been able to show wide-spread agreement. Recent review articles of experimental observations and of the proposed models were published by Shimakawa, Kolobov, and Elliot[7] and by Tanaka.[8] Examination of those reviews clearly shows that more experimental data will be required to make some progress in resolving the physical mechanisms underlying the photoinduced structural changes.

In this paper we explore the influence on the electronic structure and the photoinduced effects of introducing small concentrations of Cu into the arsenic chalcogenide glasses. It is known that the presence of 1% Cu in bulk As_2S_3 or 5% Cu in bulk As_2Se_3 eliminates the photodarkening that is normally observed in those materials.[9] Such Cu-modified compounds should therefore be good candidates for studying the structure of the glasses, as revealed by x-ray-induced photoelectron spectroscopy (XPS) and x-ray emission spectroscopy (XES), in relation to the appearance or disappearance of the photodarkening. The same samples can also be used to test the links that have been suggested[10] between, on the one hand, the centers which are responsible for the photodarkening and, on the other hand, the soft potential sites of the lattice which give rise to the low-temperature anomalies in the phonon spectrum of amorphous materials. The latter can be identified through the low-energy tunneling states (TS), which can be detected in a backward-wave phonon echo (BWE) experiment at 0.4 K. Such BWEs from Cu-free and Cu-containing samples will be compared. Finally, we will also examine the relationship between the scalar and the vectoral photoinduced effects in the light of the influence of Cu on the photodarkening.

2. EXPERIMENTAL PROCEDURE

Bulk samples of Cu-modified As_2S_3 or As_2Se_3 were prepared by the standard procedure of melt quenching after alloying of the pure compounds with copper at 900 °C for 20 h in a rocking furnace. A few samples prepared in the group of Prof. P.C. Taylor at the University of Utah were used for

comparison; no differences were observed. Films for optical measurements were prepared for some compositions by thermal evaporation of the ground compound.

2.1. X-ray photoelectron and x-ray emission spectroscopies

XPS and XES are complementary techniques for obtaining information on the electronic structure of the amorphous compounds.[11] From XPS we determine the energy levels of the core electrons and the global energy distribution of the valence band states, while XES provides information concerning the bonding arrangements of valence electrons near a particular atomic site.

For this study we have analyzed the XPS specta of the S $2p$ and As $3p,3d$ core levels, and we obtained the total valence band states (VB) modulated by the photoionization cross sections. The spectra were excited by means of a standard Mg $K\alpha$ x-ray source with $h\nu = 1253.6$ eV. In our experiment, the total instrumental broadening is estimated to be 0.6 eV for core levels and 1.0 eV for VB. The core level spectra are scanned in 0.1-eV steps and the XPS VB data in 0.2-eV steps. In the case of nonconductive samples, such as the arsenic chalcogenides, a charging effect of the sample can be observed in the data. In order to take this effect into account, we calibrated the binding energy scale by refering to the C $1s$ line observed from hydrocarbonated species, which are always present at the surface of the sample. The C $1s$ line is set at 285.0 eV. The interpretation of the core level lines is based on a reconstruction of each spectral distribution into Voigt functions. In the case of the valence band, the spectra are superimposed against the background due to the inelastic electron scattering; since no correction for this effect was made, the spectra contain a nonconstant background. We should mention that the sample thickness which contributes to the XPS spectra is limited by the mean free path of the electrons and is estimated to be $1-3$ nm in our cases.

The XES measurements concern S K_β band, which corresponds to the electronic transition $3p \Rightarrow 1s$. They are analyzed by means of a cylindrical bent-crystal vacuum spectrometer (radius 250 mm). The monochromator is a $10\bar{1}1$ quartz crystal ($2d = 0.66855$ nm) used in first order reflection. The spectra are excited with a 5-kV, 5-mA electron beam, and the detector is a proportional Ar/CH$_4$ counter. The energy resolution of the instrument is estimated to be[12] 1.0 eV. The x-ray spectra are measured as a function of the photon energy corresponding to the transition $E(\text{S } 1s) - E(\text{S } 3p)$. On this energy scale, the Fermi level position corresponds to the binding energy $E(\text{S } 1s)$; it is obtained by combining the XPS data for the S $2p_{3/2}$ binding energy and the XES determination of the S $K_{\alpha_{1,2}}$ ($2p_{1/2,3/2} - 1s$) x-ray transition energy. Then $E_F(\text{S } 1s) = E(\text{S } K_{\alpha_1}) + E(\text{S } 2p_{3/2})$. Consequently, the XPS and XES spectra can be obtained on a common energy scale with the Fermi level as the reference point.

2.2. Backward-wave echoes

In a backward-wave echo experiment two microwave pulses, separated by a time τ, are applied to the sample in a re-entrant cavity. Via the surface-excitation method a forward-propagating hypersonic wave is generated by the first pulse. (A coating of ZnO powder suspended in glyptol varnish is used in our experiments as a piezoelectric transducer.) A reversal of the wave vector ($\mathbf{k} \rightarrow -\mathbf{k}$) is induced through the interaction between the hypersonic wave and the microwave electric field of the second pulse at some nonlinear entities. At the time 2τ, this backward propagating wave reaches the transducer again and gives rise to an echo.

In chalcogenides the nonlinear coupling between the electric field and the acoustic wave is due to the tunneling systems present in these materials. Indeed, later studies have indicated that TS act as such nonlinearities.[13] Experimentally, the intensity of the echo will increase with increasing intensity, I_a, of the acoustic wave until the TS become saturated; i.e., the populations of the tunneling levels have been equalized at the critical asoustic intensity, I_{ca}. Theoretical considerations[14] then allow us to distinguish two regions in the behavior of the echo intensity I_E as a function of the incident power P_{in}, depending on the value of $Y_a = I_a/I_{ca}$:

1. If $Y_a \ll 1$ (TS are unsaturated), then $I_E \sim P_{in}^3$.
2. If $Y_a \gg 1$ (TS are saturated), then I_E is independent of the incident power; I_E shows a plateau, where the saturation value P_{ex} is a measure of the number of tunneling states in the sample.

We have measured the input power dependence of the backward-wave echo power in pure and Cu-modified As$_2$S$_3$ and As$_2$Se$_3$ compounds. The bulk samples were prepared from melt-quenched glasses, out of which cylindrical samples of 3-mm diameter by 10-mm length were drilled to fit the cylindrical microwave cavity. Our measurements were carried out at a frequency of 9.3 GHz and at a constant temperature of 0.37 K. Since the tunneling systems envisioned here are indeed those of the soft-potential model (SPM), which has been deduced from the low-temperature anomalies that are characteristic of all glasses,[15] we have to study them below 1 K to obtain sufficient sensitivity.

2.3. Photodarkening and photoinduced dichroism

The 514.5-nm beam of a polarized Ar$^+$-laser was used for measuring the photoinduced optical effects. Relative changes in optical transmission caused by the illumination were recorded to compare the degree of photodarkening in both unmodified and Cu-containing samples. The values for the linear photoinduced dichroism—this is the difference in optical absorption coefficients $\alpha_\perp - \alpha_\parallel$, where $\alpha_{\perp,\parallel}$ are the absorption coefficients in the direction perpendicular to and parallel to the direction of the polarization of the inducing beam—were obtained by measuring transmitted light intensities $I_\perp$ and $I_\parallel$ by standard lock-in detection techniques when the polarization of a probe beam is modulated between the parallel and orthogonal directions at a frequency of 1 kHz by means of an electrooptic modulator and then making use of the relation that was derived in Ref. 16:

$$\alpha_\perp - \alpha_\| = \frac{I_\| - I_\perp}{h(I_\| + I_\perp)/2}, \qquad (1)$$

where h is the thickness of the sample.

3. RESULTS

The addition of Cu to the arsenic chalcogenides modified some characteristics while leaving others unchanged. We will first summarize the results, technique by technique, before attempting an encompassing interpretation.

3.1. Electronic energy levels

The core levels S $2p$, As $3p$ and As $3d$ were examined by XPS for a pure As_2S_3 sample and for one which contained 6% of Cu. We observed virtually no shift for the As lines, with $3p_{1/2}$ at 146.2 eV, $3p_{3/2}$ at 141.2 eV, and $3d_{5/2}$ at 41.7 eV. For S $2p_{1/2}$ (163.6 eV) and S $2p_{3/2}$ (162.5 eV), a broadening of the line is observed when Cu is added. This broadening is asymmetric and occurs toward the lower binding energies (BE). It reveals a shift of ~ 0.2 eV toward low BE in the presence of Cu. Figure 1 shows the S $2p$ spectra and their decomposition into the spin-orbit splitted $2p_{1/2}$ and $2p_{3/2}$ lines.

The XPS valence band spectra observed for As_2S_3 and As_2S_3(Cu) are shown in Fig. 2. Both spectra exhibit a wide peak between E_F and about 8 eV, followed by a broad band from ~ 8 to ~ 17 eV. It is known[17] that the structure which is seen in the first peak of As_2S_3 consists of a leading feature at about 3 eV, which is associated with the lone pair p electrons of the chalcogen atoms, and a second contribution centered around 6 eV, which is related to the bonding p states. A strong minimum separates the p states of the first peak from the deeper-lying broad band, which consists of s states and also shows some structure. In As_2S_3(Cu), the width of the p band is approximately the same as in As_2S_3 but strong modifications occur at the top of the valence band, with the 3-eV peak becoming more prominent. Differences in the s bands of As_2S_3 and As_2S_3(Cu) are less pronounced.

The S $3p$ valence band states were also examined through the XES sulfur K_β spectrum. As explained in the previous section, these x-ray spectra were obtained in the BE scale with E_F as the origin. The results for the two types of samples are shown in Fig. 3. The S K_β spectrum exhibits an asymmetric distribution with the steep edge toward the low BE. The most prominent feature is again due to the lone pair electrons, while the adjoining shoulder on the high BE side marks the position of the bonding sulfur p states. These S K_β spectra correspond to earlier ones reported in Ref. 18 for As_2S_3. For our two compositions the low BE edge is observed in the same energy position and the slope of the edge is the same. However, a significant broadening is observed at about 5 eV from E_F in the As_2S_3(Cu) sample as compared to As_2S_3.

B. Tunneling states

We have studied the BWEs from As_2Se_3 and $Cu_5(As_2Se_3)_{95}$ glasses, as well as for As_2S_3, $Cu_1(As_2S_3)_{99}$, and $Cu_{1.5}(As_2S_3)_{98.5}$ glasses. Figure 4 and Fig. 5 show the
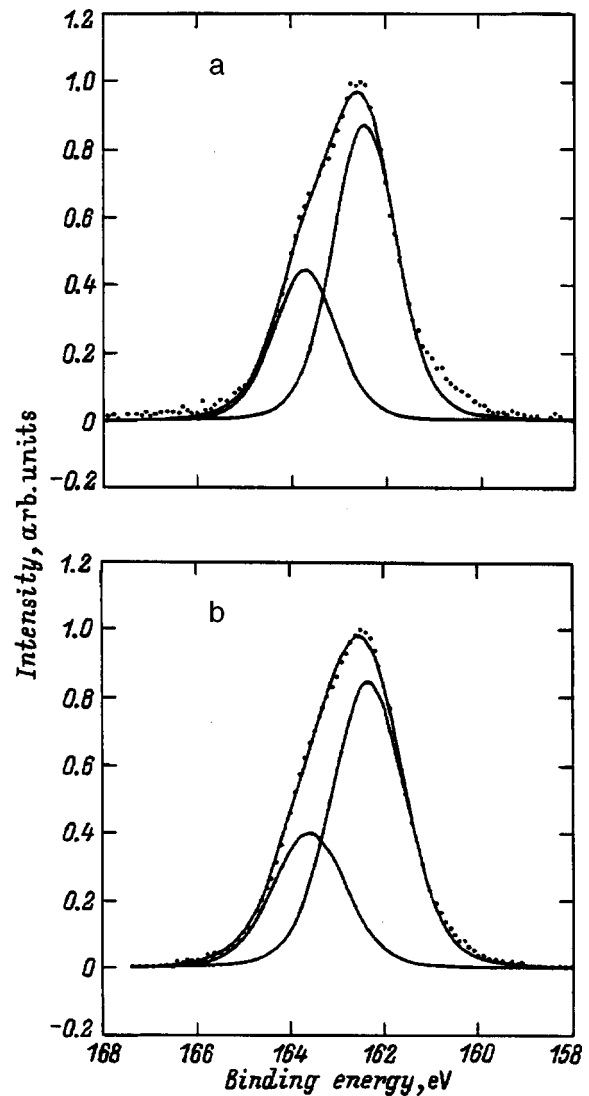

FIG. 1. XPS binding energy spectrum of S $2p$ core electrons in (a) As_2S_3 and (b) $Cu_6(As_2S_3)_{94}$, together with a decomposition into their $2p_{1/2}$ and $2p_{3/2}$ components.

results of the measurements of the backward-wave echo power as a function of input power for the selenide and sulfide glasses, respectively, The lowest echo powers given in both figures represent the minimum power that could be detected, and the other values are given relative to that one.

While the data sets are obviously not identical, no significant difference in the behavior of the echo power as a function of input power can be seen between the Cu-modified and the unmodified chalcogenides. Specifically, the saturation, which is a signature of the presence of TS (and hence soft potentials), is equally prominent in all cases. However, the magnitude of the backward-wave echo depends on experimental factors such as the bonding of the transducer and the quality factor of the cavity. Since these are different for the different samples, the saturation value of the echo power P_{ex}, and the number of TS, unfortunately cannot be compared for the different samples. In fact, increasing Cu content increases the conductivity of the samples, thereby decreasing the Q value of the cavity to the
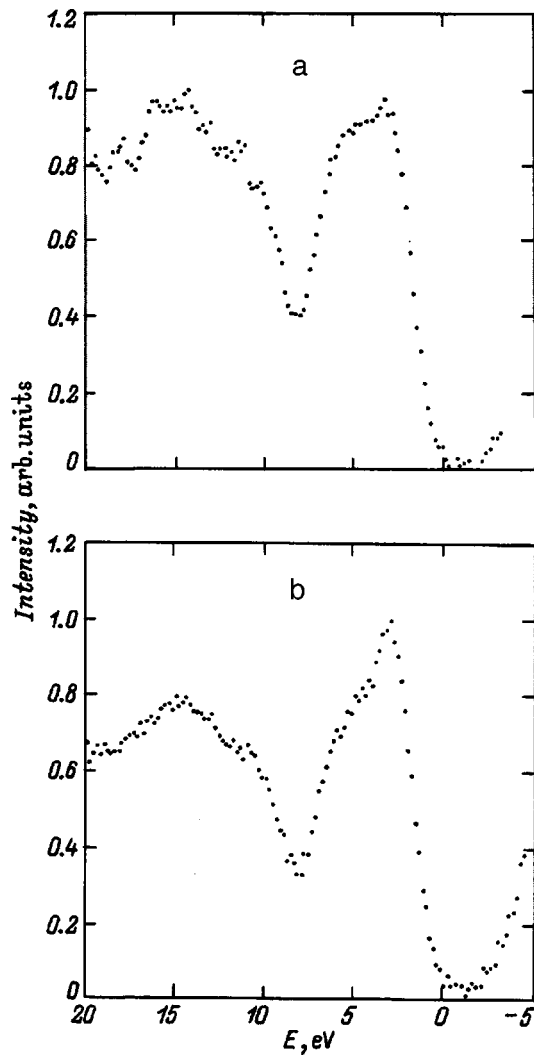
FIG. 2. XPS valence band spectra from (a) As_2S_3 (b) $Cu_6(As_2S_3)_{94}$.

FIG. 3. XES S K_β spectra of the valence bnd S $3p$ electrons in (a) As_2S_3 (b) $Cu_6(As_2S_3)_{94}$.

extent that measurements become impossible. This happens sooner for the sulfur chalcogenides than for the selenium chalcogenides.

C. Photoinduced changes

Thermally evaporated films were used for these measurements. The results reported here originate with a 2-μm-thick film evaporated from pure As_2S_3 and with a 3.8-μm-thick one prepared on the basis of $Cu_4(As_2S_3)_{96}$ glass. Progressive photodarkening under continuous illumination was measured for both films, in contrast with the observations on bulk glasses[9] where the 4% Cu would have prevented the photodarkening. It has already been reported, however, that in the corresponding evaporated films the photodarkening is not eliminated.[19] We, nevertheless, observed a clear difference between the two materials: while in the As : S films the measured transmission drops below 10% of its initial value, the drop is only to ~30% in the As : S : Cu films. These numbers slightly decrease with increasing light intensity. The photodarkening kinetics speed up in similar fashion for both types of films with more intense illumination.

The photoinduced dichroism was also measured for the above films, and here no significant differences could be observed. We found that the total reversible variation in the dichroism, when the polarization direction of the inducing beam is changed between orthogonal directions, does not

FIG. 4. The BWE power as a function of the microwave power for the selenide glasses at 0.37 K: As_2Se_3 (*1*) and $Cu_5(As_2Se_3)_{95}$ (*2*). 0 dB corresponds to a peak power of 1.2 W.

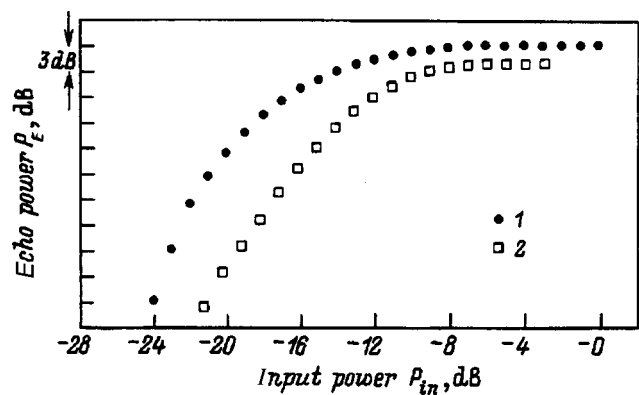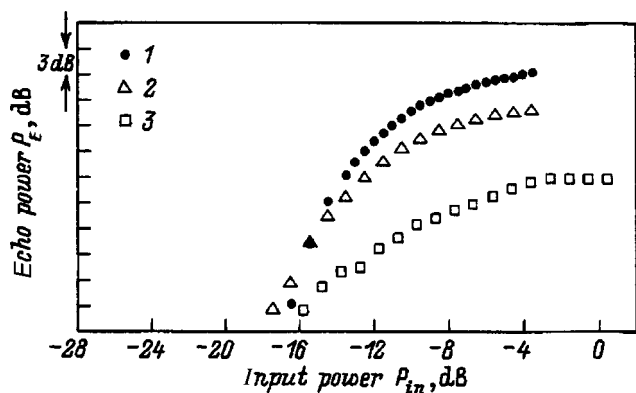FIG. 5. The BWE power as a function of the microwave power for the sulfide glasses at 0.37 K: As_2S_3 (*1*), $Cu_1(As_2S_3)_{99}$ (*2*) and $Cu_{1.5}(As_2S_3)_{98.5}$ (*3*). 0 dB corresponds to a peak power of 1.2 W.

change by more than 10% among the various As : S and As : S : Cu films, in contrast with the photodarkening, where the changes are stronger by a factor of 3 in films without Cu with respect to films which contain Cu.

4. DISCUSSION

Some of the questions that were raised in the introduction were answered directly by the results in the previous section. It is clear, for example, that photodarkening and photoinduced anisotropy do not have a common origin; the former is strongly influenced by the presence of Cu, the latter is not influenced in a significant way. Also the proposed link between centers, which are responsible for the photostructural changes in the chalcogenide glasses, and the soft atomic potentials, which are implicated in the low-temperature anomalies, can be ruled out. Indeed, the results for the backward wave echo measurements confirm the presence of an essentially unchanged number of tunneling systems in a region where the photodarkening has disappeared from the bulk glasses. In other words, while the presence of Cu inhibits the photodarkening, it leaves other characteristic properties of the chalcogenide glasses such as the photoinduced anisotropy or the soft-potential sites unimpaired.

Our results from XPS, XES, and BWE show that the Cu atoms become an integral part of the amorphous lattice to form a real alloy. Indeed comparing the S K_β XES spectra of Fig. 3 with a corresponding one from CuS (Ref. 20), we see that the added intensity near 6 eV in the As : S : Cu sample agrees with the position of the main S $3p$ density in the CuS bond. The changes in the distribution of p states in the valence band XPS spectra primarily result in a sharper definition of the lone-pair component, as is normally seen in chalcogen-rich compounds. This need not be interpreted as evidence for a somewhat increased density of S–S bonds (as would occur when the Cu mostly bonds to As), but probably just reflects the change in the average bonding angle at the S when a Cu atom substitutes for As. From early EXAFS studies[21] we know that Cu is fourfold coordinated in the arsenic chalcogenide glasses, while a normal As site is of course only threefold coordinated.

When we take a closer look now at the BWE results, we notice that there is a decrease of the slope at low input powers for the Cu containing samples with respect to the standard chalcogenides. In a previous study[22] we found a correlation between these different slopes and the mean coordination number of the lattice. The third power (P_{in}^3) predicted by the theory holds for the compositions with mean coordination $\langle r\rangle \leqslant 2.4$. According to Thorpe,[23] these networks are all floppy. The rigid samples, those with a higher value of $\langle r\rangle$, are found to have a lower slope. As a result, the input power dependence of the echo power deviates from the theory. In addition, Thorpe predicts that the number of TS should be smaller in a rigid glass that in a floppy glass.

The BWE results presented here and the lower slope of the Cu-containing samples thus agree with a forfold coordination of the Cu atoms, which results in a higher average lattice coordination. The effect on the average coordination of group I metals such as Cu is described by a general model proposed by Liu and Taylor[24] for a wide range of semiconductor glasses, including the As : Se and As : S systems. Their model for the bonding in glasses is based on analogies with bonding in minerals of the Cu : As : S system. In these minerals Cu is fourfold coordinated, As threefold coordinated for low enough Cu concentration ($x < 31.6\%$), and S is either twofold or fourfold coordinated. Further on, only Cu–S and As–S bonds are present. Liu and Taylor assume that the same rules hold for the Cu : As : S and Cu : As : Se glasses. They calculated the coordination number for glasses in the systems $Cu_x(As_{0.4}Se(S)_{0.6})_{1-x}$ and the following relation was found: $\langle r\rangle = 2.4 + 4.6x$. The excellent agreement of the predictions for the average coordination number with x-ray radial distribution date[25] confirms that the local bonding configurations are very well understood. Using this prediciton, the average coordination of our Cu-modified samples will be larger than 2.4, which means that the samples are rigid. This confirms our interpretation for the reduced slope of the echo power as a function of the input power found in these materials. Notice that the decrease of the slope appears at a smaller concentration of Cu atoms for the sulfide than for the selenide glasses. This is not surprising because the same effect is seen for other phenomena such as the photodarkening and the conductivity of these systems.

It is widely assumed that the arsenic chalcogenide glasses still exhibit much of the layered structure of their crystalline phase in the amorphous one. However, fourfold coordinated Cu atoms could easily link adjacent layers and thus modify the characteristics of the glass. Exactly such effect has recently been proposed by Shimakawa *et al.*[26] to explain the role of Cu in the inhibiting of photodarkening, which in their model is related to a relative sliding motion of adjoining lattice planes. Other phenomena, which do not depend on that motion, should then not be affected by the presence of the Cu cross-links. That would be the case for the photoinduced anisotropy, where the intrinsic charged defects of the chalcogenide glasses have been proposed as the active elements,[27] and for the soft potential sites that generate the tunneling systems seen through the low-temperature BWEs.

5. CONCLUSIONS

Our XPS and XES measurements have confirmed that Cu atoms, which are added to the arsenic chalcogenide glasses, become an integral part of the amorphous lattice, and our low-temperature phonon studies show a concomitant increase in the average lattice coordination, in agreement with fourfold Cu coordination. From the fact that Cu levels, which eliminate photodarkening in As_2S_3 or As_2Se_3, leave the vectoral photoinduced anisotropy or the density of low-energy tunneling states intact, we conclude that the photodarkening must be related to the chalcogenide network as a whole, rather than to the specific defect configurations or soft potentials, which are implicated in the anisotropy phenomena or in the low-temperature anomalies.

However, the most obvious conclusion of all the above considerations must undoubtedly be that more than 35 years after the beginning of chalcogenide semiconductor research by Kolomiets and his co-workers, we are still far removed from a comprehensive understanding of these fascinating materials.

[1] B. T. Kolomiets, V. L. Averyanov, V. M. Lyubin, and O. J. Prikhokdo, Sol. Energy Mater. **8**, 1 (1982).

[2] B. T. Kolomiets and V. M. Lyubin, Mater. Res. Bull. **13**, 1343 (1978).

[3] V. L. Averyanov, A. V. Kolobov, B. T. Kolomiets, and V. M. Lyubin, Phys. Status Solidi A **57**, 81 (1980).

[4] V. G. Zhdanov, B. T. Kolomiets, V. M. Lyubin, and V. K. Malinovskii, Phys. Status Solidi A **52**, 621 (1979); V. M. Lyubin and V. K. Tikhomirov, J. Non-Cryst. Solids **144**, 133 (1989).

[5] K. Tanaka, Solid State Commun. **15**, 1521 (1974).

[6] H. Hisakuni and K. Tanaka, Appl. Phys. Lett. **65**, 2925 (1994); P. Krecmer, A. M. Moulin, R. J. Stephenson, T. Rayment, M. E. Welland, and S. R. Elliott, Science **277**, 1799 (1997).

[7] K. Shimakawa, A. Kolobov, and S. R. Elliott, Adv. Phys. **44**, 475 (1995).

[8] K. Tanaka, *Current Opinion in Sol. St. & Mater. Sci.* **1**, 567 (1996).

[9] J. Z. Liu and P. C. Taylor, Phys. Rev. Lett. **59**, 1938 (1987).

[10] M. I. Klinger, Phys. Rep. **165**, 275 (1988); M. Klinger, J. Non-Cryst. Solids **137&138**, 939 (1991).

[11] C. Sénémaud, J. Non-Cryst. Solids **198−200**, 85 (1996).

[12] S. Dupont, A. Gheorghiu, C. Sénémaud, J.-M. Mariot, C. F. Hague, P. E. Lippens, J. Olivier-Fourcade, and J.-C. Jumas, J. Phys.: Condens. Matter **8**, 8421 (1996).

[13] N. Vanreyten and L. Michiels, Phys. Rev. B **37**, 9079 (1988).

[14] L. Michiels and N. Vanreyten, J. Phys. C: Sol. St. Phys., **21**, 4629 (1988).

[15] D. A. Parshin, Phys. Rev. B **49**, 9400 (1994).

[16] V. M. Lyubin and V. K. Tikhomirov, Fiz. Tverd. Tela, **32**, 1838 (1990) [Sov. Phys. Solid State **32**, 1069 (1990)].

[17] S. G. Bishop and N. J. Shevchik, Phys. Rev. B **12**, 1567 (1975).

[18] G. Leonhardt, H. Neumann, A. Kosakov, T. Götze, and M. Petke, Physica Scripta **16**, 448 (1977).

[19] J. Z. Liu and P. C. Taylor, J. Non-Cryst. Solids **97 & 98**, 1123 (1987).

[20] V. I. Anisimov, V. A. Gubanov, and E. Z. Kurmaev, J. Struct. Chem. **21**, 291 (1981).

[21] S. Hunter and A. Bienenstock, in *Structure and Properties of Non-crystalline Semiconductors*, edited by B.T. Kolomiets (Academy of Sciences, A. F. Ioffe Institute, Leningrad, 1976), p. 151.

[22] N. Bollé, L. Michiels, and G. J. Adriaenssens, J. Non-Cryst. Sol. (in press).

[23] M. F. Thorpe, J. Non-Cryst. Solids **57**, 355 (1983).

[24] J. Z. Liu and P. C. Taylor, Solid State Commun. **70**, 81 (1989).

[25] K. S. Liang, A. Bienenstock, and C. W. Bates, Phys. Rev. B **10**, 1528 (1974).

[26] K. Shimakawa, N. Yoshida, A. Ganjoo, and Y. Kuzukawa, Philos. Mag. Lett. **77**, 153 (1998).

[27] G. J. Adriaenssens, and V. K. Tikhomirov, and S. R. Elliott, Non-Cryst. Sol. (in press).

Doping in metal chalcogenide glasses

S. A. Girlani, B. Yan, and P. C. Taylor

University of Utah, Salt Lake City, UT, USA
(Submitted March 16, 1998; accepted for publication March 17, 1998)
Fiz. Tekh. Poluprovodn. **32**, 982–986 (August 1998)

Chalcogenide glasses that contain sufficient concentrations of metal atoms can be *p*-type doped. This doping results in part because the local structural order is tetrahedral at the metal and the chalcogen sites in these glasses. At concentrations exceeding 10^{19} cm^{-3}, oxygen promotes doping by increasing the densities of dangling-bond defects at threefold-coordinated chalcogens, which are the doping sites in these glasses. For oxygen concentrations below 10^{19} cm^{-3}, the conductivity is independent of oxygen, and therefore is controlled by other mechanisms. The compositions $Cu_6As_4S_9$ and $Cu_6As_4Se_9$ are studied, because at these compositions the S (or Se) and Cu atoms are all tetrahedrally coordinated and there exist only Cu–S and As–S (or Cu–Se and As–Se) bonds. © *1998 American Institute of Physics.*
[S1063-7826(98)01508-7]

INTRODUCTION

There is strong experimental evidence[1–3] that many metal atoms, such as copper, are incorporated in chalcogenide glasses at tetrahedral sites. Based on the covalent nature of the local bonding, models of these glass structures[4–7] suggest that the chalcogen atoms also exist at tetrahedral sites when the metal concentrations are large enough. In ternary metal chalcogenide systems, such as Cu–As–S and Cu–As–Se, chemical ordering (Cu–S and As–S bonds only, for example) is preserved along a specific tie line in the ternary phase diagram. For the Cu–As–S and Cu–As–Se systems these tie lines are $(Cu_{2/3}S_{1/3})_x(As_{2/5}S_{3/5})_{1-x}$ and $(Cu_{2/3}S_{1/3})_x(As_{2/5}Se_{3/5})_{1-x}$ provided that $x \leqslant 9/19$. At $x = 9/19$ the stoichiometry is particularly simple: copper and chalcogen atoms are fourfold coordinated, arsenic atoms are threefold coordinated, and there exist only Cu-chalcogen and As-chalcogen bonds. This composition, which can be expressed as $Cu_6As_4S_9$ or $Cu_6As_4Se_9$, corresponds to a well-known crystalline structure, a natural mineral called sinnerite, where the numbers of nearest neighbors (local coordination numbers) are also 4, 3, and 4 for the copper, arsenic, and sulfur atoms, respectively.[8] At even higher copper concentrations, there are two well-studied crystalline structures in the sulfur system that also occur as natural minerals: enargite[8] and luzonite.[8] Enargite exhibits the wurtzite structure and luzonite the zincblend structure. For all of these reasons, one may be reasonably confident that the nearest-neighbor order in the glasses $Cu_6As_4S_9$ and $Cu_6As_4Se_9$ is well understood.

Although the local structural order in the glasses, $Cu_6As_4S_9$ and $Cu_6As_4Se_9$, is reasonably well understood, much less is known about the electronic defects, especially those that contribute to large changes in *p*-type conductivity that have been observed.[9–12] In the prototypical chalcogenide glasses, such as As_2S_3 and As_2Se_3, the chalcogens are two fold coordinated and the defects are dramatically influenced by strong electron-lattice interactions. In fact, these interactions are so strong that the characteristic defects possess negative effective electron-electron correlation energies (negative U^{eff}) that make the glasses impossible to dope. The twofold coordination of the chalcogens results in nonbonding *p*-orbitals that form the highest-lying states in the valence band.

As far as the electronic states are concerned, the major difference between As_2S_3 or As_2Se_3 and $Cu_6As_4S_9$ or $Cu_6As_4Se_9$ is that the highest-lying states in the valence band in the latter compositions are made from sp^3 hybrids on the tetrahedrally coordinated Cu and chalcogen atoms. A second important distinction is that, because of the large increase in average, local coordination number, the flexibility of the lattice is drastically reduced for the compositions, $Cu_6As_4S_9$ or $Cu_6As_4Se_9$. In $Cu_6As_4S_9$ or $Cu_6As_4Se_9$ the average local coordination number is $n = 3.8$, which is similar to that of the hydrogenated amorphous silicon (*a*-Si:H) alloys used in thin-film transistors and solar cells. As a result, as in *a*-Si:H lattice relaxation plays little role for the characteristic defects in $Cu_6As_4S_9$ or $Cu_6As_4Se_9$ where the important defect identified with the doping site possesses a positive value for U^{eff} (Refs. 9 and 13). This defect has been attributed to an electron trapped at a dangling sulfur or selenium bond at a tetrahedral chalcogen site.[9,10,13] Presumably the wave function for this paramagnetic defect is predominantly sp^3, as is the case for the silicon dangling bond at a tetrahedral silicon site in *a*-Si:H.

Oxygen is a pervasive impurity in most chalcogenide glasses, and the glasses $Cu_6As_4S_9$ and $Cu_6As_4Se_9$ are no exception. As will be shown below, addition of oxygen to these glasses increases the conductivities by more than three orders of magnitude.[10,11] The conductivity appears to be through extended stated and not simply a hopping conductivity in a defect band introduced by the oxygen.[10] The doping sites have been attributed[9] to the analog of cation vacancies that are known to produce *p*-type conductivity in $A^{II}B^{VI}$ crystals. One must be careful with this analogy since the concert of ''missing Cu atoms at Cu sites'' does not have the
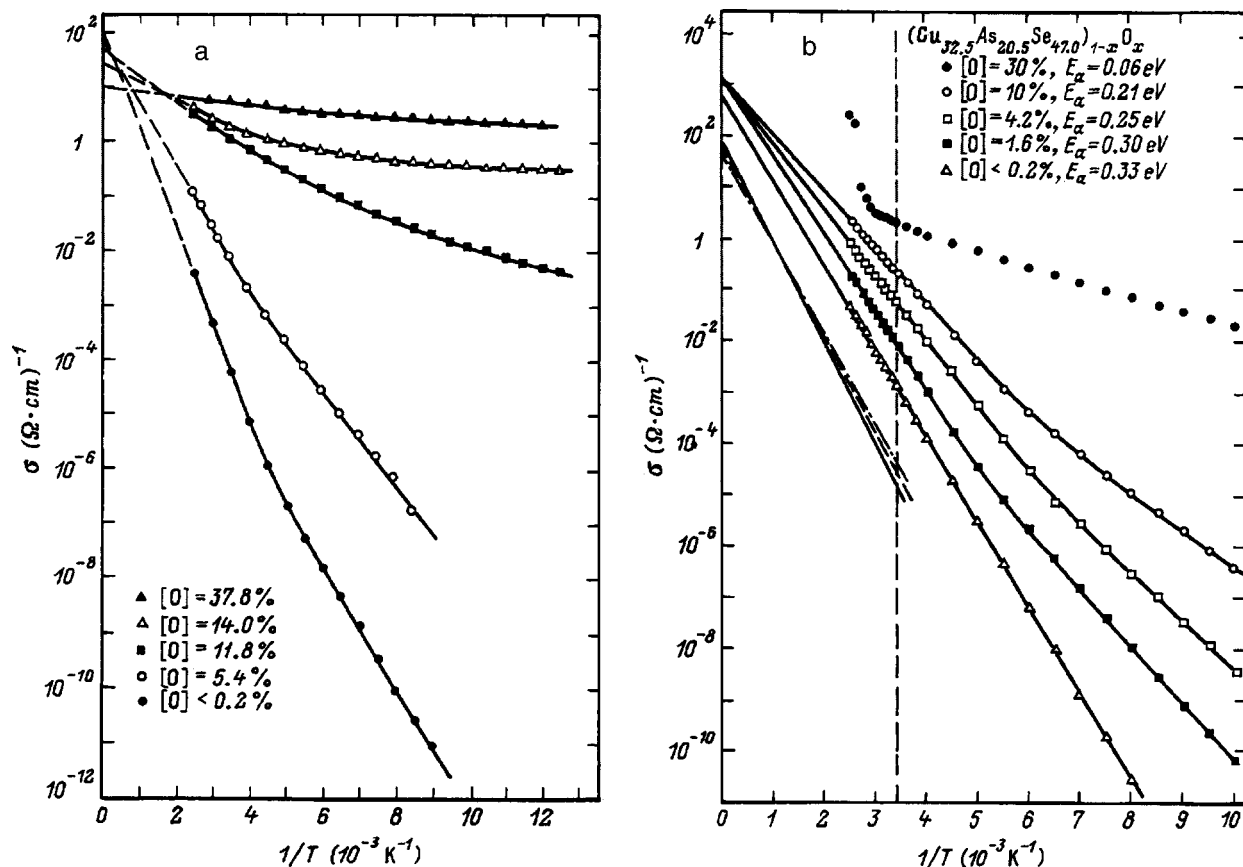
FIG. 1. Electrical conductivity plotted as a function of inverse temperature in a series of (a) $Cu_6As_4S_9$ glasses and (b) $Cu_6As_4Se_9$ glasses with varying oxygen concentrations [O]. Electrical activation energies can be determined from the higher temperature portions of the curves. The three lower curves (solid line, dashed line, dot-dashed line) in (b) represent conductivities for $(Cu_{2/3}Se_{1/3})_{0.14}(As_{2/5}Se_{3/5})_{0.86}$ glasses with 0.2, 10 and 30 at. % oxygen, respectively.

precise meaning that it does in crystalline solids. Since essentially all that is preserved in the amorphous solid is nearest-neighbor order, the signature of a "missing Cu at a Cu site" is the presence in the nominally stoichiometric glass of chalcogen–chalcogen bonds and chalcogen dangling bonds. These bonding configurations represent analogs in the glass to the reconstructed (Se–Se bonds) and unreconstructed (Se dangling bonds) nearest-neighbors of a Cu vacancy in the crystalline phase.

This kind of reasoning leads to the attribution of the doping site in $Cu_6As_4S_9$ or $Cu_6As_4Se_9$ glasses to chalcogen dangling bonds at tetrahedral chalcogen sites. Electron spin resonamce (ESR) measurements[9,10,13] on both $Cu_6As_4S_9$ and $Cu_6As_4Se_9$ are consistent with this interpretation. The ESR spectra are attributed to paramagnetic spins located on chalcogen atoms, and the lineshapes are different from those attributed to spins on chalcogen atoms at sites that are normally twofold coordinated, such as those that occur in As_2S_3 and As_2Se_3.

The energy levels in the gap for the chalcogen, dangling-bond defects that generate the doping are not well known, but optical absorption measurements[9,12] show an absorption below the optical gap that scales with the electrical conductivity. This absorption rises at about 0.4 eV in $Cu_6As_4S_9$ (Ref. 12) and at about 0.2 eV in $Cu_6As_4Se_9$ (Ref. 9).

It this paper we review the measurements of electrical conductivity, optical absorption, and ESR in oxygen-doped and nominally undoped $Cu_6As_4S_9$ and $Cu_6As_4Se_9$ glasses. We discuss the evidence for the *p*-type conduction process, and we present a microscopic picture for the defects that produce the doping effect.

EXPERIMENTAL DETAILS

Because the glass-forming regions in the Cu–As–S and Cu–As–Se systems do not include the $Cu_6As_4S_9$ and $Cu_6As_4Se_9$ compositions, all samples studied were prepared by sputtering. Normally, the films were deposited on glass or ESR-grade quartz substrates. Sputtering targets were made from ceramic samples of the appropriate composition. Bulk samples were powdered and pressed at 6000 psi and 200 °C. Ultrahigh purity argon was used as the sputtering gas, and oxygen was introduced to produce intentionally doped samples. Details of the sputtering procedures are available elsewhere.[11,14] Typical sample thicknesses were 1 to 5 μm. Glass compositions were measured using electron microprobe analysis, and impurity concentrations using secondary ion mass spectroscopy (SIMS). Electrical measurements were performed using evaporated gold contacts. Variable temperatures were obtained using standard He-flow cryostats. Optical absorption experiments employed standard infrared and visible spectrometers. ESR measurements were made using a 9-GHz spectrometer (Bruker ER200D-SRC)
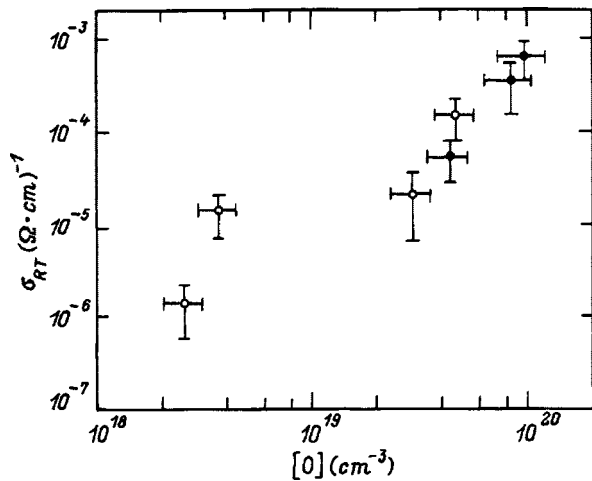
FIG. 2. Electrical conductivity at 300 K (σ_{RT}) as a function of oxygen concentration ([O]) in $Cu_6As_4S_9$ glasses. Closed and open circles represent intentionally oxygen-doped and nominally undoped films, respectively.
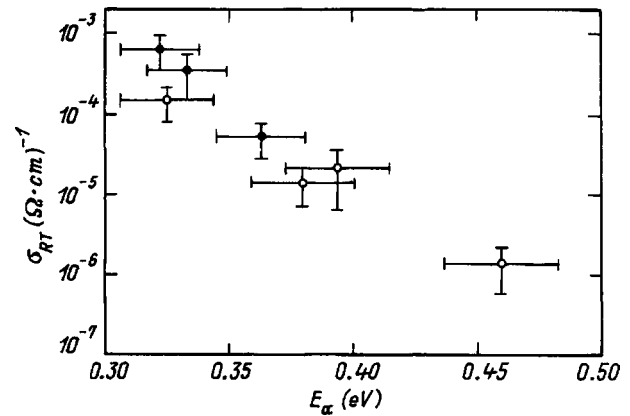

FIG. 3. Electrical conductivity at 300 K (σ_{RT}) as a function of activation energy for conduction (E_a) for various films of glassy $Cu_6As_4S_9$. Closed and open circles represent intentionally oxygen-doped and nominally undoped films, respectively.

and standard techniques to obtain variable temperatures. Details of the measurement apparatus and techniques are available elsewhere.[14]

RESULTS

The variations of the electrical conductivities in $Cu_6As_4S_9$ and $Cu_6As_4Se_9$ glasses with oxygen concentration are shown in Figs. 1a and 1b, respectively. From this figure it is clear that oxygen dramatically changes the temperature dependence of the electrical conductivity and hence the activation energies extracted from the data. The trends are obvious. The conductivity at a given temperature increases dramatically with oxygen concentration and the activation energy decraeses correspondingly. (The rapid rise in conductivity at high temperatures for the sample of glassy $Cu_6As_4Se_9$ with 30 at. % oxygen is due to crystallization of the sample.) Although the breaks in the slopes at low temperatures may be evidence for hopping conductivity, the values of the prefactors for the thermally activated conductivities at higher temperatures are consistent with conduction involving extended states.

Figure 1b also shows data for a sample of Cu–As–Se, where the copper concentration is 21 at. %, which is lower than in $Cu_6As_4Se_9$ (where the Cu concentration is nominally 31.5 at. %). For this lower copper concentration, shown by the lines without data points in Fig. 1b, simple bonding models, such as the formal valence shell or FVS model,[5,7] suggest that the copper and arsenic remain four- and threefold coordinated, respectively, but that the chalcogen is essentially threefold coordinated. (The average local coordination number for selenium at this composition is calculated to be 3.2). It is clear from Fig. 1b that for the glass where the chalcogen is mostly threefold coordinated, there is little if any doping generated by the presence of oxygen. One therefore requires tetrahedral coordination of the chalcogen for the *p*-type doping process to occur.

For oxygen concentrations above about 3×10^{19} cm^{-3}, the dark conductivity at a given temperature scales linearly with the oxygen content. This behavior is shown for $Cu_6As_4S_9$ glasses in Fig. 2. For oxygen concentrations below 3×10^{19} cm^{-3}, the conductivity becomes insensitive to oxygen content. Therefore, below this critical value of oxygen concentration another mechanism determines the number of defects that control the doping in the glass. It is probable that at these low oxygen levels the defect formation is determined by kinetics during growth, as is often the case for the densities of vacancies and intersitials during the growth of $A^{II}B^{VI}$ crystals.

A second example of the lack of correlation between oxygen concentration and electrical conductivity for low oxygen concentrations is shown in Fig. 3. In this figure the conductivities are plotted as a function of the measured activation energies. The data in Fig. 3 follow the usual trend that the activation energy scales inversely with the log of the electrical conductivity at a given temparature. A comparison with Fig. 2 shows that the oxygen concentrations differ by an order of magnitude for the two glasses with activation energies between 0.38 and 0.40 eV.

There exists an optical absorption band that scales with the electrical conductivity and with the oxygen concentration for high oxygen content ($>3 \times 10^{19}$ cm^{-3}). This absorption is shown for $Cu_6As_4S_9$ glass in Fig. 4. A similar plot exists for $Cu_6As_4Se_9$ glass,[9,12] except that the absorption for the selenium glasses rises near 0.2 eV while for the sulfur glasses shown in Fig. 4 the absorption rises near 0.4 eV. For oxygen concentrations below 3×10^{19} cm^{-3}, the absorption cannot be distinguished from the exponential band-gap absorption that is always present. The fact that this absorption scales with the electrical conductivity suggests that the onsets (0.2 and 0.4 eV in the selenium and sulfur glasses, respectively) can be associated with the energies of the acceptor levels with respect to the valence band mobility edge.

The microscopic nature of these doping sites can be elucidated by measuring the ESR spectra of $Cu_6As_4S_9$ and $Cu_6As_4Se_9$ glasses with varying electrical conductivities. As mentioned above, the lineshapes of the ESR spectra indicate that the electronic states are closely associated with the chalcogen atoms. In particular, these lineshapes have been
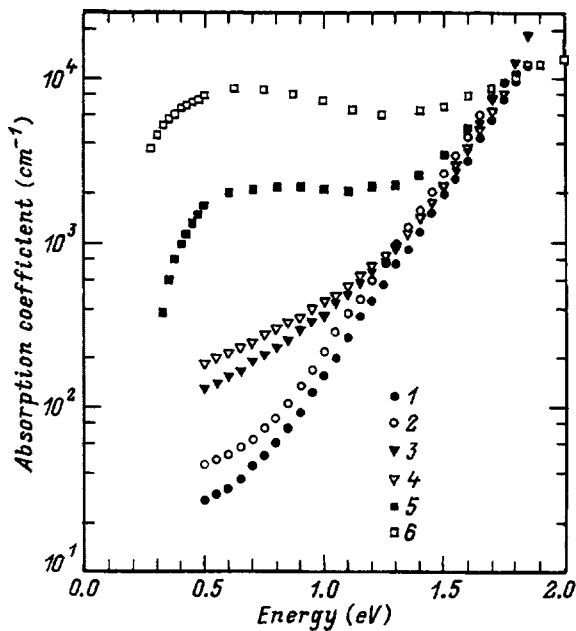
FIG. 4. Optical absorption coefficient as a function of energy for glassy $Cu_6As_4S_9$ films. Oxygen concentrations [O], 10^{19} cm^{-3}: *1* — 3.0, *2* — 4.4, *3* — 8.5, *4* — 9.8, *5* — 18, *6* — 45.

attributed[9,10,13] to holes trapped at sulfur or selenium ''dangling bonds'' where the site symmetries remain essentially tetrahedral. If this is the case, then the unpaired spin resides predominantly in an sp^3 hybrid orbital on the chalcogen atom much as is the case for the silicon dangling bond in *a*-Si and *a*-Si:H. Figure 5 shows the intensity of this ESR signal in $Cu_6As_4S_9$ glass as a function of the electrical conductivity. For technical reasons, the ESR is measured at low temperatures (20 K) while the conductivity is measured at room temperature ($\sim$300 K), but this detail should not affect the proportionality between the two measurements, provided that the electronic levels contributing to the *p*-type conductivity are the paramagnetic centers measured by ESR. From the data of Fig. 5 (filled circles) it appears that this
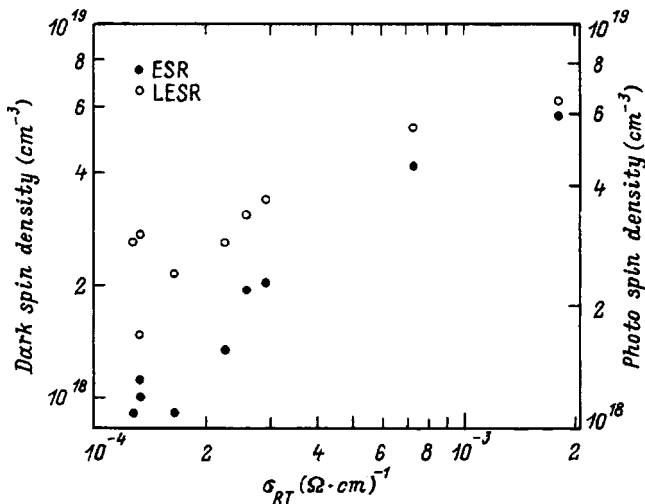

FIG. 5. ESR spin densities at 20 K as a function of electrical conductivity at 300 K σ_{RT}) in various films of glassy $Cu_6As_4S_9$. Filled and open circles represent dark and metastable, photo-induced spin densities, respectively.

assumption is correct. It is interesting to note that although the conductivity does not scale with oxygen concentration at low oxygen concentrations, the conductivity does scale with the ESR for all oxygen levels. This result means that although oxygen does not determine the densities of defects when the oxygen concentrations are low, the defects that are formed and measured by ESR control the conductivity. Because the ESR lineshape does not change, the same defects (holes trapped at threefold coordinated chalcogen sites) determine the conductivities in all samples.

Also plotted in Fig. 5 are metastable, photoinduced increases in the ESR spin densities; similarly the photoinduced ESR is observed in glassy As_2S_3 and As_2Se_3 at low temperatures. However, in this case the photo-induced ESR results in a concomitant increase in the dark conductivity (so-called persistent photoconductivity) at low temperatures,[13] as would be expected since these sites contribute to the electrical conductivity in the $Cu_6As_4S_9$ and $Cu_6As_4Se_9$ glasses. The mechanism for optically activating these additional acceptor sites is not known at present.

DISCUSSION

From the data presented in the previous section, a consistent model emerges to explain the electrical conductivity in the tetrahedrally coordinated chalcogenide glasses. When metals, such as the group I metal—copper, are added to chalcogenide glasses, the average local coordination number of the chalcogen increases to 4 from its usual value of 2. Concomitant with this increase in average local coordination number is a change in the characteristic defects that are formed. In place of the ''soft'' lattice in As_2S_3 or As_2Se_3 is a ''hard'' lattice in $Cu_6As_4S_9$ or $Cu_6As_4Se_9$. This change means that the characteristic defects possess a positive, effective, electron-electron correlation energy, and if the defect energies are close enough to the valence or conduction band edges, then doping can occur.

In glassy $Cu_6As_4S_9$ or $Cu_6As_4Se_9$ the characteristic defect is found to be a hole trapped at a tetrahedral chalcogen site, because one of the four nearest-neighbor bonds is missing. The production of these defects can be enhanced by the incorporation of oxygen in the glasses, but there appears to be a basic, lower level for these defects that is controlled by the kinetics during growth.

An analogy between the doping in $A^{II}B^{VI}$ crystals by vacancies and interstitials and the doping in $Cu_6As_4S_9$ and $Cu_6As_4Se_9$ glasses is useful. This analogy makes some sense because in both the crystals and the glasses the structure is strongly influenced by the covalent nature of the bonds, but the defects are dominated by ionic considerations. In $A^{II}B^{VI}$ crystals one type of vacancy or vacancy-interstitial pair tends to dominate in a specific crystal. Therefore, a $A^{II}B^{VI}$ crystal tends to be either *p*-type or *n*-type, and it is very difficult to change the carrier type. This trend occurs because one type of vacancy (cation or anion) dominates in any given crystal and because cation vacancies generate *p*-type conduction while anion vacancies generate *n*-type conduction.

To the extent that this analogy holds, one would expect that *n*-type conductivity would be very difficult to achieve in

glassy $Cu_6As_4S_9$ or $Cu_6As_4Se_9$. To date, this expectation has been fulfilled since attempts to co-dope with other elements or to compensate for the chalcogen-based acceptors have all failed. Assuming that substitutional doping is as difficult to achieve in the tetrahedrally coordinated chalcogenide glasses as it is in the $A^{II}B^{VI}$ crystals, one might expect that the only hope to produce *n*-type conductivity is to change the host lattice. Again by analogy with the $A^{II}B^{VI}$ crystals, the production of anion vacancies is promoted by decreasing the size of the anion with respect to the cation. To date, attempts to do the same in the tetrahedrally coordinated chalcogenide glasses have also failed perhaps because the larger cations (metals) tend to form fewer than four bonds in the glasses.

SUMMARY

As metals are added to the chalcogenide glasses, the average, local coordination number of the chalcogen atoms increases from 2 to 4. When the chalcogens are tetrahedrally coordinated, the glasses can be doped *p*-type. The addition of oxygen to the glass generates an increase in the *p*-type conductivity, but at low oxygen concentrations ($<10^{19}$ cm^{-3}) residual doping sites exist. These sites are probably determined by the kinetics during growth. From optical absorption measurements the doping levels for the acceptors are determined to be approximately 0.4 and 0.2 eV from the valence band mobility edge in glassy $Cu_6As_4S_9$ and $Cu_6As_4Se_9$, respectively. From ESR measurements the doping site is determined to be a hole trapped at a threefold coordinated chalcogen site which retains its tetrahefral symmetry. In other words, the hole exists predominantly in an sp^3-hybridizedorbital on the chalcogen atom, in contrast with the *p* orbital for the hole generated in the prototypical chalcogenide glasses, such as As_2S_3 and As_2Se_3. As expected, the doping sites in glassy $Cu_6As_4S_9$ and $Cu_6As_4Se_9$ possess positive, effective, electron-electron correlation energies.

[1] K. S. Liang, A. Bienenstock, and C. W. Bates, Phys. Rev. B **10**, 1528 (1974).

[2] S. Laderman, A. Bienenstock, and K. S. Liang, Sol. Energy Mater. **8**, 15 (1982).

[3] S. H. Hunter, A. Bienenstock, and T. M. Hayes, in *Amorphous an Liquid Semiconductors*, edited by W. E. Spear (University of Edinburgh, Edingurgh, 1977), p. 78.

[4] J. Z. Liu and P. C. Taylor, Phys. Rev. Lett. **59**, 1938 (1987).

[5] J. Z. Liu and P. C. Taylor, Solid State Commun. **70**, 81 (1989).

[6] J. Z. Liu and P. C. Taylor, J. Non-Cryst. Solids **114**, 25 (1989).

[7] P. C. Taylor, Z. M. Saleh, and J. Z. Liu, in *Advances in Disordered Semiconductors*, Vol. 3, edited by H. Fritzsche (World Scientific, Singapore, 1990), p. 23.

[8] A. S. Wells, *Structural Inorganic Chemistry* (Clarendon, Oxford, 1975).

[9] J. Hautala and P. C. Taylor, in *Optical Processes in Disordered Solids*, edited by Z. V. Vardeny and P. C. Taylor (Elsevier, Amsterdam, 1991).

[10] J. Hautala, B. Moosman, and P. C. Taylor, J. Non-Cryst. Solids **137&138**, 1043 (1991).

[11] R. E. Shirey and P. C. Taylor, Univ. Utah. J. Undergrad. Res. **3**, 40 (1992).

[12] P. C. Taylor, R. E. Shirey, S. Girlani, and J. Hautal, J. Non-Cryst. Solids **164−166**, 1191 (1993).

[13] B. Yan, S. Girlani, and P. C. Taylor, Phys. Rev. B **56**, 1 (1997).

[14] S. A. Girlani, Ph. D. Thesis (1998).

Luminescence of erbium in amorphous hydrogenated silicon obtained by the glow-discharge method

E. I. Terukov, O. I. Kon'kov, V. Kh. Kudoyarova, and O. B. Gusev

A. F. Ioffe Physicotechnical Institute, Russian Academy of Sciences, 194021 St. Petersburg, Russia

G. Weiser

Marburg University, 35032 Marburg, Germany

We report the first observation of efficient room-temperature photoluminescence of erbium in amorphous hydrogenated silicon prepared by the plasma chemical-deposition method. © *1998 American Institute of Physics.* [S1063-7826(98)01608-1]

The considerable current interest in the investigation of the luminescence of erbium in different semiconductor matrices is attributable to the possibility of electronic pumping of the luminescence of rare-earth metal (REM) ions.[1,2] Erbium-doped silicon attracts greatest interest because of its promising future in the development of light-emitting diodes and lasers operating at the wavelength 1.54 μm, which falls at the absorption minimum of optical fibers. The main method of introducing erbium into crystalline silicon is implantation. The intensity of the photoluminescence of erbium in this matrix falls off by more than an order of magnitude when the temperature is increased from liquid-nitrogen temperature to room temperature.[3,4] This behavior is due to the deactivation of excitons bound on relatively shallow donor levels.

The 1.54-μm photoluminescence of erbium was recently observed in amorphous hydrogenated silicon.[5–7] Amorphous silicon films were obtained by cosputtering silicon and metallic erbium from a mosaic target using the magnetron[7] or the MASD method.[6] It is known that the temperature quenching of the luminescence of erbium in a crystalline matrix differs considerably from that in an amorphous matrix because of the difference in the mechanisms for the excitation of erbium.[3,8] The intensity of the erbium luminescence in amorphous silicon is essentially temperature-independent right up to room temperature. For this reason, the search for new methods of producing amorphous silicon that contains erbium is an important task in the technology of producing optoelectronic devices.

In the present paper we report the first observation of efficient room-temperature photoluminescence of erbium in amorphous hydrogenated silicon obtained by plasma-chemical deposition. As we know, this is the main method used for obtaining device-quality amorphous silicon for solar cells and structures based on it.

The films of erbium-doped amorphous hydrogenated silicon (a-Si:H$\langle$Er$\rangle$) were grown on quartz or crystal silicon substrates by decomposition of silane in an argon atmosphere. The substrates were placed on an rf electrode at room temperature. The erbium source consisted of Er(TMHD)$_3$ powder heated to a temperature above 160 °C. The growth rate of the a-Si:H$\langle$Er$\rangle$ film was equal to 0.02 μm/min. The films studied by us were on the order of 1 μm thick. The composition of these films, i.e., the erbium, oxygen, and carbon concentrations, was investigated by Rutherford backscattering (RBS) with the films irradiated by accelerated 3.17-MeV α particles. The Er and O densities were equal to 2.1×10^{20} and 1.4×10^{21} cm^{-3}, respectively.

The structure of the a-Si:H$\langle$Er$\rangle$ films was investigated by Raman and infrared spectroscopy methods. The Raman spectra were obtained on an U-1000 spectrometer in the reflection geometry. The wavelength of the incident radiation was λ =514.5 nm and the power level was P=100 W. Lines corresponding to TA (150 cm^{-1}), LA (310 cm^{-1}), LO (380 cm^{-1}), and TO (475 cm^{-1}) phonons were observed in the Raman spectra of the films. The line positions are typical positions for films of amorphous hydrogenated silicon. The difference from the Raman spectrum of undoped a-Si:H obtained by the same method is a small increase in the half-width of the TO peak. The latter can be explained by the increase in the compositional and structural disorder as a
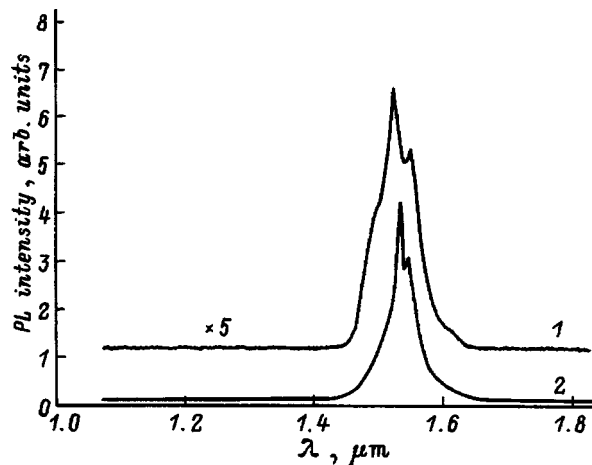

FIG. 1. Photoluminescence (PL) spectra of erbium in Er(TMHD)$_3$ powder (*1*) and in an a-Si:H$\langle$Er$\rangle$ film before annealing (*2*).
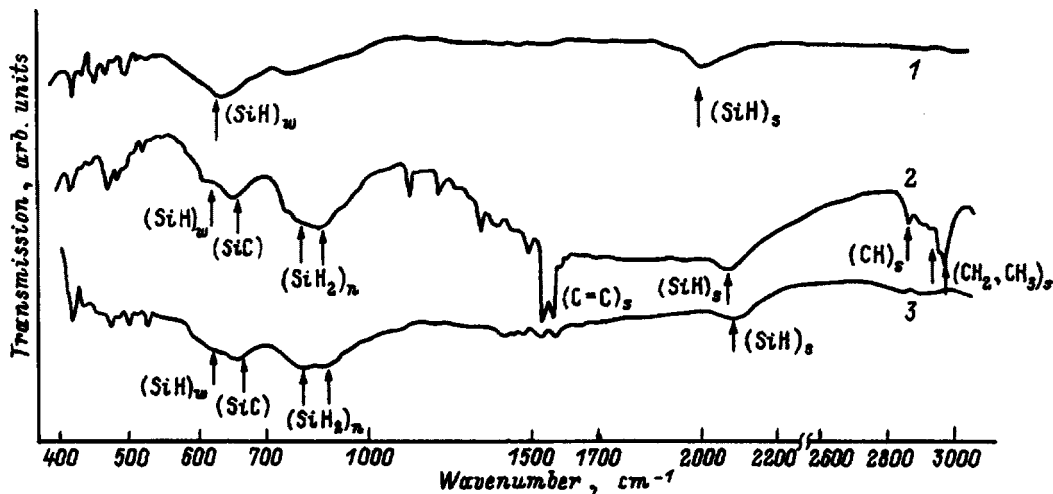
FIG. 2. Infrared spectra of *a*-Si:H (*1*) and *a*-Si:H⟨Er⟩ samples before (*2*) and after (*3*) annealing.

result of the incorporation of the impurities (Er, O, C) into the amorphous hydrogenated silicon matrix.

The infrared (IR) spectra were measured at room temperature on an UR-20 two-beam spectrophotometer in the spectral range from 400 to 5000 cm^{-1}.

The photoluminescence spectra were measured with excitation by a 30-mW argon laser at $\lambda = 488$ nm using a liquid-nitrogen-cooled germanium detector. Figure 1 shows the photoluminescence spectra of Er(TMHD)$_3$ powder (spectrum 1) and an *a*-Si:H⟨Er⟩ film before annealing (spectrum 2).

Worth noting is that the photoluminescence (PL) spectrum of the powder differs markedly from that of the *a*-Si:H film. The characteristic lines of erbium in the powder are strongly broadened, and their position is different from that in amorphous silicon films. This indicates that the local environment surrounding the erbium ions in these matrices is different, i.e., it reflects the result of the incorporation of the Er atoms into the *a*-Si:H matrix by the technology used by us.

We note that the intensity of the erbium photoluminescence of the synthesized samples is comparable in magnitude to that of *a*-Si:H⟨Er⟩ samples obtained by the MASD method and optimized with respect to the erbium and oxygen concentrations.[6] Vacuum annealing of the samples under a residual pressure of less than 10^{-6} Torr at 300 °C for 1 h increased the intensity of the erbium PL by more than an order of magnitude.

Figure 2 shows the IR spectra of the *a*-Si:H⟨Er⟩ films before annealing (spectrum 2) and after vacuum annealing at 300 °C for 1 h (spectrum 3). The figure also shows for comparison the IR spectrum of an undoped *a*-Si:H film (spectrum 1).

We call attention to the following features:

— the presence of the modes of CH$_2$, CH$_3$, and (Si–H$_2$)$_n$, which indicates the existence of a polymer component in the film structure; this corresponds to the preparation conditions (low temperature and placement of the substrates on the rf electrode);

— presence of C–C bonds, which is due to the presence

of a large quantity of carbon in the powder employed for introducing erbium; according to the RBS data, the carbon content in the film is 10–15 at. %.

It should be noted that, despite the high oxygen concentration, lines corresponding to vibrations of the bonds Si–O–Si (980 cm^{-1}) and C–O (1710 cm^{-1}) were not observed in the experimental films; this can be explained by the fact that oxygen is bound mainly with erbium ions.

A change is observed in the IR spectra after annealing; specifically, the intensity of the CH$_2$ and CH$_3$ modes decreases and the bands corresponding to vibrations of C–C bonds vanish. Structural rearrangement leads to the observed increase in the photoluminescence intensity.

In summary, intense room-temperature photoluminescence of erbium has been observed for the first time in *a*-Si:H⟨Er⟩ samples obtained by the glow-discharge method. There is the hope that this technology can be used to produce light-emitting diodes at the wavelength 1.54 μm.

[1] G. S. Pomrenke, P. B. Klein, and D. W. Langer [Eds.], *Rare-Earth Doped Semiconductors I*, Mater. Res. Soc. Proc., Vol. 301, Pittsburgh, PA, 1991.
[2] S. Coffa, A. Polman, and R. N. Schwartz [Eds.], *Rare-Earth Doped Semiconductors II*, Mater. Res. Soc. Proc., Vol. 422, Pittsburgh, PA, 1996.
[3] I. N. Yassievich and L. C. Kimerling, Semicond. Sci. Technol. **8**, 718 (1993).
[4] S. Coffa, G. Franzo, F. Priolo, A. Polman, and R. Serna, Phys. Rev. B **49**, 16 313 (1994).
[5] T. Oesterreich, G. Swiatkowski, and I. Broser, Appl. Phys. Lett. **56**, 446 (1990).
[6] M. S. Bresler, O. B. Gusev, V. Kh. Kudoyarova, A. N. Kuznetsov, P. E. Pak, E. I. Terukov, I. N. Yassievich, B. P. Zakharchenya, W. Fuhs, and A. Sturm, Appl. Phys. Lett. **67**, 3599 (1995).
[7] A. R. Zanatta, L. A. O. Nunes, and L. R. Tessler, Appl. Phys. Lett. **70**, 511 (1997).
[8] W. Fuhs, I. Ulber, G. Weiser, M. S. Bresler, O. B. Gusev, A. N. Kuznetsov, V. Kh. Kudoyarova, E. I. Terukov, and I. N. Yassievich, Phys. Rev. B **56**, 9545 (1997).

Translated by M. E. Alferieff

Ion implantation of porous gallium phosphide

V. V. Ushakov,[a)] V. A. Dravin, N. N. Mel'nik, T. V. Zavaritskaya, and N. N. Loĭko

P. N. Lebedev Physics Institute, Russian Academy of Sciences, 117924 Moscow, Russian

V. A. Karavanskiĭ

Institute of General Physics, Russian Academy of Sciences, 117924 Moscow, Russia

E. A. Konstantinova and V. Yu. Timoshenko

M. V. Lomonosov Moscow State University, 119899 Moscow, Russia

The effect of irradiation by Ar ions and thermal annealing on the properties of porous gallium phosphide (*por*-GaP) obtained by electrolytic methods is investigated. It is shown on the basis of Raman scattering and photoluminescence data that, in contrast with porous silicon, *por*-GaP does not have high radiation hardness, and that thermal annealing of defects in layers amorphized by ion implantation is impeded by the absence of a good crystal base for solid-state epitaxial recrystallization processes. Data on radiation-induced defect formation and from probing of the material with a rare-earth ''luminescence probe'' are consistent with a mesoporous structure of the material. © *1998 American Institute of Physics.*
[S1063-7826(98)01708-6]

1. INTRODUCTION

The unabating interest in porous semiconductors stems from the attractiveness of the relatively simple electrochemical methods of obtaining nanosize objects and from the prospects for producing combined optomicroelectronic devices. The impressive progress made recently in the study of the properties of porous silicon (see the review articles in Refs. 1 and 2) has stimulated similar investigations for III–V semiconductor compounds. The as yet few studies in this field have mostly involved GaP, and actually their goal was to test the technological regimes for preparation of porous layers and to obtain the first data on their structure and properties.[3–8] Just as for porous (*por*-) Si, here a controversy is beginning to appear concerning the role of quantum-well effects and surface effects in the observed phenomena

In this paper we report the results of an experimental study of the effect of ion implantation on the properties of *por*-GaP, including questions concerning radiation-induced defect formation, thermal annealing of defects, and doping of porous layers. Conclusions about the structure of *por*-GaP are drawn on the basis of the experimental data.

2. EXPERIMENTAL PROCEDURE

The starting material consisted of Czochralski-grown single-crystal *n*-GaP. Two types of porous layers were investigated: 1) layers obtained by anodization of the (100) *n*-type GaP:Te ($n = 3 \times 10^{17}$ cm^{-3}) wafers in a water solution of NH$_4$F (0.2 moles/liter, pH = 3.2), anodization current density $j = 120 - 20$ mA/cm^2, and anodization time $\tau = 10 - 20$ min and 2) layers obtained by anodization of (111) *n*-GaP wafers ($n = 3 \times 10^{17}$ cm^{-3}) in the electrolyte HF(49%) : C$_2$H$_5$OH$= 1 : 1$, $j = 80$ mA/cm^2, and $\tau = 7$ min. We note that, besides the standard HF-based electrolyte,[3,4] a solution of ammonium fluoride NH$_4$F with a controllable pH was used. Such an electrolyte is used to obtain porous gallium phosphide layers with high optical uniformity of the surface.[8] The porous layers were (1) 25–30 μm and (2) 10–15 μm thick and the porosity was on the order of 60%.

Ion irradiation of samples containing porous sections and single-crystal control sections was performed in a High Voltage Engineering Europa accelerator at room temperature. Argon ions with an energy of 700 keV and *ion flux* $5 \times 10^{14} - 5 \times 10^{15}$ cm^{-2} were used to study radiation-induced defect formation in porous layers, while Yb ions (350–680 keV, $2 \times 10^{13} - 1 \times 10^{14}$ cm^{-2}) were used to investigate the characteristic features of ion doping. In the latter case the intent was also to study the structure and impurity-defect composition of porous layers using a rare-earth ''luminescence probe'' (see below). Thermal annealing in hydrogen with additional illumination by radiation from a DKsSH3000 lamp, emitting in the ultraviolet, visible, and near-IR regions of the spectrum, was used to restore the crystal structure and to activate the implanted impurity. The properties of the samples were investigated by Raman scattering and photoluminescence. Most spectra were obtained at room temperature on an U-1000 spectrometer at normal incidence of 488 nm exciting radiation from an ILA-120 argon laser. The Yb impurity radiation was monitored with a DFS-12 spectrometer excitation by a DKsSH-1000 xenon lamp at $T = 77$ K in the spectral region 400–600 nm.

3. EXPERIMENTAL RESULTS

Amorphization and annealing of implanted layers. Figure 1 shows the Raman and luminescence spectra of the starting samples. The lines of *TO* (365 cm^{-1}) and *LO* (402 cm^{-1}) phonons were observed in the Raman spectra,
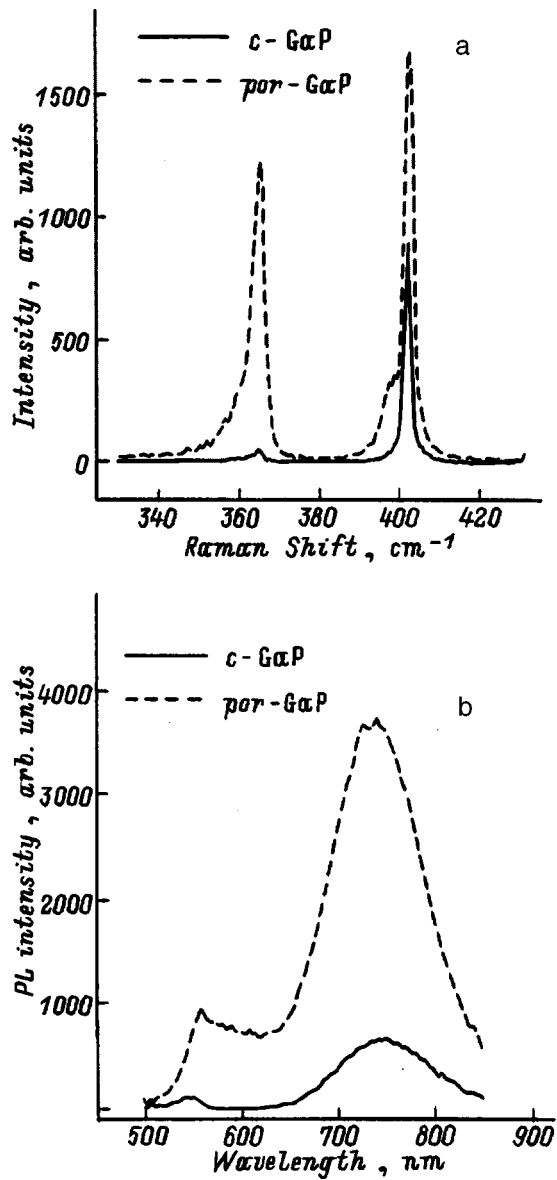
FIG. 1. Raman scattering (a) and photoluminescence (b) spectra for *c*-GaP (100) and type-1 *por*-GaP.

obtained under normal incidence, of the crystal (*c*-) and *por*-GaP. For the porous material, the 397-cm^{-1} surface mode was also observed.[9] The edge (550 nm) and ''red'' (740 nm) bands are presented in the luminescence spectra. Because of their strong broadening at 300 K, it is difficult to make an accurate identification of the corresponding radiative transitions, but there is no doubt that donors (S, O) and acceptors (C, Zn, Si, Cd) participate in them.[10] The following characteristic changes were observed on switching from the crystal to the porous material:[3] an increase in the relative intensity of the Raman *TO* phonons, appearance of a surface mode, and an overall increase in the intensities of the Raman lines and the luminescence. In what follows questions concerning the generation and annealing of radiation-induced defects in *por*-GaP will be examined for these samples, which are typical in their class. Data on the ion implantation of *c*-GaP will serve as the reference point.[11]

Monte Carlo simulation was used to estimate ion ranges

in *c*- and *por*-GaP. For *por*-GaP the material density, which decreased to 40% (in accordance with the indicated porosity) of the value for *c*-GaP, was used in the calculations. According to the results of these calculations the implanted Ar atoms penetrated to 0.9 μm in *c*-GaP and 2.2 μm in *por*-GaP. Clearly, these values can be viewed as an estimate of the depth of radiation-induced defect formation in this case.

In the case of Ar ion implantation, the threshold for amorphization of GaP is $\sim 2 \times 10^{14}$ cm^{-2}. In a previous study[12] we observed that the amorphization of *por*-Si first appears at much higher (by 1.5–2 orders of magnitude) ion fluxes than in *c*-Si, which is attributable to the efficient flow of radiation-induced defects to the extremely extended inner surface of the porous layers. In contrast, in our study, Raman and luminescence spectral lines for *por*-GaP, just as for the control *c*-GaP, were not observed even at the lowest flux 5×10^{14} cm^{-2}, which apparently indicates that the skin layer of the test material becomes disordered. In contrast with *por*-Si, the *por*-GaP investigated by us therefore does not exhibit high radiation hardness as compared with bulk single crystals.

Different forms of thermal annealing are used to restore the crystal lattice and to anneal the radiation-induced defects. The density of thermal defects, whose source is the annealing procedure itself, must be minimal. Our procedure (annealing in hydrogen with additional illumination) does not require protective insulating coatings and has been used successfully before to anneal ion-implanted III–V semiconductors.[13,14] In our case the effectiveness of the procedure was indicated by the fact that as the annealing temperature T_a was raised to 720 °C, the intensities of the Raman lines and the edge luminescence band of the *c*-GaP and *por*-GaP control (not subjected to ion implantation) samples surprisingly did not decrease, but instead increased. This behavior occurs when the correct procedure is used for heat treatment of the samples, because the nonradiative recombination centers decrease in the skin layer as a result of the action of surface getters.

To investigate the characteristic features of the recrystallization of porous layers, isochronous annealing (15 min) of implanted samples was performed at temperatures 350, 550, and 720 °C. These values correspond to certain stages of the restoration of the crystal structure of the amorphized material. In GaP restoration of the crystal structure as a whole occurs at $T_a = 350$ °C, but the samples contain many extended and point defects. The temperature $T_a = 550$ °C is sufficient for annealing extended defects. At $T_a > 700$ °C the defect density is reduced to a minimum, the implanted impurities are activated, and the intensities of the optical bands reach their maximum values, which are determined by the residual radiation-induced and thermal defects. As the annealing temperature was raised, the intensities of the Raman lines and luminescence bands of the implanted *c*-GaP and *por*-GaP gradually increased (without a change in the spectrum) in accordance with the gradual annealing of the radiation-induced defects contained in them. The data for the *c*-GaP control correspond to the known order of annealing of this implanted material. The intensities of the Raman lines and luminescence bands of all *c*-GaP samples implanted at
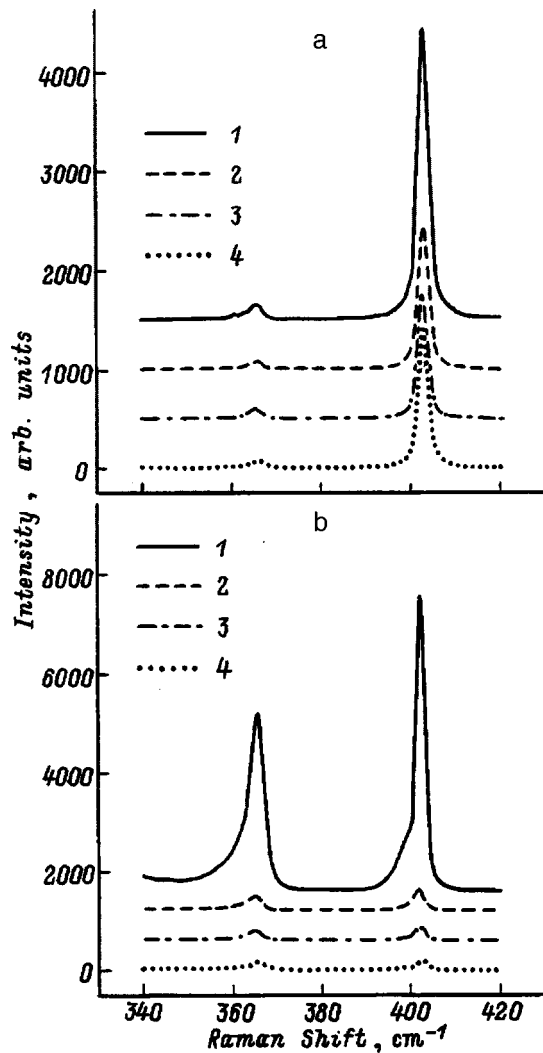
FIG. 2. Raman scattering spectra of *c*-GaP (a) and type-1 *por*-GaP (b) irradiated with different Ar ion doses and annealed at 720 °C. Irradiation doses, cm^{-2}: 2 — 5×10^{14}, 3 — 1×10^{15}, 4 — 5×10^{15}. 1 — Spectra of the initial samples.

$T_a = 720$ °C were equal to 40–50% of the corresponding values for the nonimplanted control sample (except for the edge luminescence band). They therefore indicate a relatively low level of unannealed radiation-induced defects (see Figs. 2a and 3a). At each stage of annealing the porous samples ''lagged behind'' the corresponding control bulk samples. As one can see in Fig. 2b, even at $T_a = 720$ °C the intensities of the Raman bands for *por*-GaP remain at a much lower level, thereby indicating a much higher density of residual defects. Since the material has a porous structure, this can probably be attributed to the absence of a good crystal base (substrate) for solid-phase epitaxial processes which restore the structure as a result of annealing of the amorphized layers. Nonetheless, as the data in Fig. 3b show, appreciable recovery of the luminescence properties of the irradiated samples is still possible under favorable annealing conditions.

Ion doping. c-GaP of both initial types was used in these investigations. Two methods were used to dope *por*-GaP samples with YB. The first method employed ion implanta-
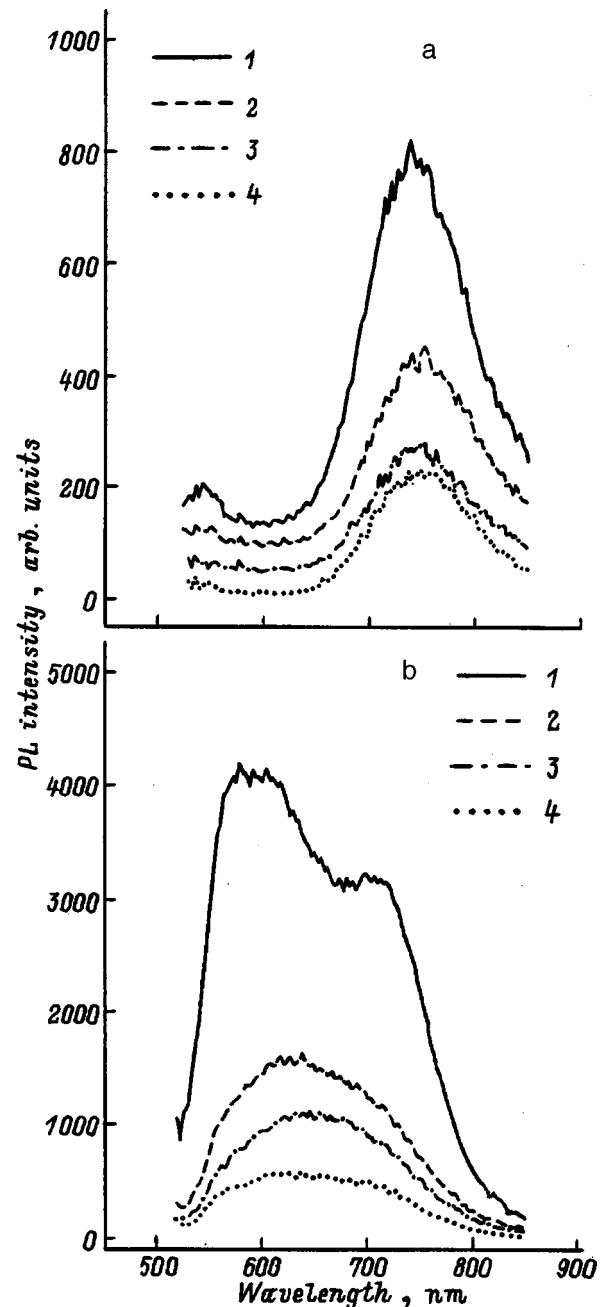
FIG. 3. Photoluminescence spectra of *c*-GaP (a) and type-1 *por*-GaP (b) irradiated with different Ar ion doses and annealed at 720 °C. Irradiation doses, cm^{-2}: 2 — 5×10^{14}, 3 — 1×10^{15}, 4 — 5×10^{15}. 1 — Spectra of the initial samples.

tion of a previously synthesized type-2 *por*-GaP sample followed by annealing at 720 °C for 15 min. The second method consisted of two stages. First, *c*-GaP:Yb was synthesized by the standard procedure of ion implantation of Yb followed by annealing. Next, type-1 porous layers were prepared from this material. Ytterbium ion doping of *por*-GaP was performed, on the one hand, to determine the characteristics of ion implantation of porous III–V semiconductors and, on the other hand, to use Yb centers as ''luminescence probes'' to investigate the structure and composition of the porous layers. Knowing the characteristic form of the spectra, the narrowness of the lines, and the effective interaction

FIG. 4. Luminescence spectra ($T = 77$ K) of Yb centers in *c*-GaP and *por*-GaP for samples obtained by a — implantation of Yb in a porous layer (type 2) and b — formation of a porous layer (type 1) from *c*-GaP:Yb.

the experimental bulk crystal layers and porous layers obtained by different methods are subject to identical conditions. Since, as was investigated in detail earlier, the Yb introduced into GaP by ion implantation does not become segregated on the surface but rather fills the volume of the crystals, according to the statistics of implanted ranges and the conditions of postimplantation annealing,[19] it can be concluded that even in the *por*-GaP studied by us most of the implanted Yb does not "feel" the surface. This condition evidently must be satisfied when the structural elements of the porous layers are relatively large. This is already indicated by the fact that the rare-earth "probe" Yb showed no evidence of quantum-well restrictions, whose influence on the properties of strongly localized d and f electronic systems (as a result of the intensification of hybridization of local and itinerant states) was investigated theoretically by Kikoin and Manakova.[20]

According to data obtained from optical measurements and scanning electron microscopy,[4,8] on the whole, the structure of *por*-GaP can terefore be characterized as intermediate between nanoporous (sizes of the voids and nonetched sections are typically on the order of several nanometers) and microporous (size scale on the order of a micron). Such a structure can be called mesoporous. The inner surface of mesoporous *por*-GaP, which is less extended than that of nonoporous *por*-Si, does not give equally efficient draining of defects as a result of exposure to radiation.

4. CONCLUSIONS

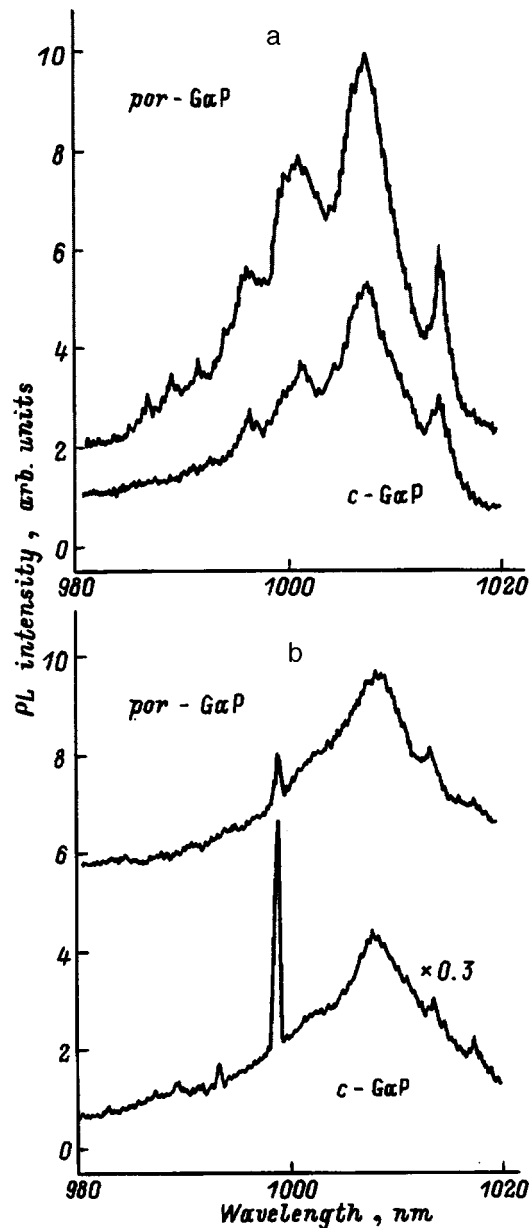1. Data on radiation-induced defect formation and from a study of the properties of *por*-GaP using a rare-earth Yb luminescence probe indicate that the test material has a mesoporous rather than nanoporous structure. The Raman and luminescence spectra presented in this paper correspond to this conclusion.

2. In contrast with nanoporous *por*-Si, mesoporous *por*-GaP does not exhibit higher radiation hardness.

3. Thermal annealing of radiation-induced defects in *por*-GaP is much more complicated than in the case of bulk crystalline material because of the absence in *por*-GaP of a good single crystal base (substrate) for solid-phase, structure-restoring epitaxial processes. Despite this circumstance, the luminescence properties of the irradiated samples can still be recovered appreciably under favorable annealing conditions.

a)Fax: (095) 1357880; E-Mail: ushakov@sci.Ipi.msk.su

[1] Y. Kanemitsu, Phys. Rep. **263**, 3 (1995).

[2] A. G. Cukkis, L. T. Canham, and P. D. J. Calcott, J. Appl. Phys. **82**, 909 (1997).

[3] A. I. Belogorokhov, V. A. Karavanskiĭ, A. N. Obraztsov, and V. Yu. Timoshenko, JETP Lett. **60**, 274 (1994).

of the rare-earth ions with defects and background impurities, this method has been used succeefully to characterize ion-implanted semiconductors.[15,16] Figure 4 shows the Yb radiation (intracenter f–f electronic transitions) for different *c*-GaP and *por*-GaP samples synthesized by us. In addition to Yb atoms, the emitting centers can also contain impurities and defects, which are often present in excess quantities in GaP. In particular, the data from "spectral analysis"[17,18] indicated that associations of Yb with group IV, V, and VI elements, including the dopants S (1014 nm) and Te (998 nm) and also the background Se (1008 nm), were present in the experimental samples. The obvious conclusion, which is crucial for us and which follows from the data in Fig. 4, is that the spectra of Yb in *c*-GaP and *por*-GaP are identical. Consequently, the overwhelming majority of the Yb atoms in

[4] F. V. Zoteev, P. K. Kashkarov, A. N. Obraztsov, and V. Yu. Timoshenko, Fiz. Tekh. Poluprovodn. **30**, 1473 (1996) [Semiconductors **30**, 775 (1996)].

[5] I. M. Tiginyanu, V. V. Ursaki, V. A. Karavanskii, V. N. Sokolov, Y. S. Raptis, and E. Anastassakis, Solid State Commun. **97**, 675 (1996).

[6] A. Aneda, A. Serpi, V. A. Karavanskii, I. M. Tiginyanu, and V. M. Ichizli, Appl. Phys. Lett. **67**, 3316 (1995).

[7] A. Meijerink, A. A. Bot, and J. J. Kelly, Appl. Phys. Lett. **69**, 2801 (1996).

[8] V. Yu. Timoshenko, J. Rappich, and Th. Dittrich, Appl. Surf. Sci. 1998, at press.

[9] S. Hayashi and H. Kanamori, Phys. Rev. B **26**, 7079 (1982).

[10] A. E. Yunovich in *Radiative Recombination in Semiconductors* [in Russian], Moscow, 1972, p. 304.

[11] H. Ryssel and R. Ingolf, *Ion Implantation*, Wiley, N. Y., 1986 [Moscow, 1983].

[12] V. V. Ushakov, V. A. Dravin, N. N. Mel'nik, V. A. Karavanskiĭ, E. A. Karavanskiĭ, E. A. Konstantinova, and V. Yu. Timoshenko, Fiz. Tekh. Poluprovodn. **31**, 1126 (1997) [Semiconductors **31**, 966 (1997)].

[13] A. M. Gukasyan, V. M. Konnov, and N. N. Loĭko, KSF, No. 3–4, 44 (1992).

[14] V. A. Dravin, V. M. Konnov, T. V. Larikova, and N. N. Loĭko, KSF, No. 3–4, 18 (1995).

[15] A. A. Gippius, V. V. Ushakov, V. N. Yakimkin, and V. S. Vavilov, Nucl. Instrum. Methods Phys. Res. B **39**, 492 (1989).

[16] V. V. Ushakov and A. A. Gippius, J. Cryst. Growth **101**, 458 (1990).

[17] V. M. Konnov and N. N. Loĭko, KSF, No. 9–10 (1997).

[18] V. M. Konnov, N. N. Loĭko, S. G. Chernook, and O. M. Borodina, KSF (1998), at press.

[19] V. N. Yakimkin, Author's Abstract of Candidate's Dissertation, Department of Physics, Moscow State University (1988).

[20] K. A. Kikoin and L. A. Manakova, Fiz. Tekh. Poluprovodn. **29**, 291 (1995) [Semiconductors **29**, 145 (1995)].

Translated by M. E. Alferieff

A model of photoinduced anisotropy in glassy semiconductors

E. V. Emel'yanova and V. I. Arkhipov[a)]

Moscow State Engineering Physics Institute (Technical University), 115409 Moscow, Russia

A model of photoinduced optical anisotropy in amorphous semiconductors is studied theoretically. The change in the optical characteristics of a sample is associated with the photogeneration of geminate electron-hole pairs. If the pairs are generated by linearly polarized light, then the dipole moments of the geminate pairs lie mainly in the polarization plane, making the sample optically anisotropic. The model associates the optical anisotropy of the sample with the mean-square projection $\langle P_z^2 \rangle$ of the dipole moment per unit volume on the polarization axis of the radiation. The evolution of $\langle P_z^2 \rangle$ is determined by the kinetics of the drift and recombination of carriers in geminate pairs. The kinetics of the photoinduced anisotropy under continuous irradiation of the sample and its relaxation as a result of irradiation with pulsed polarized light is calculated. © *1998 American Institute of Physics.* [S1063-7826(98)01808-0]

Photostimulated processes in glassy semiconductors (photoinduced anisotropy, photodarkening, photodichroism) have recently been attracting increasing attention of investigators in view of the prospects of using these phenomena for writing and processing optical information in fiber-optic communication systems.[1–4] Photoinduced changes of the optical characteristics of glasses are often associated with certain changes in the structure of these materials, generally with the appearance of new light-induced point defects or a change in the state of existing point defects. In particular, many investigators explain photoinduced anisotropy by light-induced restructuring of the intrinsic defects.[5] In this model it is assumed that exposure to polarized light results in the appearance of an anisotropic state of the glass due to rotations of the intrinsic dipole moments of the defects. For the effect to appear the photon energy must not be less than the activation energy of rotation of the dipoles. The experimental results show that the red edge of the photostimulated anisotropy is close to the red edge of the photoconductivity.[2,5] This suggests that an electronic mechanism of anisotropy is possible. Nonequilibrium carriers must be generated for the anisotropy to appear. Photogeneration of nonequilibrium electron-hole pairs is considered to be an intermediate stage of the formation of photoinduced structural defects. In view of this circumstance, we note that a short thermalization length of hot photoionized carriers is characteristic of disordered semiconductors, so that photogeneration of nonequilibrium carriers involves the formation of geminate pairs.

A geminate pair consists of an electron and a hole which are produced in the same photoionization event and are bound by their intrinsic Coulomb field. The subsequent fate of the carriers that form a geminate pair is determined by the competition between diffusion and drift processes in the intrinsic field. The carriers can either come together under the action of the field and recombine or separate from one another in the process of diffusion and become completely independent. Geminate pairs evidently possess an intrinsic dipole moment, which also varies during the evolution of a pair. When a sample is illuminated by unpolarized light, all directions of initial separation of the hot carriers in a plane perpendicular to the wave vector are equally likely and the dipole moments of the pairs are oriented in this plane absolutely randomly. However, if the pairs are generated by linearly polarized light, then the above-mentioned symmetry of separation of the carriers is destroyed, a predominant direction of initial orientation of the dipole moments of the geminate pairs arises, and a macroscopic photostimulated polarization arises in the sample and in turn can give rise to optical anisotropy. Thus, the model under consideration associates the kinetics of photostimulated anisotropy with the evolution of dipole moments of geminate pairs.

Let us consider a glassy semiconductor sample which, starting at time $t=0$, is exposed to linearly polarized light (anisotropizing radiation). The radiation generates geminate electron-hole (Onsager) pairs in the sample. Let us assume that under the action of the polarized light the carriers emerge mainly along one axis (the z axis), whose direction is determined by the polarization of the light wave. It is clear from symmetry considerations that the carriers are equally likely to emerge in both the positive and negative directions along the z axis. For this reason, the average dipole moment $\langle \mathbf{P} \rangle$ per unit volume, just as the average projection of the dipole moment onto any axis, remain equal to zero even after photoexcitation of the sample. Therefore, the photostimulated anisotropy A must be determined by the maximum difference in the mean-square projections of the dipole moment onto two mutually perpendicular axes. In the case at hand, such axes clearly are the z axis and any axis perpendicular to it: $A \sim \langle P_z^2 \rangle - \langle P_\perp^2 \rangle$ (P_z and $P_\perp$ are the corresponding projections of the dipole moment). As already mentioned above, the evolution of this quantity is determined by the kinetics of drift, diffusion, and recombination of carriers in geminate pairs. In the present paper we shall study this kinetics at low temperatures, where the effects of photoinduced anisotropy are most pronounced. Under these conditions carrier diffu-

sion can be ignored and it can be assumed that the relaxation of the dipole moments of geminate pairs is entirely due to drift of the carriers in the Coulomb field which binds them.

As is well known, the kinetics of nonequilibrium carriers in disordered materials is controlled by capture of the carriers in localized states with a distribution of energies.[6,7] In this case, at each moment t the carriers form two groups. Most carriers are captured in localized states and are immobile. Charge transport is effectuated by a smaller fraction of mobile carriers, which at this moment are in delocalized (conducting) states. We note that under real conditions the contribution of mobile carriers to their total density is negligible, and the distribution function f for the total density is virtually identical to the distribution function f_t of localized carriers. Accordingly, the kinetics of carriers in geminate pairs is described in the absence of diffusion by the Smoluchowski equation for the distribution functions of the total density and the density f_c of mobile carriers:

$$\frac{\partial f(\mathbf{r},t)}{\partial t} - \mu_c \mathrm{div}\left[\frac{e}{4\pi\varepsilon\varepsilon_0}\frac{\mathbf{r}}{r^3}f_c(\mathbf{r},t)\right] = G(\mathbf{r},t), \tag{1}$$

where $\mathbf{r}$ are the coordinates relative to the position of the immobile carrier (for example, the electron), $G(\mathbf{r},t)$ is the generation rate of geminate pairs, μ_c is the mobility of carriers in delocalized states, e is the carrier charge, ε_0 is the permittivity of free space, and ε is the dielectric constant.

Equation (1) describes the drift of charge carriers toward their partners. The presence of a singularity in the Coulomb field at $\mathbf{r}=0$ has the effect that the carrier flux Φ,

$$\Phi = -\oint_S dS\mu_c \frac{e\mathbf{r}}{4\pi\varepsilon\varepsilon_0 r^3}f_c(\mathbf{r},t), \tag{2}$$

through a sphere S of arbitrarily small radius centered at $\mathbf{r}=0$ is nonvanishing:

$$\Phi = -\frac{\mu_c e}{\varepsilon\varepsilon_0}f_c(0,t). \tag{3}$$

Carriers that approach their partners recombine with them and therefore Eq. (3) gives the time dependence of the recombination rate.

The wide energy spectrum $g(E)$ of localized states in amorphous semiconductors accounts for the fact that charge transport continues for some time under the conditions of a nonstationary equilibrium energy distribution of localized carriers. Under these conditions most carriers are captured in deep states, thermal escape from which at the time t is unlikely. Recall that $t=0$ corresponds to the time at which the carriers are generated. Clearly, the density $g_d(E,t)$ of "deep traps" determined in this manner depends on the time. Since the density of carriers captured in deep traps changes only as a result of capture, the energy distribution function of these carriers satisfies the equation

$$\frac{\partial}{\partial t}\left[\frac{\varphi_d(E,\mathbf{r},t)}{g_d(E,t)}\right] = \frac{1}{\tau_0 N_t}f_c(\mathbf{r},t), \tag{4}$$

where τ_0 is the lifetime of carriers in conducting states before capture, and N_t is the total density of localized states.

Integrating Eq. (4) with respect to time and then with respect to energy, and allowing for the fact that before thermal equilibrium is established virtually all carriers are located in deep traps, we obtain

$$f(\mathbf{r},t) = \frac{N_d}{\tau_0 N_t}\int_0^t dt' f_c(\mathbf{r},t'), \tag{5}$$

where $N_d(t) = \int_0^\infty dE g_d(E,t)$ is the total density of deep traps. Introducing the notation $\tau(t) = \tau_0[N_t/N_d(t)]$ and differentiating expression (5) with respect to time, we establish the relationship between the distribution functions of the total carrier density and the density of carriers in conducting states:

$$f_c(\mathbf{r},t) = \frac{\partial}{\partial t}[\tau(t)f(\mathbf{r},t)]. \tag{6}$$

Equation (6) is the basic equation describing nonequilibrium (dispersive) transport. Let us now turn to the calculation of the function $\tau(t)$, i.e., the time dependence of the total density of deep traps.

A localized state with energy E remains, by definition, a deep trap up to the time t if a carrier does not escape from this state before that time. The probability $w(E,t)$ that a carrier remains localized in a state with energy E up to the time t is described by the Poisson distribution

$$w(E,t) = \exp\left[-\nu_0 t\exp\left(-\frac{E}{kT}\right)\right], \tag{7}$$

where ν_0 is the frequency of escape attempts, T is the temperature, and k is Boltzmann's constant. Multiplying the probability w by the energy distribution of the total density of localized states $g(E)$ and integrating over the energy, we obtain the time dependence of the total density of deep traps and therefore the function $\tau(t)$

$$\tau(t) = \tau_0 N_t\left\{\int_0^\infty dE g(E)\exp\left[-\nu_0 t\exp\left(-\frac{E}{kT}\right)\right]\right\}^{-1}. \tag{8}$$

We use the equation for dispersive transport to describe the evolution of the dipole moment of geminate pairs. Substituting Eq. (6) into Eq. (1) and integrating over time, we obtain the dispersive form of the Smoluchowski equation

$$f(\mathbf{r},t) - \mu_c\tau(t)\mathrm{div}\left[\frac{e}{4\pi\varepsilon\varepsilon_0}\frac{\mathbf{r}}{r^3}f(\mathbf{r},t)\right]$$

$$= f(\mathbf{r},0) + \int_0^t dt' G(\mathbf{r},t'), \tag{9}$$

where the function $f(\mathbf{r},0)$ describes the initial carrier density distribution in a geminate pair generated by anisotropizing radiation. Using the relations (6) and (3), we find an expression for the recombination rate of geminate partners in terms of the total density distribution function:

$$\Phi(t) = -\frac{e\mu_c}{\varepsilon\varepsilon_0}\frac{d}{dt}[\tau(t)f(0,t)] = -R\frac{d}{dt}[\tau(t)f(0,t)], \tag{10}$$

where R is the Langevin recombination constant.

The initial carrier density distribution in a geminate pair is formed in the process of thermalization of hot photoexcited carriers. (To avoid confusion, we note that in our case we are dealing with the thermalization of carriers in a band of conducting states before capture in a trap.) The thermalization length depends on the excess energy of a hot carrier, while the latter is determined by the wavelength of the generating radiation. If pairs are generated by a pulse of monochromatic, linearly polarized light $[G(\mathbf{r},t) \sim \delta(t)]$, then the thermalization length r_0 and the direction of separation of the carriers can be assumed to be the same for all pairs. Using these approximations, we can write the initial distribution in spherical coordinates with polar axis z as follows:

$$f(\mathbf{r},0) = (1/4\pi r_0^2)\,\delta(r-r_0)[\,\delta(\cos\vartheta-1)+\delta(\cos\vartheta+1)\,],$$
$$\tag{11}$$

where ϑ is the polar angle. The boundary conditions are that the distribution function is bounded at $r=0$ and there are no geminate partners at infinite separation:

$$f(0,t)<\infty, \quad f(\infty,t)=0. \tag{12}$$

Solving Eq. (9) with the initial and boundary conditions (11) and (12), we obtain

$$f(r,\vartheta,t) = \frac{\varepsilon_0\varepsilon}{\mu_c e\,\tau(t)}\exp\left[\frac{4\pi\varepsilon_0\varepsilon(r^3-r_0^3)}{3\mu_c e\,\tau(t)}\right]$$
$$\times[1-\Theta(r-r_0)][\,\delta(\cos\vartheta-1)+\delta(\cos\vartheta+1)\,],$$
$$\tag{13}$$

where Θ is the unit step function,

$$\Theta(r-r_0)=\begin{cases}1, & r>r_0, \\ 0, & r<r_0.\end{cases} \tag{14}$$

Integrating the distribution function (13) over the coordinates, we obtain the time dependence of the density $n(t)$ of pairs which have escaped recombination up to the time t:

$$n(t)=n_0[1-\exp(-z_0)],$$

where n_0 is the initial density of geminate pairs, and $z_0=[4\pi\varepsilon_0\varepsilon/3\mu_c e\,\tau(t)]r_0^3$.

Since in our case the projection of the dipole moment onto any axis perpendicular to the z axis equals zero, the anisotropy is simply proportional to $\langle P_z^2 \rangle$:

$$\langle P_z^2 \rangle(t) = n_0 e^2 2\pi \int_0^\infty dr\,r^2 r^2 \int_0^\pi d\vartheta\sin\vartheta(\cos\vartheta)^2 f(r,\vartheta,t)$$

$$= n_0 e^2\left[\frac{3\mu_c e\,\tau(t)}{4\pi\varepsilon_0\varepsilon}\right]^{2/3}\exp\left[\frac{4\pi\varepsilon_0\varepsilon r_0^3}{3\mu_c e\,\tau(t)}\right]\int_0^{z_0} dz\,z^{2/3}\exp(z).$$
$$\tag{15}$$

The function $\langle P_z^2 \rangle(t)$ described by Eq. (15) has simple asymptotic behavior for short and long relaxation times:

$$\langle P_z^2 \rangle(t) \simeq n_0 e^2 r_0^2, \quad \tau(t)\ll\frac{4\pi\varepsilon_0\varepsilon}{3\mu_c e}r_0^3;$$

$$\langle P_z^2 \rangle(t) \simeq n_0 e^2 r_0^2\frac{4\pi\varepsilon_0\varepsilon r_0^3}{5\mu_c e\,\tau(t)}, \quad \tau(t)\gg\frac{4\pi\varepsilon_0\varepsilon}{3\mu_c e}r_0^3. \tag{16}$$

FIG. 1. Time dependence of the geminate pair density under pulsed action of polarizing light for different values of the dispersion parameter $\alpha = kT/E_0$: 1 — 0.2; 2 — 0.4; 3 — 0.6; 4 — 0.8. $\sigma I_0 = 10^2$ s^{-1}, $r_0 = 5 \times 10^{-9}$ M, $\tau_0 = 10^{-11}$ s^{-1}.

We shall illustrate the time dependence of the function $\langle P_z^2 \rangle(t)$ for the example of an exponential energy distribution of localized states which is typical for many glassy semiconductors:

$$g(E) = \frac{N_t}{E_0}\exp\left(-\frac{E}{E_0}\right), \tag{17}$$

where E_0 is the characteristic energy of the spectrum. In this case the function $\tau(t)$ is a power-law function, $\tau(t) = \tau_0(\nu_0 t)^\alpha$, $\alpha = kT/E_0$, and correspondingly the relaxation of the photoinduced anisotropy at long times also follows a power law: $\langle P_z^2 \rangle(t) \propto t^{-\alpha}$. For materials with an exponential spectrum of localized states (17) the behavior of the functions $n(t)$ and $\langle P_z^2 \rangle(t)$ after the action of a pulse of polarizing light is illustrated by the curves in Figs. 1 and 2.

We have already mentioned above that the appearance of photoinduced anisotropy is often associated with intrinsic defects in the glass. In what follows we shall analyze the time dependence of the anisotropy in a prolonged irradiation
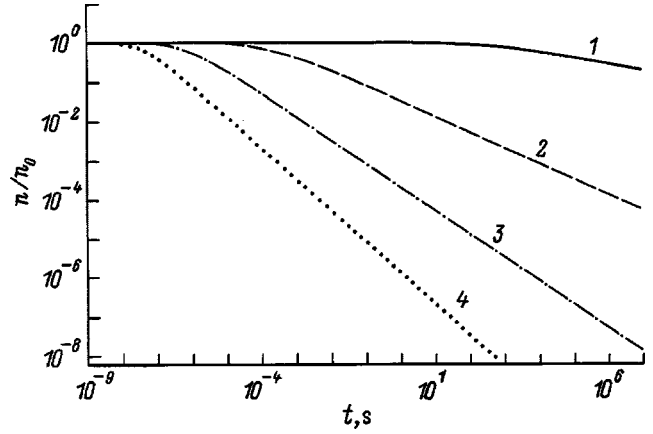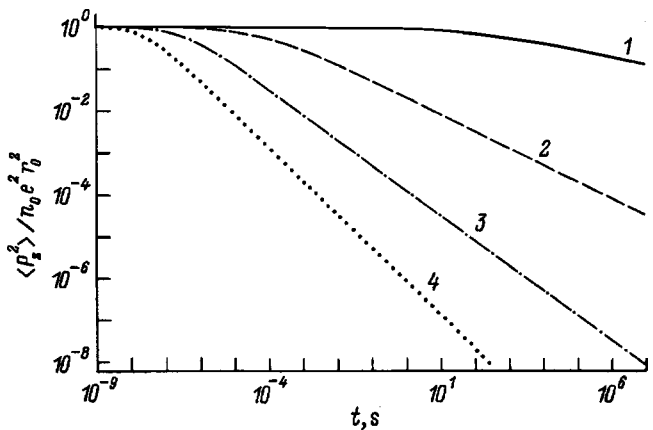

FIG. 2. Time dependence of photostimulated anisotropy under pulsed action of polarizing light for different values of the dispersion parameter $\alpha = kT/E_0$: 1 — 0.2; 2 — 0.4; 3 — 0.6; 4 — 0.8. $\sigma I_0 = 10^2$ s^{-1}, $r_0 = 5 \times 10^{-9}$ M, $\tau_0 = 10^{-11}$ s^{-1}.

regime, assuming that geminate pairs are generated only near defects. Under these conditions we can write Eq. (9) in the form

$$f(\mathbf{r},t) - \mu_c \tau(t) \mathrm{div}\left[\frac{e}{4\pi\varepsilon\varepsilon_0}\frac{\mathbf{r}}{r^3}f(\mathbf{r},t)\right] = \int_0^t dt' G(\mathbf{r},t'),$$

(18)

where the function $G(\mathbf{r},t)$ must be written in the form

$$G(\mathbf{r},t) = (1/4\pi r_0^2)\delta(r-r_0)[\delta(\cos\vartheta-1)$$
$$+ \delta(\cos\vartheta+1)]\sigma I_0[N_{\mathrm{def}}-n(t)].$$

(19)

Here σ is the cross section for the photogeneration of a geminate pair near a defect, I_0 is the intensity of the anisotropizing radiation, and N_{def} is the density of defects. The solution of Eq. (18) for the distribution function has the form

$$f(r,\vartheta,t) = \frac{\varepsilon_0\varepsilon\sigma I_0}{\mu_c e\,\tau(t)}\left\{\int_0^t dl'[N_{\mathrm{def}}-n(t')]\right\}$$
$$\times\exp\left[\frac{4\pi\varepsilon_0\varepsilon(r^3-r_0^3)}{3\mu_c e\,\tau(t)}\right][1-\Theta(r-r_0)]$$
$$\times[\delta(\cos\vartheta-1)+\delta(\cos\vartheta+1)].$$

(20)

Integrating Eq. (20) over r and ϑ, we obtain an equation for the total density of geminate pairs

$$n(t) = \sigma I_0\left\{\int_0^t dt'[N_{\mathrm{def}}-n(t')]\right\}[1-\exp(-z_0)].$$ (21)

The solution of this equation is

$$n(t) = \sigma I_0 N_{\mathrm{def}}\{1-\exp[-z_0(t)]\}\int_0^t dt'$$
$$\times\exp\left\{-\sigma I_0\int_{t'}^t dt''\{1-\exp[-z_0(t'')]\}\right\}.$$ (22)

Substituting Eq. (22) into Eq. (20), multiplying the distribution function by $e^2 r^2\cos^2\vartheta$, and integrating over the angle and the coordinate, we obtain an expression for the mean-square projection of the dipole moment onto the z axis

$$\langle P_z^2(t)\rangle = e^2 r_0^2\sigma I_0 N_{\mathrm{def}}[z_0(t)]^{-2/3}\exp[-z_0(t)]$$
$$\times\left\{\int_0^{z_0(t)} z^{2/3}\exp(z)dz\right\}\int_0^t dt'$$
$$\times\exp\left\{-\sigma I_0\int_{t'}^t dt''\{1-\exp[-z_0(t'')]\}\right\}.$$

(23)

The time dependence described by Eq. (23) has the following characteristic sections. At short times the drawing together of the carriers in pairs and the geminate recombination have not yet commenced, and the time dependence of the squared projection of the dipole moment is determined by the pair generation rate:
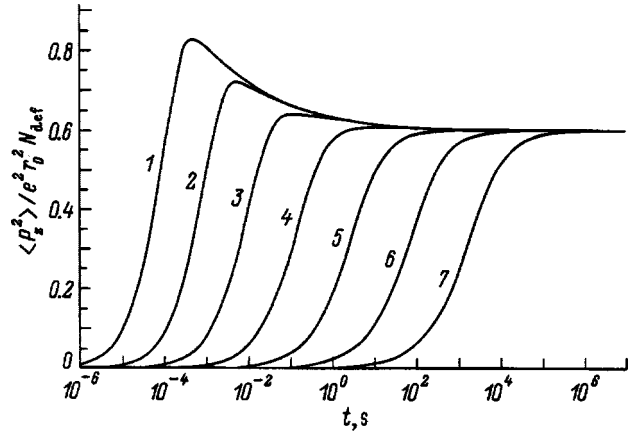
FIG. 3. Time dependence of the photostimulated anisotropy under continuous action of polarizing light with different intensities. σI_0, s^{-1}: *1* — 10^4; *2* — 10^3; *3* — 10^2; *4* — 10; *5* — 1; *6* — 10^{-1}; *7* — 10^{-2}. $\alpha = 0.3$.

$$\langle P_z^2(t)\rangle = N_{\mathrm{def}}e^2 r_0^2[1-\exp(-\sigma I_0 t)],$$
$$\tau(t) \ll \frac{4\pi\varepsilon_0\varepsilon r_0^3}{3\mu_c e}.$$ (24)

The subsequent behavior of the function $\langle P_z^2(t)\rangle$ depends on the ratio of the characteristic geminate recombination time and the total-ionization time of defects, while the latter in turn is determined by the illumination intensity. If geminate recombination starts before a significant fraction of defects is ionized, the time dependence $\langle P_z^2(t)\rangle$ is determined by the competition between generation and recombination of geminate pairs. As a result, $\langle P_z^2(t)\rangle$ increases as a sublinear function of time

$$\langle P_z^2(t)\rangle = \sigma I_0 N_{\mathrm{def}}e^2 r_0^2\frac{4\pi\varepsilon_0\varepsilon r_0^3}{5\mu_c e}\frac{t}{\tau(t)},$$
$$\frac{4\pi\varepsilon_0\varepsilon r_0^3}{3\mu_c e\,\tau(t)}\ll 1, \quad \frac{4\pi\varepsilon_0\varepsilon r_0^3}{3\mu_c e\,\tau(t)}\sigma I_0 t\ll 1.$$ (25)

If the illumination is sufficiently intense so that essentially all defects are ionized before the carriers have time to assemble in pairs and before geminate recombination commences, we see a quasistationary section $\langle P_z^2(t)\rangle = N_{\mathrm{def}}E^2 r_0^2$ on the curve $\langle P_z^2(t)\rangle$ at times that satisfy the conditions $\tau(t)\ll 4\pi\varepsilon_0\varepsilon r_0^3/3\mu_c e$, $t\gg 1/\sigma I_0$. In the limit of long times, the mean-square projection of the dipole moment onto the z axis reaches a steady-state value $\langle P_z^2(t\to\infty)\rangle = \langle P_z^2\rangle_{\mathrm{st}} = (3/5)N_{\mathrm{def}}e^2 r_0^2$, which does not depend on the generation intensity, the temperature, or the specific form of the spectrum of localized states.

The time dependences of the function $\langle P_z^2(t)\rangle$ are shown in Figs. 3 and 4 for different values of the illumination intensity and dispersion parameter. At low intensity of the anisotropizing radiation and high temperature (i.e., relatively large dispersion parameters) the quantity $\langle P_z^2(t)\rangle$ increases monotonically, reaching a steady-state value. If the radiation is sufficiently intense, and the dispersion parameter is small, which corresponds to low temperatures, a quasistationary section almost two times greater than the stationary value is observed on the curve $\langle P_z^2(t)\rangle$. It should be noted that the
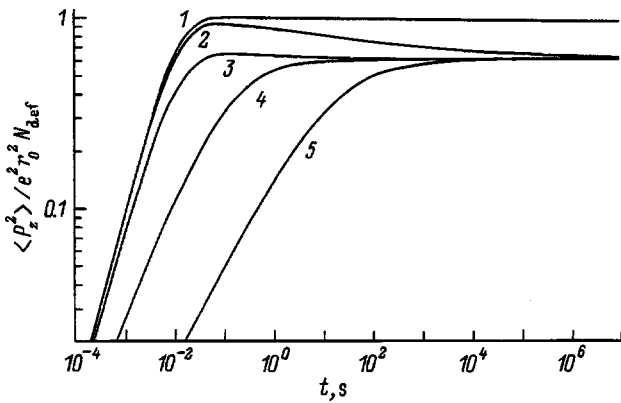
FIG. 4. Time dependence of the photostimulated anisotropy under the continuous action of polarizing radiation for different values of the dispersion parameter $\alpha = kT/E_0$: 1 — 0.1; 2 — 0.2; 3 — 0.3; 4 — 0.4; 5 — 0.5. $\sigma I_0 = 10^2$ s^{-1}.

FIG. 5. Time dependence of the geminate pair density under continuous action of polarizing radiation with different intensities. σI_0, s^{-1}: 1 — 10^4; 2 — 10^3; 3 — 10^2; 4 — 10; 5 — 1; 6 — 10^{-1}; 7 — 10^{-2}. $\alpha = 0.3$.

total density of geminate pairs is always a monotonically increasing function of time (see Fig. 5). The explosive character of the kinetics of photostimulated anisotropy is therefore explained not by the fact that the density of geminate pairs exceeds its steady-state value but rather by the fact that the dipole moment of each generated pair decreases only when the total density of pairs no longer increases, since essentially all defects are ionized. Experimental observation of the nonmonotonic kinetics of the photostimulated anisotropy under the conditions indicated above could be viewed as confirmation of the model formulated by us.

a)E-Mail: via@scon.mephi.msk.su; fax (095) 3242111

[1] V. I. Arkhipov and E. V. Emel'yanova, Fiz. Tekh. Poluprovodn. **28**, 1776 (1994) [Semiconductors **28**, 985 (1994)].

[2] V. M. Lyubin and V. K. Tikhomirov, Fiz. Tverd. Tela (Leningrad) **32**, 1838 (1990) [Sov. Phys. Solid State **32**, 1069 (1990)].

[3] A. M. Andriesh, V. V. Ponomar', V. L. Smirnov, and A. V. Mironos, Kvant. Élektron. **13**, 1093 (1986) [Sov. J. Quantum Electron. **16**, 721 (1986)].

[4] A. M. Andriesh [Ed.], *Glassy Semiconductors for Optoelectronics* [in Russian], Shniintsa, Kishinev, 1991.

[5] V. M. Lyubin and V. K. Tikhomirov, Pis'ma Zh. Tekh. Fiz. **15**, 29 (1989) [Sov. Tech. Phys. Lett. **15**, 11 (1989)].

[6] V. I. Arkhipov, Fiz. Tekh. Poluprovodn. **20**, 556 (1986) [Sov. Phys. Semicond. **20**, 351 (1986)].

[7] V. I. Arkhipov and A. I. Rudenko, Philos. Mag. B **45**, 189 (1982).

Translated by M. E. Alferieff

Light absorption and photoluminescence of porous silicon

A. N. Obraztsov

M. V. Lomonosov Moscow State University, 119899 Moscow, Russia

V. A. Karavanskiĭ

Institute of General Physics, Russian Academy of Sciences, 117942 Moscow, Russia

H. Okushi and H. Watanabe

Electrotechnical Laboratory, Tsukuba, 305 Ibaraki, Japan

The results of an experimental study of Raman scattering, photoluminescence, and light absorption and reflection in porous silicon layers obtained by electrochemical etching of single-crystal wafers are presented. It is concluded on the basis of an analysis of the experimental data that the centers responsible for radiative and nonradiative recombination in this material are of a multiple character. The experimental data show that the centers whose maximum of optical excitation lies in the blue-green region of the spectrum have a uniform distribution, in contrast with the centers whose region of efficient excitation lies in the red region of the spectrum. The radiative recombination efficiency of the latter increases in a thin, near-surface layer of a porous-silicon film. © *1998 American Institute of Physics.*
[S1063-7826(98)01908-5]

1. INTRODUCTION

Different nanostructural materials have recently been attracting close attention because of the their unusual properties. A characteristic example of such materials are layers of porous silicon (PS), which are ordinarily obtained by electrochemical etching of crystal wafers and which consist of silicon particles, several nanometers in size, separated by voids.[1,2] A distinguishing feature of PS is a large shift of the fundamental absorption edge into the short-wavelength direction with respect to crystal Si and the presence of intense luminescence in the visible region of the spectrum.[2,3] Several mutually exclusive models have been used to explain the optical properties of PS (see, for example, the review articles in Refs. 2–5). However, despite extensive studies, the nature of these features of PS has yet to be conclusively determined. This stems, in particular, from the fact that the properties of the PS obtained with even slightly different parameters of the electrochemical process[1–5] or storage conditions[6,7] differ considerably.

The high sensitivity of PS to different external perturbations makes the selection of experimental methods for its study very important. It has been shown that the method of photoacoustic (PA) spectroscopy is effective for investigating optical absorption in layers of porous silicon.[8] In our study we used this method to investigate a specially prepared series of PS samples and at the same time to analyze the light reflection and photoluminescence spectra.

2. SAMPLE PREPARATION AND MEASUREMENT METHODS

The PS samples which we have studied were synthesized as KDB-10 silicon wafers [boron-doped silicon with (100)

orientation and resistivity $\rho = 10 \ \Omega \cdot cm$]. A Teflon-type polymer, two-chamber electrochemical cell (the area of the working region was equal to about 1 cm^2) with platinum electrodes was used for anodization. The electrolyte composition was HF(49%):C$_2$H$_5$OH in a 1:1 ratio. The anodization process was conducted in the dark at room temperature. Porous silicon layers differing by the anodization current density (from 5 to 80 mA) and anodization time (from 1 to 12 min) were prepared. After anodization the samples were washed in an ethanol stream and dried in flowing air. Before the measurements were performed, all samples were held in air for one month under normal conditions.

The photoacoustic measurements were performed with an updated PA spectrometer (Model 6001) manufactured by the Princeton Applied Research Corporation. The spectral dependences for the amplitude and phase of the PA signal were recorded in the range from 200 to 1500 nm with a step of 4 nm. The spectral width of the light beam separated by the grating monochromator was 8 nm for UV and visible light and 32 nm in the infrared (IR) range. To take into account the spectral characteristics of the light source employed (1-kW ultrahigh-pressure xenon lamp) all amplitude spectra were normalized to the PA spectrum obtained for carbon black, for which the spectral dependence of the absorption can be assumed equivalent to the spectrum of an absolute blackbody.[9] The light was modulated by means of a mechanical interrupter with a frequency in the range 20~5000 Hz. The experimental samples were placed into a hermetically sealed, stainless-steel cell filled with air at atmospheric pressure.

The reflectance of the samples under normal incidence

of light was also measured using the xenon lamp and grating monochromator, which were part of a PA spectrometer. The wavelength dependence, measured with a pyroelectric detector, of the intensity of the light passing through the monochromator was used as the normalization spectrum.

The photoluminescence (PL) and Raman scattering (RS) spectra were obtained with an U1000 spectrometer (Jobin Yvon) combined with an argon laser (488 nm) and Renishaw spectrometer combined with a helium-neon laser (633-nm line). Both spectrometers were equipped with microphotometric attachments, which enabled micropositioning of the samples as well as measurements with an approximately 1.5-μm probe-laser spot on the surface of the sample. The RS and PL observations were conducted in the standard geometry, where the laser beam and the scattered light or the luminescence radiation were directed normal to the surface of the silicon substrate, and also on a transverse cleavage surface of the samples.

3. EXPERIMENTAL RESULTS AND DISCUSSION

The PS samples possessed a uniform, optically smooth surface. The thickness of the PS layer measured with an optical microscope on a transverse cleavage surface of the samples depended on the anodization current density and duration and varied from 5 to 15 μm. In all experimental samples an intense RS line (see Fig. 1) was present near the fundamental optical vibration of silicon (frequency $\nu = 520.5$ cm^{-1}). The asymmetric shape of this line and its shift in the low-frequency direction as compared with the RS spectra of the initial Si are ordinarily attributed to the spatial confinement of phonons, which is observed for silicon crystallites several nanometers in size. The spectral profile of this line, calculated in accordance with the indicated model[5] for 2, 3.5, and 9-nm silicon crystallites, is shown in Fig. 1 (solid curves), together with the experimentally obtained RS spectra (dots) for PS layers grown with 60-mA (curve *1*) and 30-mA (curve *2*) currents with 100-s anodization and for the initial silicon wafer (curve *3*). Curve *1* in Fig. 1 corresponds to a PS film with thickness $d = 12$ μm. In the entire series of experimental samples, the RS spectrum of this film differed the most from that of the initial silicon wafer. This circumstance enabled us to conclude that the size of the silicon particles in the experimental PS films lies in the range from 9 to 2 nm.

The described features of the RS spectra were observed using an argon laser (488- nm line) and helium-neon laser (633- nm line). However, in the second case the spectral position of the RS line fell into the region of intense photoluminescence of PS, as one can see from Fig. 2, where the PL spectra $I_{PL}(\lambda)$ obtained for several of the experimental samples are presented as examples (the RS line of silicon is marked by an asterisk).

It follows from Fig. 2 that pronounced features in the form of periodic modulation of the bell-shaped profile of $I_{PL}(\lambda)$ with a different period for samples prepared under different conditions are observed in the spectral contour of the PL band. The PL spectra of samples, whose thickness of the porous layers was similar, were approximately the same.
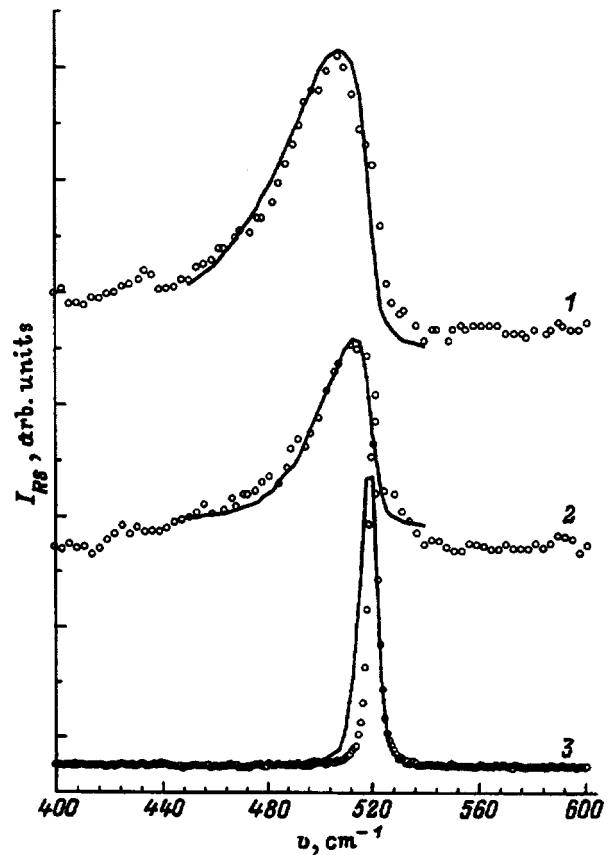
FIG. 1. Characteristic examples of RS spectra $I_{RS}(\nu)$ for porous silicon samples obtained by electrochemical etching for 100 sec with 60-mA (*1*) and 30-mA (*2*) currents. Examples of the RS spectrum of the starting silicon wafer (*3*) are also shown. The solid line shows the contour of the RS line calculated in the model of spatial confinement of phonons[5] for 2, 3.5, and 9-nm silicon particles, respectively.

The PS thickness in turn was determined by the current and anodization length — compare the spectra in Figs. 2d and 2e.

The obvious correlation between the spectral shape of the PL band and the thickness of the porous layer was confirmed by measurements of the light reflection spectra $R(\lambda)$, which are shown in Fig. 2 (dotted lines). The oscillatory character of these curves indicates that light interference occurs in the thin PS film. Using the known values of the PS film thickness (d) and the spectral position of the neighboring interference maxima and minima (λ_1 and λ_2), we determined the refractive index of PS from the formula $2nd = \lambda_1\lambda_2/(\lambda_2 - \lambda_1)$. The values obtained for n (in the interval 1.65 to 1.75 for the range 700–800 nm) agree with the results of other investigations.[2,5] Comparing the spectra presented in Fig. 2 shows that there is good agreement between the positions of the maxima in the reflectance and PL spectra.

Direct measurements of the PL for the samples obtained by cleaving a silicon wafer with a PS layer showed that the luminescence properties of the PS varied strongly for the regions of the film that are located at different distances from the outer surface of the film. A detailed discussion of the results of these measurements is presented in Ref. 10. Here we note only that the PL intensity decreased by two orders of magnitude from the region of the PS film near the surface to
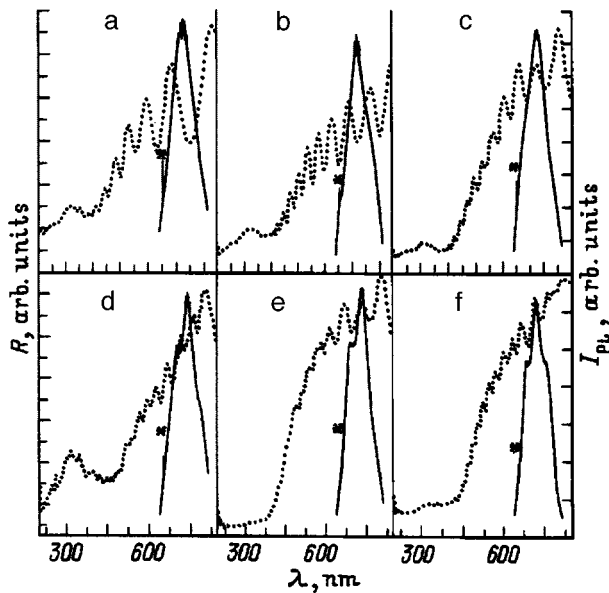
FIG. 2. Characteristic examples of light reflection $R(\lambda)$ (dotted lines) and $I_{PL}(\lambda)$ (solid lines) spectra measured with excitation by a He–Ne laser (633 nm) for PS layers obtained by anodization. Anodization regime — current, mA/time, s: a — 15/100, b — 30/100, c — 60/60, d — 15/240, e — 80/60, f — 60/100. The thickness of the PS layer was 5 (a); 7 (b); 9 (c); 12 (d, e); and 15 (f) μm.

FIG. 3. Characteristic spectral dependences of the photoacoustic signal amplitude $A_{PA}(\lambda)$ measured with a light modulation frequency of 90 Hz for PS layers obtained by anodization. Anodization regime — current, mA/time, s: *1* — 15/100; *2* — 15/240; *3* — 5/720; *4* — 30/100.

regions at the interface with crystal silicon. Just as in the experiments described in Ref. 10, using instead of the 633-nm line of the helium-neon laser light with higher energy (488-nm line of the argon laser) for excitation of PL resulted in virtually complete vanishing of the dependence of the PL intensity on the localization of the probe-laser spot on the transverse cleavage surface of the samples. Additionally, for the 488-nm line the relative amplitude of the interference-induced oscillations in the PL spectrum was much smaller than for the He–Ne laser with comparable laser-beam intensities. The amplitude of these oscillations decreased rapidly with increasing laser intensity, and the differences in the shape of the PL spectra for samples obtained with different anodization currents and durations became negligible.

Unfortunately, we did not have the technical capability of measuring the PL excitation spectra. It was noted that when the 488-nm line was used, the PL intensity recorded in the standard manner in a direction normal to the basal plane of the sample was much higher than for the 633-nm line with the same laser-beam power. This indicates that the PL excitation efficiency decreases for light with lower energy and agrees with existing data on the PL excitation spectrum (see, for example, Ref. 5). Moreover, the experimental data suggest that the PL centers located on the outer surface and in the interior of the PS film have different excitation spectra and different radiative recombination efficiencies. A result of such differences is that when a helium-neon laser is used, luminescence is observed only from a thin portion of the film near the surface. The interference oscillation arising in this case in the PL spectrum has a high enough contrast. As the energy or intensity of the exciting light is raised, the PL increases as a result of an increase in the number of photo-

excited centers and, possibly, as a result of an increase in their quantum recombination efficiency.[11] The contrast of the interference oscillations decreases at the same time, since the light source (PL) is distributed over the entire thickness of the film.
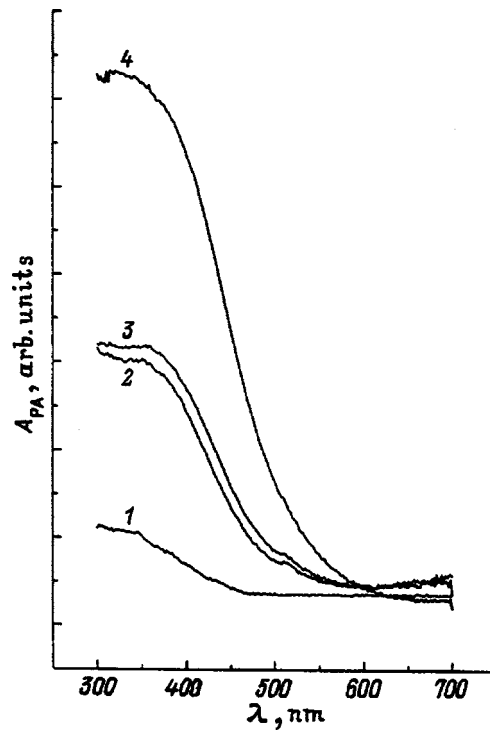
Let us now consider the results of a study of the optical absorption in PS carried out using photoacoustic spectroscopy. Figure 3 shows several characteristic spectral dependences of the PA signal amplitude $A_{PL}(\lambda)$, which is proportional to the amount of heat released in the test material as a result of light absorption. Thus, the curves $A_{PL}(\lambda)$ characterize the spectral behavior of the absorption which accounts only for the nonradiative recombination of photoexcited carriers.[8,9] The behavior of the absorption corresponding to the spectra in Fig. 3 is typical of PS films obtained under the anodization conditions indicated above.[2,5,8] These spectral dependences were obtained with a light modulation frequency of 90 Hz. For all experimental samples the PA signal amplitude at a wavelength greater than 600 nm did not exceed the noise level. Light absorption is much stronger in the blue-green region of the spectrum. This was manifested as an increase in the PA signal amplitude. A comparison of the data from PA measurements with the parameters of the anodization process and the thickness of the PS films showed that the spectral dependence of the PA signal was determined mainly by the thickness of the PS layer and was approximately the same for films which had the same thickness and which were synthesized at different current densities.

As the modulation frequency increased to 1350 Hz or higher, the spectral shape of the amplitude dependence of the
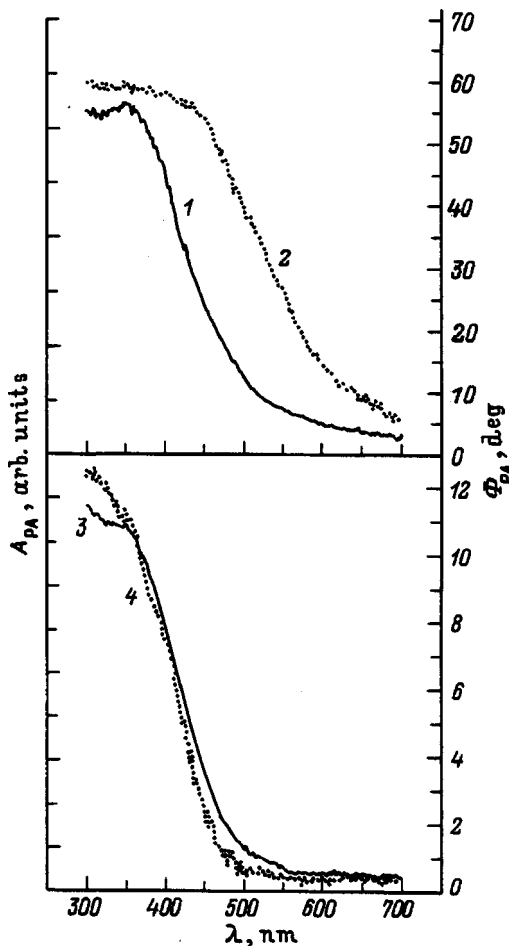
FIG. 4. Amplitude $A_{PA}(\lambda)$ and phase $\Phi_{PA}(\lambda)$ spectra of a PS sample obtained by anodization for 100 sec with a 60-mA current. *1, 3* — $A_{PA}(\lambda)$; *2, 4* — $\Phi_{PA}(\lambda)$. Modulation frequency, Hz: *1, 2* — 90; *3, 4* — 1350.

PA signal remained nearly the same, as can be seen in Fig. 4 (curves *1* and *3*). As is well known, the dominant contribution to the PA signal is the light absorbed over a distance equal to the length of thermal diffusion,[9] $\mu = (\alpha / \pi \tilde{\nu})^{1/2}$ (where $\alpha = k/\rho C$, k is the thermal conductivity, ρ is the density, C is the specific heat, and $\tilde{\nu}$ is the light modulation frequency) whose whose magnitude decreases rapidly with increasing modulation frequency. Preservation of the spectral shape of the dependence $A_{PA}(\lambda)$ as a function of the light modulation frequency therefore signifies that the PS films are uniform from the standpoint of optical absorption.

The phase of the PA signal, which is defined as the phase difference between the modulated light beam and the acoustic signal, measured in our case with a microphone, depends on the propagation time of the thermal disturbance in the test sample. This temporal delay is minimal at high light modulation frequencies, since the thermal diffusion length, which determines the extent of the region where essentially all of the heat producing the acoustic signal is released, is minimal. Additionally, because of the extremely low thermal conductivity this length for PS is evidently shorter than the effective light penetration depth.[8] Accordingly, for a high modulation frequency the form of the spectral dependence of the phase signal $\Phi_{PA}(\lambda)$ is similar to the

amplitude spectral dependence (Fig. 4, curves *3* and *4*).

For low frequencies the thermal diffusion length and hence the propagation time of a thermal disturbance in the PS film increase. This increase is all the larger, the greater the light penetration depth in the experimental sample, i.e., the lower the light absorption. As a result, the amplitude and phase spectral dependences at a modulation frequency of 90 Hz differ appreciably, and this difference increases with increasing wavelength of the light (compare curves *1* and *2* in Fig. 4). At the same time, such behavior of the spectral dependence $\Phi_{PA}(\lambda)$ confirms our assumption that light absorption occurs in the long-wavelength region of the spectrum, right up to 800 nm, even though the absorption in this range is relatively low, as follows from the amplitude spectra $A_{PA}(\lambda)$.

4. CONCLUSIONS

The photoacoustic spectroscopy data thus show that the light absorption efficiency in PS films in the blue-green region of the spectrum is approximately the same over the thickness, while in the long-wavelength region the light absorption tends to increase in regions of PS located in the interior layers of the film. At the same time, the luminescence properties of the PS have an appreciably different character and, if relatively long-wavelength radiation (633 nm) is used for excitation, the highest PL efficiency is observed on the outer surface of the porous layer. Keeping in mind the fact that the photoacoustic effect is due only to the portion of the absorbed light that is converted into heat, it can be assumed that the system of centers that determines the PL (or channels for transferring excitation to them) has different excitation spectra. The recombination properties of the centers whose highest excitation efficiency corresponds to the blue-green region of the spectrum are distributed relatively uniformly over the entire film thickness, while the centers that absorb light in the red spectral region have a higher radiative recombination efficiency (or lower nonradiative recombination efficiency) in a thin region near the surface. This conclusion agrees with the notions that the PL centers in PS are of a multiple character, as is confirmed by many experimental results.

[1] V. Lehman and U. Gosele, Appl. Phys. Lett. **58**, 856 (1991).
[2] S. V. Svechnikov, A. V. Sachenko, G. A. Sukach, A. M. Evstigneev, and E. B. Kaganovich, Optoélektron. i Poluprovodn. Tekhn., No. 27, 3 (1994).
[3] L. T. Canham, Appl. Phys. Lett. **57**, 1046 (1990).
[4] S. M. Prokes, Electrochem. Soc. Interface **4**, 41 (1994).

[5] Y. Kanemitsu, Phys. Rep. **263**, 1 (1995).

[6] M. A. Tischler, R. T. Collins, J. H. Stathis, and J. C. Tsang, Appl. Phys. Lett. **60**, 639 (1992).

[7] Chi-Huei Lin, Si-Chen Lee, and Yang-Fang Chen, J. Appl. Phys. **75**, 7728 (1994).

[8] A. N. Obraztsov, H. Okushi, H. Watanabe, and V. Yu. Timoshenko, Fiz. Tekh. Poluprovodn. **31**, 629 (1997) [Semiconductors **31**, 534 (1997)].

[9] A. Rosencwaig, in *Photoacoustics and Photoacoustic Spectroscopy,* Wiley and Sons, N. Y., 1981, p. 850.

[10] A. N. Obraztsov, V. A. Karavanskiĭ, H. Okushi, and H. Watanabe, Poverkhnost', No. 1, 64 (1998).

[11] E. Bustarret, M. Ligeon, I. Mihalcescu, and J. Oswald, Thin Solid Films **255**, 234 (1995).

Translated by M. E. Alferieff

Multimode nature and magnetophonon resonance of quaternary solid solutions of zinc, cadmium, and mercury tellurides

E. M. Sheregiĭ, J. Cebulski, and J. Polit

Institute of Physics, Rzeszow Pedagogical University, 35-310 Rzeszow, Poland

V. I. Ivanov-Omskiĭ

A. F. Ioffe Physicotechnical Institute, Russian Academy of Sciences, 194021 St. Petersburg, Russia

W. Gebicki

Institute of Physics, Polytechnical University in Warsaw, 00-664 Warsaw, Poland

The magnetophonon resonance in a multimode crystal of the solid solution $Zn_xCd_yHg_{1-x-y}Te$
($x=0.08$, $y=0.11$) was investigated in the temperature interval from 77 to 200 K. To
interpret the obtained structure of the magnetophonon resonance spectrum, the phonon modes of
three compositions of this solid solution were studied by the Raman scattering method.
The results presented confirm the three-mode behavior (excluding cluster modes) of the phonon
spectrum of the solid solutions of this class. The complicated structure of the
magnetophonon resonance bands is interpreted on the basis of the values obtained for the phonon
frequencies. The characteristic features of electron transport in such a lattice are shown.
© *1998 American Institute of Physics.* [S1063-7826(98)02008-0]

1. INTRODUCTION

In addition to the solid solutions Ge–Si, quaternary substitution solid solutions have recently been attracting increased attention from investigators. These are solid solutions of three compounds with a common anion (for example, aluminum–gallium–indium arsenides[1]) or two ions and cations in pairs (for example, gallium–aluminum arsenides and phosphides[2]). Another example are solid solutions of zinc–cadmium–mercury tellurides, i.e., $Zn_xCd_yHg_{1-x-y}Te$ (ZCHT in what follows). Attention was first drawn to this material, which could be an alternative to $Cd_xHg_{1-x}Te$ (CHT) — the main material of infrared technology, by Rogalski and Piotrowski[3] (see also Ref. 4). The phase diagram and mechanical properties of ZCHT have been investigated by R. Triboulet.[5] A series of studies of these solid solutions has been performed at the A. F. Ioffe Physicotechnical Institute.[6–8] Using the material obtained by the authors of Refs. 6–8, we have observed magnetophonon resonance (MPR),[9] investigated with its help the temperature dependences of the band parameters,[10] and observed magnetophonon resonance from the difference in the phonon frequencies,[11] first observed in CHT.[12] The uniqueness of the physical properties of ZCHT is shown in Ref. 13.

It seems to us that the multimode behavior of the phonon spectrum of solid substituion solutions, where to each vibrational branch there corresponds more than one phonon frequency associated with the vibrational spectrum of the initial crystals, is an extremely important problem. For example, bimodality in CHT was observed in the well-known study by Baars and Sorger,[14] who were first to show that there exist longitudinal optical (LO phonons) and transverse optical (TO

phonons) vibrations belonging to the HgTe- and CdTe-like sublattices of the crystal. In addition, as it turned out, the LO- and TO-phonon frequencies of one sublattice come closer to together as the content of the other increases. The bimodality of CHT was later confirmed repeatedly in both Raman scattering[15] and optical measurements,[16] as well as by the splitting of the MPR peaks.[17,18]

In ZCHT there exist three sublattices, and one would expect a trimode behavior of the phonon spectrum. However, this is not obvious. The multimodality is closely related to the internal structure of the crystal and is a reflection of the stochastically uniform distribution of substitutions of the cation atoms in the matrix by atoms of another metal. Otherwise one sees clusters of the initial binary compounds, whose reflection are the composition-independent cluster modes. Other possibilities also exist (see, for example, the review in Ref. 19).

In this article we report the results of a study of the MPR and Raman scattering from the standpoint of the multimode nature of ZCHT. A model is proposed for interpreting the structure of the MPR peaks, and the band parameters and their temperature dependences are determined. The characteristic features of electron transport in such a lattice are examined.

2. DESCRIPTION OF THE SAMPLES

The solid solutions ZCHT were obtained by liquid-phase epitaxy on substrates consisting of high-quality cadmium telluride with (111) orientation.

The parameters of the experimental samples are presented in Table I. We see that for the compositions IV and V

TABLE I. Parameters of the experimental samples.

Sample No.	x	y	Electron density, 10^{15} cm^{-3}	Electron mobility, 10^4 cm^2/(V · s)
I	0.02	0.20	–	–
II	0.07	0.21	–	–
III	0.12	0.17	–	–
IV	0.08	0.11	3.5	9.0
V	0.12	0.10	5.0	5.0
VI	0.17	0.08	2.0	2.5

it was possible to obtain *n*-type samples with comparatively high carrier mobility. The temperature dependences of the conductivity and Hall coefficient of these samples manifest an obvious activational character.

Figure 1 shows the concentration profiles (dependences of the component concentrations C on the depth h) of one of the experimental ZCHT films (Table I, composition IV). The profiles were obtained by means of x-ray microprobe analysis (COMEBAX). We see that the uniform layer with depth-independent component concentrations is about 4 μm thick. A transition layer (about 0.5 μm thick), where the cadmium concentration increases sharply and the zinc and mercury concentrations drop to zero, i.e., a transition to the substrate is observed, is located at a greater depth.

FIG. 2. Experimental dependences $d^2\rho_{xx}(B)/dB^2$ for sample IV at temperatures T, K: *1* — 115; *2* — 124; *3* — 146; *4* — 158; *5* — 165; *6* — 172.

3. EXPERIMENTAL DATA ON THE MAGNETOPHONON RESONANCE

A magnetophonon resonance was observed on three ZCHT samples (samples IV, V, and VI). The measurements were performed in pulsed magnetic fields up to $B = 10$ T in the temperature range $T = 77-200$ K. The most detailed investigations were performed for the composition IV. Figure 2 shows the resonance curves obtained for this sample at different temperatures. The distinguishing feature of the curves are the wide bands, which consist of several peaks, observed in the regions 2.0–3.5 and 1.0–1.8 T. From general considerations it can be concluded on the basis of the amplitudes of the peaks and their positions in a magnetic field that the wide peak in the region 2.0–3.5 T is due to transitions between Landau levels 0 and 1, while the peak in the field 1.0–1.8 T is due to the transitions 0→2, etc. In the first group of peaks, the peak $a1^+$ in the temperature interval 115–146 K stands out. As the temperature is raised, the nearby peak $a1^-$ intensifies and at 165 K it becomes dominant. The peak $a2$ in the magnetic field range, where the transitions 0→2 occur, corresponds to these two resonances, since it occurs in a magnetic field approximately two times weaker than $a1^+$ or $a1^-$ (the peaks $a3$ and $a4$ are observed in magnetic fields which are three and four times, respectively, weaker than in the cases $a1^+$ and $a1^-$). The series of peaks b, c, and k can be established in a similar manner.
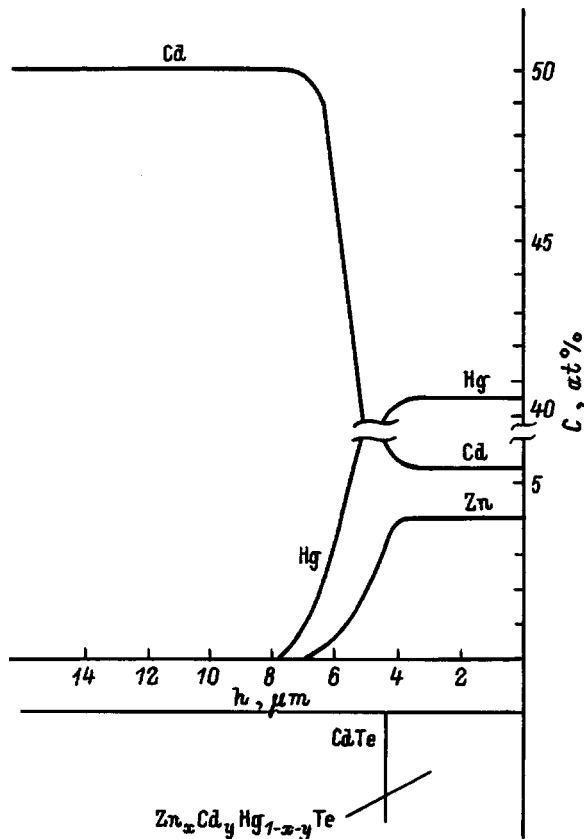

FIG. 1. Concentration profile of sample IV. The concentration distributions of three cations — mercury (Hg), cadmium (Cd), and zinc (Zn) — were obtained using an x-ray microprobe by scanning over a natural cleaved surface.
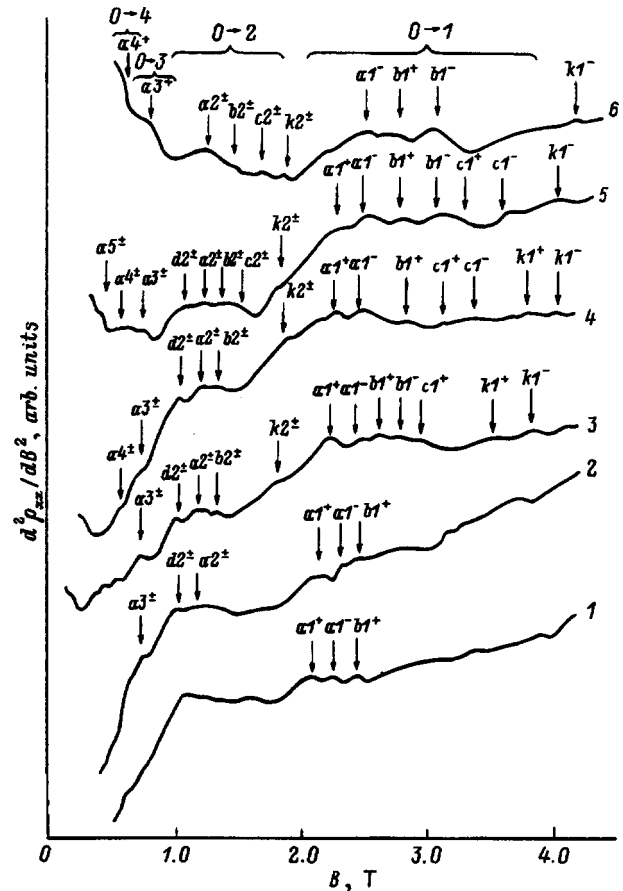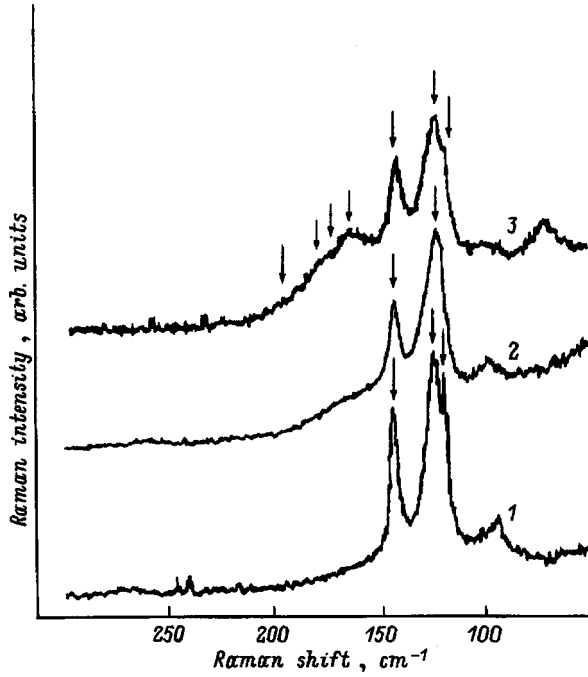
FIG. 3. Room-temperature Raman scattering spectra. Curves *1–3* correspond to samples I–III (Table I).

TABLE II. Interpretation of RS lines.

Line positions, cm^{-1}			Interpretation
Sample I	Sample II	Sample III	
118	118	118	TO HgTe-cluster
121	122	123	TO HgTe-like lattice
142	143	143	TO CdTe-like lattice
–	165–172	163	TO ZnTe-like lattice
–	165–172	174	LO ZnTe-like lattice
–	–	180	TO ZnTe-cluster
–	–	198	LO ZnTe-cluster

The structures of the wide peaks, which are clearly seen on the resonance curves in Fig. 2, correspond at first glance to four series of resonances, each of which is due to absorption of phonons of its own kind. Since the series *a* has the highest amplitude and since the peaks in this series, compared to the corresponding peaks of other series, are shifted in the direction of weaker magnetic fields, it is conceivable that these resonances are due to transitions between Landau levels with absorption of LO(Γ) phonons of the HgTe-like sublattice, which has the lowest LO(Γ) phonon frequency, of the solid solution. However, the correct interpretation of the MPR cannot be made without an independent study of the phonon spectrum of the crystal.

4. RAMAN SCATTERING DATA

Raman scattering (RS) was excited by 200-mW argon laser light (wavelength λ = 514.5 nm). The RS spectra were recorded with a Dilor XY spectrometer. The measurements were performed at room temperature with a spectral resolution of about 4 cm^{-1}. All spectra were obtained in backscattering geometry in unpolarized light. The latter was due to the weak RS signal.

Figure 3 shows the RS spectra for three samples with increasing zinc content (samples I–III). We see that two strong lines are observed on all three curves in the region 100–150 cm^{-1}. Comparing them with data from previous studies of RS in the solid solutions CHT[15] and ZCT (zinc–cadmium–tellurium),[20] we can assume that the line pairs 121 and 142 cm^{-2} (curve *3*) belong to the TO modes of the HgTe- and CdTe-like sublattices, respectively.

At the same time, on the curve *3* the 163-cm^{-1} line (a very weak line can also be distinguished at 174 cm^{-1}), which does not appear at very low zinc content (2% ZnTe —

curve *1*) or is very weak (7% ZnTe — curve *2*), is undoubtedly associated with the ZnTe-like sublattice. The weaker lines at 180 and 197 cm^{-1} on curve III nearly coincide with the frequencies of the LO and TO phonons of the binary compound ZnTe.

A very sharp line is observed at 118-cm^{-1} on curves *1* and *3* (it is virtually absent on curve *2*). This frequency corresponds to the TO mode of the binary compound HgTe.[14–16]

A characteristic feature of the RS spectra is that in them the LO modes of the HgTe- and CdTe-like sublattices are suppressed and essentially only the TO phonons are observed. This could be explained by assuming that the polarization oscillations are screened by electrons, but the CMT lines corresponding to LO phonons appear in RS very clearly in some geometries.[15] Moreover, Sochinski *et al.*[21], while investigating RS in CdTe, also observed, in unpolarized light in backscattering from the (111) plane, TO-phonon peaks which were several times stronger than the LO-phonon peaks.[1]

The positions and interpretation of the above-discussed lines in the RS spectra for the three compositions investigated are presented in Table II. It is important that the RS experiment confirm directly the trimodal character of the lattice of the solid solution $Zn_xCd_yHg_{1-x-y}Te$. At the same time, the existence of zinc telluride and mercury telluride clusters was confirmed in these measurements.

5. DETERMINATION OF THE LONGITUDINAL OPTICAL PHONON FREQUENCIES

Since it is impossible to determine the LO-phonon frequencies for the HgTe- and CdTe-like sublattices from the RS spectra presented here, it is necessary to make use of a well-known property of the dielectric function: The LO-phonon frequencies can be extracted as the roots of the equation $\mathrm{Re}\,\tilde{\varepsilon} = 0$.[22] In the multimode case this method was used in Ref. 23. Following Ref. 23, we construct the dielectric function $\tilde{\varepsilon}$ as a sum of three oscillators, which correspond to the three sublattices of the crystal of the solid solution. Using a Lorentzian for each oscillator, we obtain

$$\varepsilon_\infty + \frac{S_1(\omega_{TO1}^2 - \omega^2)}{(\omega_{TO1}^2 - \omega^2)^2 + \omega^2\gamma_1^2} + \frac{S_2(\omega_{TO2}^2 - \omega^2)}{(\omega_{TO2}^2 - \omega^2)^2 + \omega^2\gamma_2^2}$$

$$+ \frac{S_3(\omega_{TO3}^2 - \omega^2)}{(\omega_{TO3}^2 - \omega^2)^2 + \omega^2\gamma_3^2} = 0. \tag{1}$$
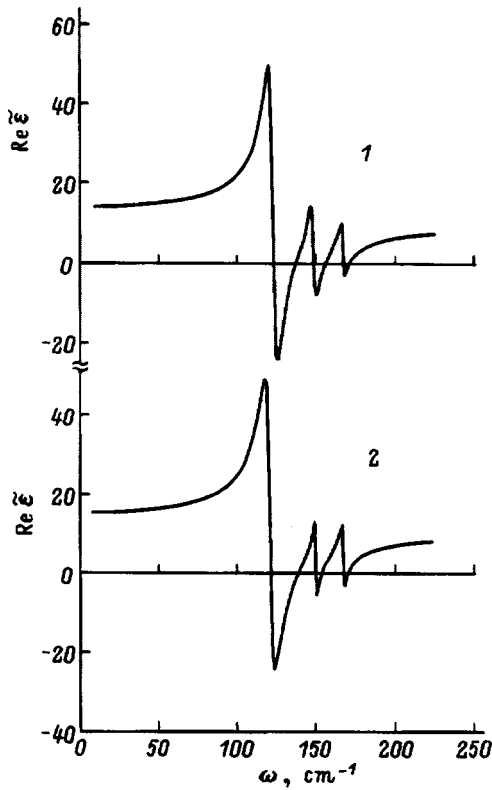
FIG. 4. Computed frequency dependences of the real part of the dielectric function for the compositions II (*1*) and IV (*2*). Computational parameters *1* — HgTe-like lattice: $\omega_{TO1} = 122$ cm^{-1}, $S_1 = 5.6 \times 10^4$ cm^{-2}, $\gamma_1 = 6.6$ cm^{-1}; CdTe-like lattice: $\omega_{TO2} = 143$ cm^{-1}, $S_2 = 1.3 \times 10^4$ cm^{-2}, $\gamma_2 = 5.5$ cm^{-1}; ZnTe-like lattice: $\omega_{TO3} = 165$ cm^{-1}, $S_3 = 6720$ cm^{-2}, $\gamma_3 = 5.5$ cm^{-1}; $\varepsilon_\infty = 10.0$. Solutions of Eq. (1) — zero points: $\omega_1 = 122.8$ cm^{-1}, $\omega_2 = 136.2$ cm^{-1}, $\omega_3 = 148.7$ cm^{-1}, $\omega_4 = 156.9$ cm^{-1}, $\omega_5 = 167.1$ cm^{-1}, $\omega_6 = 171.8$ cm^{-1}. Computational parameters *2* — HgTe-like lattice: $\omega_{TO1} = 121$ cm^{-1}, $S_1 = 6.38 \times 10^4$ cm^{-2}, $\gamma_1 = 6.6$ cm^{-1}; CdTe-like lattice: $\omega_{TO2} = 144$ cm^{-1}, $S_2 = 7790$ cm^{-2}, $\gamma_2 = 5.5$ cm^{-1}; ZnTe-like lattice: $\omega_{TO3} = 165$ cm^{-1}, $S_3 = 7680$ cm^{-2}, $\gamma_3 = 5.5$ cm^{-1}; $\varepsilon_\infty = 10.5$. Solutions of Eq. (1) — zero points: $\omega_1 = 121.6$ cm^{-1}, $\omega_2 = 137.1$ cm^{-1}, $\omega_3 = 150.2$ cm^{-1}, $\omega_4 = 155.8$ cm^{-1}, $\omega_5 = 167.2$ cm^{-1}, $\omega_6 = 171.4$ cm^{-1}.

The parameters S_i and γ_i are the oscillator strength and the damping factor of each mode, respectively, and ε_∞ is the rf permittivity of the film. The quantity S_i was determined on the basis of the oscillator strengths of the initial binary compounds by means of the simple formulas $S_1 = S_{HgTe} \cdot (1 - x - y)$, $S_2 = S_{CdTe} \cdot y$, and $S_3 = S_{ZnTe} \cdot x$. The oscillator strengths S_{HgTe}, S_{CdTe}, and S_{ZnTe} for the binary lattices were taken from Refs. 14, 24, and 25. The value of ε_∞ can be determined from its composition dependence for the solid solution CHT in Ref. 14, substituting $x + y$ for x (the cadmium telluride content); i.e., the total content of cadmium and zinc tellurides in ZCHT, bearing in mind that the rf permittivities of ZnTe and CdTe are virtually identical.

Figure 4 shows the function Re $\widetilde{\varepsilon}(\omega)$, which we computed for the composition II (curve *1*). The oscillator parameters used in the calculations are presented in the caption of the figure. The roots of Eq. (1) are also presented here; ω_1 and ω_2 are the frequencies of the longitudinal optical phonons of the HgTe-like sublattice, ω_3 and ω_4 are for the CdTe-like sublattice, and ω_5 and ω_6 are for the ZnTe-like sublattice.

TABLE III. LO(Γ)-phonon frequencies and energies for compositions II and VI.

Sample	Parameter	HgTe-like lattice	CdTe-like lattice	ZnTe-like lattice	ZnTe-cluster
II	ω_{LO}, cm^{-1}	136.0	157.0	172.0	198.0
	$\hbar\omega_{LO}$, meV	16.8	19.4	21.4	24.5
IV	ω_{LO}, cm^{-1}	137.0	156.0	171.5	198.0
	$\hbar\omega_{LO}$, meV	17.0	19.3	21.3	24.5

Curve *2* in Fig. 4 represents the function Re $\widetilde{\varepsilon}(\omega)$, for which the oscillator parameters were corrected to the composition IV with a somewhat lower cadmium content than the composition II. The oscillator strengths and the rf permittivity for the composition IV were determined in the same way as for the composition II, using the corresponding values of x and y. The values of the frequencies ω_{TO} for the three modes were changed according to the typical composition dependences of the optical phonon frequencies (see Refs. 14 and 20). It thus follows that a decrease in the molar content of the binary compound in the solid solution draws the frequencies of the longitudinal and transverse optical phonons of its sublattice closer together and vice versa. Therefore, decreasing the CdTe content (correspondingly, increasing HgTe with constant ZnTe) should slightly decrease ω_{TO} for the HgTe-like sublattice and increase it for the CdTe-like sublattice, leaving the frequency of the ZnTe transverse optical phonons the same or changing it very little. These changes in ω_{TO} on switching from the composition II to the composition IV can be estimated on the basis of the composition dependences of the phonon frequencies in CHT,[14] from which it follows that a 1% decrease of the cadmium content should decrease the HgTe-like TO-phonon frequency by approximately 0.1 cm^{-1} and increase it by the same amount for the CdTe-like sublattice. On this basis, the frequencies ω_{TO} for the HgTe-, CdTe-, and ZnTe-like lattices with the composition IV were assumed to be 121, 144, and 165 cm^{-1}, respectively, and after substituting them into Eq. (1) the corresponding values of the LO-phonon frequencies were determined. The oscillator parameters used to calculate the curve Re $\widetilde{\varepsilon}(\omega)$ for the composition IV are presented, together with the solutions of Eq. (1), in the caption of Fig. 4. The frequencies and energies of the LO phonons for composition IV (the MPR measurements are presented for this composition) which were determined in this manner are shown in Table III. For comparison, the values of ω_{LO} and $\hbar\omega_{LO}$ for the composition II are also presented here.

6. INTERPRETATION OF THE MAGNETOPHONON RESONANCE DATA

As noted above, the peaks $a1^+$ and $a1^-$ in the resonance curves in Fig. 2 can be interpreted, on the basis of general considerations, as resonances due to the electronic transitions $0^+ \rightarrow 1^+$ and $0^- \rightarrow 1^-$, respectively, with absorption of a HgTe-like LO phonon. The phonon frequency determined above and the position of the MPR peaks $a1^+$ and $a1^-$ in a magnetic field make it possible to find, to a

TABLE IV. Band-structure parameters of $Zn_{0.07}Cd_{0.12}Hg_{0.81}Te$ (sample II) for two temperatures.

Parameter	$T = 146$ K	$T = 165$ K
E_g, meV	192	205
E_p, eV	18	18
γ_1^L	33.7	31.8
$\gamma_2^L = \gamma_3^L$	15.6	14.6
K^L	13.6	12.6
F	−0.5	−0.5
Δ, eV	1	1

first approximation, the parameters of the band structure of a given composition of the solid solution ($Zn_{0.08}Cd_{0.11}Hg_{0.81}Te$).

The calculations were performed by the method used in previous studies,[10,26–28] i.e., it can be assumed, to an adequate degree of accuracy, that the matrix element of the momentum with its energy equivalent E_p and the spin-orbit splitting Δ do not depend on the composition and temperature. The latter two quantities were assumed to be 18 and 1 eV, respectively (just as in CHT[29,30]). This approximation (temperature- and composition-independence) also extends to the curvature of the heavy-hole band and to the parameter F, which determines the effect of the higher bands on the curvature of the conduction band. The Luttinger parameters were calculated using the formulas

$$\gamma_1^L = \frac{E_p}{3E_g} + 2.5, \quad \gamma_2^L = \gamma_3^L = \frac{E_p}{6E_g},$$

$$K^L = \gamma_3^L - \frac{1}{3}\gamma_1^L + \frac{2}{3}\gamma_2 - \frac{2}{3} - \frac{5}{4}\delta_{exch}. \quad (2)$$

Here E_g is the band gap, and $\delta_{exch} = 0.4$ is the correction for the nonlocality of the potential, determined for CHT in Ref. 30.

Fitting the theoretical position in a magnetic field of the resonances due to the transitions $0^+ \rightarrow 1^+$ and $0^- \rightarrow 1^-$ with absorption of a 137-cm^{-1} phonon ($\hbar\omega = 17.0$ meV) to the positions of the peaks $a1^+$ and $a1^-$, respectively, in the curve in Fig. 2, for example, for a temperature of 146 K, gave the value $E_g = 190$ meV. The next step is to calculate the theoretical position of the MPR for the transitions $0^+ \rightarrow 2^+$, $0^- \rightarrow 2^-$, $0^+ \rightarrow 3^+$, and $0^- \rightarrow 3^-$ and to match the computed positions with the peaks in the a series, i.e., $a2$ and $a3$. The refined (by minimizing the rms deviation of the experimental positions of the series-a resonances from the theoretical positions) values of E_g and other parameters of the band structure, which are shown in Table IV, make it possible at the next stage to interpret the b, c, and k series. Since the magnetic field values of the peaks $b1$, $c1$, and $k1$ increase gradually, it must be assumed that these resonances are due to transitions of electrons from the zeroth to the first Landau level with absorption of LO(Γ) phonons with an increasing sequence of frequencies, specifically, of CdTe- and ZnTe-like sublattices and a ZnTe cluster, respectively. The amplitude of the lines corresponding to the phonons of these sublattices in the spectral Raman scattering curves (see Fig. 3) corresponds to the amplitudes of the resonances interpreted in this manner (see Fig. 2). The LO(Γ)-phonon frequencies and energies used to interpret the MPR of sample VI are shown in Table III.

The positions of the MPR peaks of different series were calculated on the basis of the phonon energies (Table III) and band structure parameters (they are presented in Table IV for two temperatures). The general interpretation of the observed

TABLE V. General interpretation of the MPR peaks.

Designation	Interpretation	$T = 146$ K experiment	$T = 146$ K calculation	$T = 165$ K experiment	$T = 165$ K calculation
$a1^+$	$0^+ \rightarrow 1^+$, LO(Γ) HgTe-like lattice	2.24	2.30	2.41	2.42
$a1^-$	$0^- \rightarrow 1^-$, LO(Γ) HgTe-like lattice	2.44	2.44	2.51	2.56
$a2$	$0^+ \rightarrow 2^+$, LO(Γ) HgTe-like lattice	1.17	1.14	1.23	1.20
	$0^- \rightarrow 2^-$, LO(Γ) HgTe-like lattice		1.16		1.22
$a3$	$0^+ \rightarrow 3^+$, LO(Γ) HgTe-like lattice	0.74	0.74	0.77	0.78
	$0^- \rightarrow 3^-$, LO(Γ) HgTe-like lattice		0.76		0.80
$a4$	$0^+ \rightarrow 4^+$, LO(Γ) HgTe-like lattice	0.54	0.55	0.56	0.58
	$0^- \rightarrow 4^-$, LO(Γ) HgTe-like lattice		0.56		0.59
$b1^+$	$0^+ \rightarrow 1^+$, LO(Γ) CdTe-like lattice	2.64	2.68	2.80	2.82
$b1^-$	$0^- \rightarrow 1^-$, LO(Γ) CdTe-like lattice	2.87	2.90	3.08	3.04
$b2$	$0^+ \rightarrow 2^+$, LO(Γ) CdTe-like lattice	1.32	1.30	1.40	1.38
	$0^- \rightarrow 2^-$, LO(Γ) CdTe-like lattice		1.36		1.44
$c1^+$	$0^+ \rightarrow 1^+$, LO(Γ) ZnTe-like lattice	3.00	3.00	3.10	3.16
$c1^-$	$0^- \rightarrow 1^-$, LO(Γ) ZnTe-like lattice		3.26		3.42
$c2$	$0^+ \rightarrow 2^+$, LO(Γ) ZnTe-like lattice		1.46	1.58	1.54
	$0^- \rightarrow 2^-$, LO(Γ) ZnTe-like lattice		1.52		1.60
$k1^+$	$0^+ \rightarrow 1^+$, LO(Γ) ZnTe-cluster	3.62	3.60	3.76	3.78
$k1^-$	$0^- \rightarrow 1^-$, LO(Γ) ZnTe-cluster	3.95	3.96	4.08	4.14
$k2^+$	$0^+ \rightarrow 2^+$, LO(Γ) ZnTe-cluster	1.74	1.74	1.89	1.82
$k2^-$	$0^- \rightarrow 2^-$, LO(Γ) ZnTe-cluster	1.83	1.82	1.89	1.90
$d1^+$	MPR at phonon frequency difference[11]	1.02	1.04	1.11	1.10

FIG. 5. Spectrum and electronic transitions at MPR. Sample IV, $T = 146$ K. The theoretical resonance transitions between Landau levels are shown (E). The magnetic fields corresponding to the resonance peaks are presented in Table V.

MPR peaks is shown in Table V, where the theoretical and experimental resonance fields are given for two temperatures — 146 and 165 K. The rms deviation between the experimental and theoretical positions of the peaks equals 1.5% for $T = 146$ K and 2% for $T = 165$ K (the experimental accuracy in determining the resonance fields is about 3%). Figures 5 and 6 illustrate the interpretation of the MPR peaks for these two temperatures: The experimental resonance curves are presented and the electron transitions between the Landau levels are shown in accordance with the data in Table V (the theoretical positions of the resonances).

It is interesting that the peaks due to MPR with participation of the CdTe LO(Γ) phonons (the series of peaks b) at high temperatures (see the resonance curves for $T = 165$ and 172 K) become comparable to the peaks in the main series [MPR due to HgTe LO(Γ) phonons — series a]. The explanation could lie hidden in the fact that simultaneously with the conventional one-phonon MPRs, in weak magnetic fields this crystal exhibits MPRs, studied in Ref. 11, at the differences of the phonon frequencies. At high temperatures

"downward" transitions, in which a HgTe phonon is absorbed and a CdTe phonon is emitted, can predominate. In other words, energy is transferred from one sublattice to another and a larger number of phonons of the CdTe-like sublattice can compensate for the lower molar percentage of cadmium telluride (there may not be enough time for the difference in the sublattice temperatures to relax in the time during which a magnetic field corresponding to single-phonon MPR — about 2 ms — is reached). Longer pulses or stationary magnetic fields must be used to verify this hypothesis.

7. TEMPERATURE DEPENDENCES OF THE BAND PARAMETERS

The parameters of the band structure of sample IV that were determined above according to the position of the MPR peaks refer to conduction electrons, i.e., to the part of the volume of the experimental epitaxial film where electronic conduction occurred.
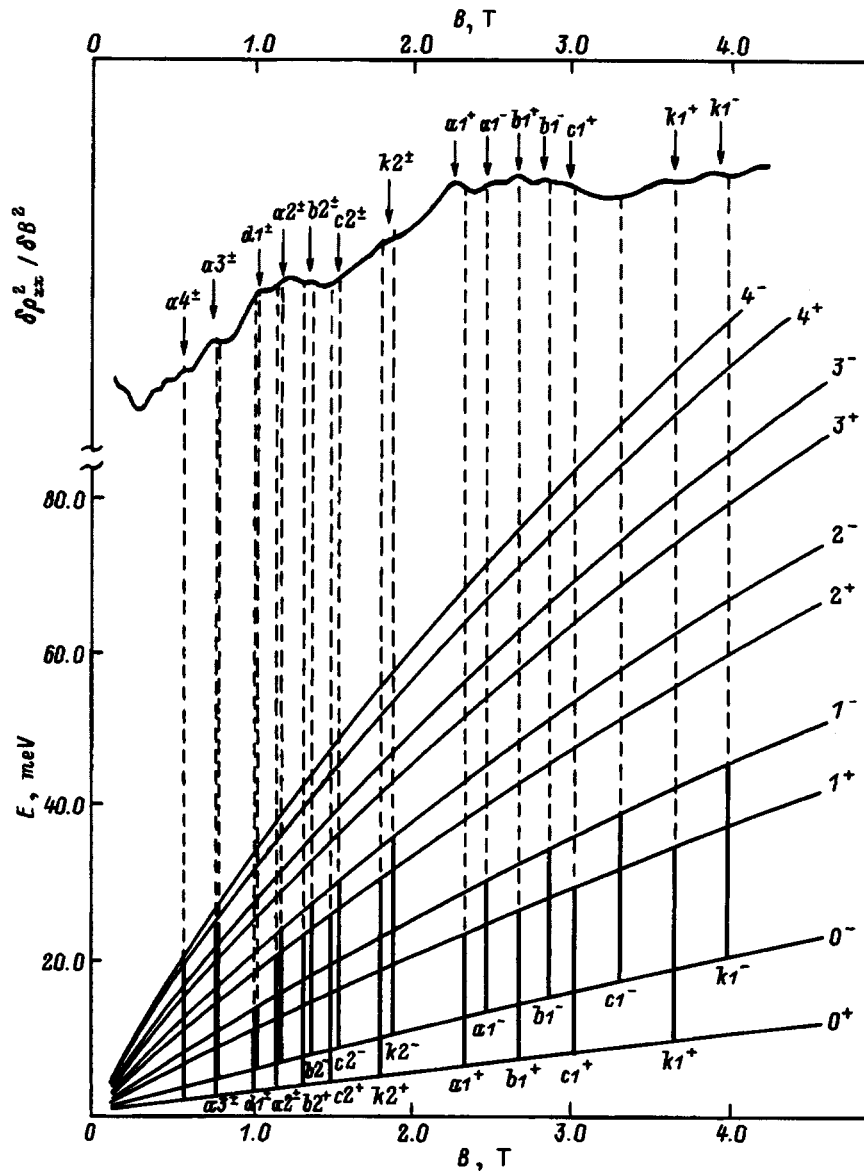
FIG. 6. Spectrum and electronic transitions at MPR. Sample IV, $T = 165$ K. The theoretical resonance transitions between Landau levels are shown (E). The magnetic fields corresponding to the resonance peaks are presented in Table V.

The composition profiles of the film, which are presented in Fig. 1 on the basis of data from x-ray microanalysis, show that the film has a uniform thickness of about 4 μm. The oscillation spectra (RS) investigated by us confirm that the dominant part of the lattice has a trimodal phonon spectrum, which attests to the stochastically uniform distribution of three atoms — cations (Hg, Cd, Zn) in the environment of the anion (Te).[2] However, it follows from the same phonon spectra that spatially bounded regions, in which an anion is surrounded predominantly by Zn atoms[3] (ZnTe clusters) or Hg atoms (HgTe clusters), occupy a certain fraction of the volume.

It is conceivable that electronic transport occurs in a much larger portion of the volume where a stochastically uniform distribution of cations is present. Here, undoubtedly, large fluctuations of the potential can also occur. Such fluctuations are mainly nullified by a sufficiently high electron density, and one can talk about an essentially spatially uniform band structure. The band parameters determined from MPR refer to such a structure.

High peaks of the potential, around which electrons flow, are present near ZnTe clusters. These regions do not participate in conduction. However, the long-wavelength longitudinal optical oscillations of the long-range polarization fields which are excited here, of course, influence electronic transport, penetrating into the portion of the lattice where it occurs, and electrons can be scattered by these oscillations, both elastically and inelastically (the latter is manifested in the MPR).

Deep electron-filled valleys of the potential (electronic lakes), on the other hand, are present near HgTe clusters. They are not coupled clusters, for otherwise conduction would occur along them and would be of a nonactivational character. The macrofields excited in them by LO phonons are screened here because of the locally high electron density
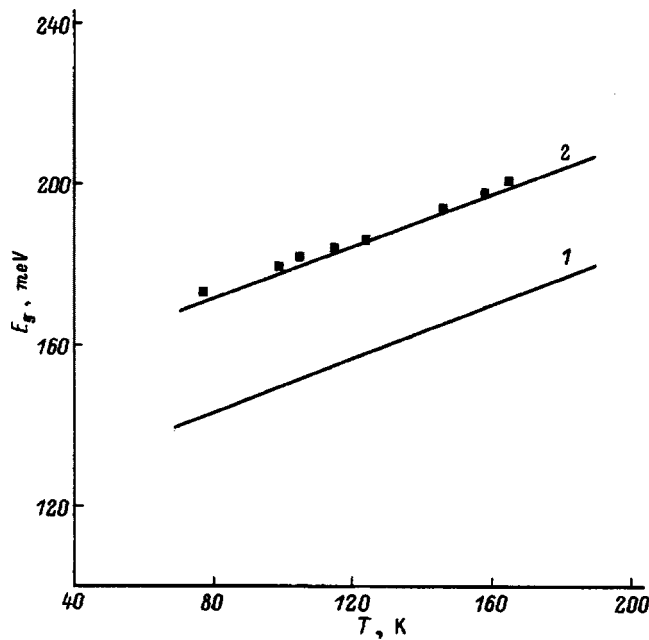
FIG. 7. Temperature dependences of the band gap. Dark squares — experimental values obtained from MPR for region IV. Solid lines — calculation using the empirical function $E_g(x,y,T)$: *1* — Composition IV, $x=0.08$, $y=0.11$; *2* — composition in which the ZnTe content is decreased by 1.5% and HgTe is decreased by 2.5%, i.e., $x=0.0775$ and $y=0.13$.

and do not influence electron transport in the lattice (they are not manifested in MPR).

The model proposed therefore correlates well with the MPR data and with the RS spectra. The temperature dependence of the band gap also fits logically into the model.

The temperature shift of the MPR peaks makes it possible to establish the temperature dependence of the band gap E_g in the temperature range investigated. The procedure, presented above, for determining the band parameters according to the position of the MPR peaks was applied to all resonance curves shown in Fig. 2. MPRs from the differences of the phonon frequencies are more clearly evident at temperatures below 115 K (see Ref. 11). Because of this circumstance, the band parameters were determined at temperatures 77, 99, and 105 K. The dark squares in Fig. 7 show the values of the band gap E_g, which were determined from MPR.

It is interesting to compare the temperature dependence $E_g(T)$ which we observed with that computed using empirical formulas which are usually used for ternary solid solutions, for the composition and temperature dependences of the band gap. For our case of the quaternary (with a common anion) solid solution $Zn_xCd_yHg_{1-x-y}Te$ ($x=0.08$, $y=0.11$) we shall employ the method proposed in Ref. 7 to calculate $E_g(x, y, T)$. In this method three empirical dependences $E_g(c,T)$ (c — concentration of one of the binary compounds) are used: for CHT,[32] for ZHT (zinc–mercury–tellurium),[33] and for ZCT,[7] which are averaged with allowance for the statistical weight of each, as determined by the composition. The dependence $E_g(T)$ calculated in this manner for composition IV is shown in Fig. 7 (curve *1*). We see that the curve lies appreciably below the

values of the band gap determined from MPR (dots in Fig. 7). This discrepancy is probably due to the deviation of the compositions in the regions of the crystal of the solid solution where electronic transport occurs (at MPR, in particular) from the average composition measured by x-ray microanalysis (the spatial resolution of such measurements is greater than 1 μm). Unconnected HgTe and ZnTe clusters were formed by the departure of mercury and zinc from these regions. The molar percentages of the HgTe and ZnTe which form these clusters can be determined by fitting the dependence $E_g(x,y,T)$ to the band gap values obtained from the temperature shift of the MPR peaks. Figure 7 shows the dependence $E_g(T)$ (curve *2*) calculated for the composition with $x=0.0775$ and $y=0.13$. We obtain this composition of the solid solution $Zn_xCd_yHg_{1-x-y}Te$ from the composition IV ($x=0.08$ and $y=0.11$) by decreasing the ZnTe content by 1.5% and the HgTe content by 2.5%. Thus, agreement between the temperature dependences obtained for the band gap from the temperature shift of the MPR and on the basis of the empirical dependence $E_g(x,y,T)$ is obtained if the composition in which the zinc telluride content is decreased by 1.5% and that of mercury telluride by 2.5% is substituted in the emiprical dependence. ZnTe and HgTe clusters, respectively, should be expected to form from this amount of material.

8. CONCLUSIONS

Our investigations of the phonon subsystem (RS) of complex quaternary solid solutions ZCHT and of its interaction with the electronic subsystem (MPR) lead to the following conclusions.

This lattice, which consists of three cations (Hg, Cd, Zn) with one common anion (Te) undoubtedly manifests trimodal behavior of the phonon spectrum. This corresponds to a stochastically uniform distribution of cations.

In a real crystal the stochastic uniformity can be destroyed and clusters in which the anion is surrounded mainly by Zn atoms (ZnTe clusters) or Hg atoms (HgTe clusters) can appear.

Electronic transport in such a lattice evidently occurs along high-mobility channels (bypassing, for example, ZnTe clusters). This does not interfere with the interaction of electrons with long-range polarization fields of the entire spectrum of long-wavelength longitudinal oscillations (including those in ZnTe clusters). At least four kinds of LO phonons participate in the electron-phonon interaction in the solid solutions ZCHT.

The band-structure parameters obtained from MPR correspond to the part of the crystal lattice of the solid solution in which the electronic transport occurs, and its composition can differ somewhat from the average composition of the sample.

[1)]The selection rules can be applied only for RS in polarized light.
[2)]An examination of the atomic configurations occurring in this case falls outside the scope of this paper.
[3)]The probability of such configurations is studied in Ref. 31.

[1]R. J. Nicholas, S. Brunel, S. Huant, K. Karrai, J. C. Portal, M. A. Brummell, Z. Razeghi, K. Y. Cheng, and A. Y. Cho, Phys. Rev. Lett. **55**, 883 (1985).

[2]S. T. Davey, E. G. Scott, B. Wakefield, and G. J. Davies, Semicond. Sci. Technol. **2**, 683 (1987); A. Yu. Egorov, A. R. Kovsh, A. E. Zhukov, V. M. Ustinov, and P. S. Kop'ev, Fiz. Tekh. Poluprovodn. **31**, 1153 (1997) [Semiconductors **31**, 989 (1997)].

[3]A. Rogalski and J. Piotrowski, Prog. Quantum Electron. **12**, 87 (1988).

[4]A. Rogalski, *New Ternary Alloy System for Infared Detectors*, SPIE, Bellingham, 1994.

[5]R. Triboulet, J. Cryst. Growth **86**, 79 (1988).

[6]A. M. Andrukhiv, O. A. Gadaev, V. I. Ivanov-Omskiĭ, K. E. Mironov, V. A. Smirnov, S. U. Yuldashev, and E. I. Tsidil'kovskiĭ, Fiz. Tekh. Poluprovodn. **26**, 1288 (1992) [Sov. Phys. Semicond. **26**, 719 (1992)].

[7]N. L. Bazhenov, A. M. Andruchiv, and V. I. Ivanov-Omskii, Infrared Phys. **34**, 357 (1993).

[8]L. M. Gutsulyak, V. I. Ivanov-Omskiĭ, D. I. Tsypishka, and A. M. Andrukhiv, Fiz. Tekh. Poluprovodn. **30**, 2042 (1996) [Semiconductors **30**, 1064 (1996)].

[9]J. Polit, E. Sheregii, A. Andruchiv, and P. Sydorchuk, in *Die Kunst of Phonons*, edited by T. Paszkiewicz (Plenum Press, N. Y., 1994) p. 415.

[10]A. M. Andrukhiv, V. I. Ivanov-Omskii, J. Polit, and E. M. Sheregii, Acta Phys. Pol. A **87**, 513 (1995).

[11]E. M. Sheregii, J. Polit, J. Cebulski, and A. M. Andrukhiv, Phys. Status Solidi B **192**, 121 (1995).

[12]E. M. Sheregiĭ, Yu. O. Ugrin, D. F. Shuptar, and O. M. Leshko, JETP Lett. **47**, 711 (1988).

[13]E. M. Sheregiĭ, Neorg. Mater. **33**, 208 (1997).

[14]J. Baars and F. Sorger, Solid State Commun. **10**, 875 (1972).

[15]K. K. Tiong, P. M. Amirtharaj, P. Parayanthal, and Fred H. Pollak, Solid State Commun. **50**, 891 (1984).

[16]S. P. Kozyrev, L. K. Vodopyanov, and R. Triboulet, Solid State Commun. **45**, 383 (1983).

[17]E. A. Mozhaev, V. I. Ivanov-Omskiĭ, V. A. Mal'tseva, and D. V. Mashovets, Fiz. Tverd. Tela (Leningrad) **11**, 2147 (1977) [Sov. Phys. Solid State **11**, 1260 (1977)].

[18]E. M. Sheregii and Yu. O. Ugrin, Solid State Commun. **83**, 1043 (1992).

[19]D. W. Taylor, in *Optical Properties of Mixed Crystals*, edited by R. J. Elliott and I. P. Ipatova, Modern Problems in Condensed Matter Sciences, Vol. 23 (North-Holland Publ., Amsterdam, 1988) p. 31.

[20]S. Perkowitz, L. S. Kim, and Z. C. Feng, Phys. Rev. B **42**, 1455 (1990).

[21]N. V. Sochinski, M. D. Serrano, and E. Di'egues, J. Appl. Phys. **77**, 2806 (1995).

[22]C. F. Klingshirn, *Semiconductor Optics* (Springer, Berlin, 1995).

[23]V. M. da Costa and L. B. Coleman, Phys. Rev. B **43**, 1903 (1991).

[24]N. Vegalatos, D. Wahne, and J. S. King, J. Chem. Phys. **60**, 3613 (1974).

[25]J. M. Rowe, R. M. Niclow, D. L. Price, and K. Zanino, Phys. Rev. B **10**, 621 (1974).

[26]E. M. Sheregiĭ and Yu. O. Ugrin, Fiz. Tekh. Poluprovodn. **24**, 1047 (1990) [Sov. Phys. Semicond. **24**, 660 (1990)].

[27]Yu. O. Ugrin, E. M. Sheregiĭ, I. M. Gorbatyuk, and I. M. Rarenko, Fiz. Tverd. Tela (Leningrad) **32**, 43 (1990) [Sov. Phys. Solid State **32**, 23 (1990)].

[28]M. H. Weiler, R. L. Aggarwal, and B. Lax, Phys. Rev. B **16**, 3603 (1977).

[29]Y. Guldner, C. Rigaux, M. Grynberg, and A. Mycielski, Phys. Status Solidi B **81**, 627 (1977).

[30]B. L. Gel'mont, R. P. Seĭsyan, and A. L. Éfros, Fiz. Tekh. Poluprovodn. **16**, 776 (1982) [Sov. Phys. Semicond. **16**, 499 (1982)].

[31]J. Konior, J. Lazewski, and A. Kisiel, Acta Phys. Pol. A **91**, 815 (1997).

[32]M. H. Weiler, in *Semiconductor and Semimetals*, Vol. 16, edited by R. K. Willardson and A. C. Beer (1981) p. 119.

[33]B. Toulous, R. Granger, S. Rolland, and R. Triboulet, J. Phys. C **48**, 247 (1987).

Translated by M. E. Alferieff

Characteristic features of the interaction of porous silicon with heavy water

D. N. Goryachev[a)] and O. M. Sreseli

A. F. Ioffe Physicotechnical Institute, Russian Academy of Sciences, 194021 St. Petersburg, Russia

G. Polisskiĭ

Technical University, Munich, D-85747 Garching, Germany

The interaction of porous silicon (*por*-Si) with heavy water (D_2O) was investigated by means of time-resolved photoluminescence and infrared Fourier spectroscopy. It is shown that contact of *por*-Si with D_2O leads to anomalously rapid oxidation of its surface — at a rate at least an order of magnitude higher than the oxidation rate of *por*-Si in ordinary (protium) water. The oxidation process transforms the chemical composition of the *por*-Si surface and is accompanied by abrupt changes in the spectral and temporal characteristics of the photoluminescence. Assumptions are made concerning the nature of the interaction of porous silicon with heavy water. © *1998 American Institute of Physics.* [S1063-7826(98)02108-5]

The study of the the effect of the surrounding medium on the character of the photoluminescence (PL) of *por*-Si stands out among the many studies of the optical properties of porous silicon (*por*-Si). These investigations are of great theoretical interest. Moreover, they are directly related to the problems of stability of a *por*-Si surface and with the use of *por*-Si as gas sensors.

It is well known that because of its strongly extended surface, *por*-Si is very susceptible to different chemical actions.[1] The optical properties of *por*-Si, specifically, the character of the PL, change substantially. Studies of the interaction of *por*-Si with water have made a large contribution to understanding the processes occurring here.[2–5]

The work done in Refs. 6 and 7 , where the PL of *por*-Si prepared by the conventional electrolytic method but with all components of the electrolyte (HF, C_2H_5OH, H_2O) replaced by the corresponding deuterium-containing compounds was studied, can be put into the same group. In those studies an appreciable (by ∼70 nm) ''blue'' shift of the maximum of the PL spectrum and a substantial slowing down of the degradation of the PL were observed. The authors concluded that the character of the PL is influenced mainly by the changes in the surface structure of *por*-Si, which are associated with the adsorption of deuterium and with the influence of the adsorbate on quantum-well effects in *por*-Si.

The formation of *por*-Si in a deuterium-containing medium can influence not only the surface properties of the silicon, but also change, to a certain extent, the morphology of the entire volume of *por*-Si. For example, in Ref. 7 it was shown that the statistical-average diameters of the nanocrystallites are different. To rule out completely the possibility of such changes, we investigated the interaction of *por*-Si, prepared in a standard electrolyte, with heavy water (D_2O).

The *por*-Si samples were prepared by anodizing compact silicon in ''protium'' electrolyte. Single-crystal *p*- and *n*-type (100) silicon with resistivity $\rho = 2-5\,\Omega\cdot$cm was used as the initial material. The electrolyte consisted of a 1:1 mixture of HF and ethanol. The current density was 10–30 mA/cm^2. The duration of the electrolysis was 5–10 min. The samples were dried in air at temperature 40–50 °C. The *por*-Si was about 4–5 μm thick. To stabilize the optical properties the samples were allowed to stand in air for at least one day and then submerged in heavy water for a certain period of time. Next, the samples were again dried for 10–15 min and transmission spectra in the infrared region (FTIR spectra) and PL spectra were obtained. In parallel, similar samples were allowed to stand in ordinary water, from which the dissolved oxygen was carefully removed beforehand. The FTIR spectra were recorded on a BOMEMDA3.02 infrared Fourier spectrometer in the range 400–4000 cm^{-1} with 1 cm^{-1} resolution. The PL spectra were obtained on a computerized setup based on a MDR-2 monochromator and a FÉU-79 photomultiplier with pulsed excitation of the PL (radiation wavelength $\lambda = 337.1$ nm, pulse time $\tau = 10$ ns) in two regimes: at the maximum of the laser pulse (so-called fast PL) and with a ∼1 μm delay. In the second case the PL spectra can be assumed to be quasistationary.

The residence of *por*-Si samples in D_2O rapidly changes the character of their emission, from red to bluish white. It is evident from Fig. 1 that as the residence time of *por*-Si in D_2O increases, the long-wavelength part of the quasistationary spectrum decreases in amplitude (b, curves *1–3*), but the intensity of the fast short-wavelength component increases at the same time (a, curves *1–3*). Such changes in the PL spectra are characteristic of thermal[8] and liquid[2] oxidation of the surface. It follows from Fig. 1 that these processes are much faster in heavy water than in ordinary water. Two-hour residence in D_2O changes the PL spectrum more strongly than 18-hour residence in H_2O (curves *2* and *4*).

Figure 2 shows the FTIR spectra of the sample before (curve *1*) and after (curve *2*) residence in heavy water for 18 h. For comparison, a portion of the same sample was held for the same amount of time in ordinary water (curve *3*).
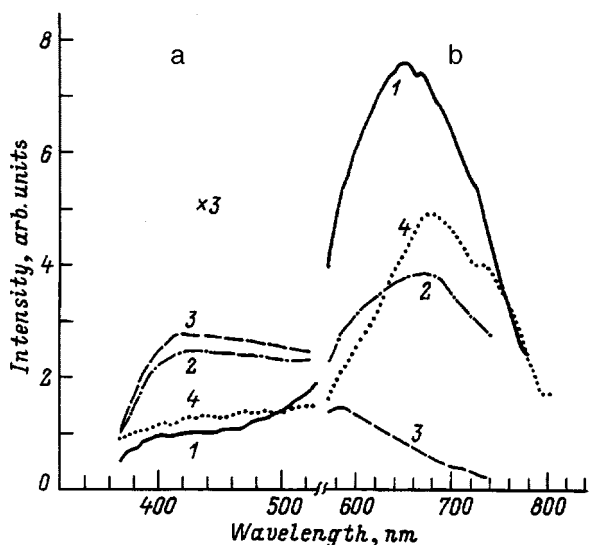
We have observed a large (more than an order of magnitude) difference in the oxidation rates of *por*-Si in heavy and ordinary water. A much more energetic release of hydrogen gas (visible to the naked eye) than in H_2O indicates that the oxidation of *por*-Si in D_2O occurs rapidly. It thus follows that the oxidizing agents are hydrogen ions (deuterium) rather than some other oxidizers.

An unexpected result of the experiments was that lines due to silicon–deuterium bonds were absent in FTIR spectra. It was logical to expect that deuterium-protium exchange, whose rate under our conditions should be quite high,[9] will replace surface structures of the type SiH_x by the corresponding deuterium structures. In particular, a SiD_x triplet was expected to appear in the region 1530–1540 cm^{-1}.[7] Instead, on curve *2* in Fig. 2 we see new lines — 1638 and 2254 cm^{-1}. The latter line was observed previously[10] and attributed to O–Si–H or O_3–Si–H bonds. The 1638 cm^{-1} line could be a "deuterium" analog of the 2254 cm^{-1} line. It is known that the spectral positions of the Si–OH and Si–OD lines are in the ratio ~1.38.[11] In our case the ratio is 2254/1638=1.376, which confirms the assumption made above.

One is forced to acknowledge that the oxidation rate of *por*-Si in heavy water is much higher than the rate of isotopic exchange between heavy water and the surface hydrogen atoms.

These conclusions are supported by experiments on the interaction of *por*-Si with deuterated ethanol C_2H_5OD (Fig. 2, curve *4*). Ethanol is a weaker oxidizer than water. For this reason, the results of isotopic exchange between hydrogen and deuterium atoms — the lines 1534 and 1634 cm^{-1} — can be clearly seen against the background of the slower oxidation of *por*-Si. The first line is attributed to $Si–D_x$ bonds, while the second line, as mentioned above, is attributed to O–Si–D. The peaks in the regions 2900–3000 and 1360–1400 cm^{-1} are due to the interaction with carbon.

At present, only certain assumptions can be made about the reasons for such energetic oxidation of *por*-Si in heavy water. It is known that the greatly extended surface of silicon is capable of reacting intensely with water as a reult of oxidation of the surface by hydrogen ions (more accurately, H_3O^+ or D_3O^+ ions). However, as-grown *por*-Si layers are protected from oxidation by a so-called passive hydrogen film, which consists of hydrogen atoms directly bound to silicon atoms ($Si–H_x$ bonds), and a monolayer of water molecules which are held at the *por*-Si surface by electrostatic attraction forces.[12] It is logical to assume that the isotopic exchange affects primarily this hydrate shell and not the hydrogen atoms that are directly bound to silicon.

Apparently, because of the differences in the effective radii of the protium and deuterium ions or in the vibrational properties of their bonds with other atoms, this exchange leads to crumbling of the protective passive film and to rapid oxidation of *por*-Si. In the process, the deuterium ions, having undergone reduction, do not form new bonds with silicon, but rather unite with molecules of hydrogen gas which is released at the *por*-Si surface. In the corresponding FTIR spectra (Fig. 1, curve *2*) there are therefore virtually no lines that are responsible for bonds of the type $Si–D_x$.

FIG. 1. Spectra of fast (a) and quasistationary (b) photoluminescence of *por*-Si. Holding time in D_2O, h: *1* — 0, *2* — 2, *3* — 18. *4* — Holding in H_2O for 18 h.

Curve *1* shows absorption on different vibrations of the Si–H, Si–H_2, and Si–H_3 bonds (triplets near 2100, 910, and 650 cm^{-1}), which is characteristic of hydrogen passivation of the silicon surface, whereas after residence in heavy water the lines due to absorption on Si–O–Si bonds (450, 800, and 1100 cm^{-1}) are brightest. Such a transformation of the spectra indicates oxidation of the *por*-Si surface.

Control experiments in which samples were held in ordinary water presaturated with oxygen were also performed. No appreciable difference in the oxidation rate of *por*-Si as compared with water without free oxygen was observed. This rules out the possibility of rapid oxidation of *por*-Si by oxygen dissolved in D_2O.
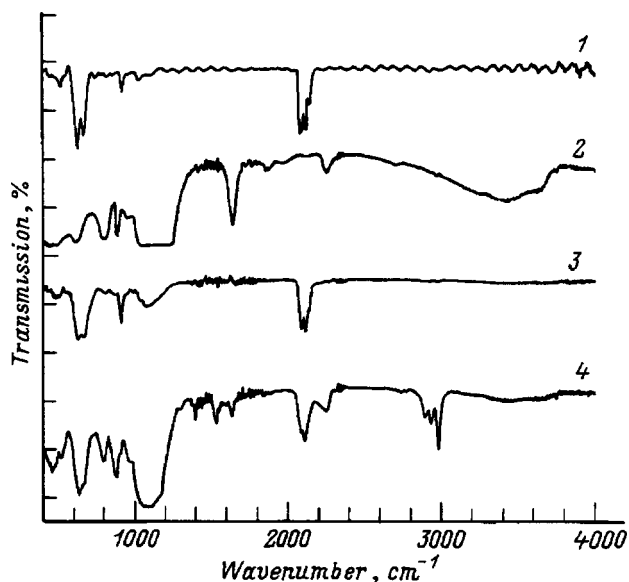

FIG. 2. FTIR spectra of *por*-Si: Samples: *1* — Initial; *2–4* — after 18 h residence in D_2O, H_2O, and deuterated ethanol, respectively.

In summary, we have observed an anomalously rapid oxidation of *por*-Si in heavy water. We showed that contact of *por*-Si with heavy water leads to oxidation of the *por*-Si surface at a rate at least an order of magnitude higher than the oxidation rate of *por*-Si in ordinary (protium) water. The process transforms the chemical composition of the *por*-Si surface and is accompanied by rapid changes in the spectral and temporal characteristics of PL.

Assumptions were made concerning the nature of the anomalous interaction of *por*-Si with heavy water. This interaction is not associated with deuterium-protium exchange of heavy water with hydrogen atoms that are chemisorbed on the *por*-Si surface.

[a] E-Mail: dng@olgas.ioffe.rssi.ru

[1] A. G. Gullis, L. T. Canham, and P. D. J. Calcott, Appl. Phys. Lett. **82**, 909 (1997).

[2] X. X. Hou, G. Shi, W. Wang, F. L. Zhang, P. N. Hao, D. M. Huang, and X. Wang, Appl. Phys. Lett. **62**, 1097 (1992).

[3] T. Tamura, A. Takazawa, and M. Yamada, J. Appl. Phys. **32**, L322 (1993).

[4] S. Zangooie, R. Bjorklund, and H. Arwin, J. Electrochem. Soc. **144**, 4027 (1997).

[5] P. Gupta, A. C. Dillon, A. S. Bracker, and S. M. George, Surf. Sci. **245**, 360 (1991).

[6] T. Matsumoto, Y. Masumoto, and N. Koshida, Mater. Res. Soc. Proc., Pittsburg, PA, 1997, Vol. 452, p. 449.

[7] T. Matsumoto, Y. Masumoto, S. Nakashima, and N. Koshida, Thin Solid Films **297**, 31 (1997).

[8] D. I. Kovalev, I. D. Yaroshetzkii, T. Muschik, V. Petrova-Koch, and F. Koch, Appl. Phys. Lett. **64**, 214 (1994).

[9] L. Melander and W. H. Saunders, *Reaction Rates of Isotopic Molecules*, New York, 1980 [Mir, Moscow, 1983].

[10] N. Ookubo, H. Ono, and Y. Ochiai, Y. Mochizuki, and S. Matsui, Appl. Phys. Lett. **61**, 940 (1992).

[11] A. V. Kiselev and V. I. Lygin, *Infrared Spectra of Surface and Adsorbed Substances* [in Russian], Nauka, Moscow, 1972.

[12] A. I. Mamykin, A. Yu. Il'in, V. A. Moshnikov, N. E. Mokrousov, A. A. Mamykin, and A. I. Pershin, Fiz. Tekh. Poluprovodn. **29**, 1874 (1995) [Semiconductors **29**, 979 (1995)].

Translated by M. E. Alferieff

Information for Authors submitting papers for publication in the Russian language

In accordance with an agreement between the publishers of the journal and the American Institute of Physics, the latter translates the journal ''Fizika i Tekhnika Poluprovodnikov'' into English and distributes the English version outside Russia under the title SEMICONDUCTORS. The Russian and English versions of the journal are published simultaneously.

In submitting a manuscript to the journal ''Fizika i Tekhnika Poluprovodnikov,'' authors grant the publishers and editorial board of the journal the right to publish the article in Russian and to give it to the American Institute of Physics for translation and publication in English. Authors retain all remaining rights to the manuscript, such as permission to reproduce their original figures in publications by other authors.

All responsibility for satisfying the copyrights of other persons or organizations rests exclusively with the authors of the submitted article.

1. RULES FOR PREPARING ARTICLES FOR THE JOURNAL "FIZIKA I TEKHNIKA POLUPROVODNIKOV"

1. Articles containing the results of works performed in institutions should have, without fail, the the approval of the institution. In the event that some authors are employees of different institutions, the place of employment of each author should be given (name of institution and postal address).

2. Two copies of the article should be submitted. The text should be printed double-spaced with 3-cm margins on the left side and at the top and bottom of the page. The letters, indices, and line spacings should conform to the standard typewriter type (in the event that the article is composed on a computer — not less than 12 pt). The print should be dark; if printed on a printer, the ''draft'' mode is not permissible.

3. The total length of an article, as a rule, should not exceed 20 pages, including the title page, the text of the article, and separate pages containing the list of references, captions, tables, and abstracts in Russian and English. The number of figures should not exceed six, including figures with letter designations (for example, Fig. 1a and Fig. 1b are counted as two figures).

4. The total length of a brief communication should not exceed nine pages, including the title page, the text of the communication, and separate pages containing the list of references, captions, tables, and abstracts in Russian and English. The number of figures should not exceed three, including figures with letter designations (for example, Fig.1a and Fig.1b are counted as two figures). Brief communications containing urgent scientific information have absolute priority in the schedule for publication in the journal (not more than five months from the moment the communication is accepted for publication).

5. The following must be included on separate pages when submitting an article and a brief communication: a) list of references, b) list of captions, c) tables (each table on a separate sheet), d) abstract in Russian (not more than 100 words for an article and not more than 50 words for a brief communication), e) abstract in English. The title page of the manuscript must contain only the title of the article, the last names of the authors, and the names and addresses of organizations where the work was performed.

6. The English abstract must contain the title of the article or brief communication, the last names of the authors, the names and addresses of organizations, and the country name. The English abstract must be a translation of the Russian abstract. Authors are free to include a fax number and/or e-mail address for communication. An example of a correct format of the English abstract is given below.

Recombination of nonequilibrium carriers in the tracks of heavy ions in silicon

V. K. Eremin, I. M. Il'yashenko, N. B. Strokan, and B. Shmidt*

A. F. Ioffe Physicotechnical Institute, Russian Academy of Sciences, 194201 St. Petersburg, Russia

*Institute for the Physics of Ion Beams and Materials Research, Rossendorf Research Center, D-01314 Dresden, Germany

The interaction of various types of nuclear radiation with semiconductors has usually been studied in two aspects, separately. First, manifestations of resulting structural defects and of a degradation of electrical properties are studied. Second, the behavior of the nonequilibrium-carrier charge is studied. The interaction of defects and carriers determines both the recombination of carriers and the recombination of the primary Frenkel pairs. For carriers which have recombined, the result is a new dependence of the electric field in the detector. It is logarithmic, in contrast with the hyperbolic law which holds for the case of α particles (''light'' ions).

7. For rapid and most objective refereeing, the authors can provide a list of possible referees together with their places of employment. The presence of such a list does not deprive the editorial board of the right to make the final choice of referee.

8. In preparating a manuscript, keep in mind that the editorial board requests the referee to draw conclusions concerning the following points: a) Does the article conform to the subject matter of the journal? b) Does the article contain clearly formulated, new scientific results? c) Are the conclusions of the article sufficiently reliably substantiated? d) Is the exposition clear? e) For whom is the article of interest?

9. Proofs are not returned to the authors, since, as a rule, they are returned to the editorial office after the issue has already been sent to the printer and it is impossible to make any changes. Prepare your manuscripts carefully. Minor misprints and stylistic errors in the manuscript and proofs will be corrected by scientific and literary editors. If you discover inaccuracies in a manuscript after it has been submitted to the journal, contact the editorial office immediately by telephone at (812)-218-36-12 or editorial board at (812)-247-91-06 or by e-mail at (semicond@pop.ioffe.rssi.ru).

2. STYLE

1. Pay careful attention to the style of your article. Avoid long constructions which often consist of a complicated combination of dependent clauses, introductory words, participial and verbal adverbial constructions.

Express scientific thoughts succinctly. Clearly formulate the purpose of the article at the beginning of the article. Single out the basic results and indicate the changes and additions which your work has made in the current state of the problem.

Avoid coining new terminology, do not use jargon, and do not use English words if a firmly established Russian term exists (for example, do not write ''gate'' instead of the standard ''zatvor,'' etc.).

For narrowly specialized terms, whose literal translation into English can lead to errors or inaccuracies, it is desirable either to indicate the accepted English equivalent in the text of the article after the term is first mentioned or to write it out on a separate sheet of paper with the note ''For translator.'' For example, ''x-ray spectral microanalysis (electron probe microanalysis).''

Do not use unexpanded abbreviations in the main text of the article and do not use abbreviations at all in the title and abstracts. Even if the abbreviation is generally accepted (such as ''IVC'' or ''IR''), the expansion should be given once at the beginning of the article. For example, ''current-voltage characteristic (IVC).''

2. Footnotes should be continuously numbered and each one should be printed on the same page to which it refers. Footnotes to tables should be printed below the table and marked by asterisks (one, two, and so on) in front of which the word ''Note'' should appear.

3. Citations to the references are indicated by a number (number in the list of references) enclosed in brackets, [1, 2] or [3–6], in the order in which they appear in the text.

3. SYMBOLS, INDICES, AND EQUATIONS

1. Only Latin and Greek letters should be used to designate physical and mathematical quantities, including indices.

Latin lower- and upper-case letters, which look alike, should be marked with a pencil: upper-case letters (for example, *C, K, P, S, V, W*) should be marked two underbars, while lower-case letters should be marked with two overbars (for example, *c, k, p, s, v, w*). The letters O or *o* should be underscored, while a zero should be left unmarked. To distinguish the letter I (''and'') from J (''iota'') and 1 (''ell'') from 1 (unity), I (''and'') should be written as a Roman numeral and marked with two underbars, while the letter l (''ell,'' lower-case) should be circled with a blue pencil.

Gothic letters should be circled with a blue pencil, and script Latin letters (for example, $\partial, \mathcal{L}, \mathcal{R}, \mathcal{H}$) should be circled with a green pencil.

All letters of the Greek alphabet should be underlined with a red pencil.

Do not use arrows to designate vectors; underline letter symbols with a blue pencil.

The use of the Cyrillic alphabet for letter symbols, including in super- and subscripts, is not permitted.

2. All notation and formulas must be written out sharply and clearly. Superscripts and subscripts must not be written on the same line as the main text. Superscripts should be marked with an underarc in pencil and subscripts should be marked with an overarc. Primes must be distinguished from one, and one should be distinguished from a comma.

Use a period, not a comma, in numbers with decimal fractions.

Endeavor to write equations in a manner so that they would not be ''multistage.'' Use $\exp x$ instead of e^x, and also write fractions with a solidus, remembering to insert parentheses clearly so that the numerator can be easily distinguished from the denominator.

Number equations in the text in order.

4. REFERENCE LISTS

The references should be listed in the order in which they are mentioned. References are cited in the text by a number enclosed in square brackets: [1, 2] or [3–6]. The last names of all authors are enumerated in the list of references. The list is formatted as follows.

For journal articles: I. O. Last Name of authors, name of the journal, volume, page (year). For journals where pages are not numbered continuously throughout the year (for example, ''Zhurnal tekhnicheskoĭ fiziki'' and ''Pis'ma v Zhurnal tekhnicheskoĭ fiziki after 1989) the volume number should be followed by the issue number — No. 3.

For books: I. O. Last Name of authors. Title (city, publisher, year). At the discretion of the author (authors) of the paper, the volume — t. 2 or v. 2, part — ch. 2 or pt. 2, chapter — gl. 2, section — § 2, page — s. 32 o rp. 32 are indicated at the end of each citation.

For articles in a collection: I. O. Last Name of authors. Title of the collection [edited by I. O. Last Name can be included] (city, publisher, year) page — s. 32 or p. 32. (In this case the starting page of the article must be indicated.)

A citation can also contain other information enabling the reader to obtain more complete information and facilitating searches. For example:

— In a citation to the proceedings of a conference, together with publishing information, the location and date of the conference can be indicated;

— if the edition is a translation, additional citations to the original can be given; etc.

An example of the format of a list of references is given below.

References

[1] O. V. Konstantinov and B. V. Tsarenkov. FTP, **24**, 2126 (1990).

[2] B. R. Nag. Appl. Phys. Lett., **65**, 1938 (1994).

[3] F. Kh. Abdullaev and É. N. Tsoĭ. ZHTF, **67**, vyp. 8, 57 (1997).

[4] L. D. Landau and E. M. Lifshitz. *Statisticheskaya fizika* (M., Nauka, 1976) ch. 1, gl. 7, s. 60.

[5] M. Kholl, *Kombinatorika* (M., Mir, 1967) t. 1, s. 137 [Per. s angl.: M. Holl. *Combination Theory*, ed. by C. Domb, M. S. Green (Toronto–London–N. Y., Academic Press, 1961) v. 1].

[6] S. Kirpatrik. V sb.: *Teoriya i svoĭstva metallov.* Ser. *Novosti fiziki tverdogo tela* (M., Izd-vo standartov, 1977) vyp. 7, s. 211.

[7] A. Green, S. Metlack and J. Zelman. *Proc. 5th Int. Conf. High Pressure in Semicond. Phys.* (Kyoto, Japan, 1993) v. 2, p. 98. or A. Green, S. Metlack, J. Zelman. *Proc. 5th Int. Conf. High Pressure in Semicond. Phys.* (Kyoto, Japan) [J. Appl. Phys., **32**, Suppl. 32–1, 178 (1993)].

[8] M. H. Moloney. *Conference on Lasers and Electro–Optics, Baltimore, MA, 1992,* OSA Technical Digest Series (Optical Society of America, Washington, DC, 1992) v. 10, p. 46.

[9] I. L. Drichko and A. M. D'yakonov. Tez. dokl. 2-ĭ Ross. konf. po fizike poluprovodnikov (SPb; 1996) t. 1, p. 152.

5. FIGURES

1. Line drawings (graphs) should be drawn clearly and in a manner so that all points and curves are visible and do not merge on reduction. A figure should not be overloaded with points and curves. 2. Every figure should be drawn on a separate sheet of standard paper. Figure should not exceed the standard page in size and margins of at least 3 cm must be left. The number of the figure, last name of the first author, and the title of the article (abbreviated) should be indicated on the back. 3. Continuous-tone figures (photographs) should be printed on glossy white paper with inking. Under no circumstances should photographs be glued to the article, and they should not be glued to paper. All labels on continuous-tone figures should be given only in one copy; the second copy should be clear. 4. All labels and designations in figures (but not captions) should be written in English. International symbols are used for units of measurement in figures; Russian symbols are used in captions and in the text. 5. Endeavor to limit labels in the figure itself; when possible, use number or letter designations and transfer all explanations to the caption or text. 6. Special symbols (circles, triangles, line segments, etc.) are not permitted in the caption. Denote such elements by numbers in the figure. The standard method for preparing figures for publication is complete reformatting of the variant provided by the author so that the figures would conform to the style adopted in the journal and would meet the requirements of polygraphy. Only absolutely necessary information is retained in the figure, and all supplementary information is transferred to the caption.

6. REQUIREMENTS FOR AUTHOR-FORMATTED FIGURES

For authors who wish to prepare figures in the final form that meet the requirements of the journal, the basic requirements for such figures (camera-ready) are presented below. Observing strictly the style adopted for figures in the journal, they can be included in the article as provided by the author, but only if all figures in the artcile (except photographs) are drawn in the same style. 1. The figures must be printed with a laser printer (not less than 300 dpi) on white paper with a density of 70 or 80 g/m^2. Figures must not be printed on a gray background, and continuous-tone figures must not be printed on dot-matrix printers. Such figures cannot be reproduced with adequate quality. 2. When reproduced in the journal, figures are generally reduced to the dimensions of a journal column (8 cm). In view of this circumstane: — all lines must be black and heavy (gray and thin lines may disappear when the figure is reduced; this pertains especially to dashed and dotted lines); — all symbols and letters must be of a size such that after reduction they are not less than 1.5 mm and not more than 3 mm in size; — in choosing designations for curves and lines in plots, the order of preference for such designations adopted in the journal should be taken into account: 1) solid, 2) dashed, 3) dot-dashed, 4) dotted, 5) other designations (alternation of short and long dashes, etc). 3. Ticks on the coordinate axes should be oriented in a direction pointing into the figure, and arrows should not be placed at the tips of the axes. 4. The numbers on the axis scales are written horizontally. In decimal fractions, periods and not commas are used. Numbers with an indication of the order of magnitude should not be written in the style 2E6 (incorrect); the format $2 \cdot 10^6$ should be used (multiplication is indicated by a centered dot). 5. Abscissa labels are written horizontally using lower-case letters (first letter capitalized) and centered. 6. Ordinate labels are written using lower-case letters (first letter capitalized) along the axes (vertically from bottom to top) and centered. 7. The name of the quantity plotted along an axis is separated from its units by a comma. 8. All labels in a figure and on the axes are written in English, including the units of the physical quantities. The Greek alphabet can be used. Cyrillic letters are not permitted. 9. The numbers on curves (*1, 2, 3, …; 1′, 2′, 3′* and so on) and on parts of figures (*a, b, c …*) should be written in italics without parentheses. 10. Physical quantities or parts of formulas on the axes of plots and within the body of a figure should be italicized, except for numbers, symbols of chemical elements, and units of measurement, which are always written using an upright font. Examples: in the body of a figure n-GaAs; $E_{CdTe}^{LO}=0.1$ meV; $T_K^{2\Omega}=10$ mK; on the axes $N_{GaSb} d_0^{3/2}$, cm$^{-3/2}$; $M_H^{1/3}$, arb. units; Intensity, arb. units; Length, μm. Note that arbitrary units of measurement (arbitrary units) on the axes should be written in the manner indicated above. 11. Helpful supplementary information is permitted in the figures, if the figures are prepared using high-resolution plots. Labels in figures are of this type (except for the cases where italics are used, as indicated in points 9 and 10 above, lower-case letters of an upright font are recommended). The editorial office retains the right to change the formatting of figures which do not satisfy the requirements indicated above. In this event, all information except that which is absolutely necessary will be transferred to the caption in order to simplify and reduce the production costs of figures in the journal. We request that authors adhere to our rules and prepare articles carefully. Articles preapred in violation of the rules will be returned to their authors. We thank all who will contribute to the improvement of our journal. We are grateful to you for your cooperation.

Editorial Board

Translated by M. E. Alferieff

ERRATA

Erratum: Diffusion saturation of undoped hydrated amorphous silicon by tin impurity [Semiconductors 32, 263–266 (March 1998)]

A. N. Kabalbin, V. B. Neĭmash, V. M. Tsmots', and V. S. Shtym

Institute of Physics, Ukrainian National Academy of Sciences, 252650 Kiev, Ukraine
Fiz. Tekh. Poluprovodn. **32,** 8, 1026 (August 1998)

A major correction was reported by the *Semiconductors* Editorial office in St. Petersburg. Specifically, the title was incorrect. The correct title should read: Magnetic ordering of radiation defects in silicon.